FERMILAB-THESIS-2018-14

Measurement of the kaon production normalization in the NuMI target using uncontained charged-current muon neutrino interactions in the NOvA Far Detector

by

José Andrés Sepúlveda-Quiroz

A dissertation submitted to the graduate faculty

in partial fulfillment of the requirements for the degree of

DOCTOR OF PHILOSOPHY

Program of Study Committee:
Mayly Sánchez, Major Professor
Frank Krennrich
Kerry Whisnant
James Vary
Ranjan Maitra

The student author, whose presentation of the scholarship herein was approved by the program of study committee, is solely responsible for the content of this dissertation/thesis. The Graduate College will ensure this dissertation/thesis is globally accessible and will not permit alterations after a degree is conferred.

Iowa State University

Ames, Iowa

2018

Copyright © José Andrés Sepúlveda-Quiroz, 2018. All rights reserved.

DEDICATION

I dedicate this work to my beloved parents, Carmen and José, to my fearless brother César, and to my dear Mehreen. To all of you with gratitude.

TABLE OF CONTENTS

Page

LIST OF TABLES

Page

LIST OF FIGURES

Page

ACKNOWLEDGEMENTS

I want to express my sincere gratitude towards everyone that lead to the accomplishment of this work. I want to start by thanking my advisor, Mayly Sanchez, for giving me the opportunity to part of the NOvA team. I am grateful for her encouragement through the ups and downs of my PhD. I want to thank her for being an amazing role model that helped me decipher the mysteries of neutrinos. "Always the big picture", as she says. I want to thank my mentor, Jonathan Paley. For all his time, patience, and willingness to teach through all these years. He showed me to do something I never thought of doing: to program. He welcomed me into his family gatherings during Thanksgiving and Christmas. I will never forget his kindness and hospitality during a time I missed my family most.

Many thanks to the members of my committee: Frank Krennrich, Kerry Whisnant, James Vary, and Ranjan Maitra. I am grateful for your generous time and willingness to review the contents of my thesis.

I want to also mention my gratitude to my collaborators in NOvA. I enjoyed learning a lot while working with everyone in the data quality, detector commissioning, calibration, and APD testing groups. Many thanks to all the crew of experts and technicians that kept both detectors up and running. Special thanks to Louise Suter, with whom I worked closely during the Near Detector FEB installation. I also want to thank my analysis group conveners Jon Paley and Greg Pawloski in the first round. And to Jeff Hartnell and Alex Radovic in the final round. I am grateful to Kirk Bays for his discussions related to the cosmic rejection and to how to add a variable to the CAFs.

I am indebted to all the talented graduate students and postdocs on NOvA who helped thought this journey: Evan Niner, Michael Baird, Chris Backhouse, Luke Vinton, Fernanda Psihas, Justin Vasel, Dominik Rocco, Leo Aliaga. And many others I am forgetting to mention.

To my colleagues at team ISU, past and present. Thanks to Gavin Davies, for his infinite patience. His advice and enthusiasm during my first year of grad school was priceless. Thanks to Karl Warburton and Ashley Back for all the help and discussions during my last months. To my roommate Tian Xin, thanks for his support. I will never forget his wisdom during endless discussions about physics. Most of the time while waiting at traffic jams. And thanks for that Pikachu song I will always remember. I want to thank my office-mate Erika Cataño-Mur for being such a great physicist. Her help and discussions were key for some of the parts of this thesis (and my defense).

To the wonderful people I met and shared memories at Fermilab: Mehreen, Kuldeep, Biswaranjan, Faiza, Prabhjot, Kousik, Barnali, Diana, Serdar, Stefano, Siva, Shaokai. Thanks for all the good times. To the FNAL Cricket Team, thanks for letting me play. To Minerba Betancourt and Jesus Orduña, thanks for their friendship. To my dearest friend Enrique Arrieta-Díaz, thanks for all his guidance. His discussions about physics, politics, life and accordions will be always present. And thanks for showing me how a good vallenato sounds like.

To the wonderful people I met in Ames, Iowa: Donna, Claudia, Caroline, Paula, Saúl, Vilma, Tomoko, and Miralba, thank you for getting me started.

To my girlfriend Mehreen, thank you for sharing this slice of space-time with me. Your advice and endless support showed me how much you love me. Your fearless way to approach life have inspired me to continue through all this time.

Finally, I want to express my gratitude towards my parents and brother. Their unconditional love brought light during the nights of many cold winters. Far from the warm ocean, I will remember all the stories of struggle, joy, and hope we shared about over the phone. I am looking forward to the many more dreams yet to achieve. And to my future self, let this work be a reminder of the accomplishment of one of my biggest dreams.

ABSTRACT

NOvA is a long-baseline neutrino oscillation experiment that uses the NuMI beam from Fermilab. Its physics goals include providing constraints to the neutrino mass hierarchy and the CP-violating phase δ by precision measurements of the electron (anti)neutrino appearance in a muon (anti)neutrino beam. Similarly, new limits on the values of $\sin^2\theta_{23}$ and Δm^2_{32} will be achieved by measurements of the muon (anti)neutrino disappearance probabilities. A combined analysis measurement will allow a better resolution of the θ_{23} octant.

The NuMI beam is produced by the collision of high energy protons into a target, giving rise to kaon and pion mesons that decay to neutrinos of a specific flavor. This thesis presents a measurement of the kaon production normalization scale using uncontained charged-current muon neutrinos at the Far Detector. Because the neutrino beam is not pure in flavor, it contains an admixture of other different neutrino flavors that become a source of background. Therefore, it is of paramount importance for accelerator experiments, such as NOvA, to have a reliable flux prediction of the neutrino beam in order to achieve its physics goals.

One method to constrain the flux is to constrain and measure each flux component independently. The kaon component contributes to the intrinsic ν_e contamination of the beam, a key background for the ν_e-appearance analysis. We observed that the uncontained sample in the 10-20 GeV region corresponds to the kaon component of the NuMI beam at the Far Detector. We also found a 60-80% correlation between the Near Detector ν_e background and the Far Detector ν_μ uncontained signal.

The data used for this analysis was collected from October 2014 to February 2017, corresponding to 7.99×10^{20} protons-on-target (POT). The ratio between the Far Detector data and the simulation is fitted to a line in the 10-20 GeV energy region. Calibration, energy scale, final state interactions

and neutrino flux (e.g. beam transport and hadron production shape only) systematic uncertainties are considered. The kaon production normalization scale is measured to be $S_K = 1.07 \pm 0.16$.

CHAPTER 1. INTRODUCTION AND HISTORY

A period of remarkable scientific discoveries in physics occurred between the end of the nineteenth century and the beginning of the twentieth century. We began to explore matter at a fundamental level, such as the idea that physical quantities can have only discrete values. And also, we began to explore the cosmos. In midst of such revolution, the main subject of this thesis -the neutrino- appears as a answer to an unexpected experimental problem. The aftermath results in one of the most prominent endeavors of scientific research, which continues until today.

1.1 The Neutrino

Neutrinos were theoretically postulated by Wolfgang Pauli in the early 1930s. The idea that a low-mass neutral particle, entitled by Enrico Fermi as the neutrino, was emitted with the electron in the β decay, solved the problem of the continuous energy spectrum first observed by J. Chadwick in 1914 and later confirmed by C. Ellis and W. Wooster in 1927 [68], In the three-body decay $n \rightarrow p + e + \nu$, the electron was allowed to share the energy of the reaction with the neutrino, keeping the conservation laws intact. The task in the following years was to detect these neutrinos postulated by Pauli.

Most of the time, neutrinos pass through matter without actually interacting. But Fermi's theory of the weak force predicts that a neutrino can produce an inverse beta decay process. The antineutrino (antiparticle of the neutrino) will occasionally interact with a nucleus $N(n, p)$, with n as the number of neutrons and p the number of protons, through the weak force via the reaction

$$\overline{\nu} + N(n, p) \rightarrow e^{+} + N(n + 1, p - 1).$$

In 1951, Fred Reines and Clyde Cowan began to collaborate in a series of novel experiments that culminated in the detection of the neutrino. They decided to use the inverse beta decay as a signature of a neutrino reaction.

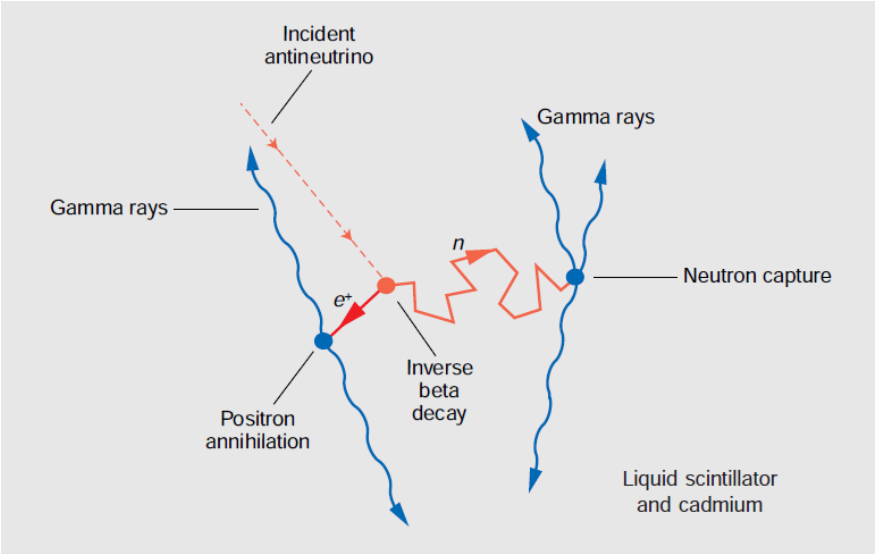

Figure 1.1: The signature of an inverse beta decay process [136].

As seen in Fig. 1.1, the final state particles in an antineutrino-nucleon reaction are a positron and a neutron. The positron eventually will encounter an electron and annihilate, producing two gamma rays. If this reaction occurs in a detector filled with liquid scintillator, the two gamma rays will produce a flash of light that would be detected by photomultiplier tubes. After approximately 10 μs, the neutron will be captured by a neutron-friendly element, in this case cadmium, which when dissolved in the medium releases about 9 MeV of energy in the form of gamma rays after the neutron capture. This gamma burst is also detected by the photomultiplier tubes. The sequence of two flashes of light separated by roughly ten microseconds is the signature of an inverse beta decay.

In 1956 Cowan and Reines conducted a decisive experiment at the Savannah River Plant, in South Carolina. After substantial improvements in the cosmic background and signal separation, two large flat plastic tanks were filled with water. The protons in the water served as the targets for

the inverse decay process. Cadmium chloride dissolved in tanks provided the cadmium nuclei that would capture the neutrons. The target tanks were sandwiched between three large scintillator detectors, having photomultiplier tubes on their sides.

On June of the same year, a telegram was sent to Pauli in which both announced the experimental detection of the neutrino [60]. In 1995, Fred Reines won the Nobel Physics Prize (C. Cowan deceased).

1.2 How many neutrino types?

Following the results of the Cowan and Reines experiment, physicist were intrigued by two questions related to the nature of the neutrino. The first question was whether the neutrino and the antineutrino were the same particle (Majorana particle) or a different particle (Dirac particle). The second was about the number of neutrino species, e.g. if the neutrino associated with the beta decay was the same as the neutral particle from the pion or muon decay.

In 1962, by using the recently developed high energy beam of neutrinos produced from the collision of protons with a fixed target and subsequent meson decay ($\pi \to \mu + \nu$), the team of Schwartz, Lederman, Steinberger and collaborators at Brookhaven tested the hypothesis of whether $\nu_e = \nu_\mu$, e.g. if the reactions

$$\nu + n \to p + e^- \qquad \overline{\nu} + p \to n + e^+ \qquad (a)$$

$$\nu + n \to p + \mu^- \qquad \overline{\nu} + p \to n + \mu^+ \qquad (b)$$

occur at the same rate. They observed a deficit of electron shower-like events and concluded that $\nu_e \neq \nu_\mu$, i.e. there are two types of neutrinos. This also resolved the problem raised by the forbiddenness of the $\mu^+ \to e^+ + \gamma$ decay, noted by T.D. Lee and C.N. Yang [63]. Schwartz, Lederman, Steinberger won the 1988 Nobel Physics Prize for this effort.

The tau-neutrino ν_τ was inferred after the evidence of a new lepton in an electron-positron experiment at the Stanford Linear Accelerator Center (SLAC). The group led by Martin Perl found

events of the form $e^+ + e^- \rightarrow e^+ + \mu^\mp +$ missing energy and noted that this was the signature for a new type of particle [132, 71, 131]. The Direct Observation of The Tau (DONUT) experiment observed two events identified as $\tau \rightarrow e + \nu_\tau + \nu_e$ and concluded that these events were indeed tau neutrino ν_τ charged-current (CC) interactions. Martin Perl won the Nobel Prize in Physics jointly with Fred Reines in 1995.

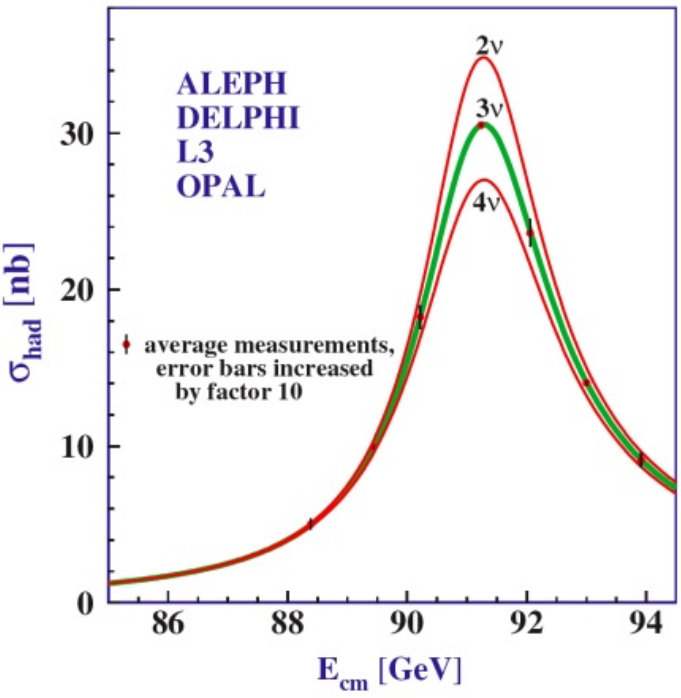

Figure 1.2: Measurements of the hadron production cross-section around the Z resonance. The curves indicate the predicted cross-section for two, three and four neutrino species with Standard Model (SM) couplings and negligible mass [145].

The current consensus is that there are three types of neutrinos: ν_e, ν_μ, and ν_τ. The evidence comes from measurements of the Z boson. The Heisenberg uncertainty principle states that if a particle has a finite lifetime then it also must have an intrinsic width. The shorter the lifetime of the particle, the larger the width. Both, lifetime and width depend on the number of ways in which a particle can decay. The more decay modes, the shorter the lifetime. The measurement of the Z decay width took place at the LEP storage ring (Large Electron-Positron collider) in 1989 [70]. The production of Z as a function of energy is shown in Fig. 1.2. The number of neutrino types is

consistent to $N = 3$, whereas by measuring the primordial helium ^{4}He abundance, physicists have set limits to the number of neutrino types consistent with $N \sim 3$ [93]. Any new family of neutrinos would therefore be non-standard. Sterile neutrinos ν_s, if they exist, are either very massive or do not participate in the weak interaction, that is, will not be able to interact with the Z and W bosons [1].

Finally, the question of whether the neutrino is a Dirac or a Majorana particle is still open. In all our discussions of the three known types or flavors of neutrinos $(\nu_e, \nu_\mu, \nu_\tau)$, it was assumed that there is a distinction between the neutrino and its antiparticle. This is a consequence of Dirac's theory in which there are two solutions to the Dirac equation, one with positive energy and one with negative energy. For charged particles is easy to notice that particle and antiparticle have the same mass but opposite charges. For neutral particles is less obvious, for example the neutron and antineutron have opposite magnetic moments. Some other neutral particles such as the photon and the neutral pion (π^0) are their own antiparticles. A way to distinguish between the Dirac and Majorana hypothesis for the neutrino is through double beta decay, as first noted by Wendell Furry in 1939 [82].

Double beta decay is a process in which a radioactive nucleus with charge Z and mass A decays into a daughter nucleus with charge $Z \pm 2$ and mass A, with the emission of two electrons (positrons) and two antineutrinos (neutrinos) in the Dirac framework. For example, considering neutrinos as Dirac particles, a possible reaction with two antineutrinos in the final state would be

$$^{82}\mathrm{Sr} \rightarrow ^{82}\mathrm{Kr} + 2e^- + 2\overline{\nu}_e$$

(and abbreviated $2\nu2\beta$) but in the case of neutrinos being Majorana particles, one could have neutrinoless double beta decay,

$$^{82}\mathrm{Sr} \rightarrow ^{82}\mathrm{Kr} + 2e^-$$

(abbreviated $0\nu2\beta$) that is, without the emission of neutrinos. Both processes are very rare, but Furry calculated that the rate for $0\nu2\beta$ would be higher that the expected rate for $(2\nu2\beta)$. Current experiments searching for $0\nu2\beta$ processes are CUORE [26], GERDA [13], EXO-200 [29] and

KamLAND-Zen [83]. KATRIN is an experiment looking for the mass of the electron antineutrino by using the single β decay of tritium $^3\mathrm{H} \rightarrow ^3\mathrm{He} + e^- + \overline{\nu}_e$.

Understanding the Dirac or Majorana nature of neutrinos will help us understand why this elusive particles have such a small mass.

1.3 The solar neutrino anomaly

The detection of neutrinos by Cowan and Reines opened up a new are of research[1]. It was suggested that one application of the new detector technology was the investigation of the interior of the sun. Ray Davis led the construction of a chloride experiment designed to catch solar neutrinos. Located more than 1 km underground in the Homestake Mine, in South Dakota, Davis's experiment used a large tank filled with perchloroethylene (C_2Cl_4). The electron neutrinos ν_e from the Sun are detected by the means of an inverse beta decay reaction

$$\nu_e + ^{37}\mathrm{Cl} \rightarrow ^{37}\mathrm{Ar} + e^-.$$

with an argon nucleus and the emission of an electron. The incoming neutrino must have at least an energy of 0.814 MeV in order to drive this reaction. This means that the chloride experiment is sensitive to neutrinos from the ^{7}Be, *pep* and ^8B reactions as shown in Fig. 1.3. After being produced, the unstable ^{37}Ar atoms decay by recapturing an orbital electron and become ^{37}Cl again. X-rays are emitted as signature of the decay, but they can be only detected after the ^{37}Ar atoms have been removed from the chloride tank using helium gas and a highly efficient extraction procedure. After 27 years of operation, the chloride experiment of Ray Davis measured an average neutrino flux that falls by a factor of 3 below the predictions of the standard solar model [53]. This was known as the solar neutrino anomaly.

A second generation of experiments was build in order to further investigate the solar neutrino problem. The Kamiokande experiment, situated 1 km underground the Kamioka mine in Japan,

[1] Just as today's LIGO detection of gravitational waves opened up a new era in astronomy.

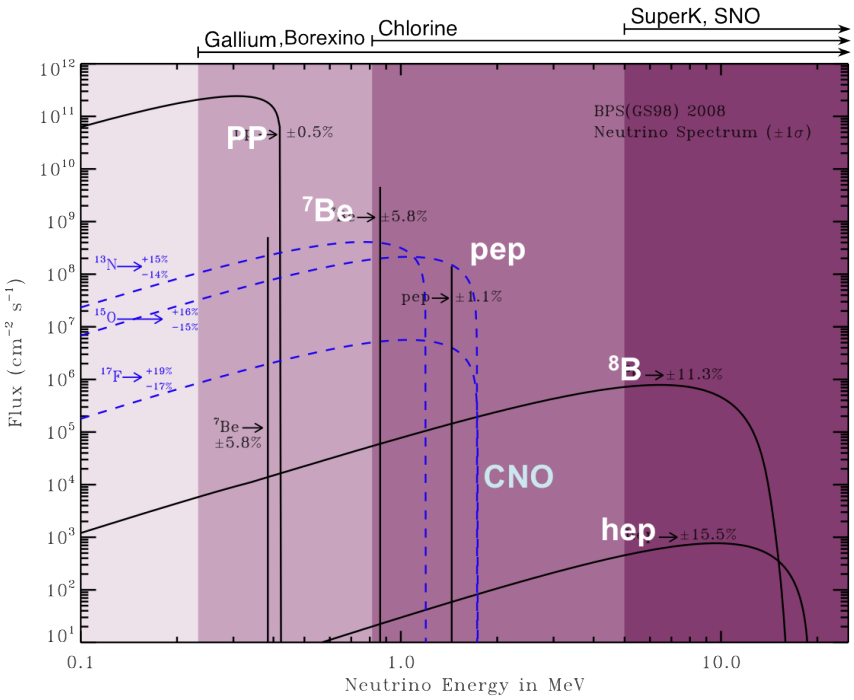

Figure 1.3: The solar neutrino flux [64].

was originally constructed to search for proton decay (as predicted by Grand Unified Theories). The Kamiokande detector was a large cylindrical Cherenkov detector, filled with 3 000 tons of purified water (H_2O). Incoming neutrinos undergo elastic scattering with electrons in the water via

$$\nu_e + e^- \rightarrow \nu_e + e^-.$$

The neutrino imprints its energy to the electron, which streaks the water at ultrarelativistic speeds. This produces Cherenkov radiations which is collected by an array of photomultiplier tubes surrounding the tank. Kamiokande was the first experiment to verify that the detected neutrinos originated in the Sun. The experiment was sensitive to the high energy portion of the ^{8}B solar neutrino flux. After nearly 2000 days of running, the collaboration reported a factor of 2 below the predictions of the standard solar model [80].

Two radio-chemical experiments using gallium as neutrino target, SAGE (Soviet-American Gallium Experiment) [2] and GALLEX (Gallium Experiment) [89] used the properties of gallium and become

sensitive to the lower energy *pp* neutrinos by the reaction

$$\nu_e + {}^{71}\text{Ga} \rightarrow {}^{71}\text{Ge} + \nu_e$$

and, again by looking at Fig. 1.3, to most of the solar neutrino flux spectrum. These experiments confirmed what theorists postulated about the sun shining by thermonuclear fusion, confirming astrophysical models. But they also confirmed the solar neutrino deficit, since only half of the expected flux was observed.

1.4 Neutrino Oscillations

Cumulative experimental evidence showed that the observed solar neutrino flux was far less than that predicted by the standard solar model, the latter also being consolidated by experimental data. Two alternative explanations started to circulate within the community. The first idea was that neutrinos have a finite lifetime (less than 8 minutes coming from the sun) and simply decay before being detected. But that idea was ruled out when (anti)neutrinos from the supernova SN-1987A were observed here on Earth [91], implying survival times (if any) much longer than the Sun-Earth distance.

The second alternative was that neutrinos oscillate, that is, one type of neutrino (say ν_e) can transform into a second type ($\nu_e \rightarrow \nu_\mu$), and vice versa as it travels. By studying atmospheric neutrinos, an upgraded water-Cherenkov experiment such as Super-Kamiokande found a deficit in the number of muon neutrinos going up to the detector with respect to the number of muon neutrinos going down the detector (see Fig. 1.4). This zenith angle relation was inconsistent with the calculations of the atmospheric flux. Nevertheless, the data was consistent with the neutrino oscillation hypothesis, in particular, with a two flavor $\nu_\mu \longleftrightarrow \nu_\tau$ oscillation [81].

In 2002, the Sudbury Neutrino Observatory (SNO) determined the total flux of ^{8}B neutrinos [16] after measuring the rate of charged-current electron neutrino events and the rate of neutral current events. The former event rate is relevant for electron neutrinos only, whereas the latter is sensitive

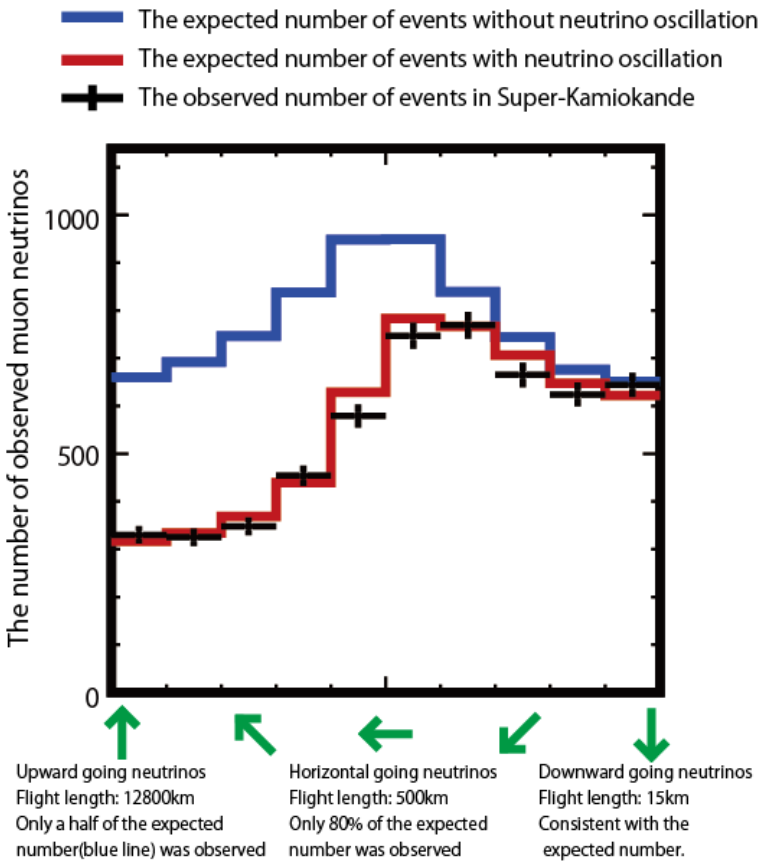

Figure 1.4: The discovery of atmospheric neutrino oscillations in Super-Kamiokande. The observed number of muon-neutrinos going up to the detector through the Earth was only half of the observed number of muon neutrinos going down the detector.

to all neutrino flavors. The SNO collaboration found a deficit in the measured flux of electron neutrinos but the measured neutral current flux was consistent with the solar model prediction. Neutrino oscillations was interpreted as the solution to the solar neutrino anomaly.

1.5 Current status and outlook

1.5.1 Current reactor and accelerator experiments

After the experimental confirmation of neutrino oscillations, the physics community transitioned towards precision experiments whose goal was to characterize the properties of the neutrino. Most of the effort has been invested in the measurement of the parameters governing neutrino oscillations, the value of their masses, their interaction with matter, and an accurate understanding of the neutrino flux, just to mention a few.

Reactor experiments, for example, use electron antineutrinos coming from β-decay fission isotopes, with energies in the MeV range, to measure the mixing angle parameter θ_{13} (see Section 2.2.1) via $\overline{\nu}_e$- disappearance. Advancement in detector technology combined with better understanding of detector systematics and backgrounds led to experiments such as Daya Bay [22], the Reactor Experiment for Neutrino Oscillations (RENO) [17] and Double Chooz [4] to provide precise constraints on the value of θ_{13} and to help understand the reactor neutrino flux.

Accelerator experiments, which measure neutrinos at the GeV range, use a beam of high energy protons colliding into a target, producing secondary particles (e.g. kaons and pions) which later decay into a beam of neutrinos. These experiments differ from solar and atmospheric experiments in that they are able to control the neutrino flux, the distance L between the source and the detector (baseline), and the energy E of the neutrinos. NOvA, which will be described in Chapter 3, is an example of accelerator experiment. Other examples of accelerator-based oscillation experiments are MINOS [8], T2K [3], which uses a similar off-axis technology (see Section 3.3) as NOvA, and DUNE [5], which is currently in the design phase.

1.5.2 The neutrino flux from accelerator beams

In this era of precision experiments, it is of paramount importance for accelerator experiments, such as NOvA, to have a reliable prediction of the neutrino flux, and its composition. The neutrino

flux is used as input for measuring neutrino cross sections and provides an estimate of the expected signal for neutrino oscillation analysis.

Experiments such as MiniBooNE [15], determine the expected neutrino flux and background contamination from simulation tuned with external measurements. The proton-target interaction is modeled by custom tables with double differential cross section information on hadron production as a function of transverse (p_T) and forward (p_Z) momentum, based on external data [14]. In particular, the external measurements of pion and kaon production from proton-target interactions overlap in the same phase space with the kaons and mesons that contribute the majority of the neutrino flux in the MiniBooNE detector. Unfortunately, for charged kaons whose decay result in the significant contribution to the high energy neutrino flux as well as for the electron neutrino flux component, no measurements are available from the HARP or BNL E910 experiments [14], and approximations were used instead. The estimated flux uncertainties are dominated by proton-target production cross section, which correspond to 15% [45].

MINOS in contrast, used data from the Near Detector with six different beam configurations (including target positions and horn currents) in order to constrain the particle production at the target. There were large uncertainties ($\sim$ 40%) between data and simulation, reported due to discrepancies in the calculations of the neutrino flux. Ultimately, this was tracked down to poor knowledge of the hadron production in the target [45].

NOvA uses a comprehensive flux prediction package that uses all available and relevant hadron production data (discussed in Section 4.1.1). It uses data from the pion and kaon yields measured by the MIPP [127] and from NA49 [21] experiments. The uncertainty in the flux prediction when integrated from 0-20 GeV is 7.8%, with hadron production uncertainties still dominating [18]. This method can be applied to similar beams, in particular, for future experiments such as DUNE.

1.5.3 Unanswered questions and summary

Today we know that neutrinos exist, that there are three different types (ν_e, ν_μ, ν_τ) each associated with a lepton, that the Sun is a source of neutrinos and that neutrinos oscillate between flavors, the latter fact solving the solar neutrino anomaly. But several questions remain open in the field. For example,

- we do not know what is the mass of neutrinos, what is their order and why is so "small" compared with the other particles,
- we do not know if neutrinos are their own antiparticle (Majorana) or if they are different (Dirac) particles,
- we do not know if the parameters describing neutrino oscillations mix the neutrino types (e.g. flavors states) with the neutrino mass states in a maximal fashion and if neutrinos behave different than antineutrinos (CP-violation),
- we do not know very well how neutrinos interact with matter (nucleons, nuclei),
- we do not know if sterile neutrinos really exist, opening the door to new physics.

For each of the above statements, a set of neutrino experiments are currently running, or being constructed, or in the process of conception. For the subsequent chapters we will focus more deeply in the physics of neutrino oscillations, and the reach of the long-baseline neutrino accelerator NOvA experiment.

The main uncertainty for the prediction of the neutrino flux in accelerator based experiments comes from uncertainties associated to the interaction of hadrons in the target. Historically, the mayor uncertainties arise from the production yields of kaons.

The main work on this thesis is presented on Chapter 7. By using kaon-related charged current muon neutrinos of the type $\nu_\mu + X \to \mu + X'$, where the muon escaped the Far Detector, we make

a measurement of the kaon production normalization scale. This is later linked to events in the Near Detector constraint some of the backgrounds that are associated to oscillation analysis.

CHAPTER 2. THEORY OF NEUTRINO OSCILLATIONS

2.1 The Standard Model

The Standard Model (SM) describes three out of four interactions known in nature (electromagnetic, weak and strong) that affect the behavior of the elementary particles. The SM is a renormalizable (i.e. calculable) gauge theory that is build in the framework of quantum field theory [85].

Even though the SM has great predicting power and is able to explain a large amount of physical phenomena (such as predicting the third family of quarks or the anomalous magnetic moment of the electron) consolidating it as a precise theory [47], the SM needs to be extended in order to explain other fundamental phenomena. For example, the SM does not explain the masses of the fermions (spin-1/2 particles) or the number of families of quarks and leptons (see Table 2.1).

Table 2.1: Table of elementary particles

Quarks (mass)			Charge Q[e]
u (2.2 MeV)	c (1.27 GeV)	t (173.2 GeV)	2/3
d (4.7 MeV)	s (96 MeV)	b (4 GeV)	$-1/3$
Leptons			Q[e]
e (0.510 MeV)	μ (105.66 MeV)	τ (1.77 GeV)	-1
ν_e (< 2 eV)	ν_μ (< 2 eV)	ν_τ (< 2 eV)	0
Force carries and Higgs			
γ ($< 1 \times 10^{-18}$ eV)	gluons (0 eV)	$W^\pm$ (80.38 GeV)	
Z^0 (91.18 GeV)	graviton (?)	Higgs (125.09 GeV)	

In the SM, quarks and leptons obtain their masses in the same way W and Z^0 bosons obtain theirs: through interactions with the Higgs boson. Neutrinos being spin-1/2 with no electric charge, however, do not follow the same path, and therefore are predicted with zero mass. But

experimental evidence provided by the SuperKamiokande [28] and SNO [16] collaborations have shown that neutrinos oscillate, and as a consequence, they have non-zero mass. The mechanism that originates the neutrino mass could be different from the one prescribed in our current theories. Therefore, neutrino properties are a link beyond standard model physics.

Neutrino oscillation is one of the most interesting phenomena related to these particles, which has a direct connection to the fact that they have mass. Since flavor states are a mixture of mass states, a neutrino with an initial flavor α may be observed as a flavor state β when it propagates. The details of this transitions will become evident in the following sections.

2.2 Neutrino oscillations in vacuum

Neutrino oscillations is a quantum mechanics phenomenon proposed for the first time by Bruno Pontecorvo [36] in analogy to the oscillations of the neutral mesons $K^0 \rightarrow \bar{K}^0$. These oscillations are generated by the interference of different massive neutrino states, which are produced and detected coherently due to its tiny mass differences. Since at that time only one active neutrino species was known (ν_e), in order to explain the phenomena of oscillations Pontecorvo invented the concept of sterile neutrino, which is a neutral fermion that does not interact with the weak force.

Only massive neutrinos oscillate and as a consequence, observing neutrino oscillations gives information about the neutrino masses, specifically, difference of the squared masses.

As we will see in subsequent sections, neutrino oscillation depend upon the ratio of the distance traveled (L) to the neutrino energy (E). The typical sensitivity of an experiment is given by $\Delta m^2(\mathrm{eV}^2) \approx E(\mathrm{MeV})/L(\mathrm{m})$, which for some experiments can be as small as $10^{-11}\mathrm{eV}^2$ (see Table 2.2).

The muon neutrino (ν_μ) was discovered in 1962 by an experiment in Brookhaven, thanks to the efforts of Lederman, Schwartz, and Steinberger [63] and recommendations of Pontecorvo himself back in 1959. Since then it was clear that the oscillations between different active flavor states

are possible if and only if neutrinos were massive and mixed. In the same year of 1962, Maki, Nakagawa and Sakata [111] considered for the first time a model with the mixing of different neutrino flavors. In 1967 Pontecorvo predicted the solar neutrino problem as a consequence of the $\nu_e \to \nu_\mu$ (or $\nu_e \to \nu_{\text{sterile}}$) transition way before the first actual measurement of the electron neutrino flux realized by Homestake experiment [54]. In 1969 Gribov and Pontecorvo introduced seminal work on the theory of solar neutrino oscillations in a similar fashion due to mixing [36]. Finally, the theory of neutrino oscillations using the plane wave approximation was first developed between 1975 and 1976 by Eliezer, Swift, Bilenky, Pontecorvo, among others [85]. In the following sections we will derive the transition probabilities for the case of two and three neutrino families.

2.2.1 Derivation of the oscillation probability

Let us suppose we have a quantum mechanic state $|\nu_\alpha\rangle$ written as a superposition of the mass eigenstates $|\nu_i\rangle$ (with $\langle\nu_i|\nu_j\rangle = \delta_{ij}$), whose coefficients are constants given by the elements of the unitary matrix U (where $U^\dagger U = 1$) expressed in the (Dirac) notation as

$$|\nu_\alpha\rangle = \sum_i U_{\alpha i}|\nu_i\rangle \qquad (\alpha = e, \mu, \tau). \tag{2.1}$$

Such quantum state is called flavor state[1], with a flavor (weak charge) α and will be describing a neutrino created in some charged-current process or attached to a given charged anti-lepton due to the weak interaction. This neutrino state will be assumed to have a defined momentum $\mathbf{p}$. The corresponding bra vector is given by

$$\langle\nu_\alpha| = \sum_i U^*_{\alpha i}\langle\nu_i|. \tag{2.2}$$

[1] According to [85], the number of massive neutrinos in the equation (2.1) is not explicitly limited as in the flavor case. As far as we know, three active neutrino flavors have been found ν_e, ν_μ and ν_τ, therefore the number of massive neutrinos must be equal or greater than three. In the latter case, additional neutrinos in the flavor base will be sterile since will not participate in the electroweak interactions. Active to sterile transitions could be observed by the disappearance of active neutrino states.

The unitary matrix U can be parametrized in several ways [51]. The most accepted version has 3 mixing angles and, depending whether or not neutrinos are Majorana or Dirac particles, by one or three additional Charge-Parity (CP) violating phases

$$
\begin{aligned}
U_{\text{PMNS}} &= \begin{pmatrix} U_{e1} & U_{e2} & U_{e3} \\ U_{\mu 1} & U_{\mu 2} & U_{\mu 3} \\ U_{\tau 1} & U_{\tau 2} & U_{\tau 3} \end{pmatrix} = \begin{pmatrix} U_{11} & U_{12} & U_{13} \\ U_{21} & U_{22} & U_{23} \\ U_{31} & U_{32} & U_{33} \end{pmatrix} \\
&= \underbrace{\begin{pmatrix} c_{12} & s_{12} & 0 \\ -s_{12} & c_{12} & 0 \\ 0 & 0 & 1 \end{pmatrix}}_{\text{Solar, Reactor}} \underbrace{\begin{pmatrix} c_{13} & 0 & s_{13}e^{-i\delta_{CP}} \\ 0 & 1 & 0 \\ -s_{13}e^{i\delta_{CP}} & 0 & c_{13} \end{pmatrix}}_{\text{Mixing sector}} \underbrace{\begin{pmatrix} 1 & 0 & 0 \\ 0 & c_{23} & s_{23} \\ 0 & -s_{23} & c_{23} \end{pmatrix}}_{\text{Atm., Accelerator}} \\
&= \begin{pmatrix} c_{12}c_{13} & s_{12}c_{13} & s_{13}e^{-i\delta_{CP}} \\ -s_{12}c_{23} - c_{12}s_{23}s_{13}e^{i\delta_{CP}} & c_{12}c_{23} - s_{12}s_{23}s_{13}e^{i\delta_{CP}} & s_{23}c_{13} \\ s_{12}s_{23} - c_{12}c_{23}s_{13}e^{i\delta_{CP}} & -c_{12}s_{23} - s_{12}c_{23}s_{13}e^{i\delta_{CP}} & c_{23}c_{13} \end{pmatrix}
\end{aligned}
\tag{2.3}
$$

Where $c_{ij} = \cos\theta_{ij}$, $s_{ij} = \sin\theta_{ij}$, the angles $\theta_{12}, \theta_{13}, \theta_{23}$ and the CP-violating phase δ_{CP}[2]. The reason for using the above ordering is since most of the information on this matrix comes from ν_e and ν_μ disappearance experiments, which measure $|U_{e2}|^2$, $|U_{e3}|^2$ and $|U_{\mu 3}|^2$, we want the first row (U_{e1}, U_{e2}, U_{e3}) and the third column $(U_{e3}, U_{\mu 3}, U_{\tau 3})$ of U_{PMNS}[3] to be as simple as possible. Any other ordering makes elements of either the first row or the third column or both more complicated.

Given that $U^\dagger U = 1$, then

$$
\begin{aligned}
\sum_i U_{\alpha i} U^*_{\beta i} &= \sum_i U_{\alpha i} U^\dagger_{i\beta} & U^*_{\beta i} &= U^\dagger_{i\beta} \\
&= \sum_i \langle \alpha | U | i \rangle \langle i | U^\dagger | \beta \rangle & U_{rs} &= \langle r | U | s \rangle \\
&= \langle \alpha | U U^\dagger | \beta \rangle = \langle \alpha | I | \beta \rangle \\
\sum_i U_{\alpha i} U^*_{\beta i} &= \delta_{\alpha\beta}
\end{aligned}
\tag{2.4}
$$

[2]For the Majorana case, $U_{\text{PMNS}} = U \cdot diag(1, e^{i\alpha_{21}/2}, e^{i\alpha_{31}/2})$

[3]Also known as Pontecorvo-Maki-Nakagawa-Sakata (PMNS).

Similarly,

$$\sum_{\alpha} U_{\alpha i} U^{*}_{\alpha j} = \delta_{ij} \tag{2.5}$$

hence, when computing the bra-ket product, we have

$$\begin{aligned}
\langle \nu_\beta | \nu_\alpha \rangle &= \sum_i U^{*}_{\beta i} \langle \nu_i | \sum_i U_{\alpha i} | \nu_i \rangle \\
&= \sum_i U^{*}_{\beta i} U_{\alpha i} \sum_i |\nu_i\rangle\langle\nu_i| && \text{completeness } \textstyle\sum_i |\nu_i\rangle\langle\nu_i| = 1 \\
&= \sum_i U^{\dagger}_{i\beta} U_{\alpha i} && U^{*}_{\beta i} = U^{\dagger}_{i\beta} \\
&= \sum_i U_{\alpha i} U^{\dagger}_{i\beta} && U U^{\dagger} = U^{\dagger} U \\
\langle \nu_\beta | \nu_\alpha \rangle &= \delta_{\alpha\beta}.
\end{aligned} \tag{2.6}$$

We conclude that the flavor states are orthonormals. For the antineutrino case, the element $U_{\alpha i}$ is replaced by $U^{*}_{\alpha i}$

$$|\bar{\nu}_\alpha\rangle = \sum_i U^{*}_{\alpha i} |\bar{\nu}_i\rangle. \tag{2.7}$$

Mass states $|\nu_i\rangle$ are eigenstates of the Hamiltonian

$$\mathcal{H}|\nu_i\rangle = E_i |\nu_i\rangle \tag{2.8}$$

with energy eigenvalues given by

$$E_i = \sqrt{\mathbf{p}^2 + m_i^2}. \tag{2.9}$$

By the time dependent Schrödinger equation (with natural units $\hbar = c = 1$)

$$i \frac{d}{dt} |\nu_i(t)\rangle = \mathcal{H} |\nu_i(t)\rangle \tag{2.10}$$

and after solving the differential equation, we obtain that the neutrino mass states evolve in time as plane waves

$$|\nu_i(t)\rangle = e^{-iE_i t} |\nu_i\rangle. \tag{2.11}$$

Now let us consider the time evolution of a flavor state $|\nu_\alpha\rangle$. Such state describes physically a neutrino created with definite flavor α at time $t = 0$. Using equation (2.11) we can substitute (2.1)

obtaining

$$|\nu_\alpha(t)\rangle = \sum_i U_{\alpha i} e^{-iE_i t} |\nu_i\rangle \tag{2.12}$$

such that

$$|\nu_\alpha(t=0)\rangle = |\nu_\alpha\rangle.$$

Using (2.5) on equation (2.1)

$$\begin{aligned}
|\nu_\alpha\rangle &= \sum_i U_{\alpha i} |\nu_i\rangle \\
\sum_\alpha U^\dagger_{i\alpha} |\nu_\alpha\rangle &= \sum_\alpha \sum_i U_{\alpha i} U^\dagger_{i\alpha} |\nu_i\rangle \\
&= \sum_\alpha \sum_i \langle\alpha|U|i\rangle\langle i|U^\dagger|\alpha\rangle|\nu_i\rangle \\
&= \sum_\alpha \sum_i |i\rangle\langle i|\langle\alpha|UU^\dagger|\alpha\rangle|\nu_i\rangle \\
&= \sum_\alpha \langle\alpha|I|\alpha\rangle|\nu_i\rangle \\
\sum_\alpha U^*_{\alpha i} |\nu_\alpha\rangle &= |\nu_i\rangle
\end{aligned} \tag{2.13}$$

where the mass states can be expressed in flavor state terms after inverting expression (2.1).

$$|\nu_i\rangle = \sum_\alpha U^*_{\alpha i} |\nu_\alpha\rangle \tag{2.14}$$

Substituting the previous expression (2.14) in (2.12) we obtain

$$|\nu_\alpha(t)\rangle = \sum_{\beta=e,\mu,\tau} \left(\sum_i U_{\alpha i} e^{-iE_i t} U^*_{\beta i} \right) |\nu_\beta\rangle \tag{2.15}$$

The last expression is worth discussing. It tell us that starting from a superposition of mass states given by (2.12), that is, a pure flavor state that identifies a single particle (the general case of (2.1) when $t = 0$), such state becomes a superposition of different flavor states for future times $t > 0$ (assuming the mixing matrix is non-diagonal, that is, neutrinos mix).

Now, when combining with the bra $|\nu_\beta\rangle$

$$A_{\nu_\alpha \to \nu_\beta}(t) \equiv \langle\nu_\beta|\nu_\alpha(t)\rangle = \sum_i U_{\alpha i} U^*_{\beta i} e^{-iE_i t} \tag{2.16}$$

we obtain the transition amplitude between states $\nu_\alpha \to \nu_\beta$ as a function of time. Similarly, for antineutrinos

$$A_{\bar{\nu}_\alpha \to \bar{\nu}_\beta}(t) = \sum_i U_{\beta i} U^*_{\alpha i} e^{-iE_i t} \tag{2.17}$$

The transition probability $\nu_\alpha \to \nu_\beta$ becomes

$$P_{\nu_\alpha \to \nu_\beta}(t) = |A_{\nu_\alpha \to \nu_\beta}(t)|^2 = \sum_i \sum_j U_{\alpha i} U^*_{\beta i} U^*_{\alpha j} U_{\beta j} e^{-i(E_i - E_j)t}. \tag{2.18}$$

For ultra-relativistic neutrinos ($|\mathbf{p}| \gg m_i$) the energy equation (2.9) can be approximated by

$$E_i = \sqrt{\mathbf{p}^2 + m_i^2} \simeq |\mathbf{p}| + \frac{m_i^2}{2|\mathbf{p}|} \simeq E + \frac{m_i^2}{2E} \qquad \text{where } E \approx |\mathbf{p}| \tag{2.19}$$

where the neutrino energy is approximated to its momentum magnitude. Because of the above

$$E_i - E_j \simeq \frac{m_i^2 - m_j^2}{2E} = \frac{\Delta m_{ij}^2}{2E} \tag{2.20}$$

in this case Δm_{ij}^2 is the squared mass difference. Hence, the transition probability (2.18) is approximately

$$P_{\nu_\alpha \to \nu_\beta}(t) = \sum_i \sum_j U_{\alpha i} U^*_{\beta i} U^*_{\alpha j} U_{\beta j} \; exp\left(-i \frac{\Delta m_{ij}^2 \; t}{2E}\right) \tag{2.21}$$

The last step is to note that in most (if not all) of the neutrino oscillation experiments, propagation time is not the usual measured quantity but the distance L between the neutrino source and the detector location. Assuming again that neutrinos travel nearly the speed of light (ultra-relativistic case) is possible to approximate $t = L$ given that $c = 1$, thus

$$P_{\nu_\alpha \to \nu_\beta}(L, E) = \sum_i \sum_j U_{\alpha i} U^*_{\beta i} U^*_{\alpha j} U_{\beta j} \; exp\left(-i \frac{\Delta m_{ij}^2 \; L}{2E}\right) \tag{2.22}$$

while for antineutrinos

$$P_{\bar{\nu}_\alpha \to \bar{\nu}_\beta}(L, E) = \sum_i \sum_j U^*_{\alpha i} U_{\beta i} U_{\alpha j} U^*_{\beta j} \; exp\left(-i \frac{\Delta m_{ij}^2 \; L}{2E}\right). \tag{2.23}$$

It is important to notice that the transition probability (2.22) and (2.23) satisfy two rules of conservation of probability which are a consequence of the unitary evolution of the states

1. The sum of the transition probabilities of a flavor neutrino state ν_α to all the remaining flavors ν_β, including $\alpha = \beta$, is equal to one.

$$\sum_\beta P_{\nu_\alpha \to \nu_\beta}(L, E) = P_{\nu_\alpha \to \nu_e} + P_{\nu_\alpha \to \nu_\mu} + \ldots = 1 \tag{2.24}$$

2. The sum of the transition probabilities of any neutrino flavor ν_α, including $\alpha = \beta$, to a specific flavor ν_β is equal to one.

$$\sum_\alpha P_{\nu_\alpha \to \nu_\beta}(L, E) = P_{\nu_e \to \nu_\beta} + P_{\nu_\mu \to \nu_\beta} + \ldots = 1 \tag{2.25}$$

By inspection is evident that the transition probability is function of two parameters (distance source-detector L and the neutrino energy E) associated to the experiment, which will help to determine the oscillation phase

$$\Phi_{ij} = \frac{-\Delta m^2_{ij} L}{2E} \tag{2.26}$$

that is also function of the squared mass difference Δm^2_{ij}. On the other hand, the oscillation amplitude is determined by the mixing matrix elements, also natural constants. We conclude that by studying neutrino oscillations we will gain insights on the values of both the squared mass differences Δm^2_{ij} and the values of the elements of the mixing matrix U. The transition between different flavors is shown for values $L > 0$ only due to the relation (2.4) implies that

$$P_{\nu_\alpha \to \nu_\beta}(L = 0, E) = \sum_i \sum_j U_{\alpha i} U^*_{\beta i} U^*_{\alpha j} U_{\beta j} = (\delta^2_{\alpha\beta}) = \delta_{\alpha\beta}.$$

Some comments on the transition probability expression (2.22) A convenient way to write equation (2.22) is as follows [172]. Expanding by each entry and grouping, we obtain

$$P_{\nu_\alpha \to \nu_\beta}(L, E) = \sum_i |U_{\alpha i} U^*_{\beta i}|^2 + 2\mathrm{Re} \sum_{j>i} U_{\alpha i} U^*_{\beta i} U^*_{\alpha j} U_{\beta j} \; exp\left(-2\pi i \frac{L}{L^{osc}_{ij}}\right) \tag{2.27}$$

where we obtain a constant term separated from the oscillatory term. We can now define the oscillation length

$$L^{osc}_{ij} = \frac{4\pi E}{\Delta m^2_{ij}}. \tag{2.28}$$

The oscillation length is the distance on which the phase generated by the squared mass difference Δm^2_{ij} equals 2π. The first term of (2.27) is an average of the transition probability, which can be written as

$$\langle P_{\nu_\alpha \to \nu_\beta} \rangle = \sum_i |U_{\alpha i} U^*_{\beta i}|^2 = \sum_i |U_{\alpha i}|^2 |U_{\beta i}|^2 = \sum_i |U^*_{\alpha i} U_{\beta i}|^2 = \langle P_{\nu_\beta \to \nu_\alpha} \rangle. \tag{2.29}$$

On the other hand, an useful way of expressing equation (2.22) is if first we separate the real and imaginary parts of the $U_{\alpha i} U^*_{\beta i} U^*_{\alpha j} U_{\beta j}$ factor and then square the expression (2.4). After substituting in (2.27) we obtain

$$\begin{aligned} P_{\nu_\alpha \to \nu_\beta}(L, E) = \delta_{\alpha\beta} &- 4 \sum_{i>j} \mathrm{Re}[U_{\alpha i} U^*_{\beta i} U^*_{\alpha j} U_{\beta j}] \sin^2 \left(\frac{\Delta m^2_{ij}\, L}{4E} \right) \\ &+ 2 \sum_{i>j} \mathrm{Im}[U_{\alpha i} U^*_{\beta i} U^*_{\alpha j} U_{\beta j}] \sin \left(\frac{\Delta m^2_{ij}\, L}{2E} \right) \end{aligned} \tag{2.30}$$

and for the antineutrino case

$$\begin{aligned} P_{\bar{\nu}_\alpha \to \bar{\nu}_\beta}(L, E) = \delta_{\alpha\beta} &- 4 \sum_{i>j} \mathrm{Re}[U_{\alpha i} U^*_{\beta i} U^*_{\alpha j} U_{\beta j}] \sin^2 \left(\frac{\Delta m^2_{ij}\, L}{4E} \right) \\ &- 2 \sum_{i>j} \mathrm{Im}[U_{\alpha i} U^*_{\beta i} U^*_{\alpha j} U_{\beta j}] \sin \left(\frac{\Delta m^2_{ij}\, L}{2E} \right). \end{aligned} \tag{2.31}$$

which is different to the previous expression only in the sign of the imaginary part.

When $\alpha = \beta$, the transition probability is called survival probability $\nu_\alpha \to \nu_\alpha$. In this case the products $U_{\alpha i} U^*_{\beta i} U^*_{\alpha j} U_{\beta j}$ are real and equal to $|U_{\alpha i}|^2 |U_{\beta i}|^2$, therefore the survival probability acquires the form

$$P_{\nu_\alpha \to \nu_\alpha}(L, E) = 1 - 4 \sum_{i>j} |U_{\alpha i}|^2 |U_{\alpha j}|^2 \sin^2 \left(\frac{\Delta m^2_{ij}\, L}{4E} \right). \tag{2.32}$$

2.2.2 Neutrinos under transformations CPT, CP and T

The state of a particle can be identified by the three components of the momentum $\mathbf{p}$ and by the helicity, defined as

$$H = \frac{\mathbf{s} \cdot \mathbf{p}}{|\mathbf{s} \cdot \mathbf{p}|}, \tag{2.33}$$

that is, the projection of the spin vector in the direction of the particle's vector momentum. Until the 1950s, it was believed that the laws of physics were invariant under a mirror reflection or inversion of spatial coordinates (parity inversion). If parity were conserved, a spin-1/2 particle such as the neutrino, would exist in both left- and right helicity states (see Fig. 2.1). But in 1956, C. N. Yang and T. D. Lee suggested that the weak force might violate parity conservation, and six months later C. S. Wu confirmed it in an experiment measuring the beta decay of cobalt-60 [165].

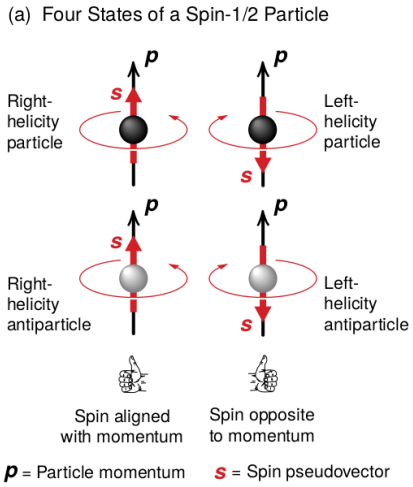

Figure 2.1: The four states of a spin-1/2 particle.

Physically, neutrinos and antineutrinos are related by a charge-parity (CP) transformation that interchange neutrinos with antineutrinos and inverts its helicity[4]

$$\nu_\alpha \leftrightarrow \bar{\nu}_\alpha \qquad \text{(CP)}. \tag{2.34}$$

[4]For the case of Majorana neutrinos, the the charge (C) transformation equals unity, by convention the states with negative helicity are called neutrinos and the states with positive helicity are called antineutrinos.

Therefore, a CP transformation interchange the channels $\nu_\alpha \to \nu_\beta$ and $\bar{\nu}_\alpha \to \bar{\nu}_\beta$

$$\nu_\alpha \to \nu_\beta \leftrightarrow \bar{\nu}_\alpha \to \bar{\nu}_\beta \qquad \text{(CP)}. \tag{2.35}$$

A time T transformation interchanges the initial and final states. Therefore, a T transformation interchanges the channels $\nu_\alpha \to \nu_\beta$ and $\nu_\beta \to \nu_\alpha$,

$$\nu_\alpha \to \nu_\beta \leftrightarrow \nu_\beta \to \nu_\alpha \qquad \text{(T)}, \tag{2.36}$$

or for antineutrinos

$$\bar{\nu}_\alpha \to \bar{\nu}_\beta \leftrightarrow \bar{\nu}_\beta \to \bar{\nu}_\alpha \qquad \text{(T)}. \tag{2.37}$$

Finally, the transformation CPT interchanges

$$\nu_\alpha \to \nu_\beta \leftrightarrow \bar{\nu}_\beta \to \bar{\nu}_\alpha \qquad \text{(CPT)}. \tag{2.38}$$

This CPT transformation is a symmetry in any quantum field theory, such as the SM. By extension, CPT is a symmetry of the transition probabilities

$$P_{\nu_\alpha \to \nu_\beta} = P_{\bar{\nu}_\beta \to \bar{\nu}_\alpha}. \tag{2.39}$$

We can infer the latter from the equations (2.22) and (2.23) and from the fact that its invariant under CP changes $U \leftrightarrows U^*$, following a transformation T that changes $\alpha \leftrightarrows \beta$.

In the case of three neutrino mixing, the matrix (2.3) is in general complex and has a CP violating phase associated to it. Such asymmetry can be revealed by neutrino oscillation when measuring the difference

$$A^{CP}_{\alpha\beta} = P_{\nu_\alpha \to \nu_\beta} - P_{\bar{\nu}_\alpha \to \bar{\nu}_\beta}. \tag{2.40}$$

and is only accessible between transitions of different flavors, due to (2.39), $P_{\bar{\nu}_\alpha \to \bar{\nu}_\beta} = P_{\nu_\beta \to \nu_\alpha}$.

Noticing the expression (2.30) and (2.31) we can state the the only term that contributes to the CP violation is given by

$$A^{CP}_{\alpha\beta}(L,E) = 4\sum_{i>j} \mathrm{Im}[U_{\alpha i}U^*_{\beta i}U^*_{\alpha j}U_{\beta j}] \sin\left(\frac{\Delta m^2_{ij}\ L}{2E}\right) \tag{2.41}$$

Thus, the CP asymmetry can be measured only in transitions between different neutrino flavor states, because for the survival $\alpha = \beta$, the imaginary part of (2.41) becomes zero.

2.2.3 Two flavor neutrino mixing

We now consider the case of two flavor states ν_α, ν_β as an approximation that is used for simplification. Such states are superposition of the two mass states ν_1, ν_2 with coefficients given by the mixing matrix

$$U = \begin{pmatrix} \cos\theta & \sin\theta \\ -\sin\theta & \cos\theta \end{pmatrix} = \begin{pmatrix} U_{\alpha 1} & U_{\alpha 2} \\ U_{\beta 1} & U_{\beta 2} \end{pmatrix} \tag{2.42}$$

with θ as the mixing angle with range $0 \leq \theta \leq \pi/2$. This simplified model results in a single squared mass difference

$$\Delta m^2_{21} \equiv m^2_2 - m^2_1. \tag{2.43}$$

Conveniently, we define the ν_1 as the lightest of the two states, such that Δm^2_{21} is positive.

From (2.22) we derive the transition probability $\nu_\alpha \to \nu_\beta$ with $\alpha \neq \beta$

$$\begin{aligned} P_{\nu_\alpha \to \nu_\beta}(L,E) &= \cos^2\theta \sin^2\theta - \cos^2\theta \sin^2\theta\ exp\left(i\frac{\Delta m^2_{21}L}{2E}\right) \\ &\quad - \cos^2\theta \sin^2\theta\ exp\left(-i\frac{\Delta m^2_{21}L}{2E}\right) + \cos^2\theta \sin^2\theta \end{aligned}$$

where we have used $\Delta m^2_{21} = -\Delta m^2_{12}$

$$\begin{aligned} &= \cos^2\theta \sin^2\theta \left[2 - \left(exp\left(i\frac{\Delta m^2_{21}L}{2E}\right) + exp\left(-i\frac{\Delta m^2_{21}L}{2E}\right)\right)\right] \\ &= 2\cos^2\theta \sin^2\theta \left[1 - \cos\left(\frac{\Delta m^2_{21}L}{2E}\right)\right] \end{aligned}$$

finally using the identity $\sin 2\theta = 2\sin\theta\cos\theta$

$$P_{\nu_\alpha\to\nu_\beta}(L,E) = \frac{1}{2}\sin^2 2\theta\left[1-\cos\left(\frac{\Delta m^2_{21}L}{2E}\right)\right] \tag{2.44}$$

or in similar fashion

$$P_{\nu_\alpha\to\nu_\beta}(L,E) = \sin^2 2\theta\sin^2\left(\frac{\Delta m^2_{21}L}{4E}\right) \tag{2.45}$$

When $\alpha=\beta$, the survival probability $P_{\nu_\alpha\to\nu_\beta}(L,E)$ (e.g., the probability that a flavor state neutrino α remains in that state after its propagation over a distance L), becomes

$$P_{\nu_\alpha\to\nu_\alpha}(L,E) = 1 - P_{\nu_\alpha\to\nu_\beta}(L,E) = 1-\sin^2 2\theta\sin^2\left(\frac{\Delta m^2_{21}L}{4E}\right). \tag{2.46}$$

The oscillation length defined in (2.28) in this case is

$$L^{osc}_{21} = \frac{4\pi E}{\Delta m^2_{21}} \tag{2.47}$$

and the average value of the transition probability can be calculated using the relation (2.29) or from the expression (2.44) directly (where we know that the average value of cosine is zero)

$$\langle P_{\nu_\alpha\to\nu_\beta}\rangle = \frac{1}{2}\sin^2 2\theta. \tag{2.48}$$

We can rewrite (2.45) with the proper units and $1/4\hbar c \propto 1.27$ as

$$\begin{aligned} P_{\nu_\alpha\to\nu_\beta}(L,E) &= \sin^2 2\theta\ \ \sin^2\left(1.27\ \frac{\Delta m^2_{21}[\mathrm{eV}^2]L[\mathrm{m}]}{E[\mathrm{MeV}]}\right) \\ &= \sin^2 2\theta\ \ \sin^2\left(1.27\ \frac{\Delta m^2_{21}[\mathrm{eV}^2]L[\mathrm{km}]}{E[\mathrm{GeV}]}\right) \end{aligned} \tag{2.49}$$

and the oscillation length ($4\pi\hbar c \propto 2.47$) becomes

$$L^{osc} = 2.47\frac{E[\mathrm{MeV}]}{\Delta m^2[\mathrm{eV}^2]}\mathrm{m} = 2.47\frac{E[\mathrm{GeV}]}{\Delta m^2[\mathrm{eV}^2]}\mathrm{km}. \tag{2.50}$$

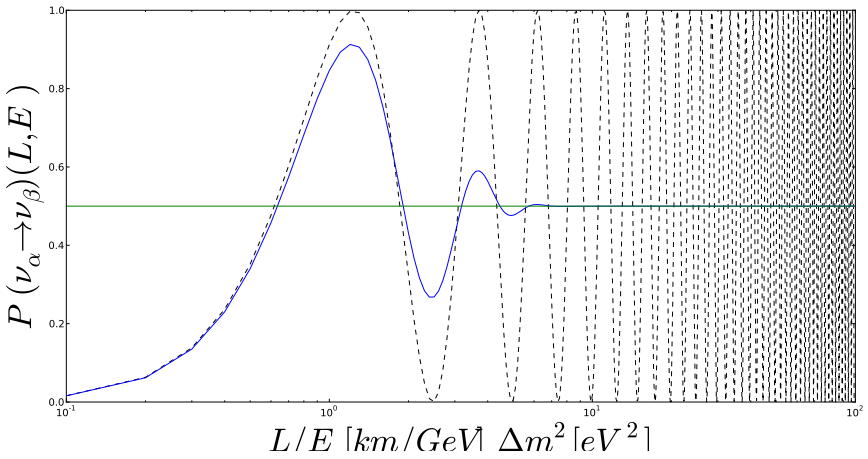

Figure 2.2: Transition probability of $\nu_\alpha \to \nu_\beta$ for a maximal value of $\sin^2 2\theta = 1$. The dashed line represents the expression (2.49), where the first zero of the function after the origin corresponds to $L^{osc} = 2.47$. The average value (solid line) is the graph of the expression (2.52) with the cosine value given by (2.55) and $\sigma_{L/E} = 0.2$ (the greater the value of $\sigma_{L/E}$ the bigger the suppression). The constant line at $P = 0.5$ is the plot of (2.48).

At this point, let us analyze in detail the expression (2.45). Suppose a maximal amplitude ($\sin^2 2\theta = 1 \to \theta = \pi/4$). A graph related to (2.49) as function of the ratio $\Delta m^2 L/E$ is shown in Figure 2.2. For fixed values of the squared mass difference Δm^2 and the energy E, the parameter L is shown on the horizontal axis. Is important to note that the value of the oscillation length in (2.50) will give us the distance in which the probability becomes zero after the origin. In the figure we normalize to $L^{osc} = \pi/1.27 \simeq 2.47$. The transition probability is very small for values $L \ll L^{osc}$ and oscillates dramatically when $L \gg L^{osc}$.

Due to the absence of phases in the matrix for the two-neutrino case given by (2.42), there are no CP or T symmetry violations and the transition probabilities of both neutrinos and antineutrinos, are equal

$$P_{\nu_\alpha \to \nu_\beta}(L,E) = P_{\nu_\beta \to \nu_\alpha}(L,E) = P_{\bar{\nu}_\alpha \to \bar{\nu}_\beta}(L,E) = P_{\bar{\nu}_\beta \to \bar{\nu}_\alpha}(L,E). \tag{2.51}$$

It is convenient for practical reasons to calculate the averaged oscillation probability over the distance L and energy E distributions. For example, the transition probability is obtained by averaging the cosine from the expression (2.44) over a distribution $\phi(L/E)$ de L/E, with $\alpha \neq \beta$

$$\langle P_{\nu_\alpha \to \nu_\beta}(L,E)\rangle = \frac{1}{2}\sin^2 2\theta \left[1 - \left\langle \cos\left(\frac{\Delta m^2 L}{2E}\right)\right\rangle\right] \tag{2.52}$$

from where

$$\left\langle \cos\left(\frac{\Delta m^2 L}{2E}\right)\right\rangle = \int \cos\left(\frac{\Delta m^2 L}{2E}\right)\, \phi\left(\frac{L}{E}\right)\, d\frac{L}{E} \tag{2.53}$$

As an illustration, let us consider the simplest case of a Gaussian distribution L/E with average $\langle L/E\rangle$ and standard deviation $\sigma_{L/E}$

$$\phi\left(\frac{L}{E}\right) = \frac{1}{\sqrt{2\pi\sigma^2_{L/E}}}\, exp\left[\frac{(L/E - \langle L/E\rangle)^2}{2\sigma^2_{L/E}}\right] \tag{2.54}$$

In this case, the average cosine from equation (2.52) can be calculated analytically resulting in

$$\left\langle \cos\left(\frac{\Delta m^2 L}{2E}\right)\right\rangle = \cos\left(\frac{\Delta m^2}{2}\left\langle\frac{L}{E}\right\rangle\right)\, exp\left[-\frac{1}{2}\left(\frac{\Delta m^2}{2}\sigma_{L/E}\right)^2\right] \tag{2.55}$$

therefore, the value

$$\langle P_{\nu_\alpha \to \nu_\beta}(L,E)\rangle = \frac{1}{2}\sin^2 2\theta \left[1 - \cos\left(\frac{\Delta m^2}{2}\left\langle\frac{L}{E}\right\rangle\right)\, exp\left[-\frac{1}{2}\left(\frac{\Delta m^2}{2}\sigma_{L/E}\right)^2\right]\right] \tag{2.56}$$

is plotted in Figure 2.2 next to the oscillation given in (2.49).

2.2.4 Three neutrino mixing

A more realistic case is when we consider three neutrino flavors. In this case the mixing matrix is given by the unitary matrix U_{PMNS}, similar to the U_{CKM} from the quarks, which can be parametrized by three mixing angles $(\theta_{12}, \theta_{13}\theta_{23})$ and one physical phase (δ_{CP}), assuming Dirac neutrinos.

In the absence of any matter effects, the transition probability of a flavor state to another for the three neutrino case is given by

$$P_{\nu_\alpha \to \nu_\beta}(L,E) = \delta_{\alpha\beta} - 4 \sum_{i>j=1}^{3} \mathrm{Re}(K_{\alpha\beta,ij}) \sin^2\left(\frac{\Delta m^2_{ij} L}{4E}\right) + 2 \sum_{i>j=1}^{3} \mathrm{Im}(K_{\alpha\beta,ij}) \sin\left(\frac{\Delta m^2_{ij} L}{2E}\right) \tag{2.57}$$

where $K_{\alpha\beta,ij} = U_{\alpha i} U^*_{\alpha j} U^*_{\beta i} U_{\beta j}$.

2.3 Neutrino oscillations in matter

In an article published in 1978, L. Wolfenstein [164] showed that neutrinos propagating in matter are subject to a potential due to head-on coherent elastic dispersion with particles in the media, such as electrons and nucleons. This potential is in analogy compared with an index of refraction, which modifies the frequency of neutrino mixing.

In the case of two-neutrino flavors, the mixing angle in vacuum is replaced by an effective angle in matter, that for certain densities can increase in its magnitude even if the vacuum angle is small. In the 80's, Wolfenstein and other physicists studied the neutrino propagation of neutrinos in constant density media. In 1985, S.P. Mikheev y A.Yu. Smirnov [36] discovered that is possible to have resonance effects in the flavor neutrino transitions if they propagate in media with variable density and if the region along the neutrino trajectory reaches an effective angle near the maximal $\pi/2$.

The Mikheyev-Smirnov-Wolfenstein (MSW) mechanism was able to explain the solar neutrino conversions during the propagation outside the sun despite the small value in the mixing angle [142].

Propagation of neutrino flavor states Let us suppose we have a left-handed ultra-relativistic neutrino with flavor $\alpha(i.e. \alpha = e, \mu, \tau)$ and momentum $\mathbf{p}$. Such neutrino is described by the state (2.1)

$$|\nu_\alpha\rangle = \sum_i U_{\alpha i} |\nu_i\rangle$$

with the normalization conditions $\langle\nu_\beta|\nu_\alpha\rangle = \delta_{\alpha\beta}$, $\langle\nu_j|\nu_i\rangle = \delta_{ij}$. The mass state $|\nu_i\rangle$ with momentum $\mathbf{p}$ is an eigenstate of the vacuum Hamiltonian $\mathcal{H}_0$

$$\mathcal{H}_0|\nu_i\rangle = E_i|\nu_i\rangle, \qquad E_i = \sqrt{\mathbf{p}^2 + m_i}. \tag{2.58}$$

The total Hamiltonian in matter is

$$\mathcal{H} = \mathcal{H}_0 + \mathcal{H}_\mathcal{I}, \qquad \mathcal{H}_\mathcal{I}|\nu_\alpha\rangle = V_\alpha|\nu_\alpha\rangle, \tag{2.59}$$

where V_α, the ultra-relativistic neutrino potential energy with flavor α is given by

$$V_\alpha = V_{CC}\delta_{\alpha e} + V_{NC} = \sqrt{2}G_F(N_e\delta_{\alpha e} - \frac{1}{2}N_n) \tag{2.60}$$

and as we can see, G_F is the Fermi constant, N_e and N_n are electron and neutrino density in the media. This potential is very small

$$\sqrt{2}G_F \simeq 7.63 \times 10^{-14} \text{ eV cm}^2/N_A \tag{2.61}$$

with $N_A \sim 10^{23}$ being Avogadro's number.

A state with initial flavor state α obeys the equation given by

$$i\frac{d}{dt}|\nu_\alpha\rangle = \mathcal{H}|\nu_\alpha(t)\rangle, \qquad |\nu_\alpha(0)\rangle = |\nu_\alpha\rangle \tag{2.62}$$

(Schrödinger picture). The transition amplitude $\nu_\alpha \to \nu_\beta$ after a time t is given by

$$\psi_{\alpha\beta}(t) = \langle\nu_\beta|\nu_\alpha(t)\rangle, \qquad \text{with} \qquad \psi_{\alpha\beta}(0) = \delta_{\alpha\beta}. \tag{2.63}$$

As a consequence, the probability that a neutrino created at $t = 0$ with flavor α is detected with a flavor β after a time t is

$$P_{\nu_\alpha\to\nu_\beta}(t) = |\psi_{\alpha\beta}(t)|^2. \tag{2.64}$$

Using the previous equations, it is possible to show that the time evolution expression for the transition amplitudes is

$$i\frac{d}{dt}\psi_{\alpha\beta}(t) = \sum_\eta \left(\sum_k U^*_{\beta\eta}E_k U_{\eta k} + \delta_{\eta\beta}V_\beta \right) \psi_{\alpha\eta}. \tag{2.65}$$

It is easy to see

$$\sum_{\eta} \psi_{\alpha\eta}(t)\psi^{*}_{\beta\eta}(t) = \delta_{\alpha\beta}. \tag{2.66}$$

The previous expression gives the conservation of probability when $\alpha = \beta$. For ultra-relativistic neutrinos,

$$E_k \simeq E + \frac{m_k^2}{2E}, \quad p \simeq E, \quad t \simeq x, \tag{2.67}$$

where x is the distance to the source. With this, expression (2.65) describes spatial evolution

$$\begin{aligned} i\frac{d}{dt}\psi_{\alpha\beta}(x) = &\left(p + \frac{m_1^2}{2E} + V_{NC}\right)\psi_{\alpha\beta}(x) \\ &+ \sum_{\eta}\left(\sum_{k} U^{*}_{\beta\eta}\frac{\Delta m^2_{k1}}{2E}U_{\eta k} + \delta_{\beta e}\delta_{\eta e}V_{\beta}\right)\psi_{\alpha\eta}. \end{aligned} \tag{2.68}$$

We have separated the term $(p + m_1^2/2E + V_{NC})\psi_{\alpha\beta}(x)$ because is irrelevant when generating a common phase for all the flavor states that can be eliminated with a phase change, leaving the transition probability invariant.

Thus, the equation for the transition amplitude is

$$i\frac{d}{dt}\psi_{\alpha\beta}(x) = \sum_{\eta}\left(\sum_{k} U^{*}_{\beta\eta}\frac{\Delta m^2_{k1}}{2E}U_{\eta k} + \delta_{\beta e}\delta_{\eta e}V_{\beta}\right)\psi_{\alpha\eta}. \tag{2.69}$$

showing once again its similarity with the vacuum oscillations, where the matter neutrino oscillations also depend on the squared mass differences. As an example, consider the three-flavor oscillation probability $P(\nu_\mu \to \nu_e)$ with matter effects

$$P(\nu_\mu \to \nu_e) = P_1 + P_2 + P_3 + P_4 \tag{2.70}$$

where

$$P_1 = \sin^2(\theta_{23})\sin^2(2\theta_{13})\left(\frac{\Delta_{13}}{B_\pm}\right)^2 \sin^2\left(\frac{B_\pm L}{2}\right) \tag{2.71}$$

$$P_2 = \cos^2(\theta_{23})\sin^2(2\theta_{12})\left(\frac{\Delta_{12}}{A}\right)^2 \sin^2\left(\frac{AL}{2}\right) \tag{2.72}$$

$$P_3 = J \cdot \cos(\delta_{CP}) \left(\frac{\Delta_{13}}{B_\pm}\right) \left(\frac{\Delta_{12}}{A}\right) \cos\left(\frac{\Delta_{13}L}{2}\right) \sin\left(\frac{AL}{2}\right) \sin\left(\frac{B_\pm L}{2}\right) \tag{2.73}$$

$$P_4 = \mp J \cdot \sin(\delta_{CP}) \left(\frac{\Delta_{13}}{B_\pm}\right) \left(\frac{\Delta_{12}}{A}\right) \cos\left(\frac{\Delta_{13}L}{2}\right) \sin\left(\frac{AL}{2}\right) \sin\left(\frac{B_\pm L}{2}\right) \tag{2.74}$$

where $\Delta_{ij} = \Delta m^2_{ij}/(2E)$, $A = \sqrt{2} G_F N_e$, $B_\pm = |A \pm \Delta_{13}|$ and $J = \cos(\theta_{13}) \sin(2\theta_{12}) \sin(2\theta_{13}) \sin(2\theta_{23})$, the Jarlskog-invariant. The $+$ sign is for neutrinos and $(-)$ for antineutrinos. It is intresting to note that the CP-phase appears as a product with all the mixing angles.

2.4 Experimental landscape

In the previous sections, the theory of neutrino oscillations in both, vacuum and matter was described. Having established that, one of the major goals in the field is to determine within reasonable errors the values of the PMNS matrix elements and the CP-violation phase described in (2.3). Since the value of Δm^2 is fixed by nature, choosing L/E appropriately allows different designed experiments to be sensitive to the values of Δm^2. The sensitivity to Δm^2 in an experiment is the value of Δm^2 for which

$$\frac{\Delta m^2 L}{2E} \sim 1.$$

Neutrino oscillation experiments tend to be classified by the value of the L/E ratio, as shown by Table 2.2.

Table 2.2: Regions of sensitivity for different neutrino oscillation experiments [129]

Source	Neutrino type	$\overline{E}$ [MeV]	L [km]	sensitivity Δm^2 [eV]^2
Reactor	$\overline{\nu}_e$	~ 1	1	$\sim 10^{-3}$
Reactor	$\overline{\nu}_e$	~ 1	100	$\sim 10^{-5}$
Accelerator	$\nu_\mu, \overline{\nu}_\mu$	$\sim 10^3$	1	~ 1
Accelerator	$\nu_\mu, \overline{\nu}_\mu$	$\sim 10^3$	1000	$\sim 10^{-3}$
Atmospheric	$\nu_{\mu,e}, \overline{\nu}_{\mu,e}$	$\sim 10^3$	10^4	$\sim 10^{-4}$
Solar	ν_e	~ 1	1.5×10^8	$\sim 10^{-11}$

Reactor experiments use isotropic fluxes of electron-antineutrinos, such as Chooz, Daya Bay, RENO, Double Chooz have a typical baseline (neutrino source-to-detector distance) of $L \sim 1$ km. Accelerator experiments, which use a beam of (anti)neutrinos produced by the decay of pions and kaons produced by colliding high energy protons into a target, have a baseline of $L \sim (250 - 1300)$ km. Examples are K2K, MINOS, OPERA, T2K, NOvA, and in the near future, DUNE. A short-baseline neutrino (SBN) program has been developed at Fermilab in order to resolve previous experiment anomalies (appearance excess at the LSND experiment), search for sterile neutrinos at the eV-mass scale, and serve as prototype for the large scale DUNE experiment [25]. Finally, experiments such as Super-Kamiokande, MINOS, IceCube use cosmic rays interacting with the upper layers of the atmosphere, producing mesons that decay into neutrinos. The source-detector distance ranges from 20 km from neutrinos coming from above, to about 1.3×10^4 km for neutrinos coming from below, initially produced on the other side of the Earth. Solar experiments detect neutrinos produced at the core of the Sun by thermonuclear reactions (discussed in the previous chapter). Experiments which have been performed in the past are Homestake, Kamiokande, SAGE, GALLEX. Some of the experiments which were contemporary to the latter are SNO, KamLAND, BOREXINO.

2.5 The ν_e-appearance case

According to Eqs. 2.70 and 2.71, the oscillation probability of muon neutrinos to electron neutrinos $P(\nu_\mu \to \nu_e)$ is proportional to $\sin^2(2\theta_{13})$, and from measurements of reactor experiments [17, 22] we know the value of the mixing angle θ_{13} is non zero. This allows NOvA to make statements about the CP-violation phase δ and the neutrino mass ordering by measuring electron (anti)neutrino appearance in a muon (anti) neutrino beam. To observe muon neutrino to electron neutrino oscillations, ν_e-charged current interactions must be properly identified at the Far Detector. Signal events will be characterized by an electromagnetic shower, attached to the vertex of interaction with any other hadronic activity. NOvA uses an energy spectrum strategically tuned with a peak at about 2 GeV, which is where the maximal ν_e signal is expected to appear given the beamline

distance. Backgrounds to the electron appearance signal are the intrinsic beam ν_e component of the beam, originated from the decay of kaons after exiting the target. Neutral current (NC) events are also background to this signal specially when the hadronic system contains a neutral pion, which decays into two photons $\pi^0 \rightarrow \gamma + \gamma$. Muon neutrino charged-current events are a relatively small background in the Far Detector since most of them are suppressed by oscillations. In an even smaller fraction are the backgrounds due to tau charged-current interactions and muon antineutrinos. The total background selected in the Near Detector is broken down into NC, beam ν_e CC, and ν_μ CC components, using a data driven approach [50]. They are broken independently since each of them gets affected differently by oscillations. These components are later used to compute the corresponding components in the Far Detector. From the pion and muon decays $\pi^+ \rightarrow \mu^+ + \nu_\mu$ and $\mu^+ \rightarrow e^+ + \overline{\nu}_\mu + \nu_e$ the intrinsic ν_μ and ν_e components of the beam arise. At higher energies ($E_\nu \gtrsim 4$ GeV), this is produced by kaons. In order to correct the ν_e CC rate in sumulation, the pion and kaon yields are derived from the low and high energy ν_μ CC Near Detector rate, respectively. The former is computed in bins of transverse (p_T) and longitudinal (p_Z) momentum from the neutrinos whose particle exiting the target is a pion. The kaon yield is computed as a single scale. This results in a pion yield 3% lower and a kaon yield 17% higher than simulation and translates in an overall 1% increase in the estimated Near Detector beam ν_e background rate in the 1-3 GeV region [10].

The muon neutrino disappearance measurement will be discussed in detail on Chapter 6. In the next chapter we will start the description of the NOvA experiment and its role in the neutrino physics community.

CHAPTER 3. THE NOvA EXPERIMENT

In this chapter we will present a description of the NOvA experiment. We will first discuss how the beam of neutrinos is produced at Fermilab, starting from the Linac to the target area. Then we will comment on the motivation for the off-axis technology and how it will help NOvA achieve its physics goals. Finally, we will talk about the NOvA detectors and how they work, concluding with a description of readout electronics and the data acquisition system.

3.1 Experimental design and and physics goals

NOvA is a long baseline neutrino oscillation experiment with $L/E \sim 400$ km/GeV (where L is the source-detector distance and E is the neutrino energy), sensitive to the atmospheric mass splitting parameter Δm^2_{32} (where $\Delta m^2_{ij} = m^2_i - m^2_j$). It consists of two functionally identical, high sampling liquid scintillator calorimeters: the 0.3 kton Near Detector (ND) located 105 m underground, 1 km from the production target at Fermilab and a 14 kton Far Detector (FD) located on the surface 810 km from the source along the Ash River Trail, MN.

The NOvA experiment uses the NuMI beam with both detectors aligned 14.6 mrad off the main axis. The off-axis location provides a neutrino flux narrowly peaked at around 2 GeV. With such configuration, the suppression of the high energy tail reduces the neutral current background at the measured energies where the probability of electron neutrino appearance is greatest.

The NOvA physics portfolio includes measurements of the $\nu_\mu \to \nu_\mu (\overline{\nu}_\mu \to \overline{\nu}_\mu)$ muon disappearance probability, allowing NOνA to measure $\sin^2 2\theta_{23}$ and the atmospheric Δm^2_{32}, and measurements of $\nu_\mu \to \nu_e (\overline{\nu}_\mu \to \overline{\nu}_e)$ electron appearance probability. From these measurements, NOvA will have a chance to resolve the mass hierarchy, a chance to measure the δ_{CP} phase in the neutrino sector using

electron appearance and the θ_{23} octant using the information from muon disappearance. NOvA will also look for evidence of new physics and make measurements of a variety of neutrino-nucleus interaction cross sections.

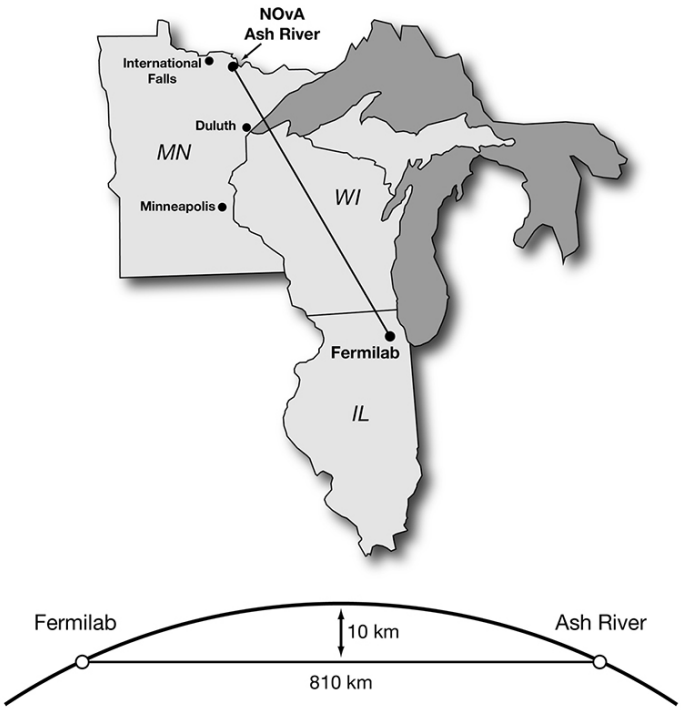

Figure 3.1: Geographical location of the NOvA detectors. The Near Detector is located on the Fermilab campus, 100 meters underground and about 1 km from the NuMI target. The Far Detector is located on the surface along the Ash River Trail, Minnesota, 810 km from the target. Both detectors are 14 mrad off-axis the center of the beam. The beam is bent 58 mrad into Earth's crust in order to reach the location at Minnesota.

3.2 The NuMI neutrino beam

The Fermilab accelerator complex is a set of seven facilities that together produce and deliver a diversity of particle beams (as shown in Fig. 3.2), including the most powerful high energy neutrino beam for neutrino experiments, a muon beam for muon experiments, and proton beams for various fixed-target experiments as well as Research and Development (R&D) programs [73].

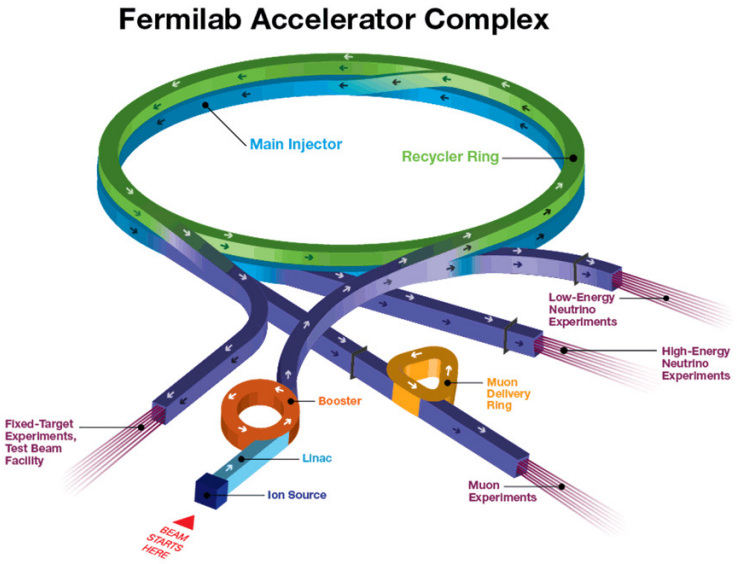

Figure 3.2: The Fermilab accelerator complex is composed of seven parts including five accelerators and two storage rings: Radio-frequency quadrupole (RFQ), Linear Accelerator, Booster, Recycler, Main Injector, Muon Delivery Ring and the Fermilab Accelerator Science and Technology Facility (FAST).

The NuMI beamline was built at Fermilab with the original idea of producing the neutrinos for the Main Injector Neutrino Oscillation Search experiment (MINOS), a long-baseline neutrino experiment designed to observe the phenomena of neutrino oscillations with significant contributions to the measurement of the parameter Δm^2_{32}. With the addition of several hardware upgrades over time and thanks to the flexibility of its design, the NuMI beam has been delivering neutrinos not only to MINOS but to other neutrino experiments such as MINERvA and NOvA.

The accelerator chain starts in the radio-frequency quadrupole (RFQ) accelerator, which provides the particle beam source for the entire accelerator complex. This 3-meter-long accelerator takes in negative hydrogen ions H^- from an ion source and accelerates them in pulses of approximately 100 μs long at a rate of 15 Hz from 35 keV to 750 keV towards the linear accelerator.

The Linac is a 150-meter long linear accelerator that brings the ion beam up to 400 MeV. The Linac contains two sections: the Low Energy (LE) Linac and the High Energy (HE) Linac. There is a transition section between the two. The LE Linac is a Drift Tube Linac (also known as Alvarez Linac) that operates at a resonant frequency of 201.24 MHz and accelerates the beam from 750 keV to 116.5 MeV. The HE Linac is a Side-Coupled cavity Linac that accelerates the beam from 116.5 MeV to 400 MeV at a resonant frequency of 804.96 MHz [6].

The ion beam is then sent to the Booster, which is a synchroton ring of approximately 470 meters in circumference, made up primarily of magnets and radio-frequency (RF) cavities. Booster accelerators are used to increase the energy of the beam from the Linac stage to an acceptable input energy for the final accelerator (e.g. the Main Injector). The beam of H^- ions passes through a stripping foil at the injection point to remove the electrons, in a process called "charge exchange injection" which reduces beam losses. The resulting protons are accelerated from 400 MeV to 8 GeV. Since the Booster is a synchroton, the cavity resonant frequency sweeps from 37.8 MHz to 52.8 MHz as the beam revolution period decreases from 2.2 μs at injection to 1.6 μs at extraction.

Bunches are discrete groups of beam created by interaction with the RF waveform. The maximum number of bunches the Booster can accelerate is 84. All 84 bunches are extracted from the Booster at once, and each string of 84 bunches is called a Booster batch. It is in this step that the 8 GeV proton beam is either directed towards the Booster Neutrino Beam target and/or towards the Recycler and Main Injector (MI) rings.

The Recycler is a fixed energy machine of 8 GeV composed mostly of permanent magnets and located on top of the MI with the same circumference of 3.3 km. The current role of the Recycler is to facilitate proton injection to the Main Injector. The Recycler receives beam from the Booster, performs radio-frequency manipulation technique called "slip-stacking", and extracts the beam to MI. The Recycler RF cavity resonant frequency is at 52.8 MHz, the same resonant frequency of the Booster at extraction and MI at injection.

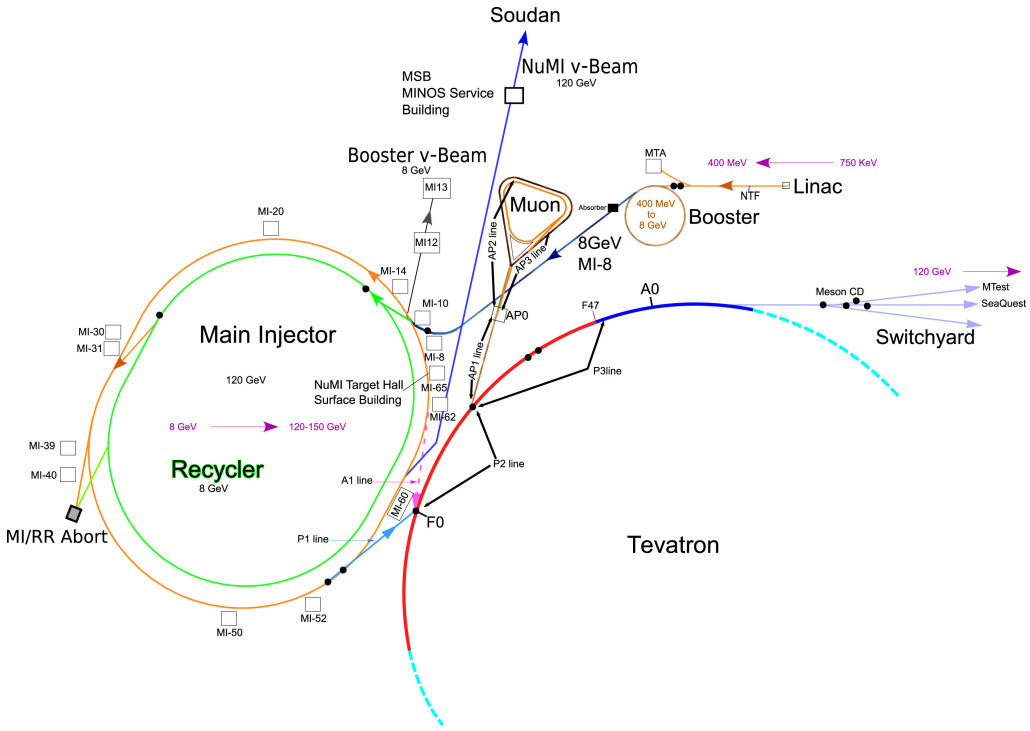

Figure 3.3: Technical diagram of the Fermilab accelerator complex [9].

Slip-stacking is the process of injecting pairs of batches into the Recycler and then merging the pairs to form double-intensity batches. The Recycler is capable of slip-stacking up to twelve batches, which results in six double-intensity batches for extraction to MI.

The Main Injector is another synchroton machine with an injection energy of 8 GeV and an extraction energy of 120 GeV. The RF frequency ranges from 52.8 MHz to 53.1 MHz. It is made up of dipoles, quadrupoles and RF cavities. A typical MI machine cycle is 1.33 s.

The NuMI beamline directs the 120 GeV protons from the MI to the NuMI target located underground at MI-65, as shown in Fig. 3.3. In order to reach the MINOS detector located in the Soudan mine in Minnesota, the proton beam is bent downward at an angle of 58 milliradians. The beam is transported 350 meters from the extraction hall to the target hall where the NuMI target is located. Figure 3.4 shows the schematics of the NuMI beamline from the extraction hall to the MINOS hall. The target hall is located 41 meters underground. The high energy protons

collide with a 1 meter-long, graphite-and-beryllium NuMI target [103, 90] with a graphite density of 1.78 g/cm^3. The recent addition of 3 fins of beryllium were the result of a set of studies that show its superior resistance to radiation damage compared to graphite and due to its similar density, the replacement implied no mayor effect in the physics of the experiment.

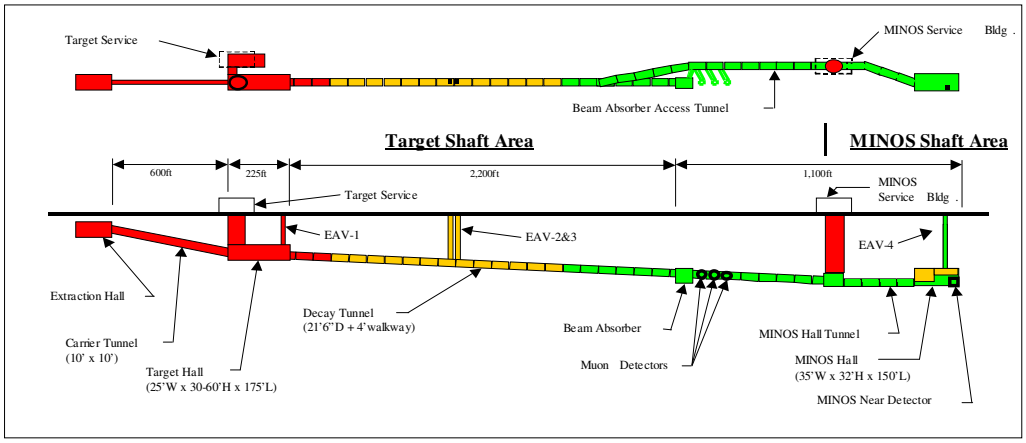

Figure 3.4: Aerial view (top) and side view (bottom) of the NuMI beamline from the extraction hall to the MINOS hall.

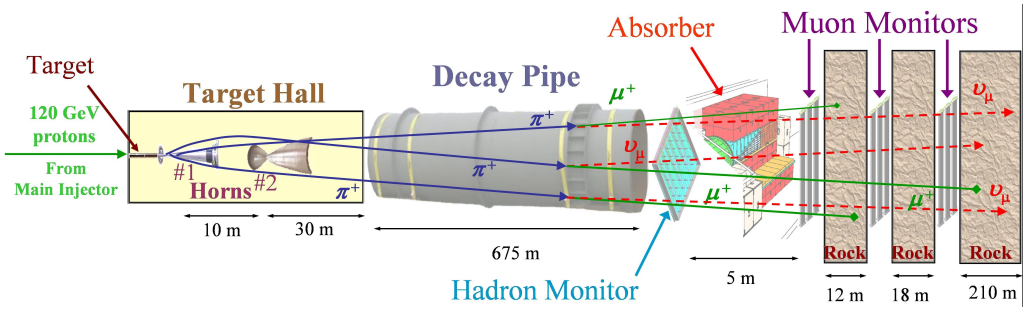

Figure 3.5: Schematic diagram for the particle beam used in NOvA. The dimensions shown in the horns correspond for the Low Energy (LE) tune, not the Medium Energy (ME) tune relevant for NOvA. In particular, horn 2 has been moved from the LE position (10 m from zero point) to the ME position (19.18 m from zero point) [100]

The particle beam used in NOvA is shown in Fig. 3.5. After the interaction of protons with the carbon/beryllium nuclei, secondary particles are produced in the neighborhood of the target. Two parabolic aluminum horns act as hadron lenses, producing a magnetic field that focus or defocus the outgoing flux of charged particles according to the sign of the current. For example, a magnetic field

produced by a forward current in the horn will focus positive mesons (and deflect negative mesons) towards the center (see Fig. 3.6). The position of the target with respect to the first horn, as well as the intensity of the current through the horns and the separation between them shapes the neutrino energy spectrum and its background contamination. Once secondary particles are focused (mainly pions and kaons), they decay via the weak interaction $\pi^+ \to \mu^+ + \nu_\mu$ and $K^+ \to \mu^+ + \nu_\mu$ resulting in a muon neutrino ν_μ beam. There is also a small component of antineutrinos coming from the negatively charged low-transverse momentum pions and kaons, and even a electron neutrino ν_e component, from the analogous $K^+ \to e^+ + \nu_e$ reaction. This secondary particles exit the horns and decay in the 2 m wide decay pipe, whose nearly 700 meters in length was calculated to closely match the decay length of a 10 GeV pion. At the end of the decay pipe there is a absorber made of aluminum, steel and concrete, whose function is to stop most of the particles that are not neutrinos and protect from irradiation downstream the line.

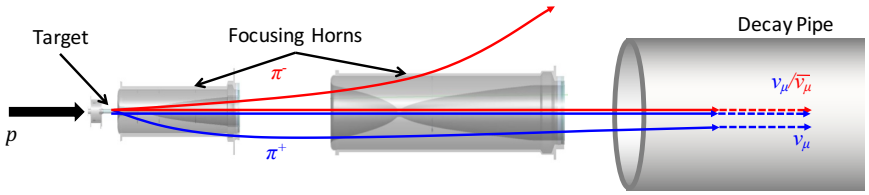

Figure 3.6: Forward horn current (FHC) configuration of the NuMI beam line. The magnetic field produced by this configuration focuses positively charged mesons, producing neutrinos in the final state.

3.3 Off-axis technology

NOvA is an off-axis neutrino experiment. Historically, the idea was first proposed and developed in the E-889 experiment, in Brookhaven National Laboratory [135]. The physics motivation will be explained as follows. Let us suppose we have a reaction producing a muon neutrino in the final state,

$$\pi^+ \to \mu^+ + \nu_\mu.$$

In the frame of reference of the pion, which is also the frame of the center of mass (**CM**), the reaction can be written using four-vector as

$$q_\pi = q_\mu + q_\nu$$

where $q = (E, \boldsymbol{p})$ and $q^2 = E^2 - p^2 = m^2$. Since we are solving for the neutrino energy in the center of mass frame, we get

$$q_\pi - q_\nu = q_\mu$$

taking squares (and since $q_\nu^2 = 0$)

$$(q_\pi - q_\nu)^2 - 2q_\pi \cdot q_\nu = m_\mu^2$$

$$q_\pi^2 - 2q_\pi \cdot q_\nu =$$

Once again, in the frame of reference of the pion, we have that $q_\pi = (m_\pi, 0, 0, 0)$, and under the assumption that $m_\nu = 0$, then $\boldsymbol{p}_\nu = 0$ and $E_\nu = p_\nu$, therefore

$$m_\pi^2 - 2E_\nu^{CM} m_\pi = m_\mu^2$$

hence,

$$E_\nu^{CM} = \frac{m_\pi^2 - m_\mu^2}{2m_\pi}. \tag{3.1}$$

We can also rewrite the previous expression as

$$E_\nu^{CM} = p_\nu^{CM} = \frac{m_\pi}{2}\left(1 - \frac{m_\mu^2}{m_\pi^2}\right) \simeq 29.79 \text{ MeV} \tag{3.2}$$

Let us consider the motion of the pion as seen from the Lab frame of reference, with speed given by $V = p_\pi/E_\pi \simeq 1$ along the z axis and $\gamma = (1 - V)^{-1/2} = E_\pi/m_\pi \gg 1$ with $c = 1$. The energy and momentum transformations in general from Lab to CM is given by

$$E^{CM} = \gamma(E^{CM} - \beta p_z) \tag{3.3}$$

$$p_z = \gamma(p_z^{CM} - \beta E^{CM}) \tag{3.4}$$

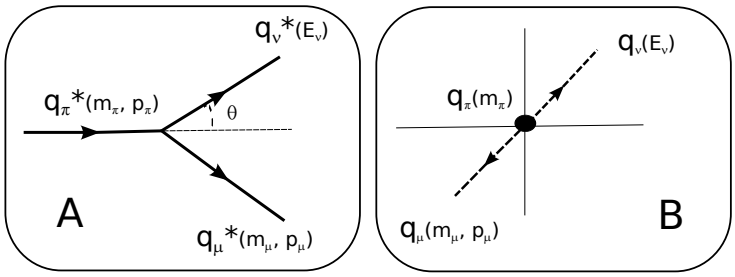

Figure 3.7: Pion decay given by the reaction $\pi^+ \to \mu^+ + \nu_\mu$. Figure A shows the Lab frame of reference whereas figure B shows the center of mass frame of reference.

but since $E_\nu = p_\nu$ and $p_z = p\cos\theta$, then

$$E_\nu^{CM} = \gamma(E_\nu^{Lab} - V \cdot E_\nu^{Lab}\cos\theta) = \gamma E_\nu^{Lab}(1 - V \cdot \cos\theta) \tag{3.5}$$

Our goal is to find an angular relation for the neutrino energy $E_\nu = E_\nu(\theta)$, for small θ. Solving for E_ν^{Lab} and approximating $\cos\theta \simeq 1 - \theta^2/2$, from the previous expression we get

$$E_\nu^{Lab} = \frac{E_\nu^{CM}}{\gamma(1 - \cdot\cos\theta)} \simeq \frac{E_\nu^{CM}\gamma(1+V)}{1 + \gamma^2\theta^2 V(1+V)/2}$$

where we had multiplied both numerator and denominator by a $\gamma(1+V)$ factor. Noting that $V \simeq 1$, we get

$$E_\nu^{Lab} \simeq \frac{2\gamma E_\nu^{CM}}{1 + \gamma^2\theta^2} \tag{3.6}$$

and using Eq. (3.2) together with $\gamma = E_\pi/m_\pi$ for simplification, we finally obtain

$$E_\nu^{Lab} \simeq \left(1 - \frac{m_\mu^2}{m_\pi^2}\right)\frac{E_\pi}{1 + \gamma^2\theta^2} = \left(1 - \frac{m_\mu^2}{m_\pi^2}\right)\frac{E_\pi m_\pi^2}{m_\pi^2 + E_\pi^2\theta^2} \tag{3.7}$$

The expression (3.7) is crucial, because shows the monochromatic nature of the neutrino energy when using the off-axis idea.

For a detector located along the beam axis (e.g. when $\theta = 0$) it follows that the energy spectrum is proportional to the pion energy, resulting in a wide-band beam. On the other hand, if we locate the detector off-axis, it can be shown that the neutrino energy depends less on the pion energy and it reaches a maximum value (see 3.8). This can be calculated by taking the derivative with respect to E_π,

$$\frac{dE}{dE_\pi} \simeq \frac{0.43 m_\pi^2(m_\pi^2 - E_\pi^2\theta^2)}{(m_\pi^2 + E_\pi^2\theta^2)^2}. \tag{3.8}$$

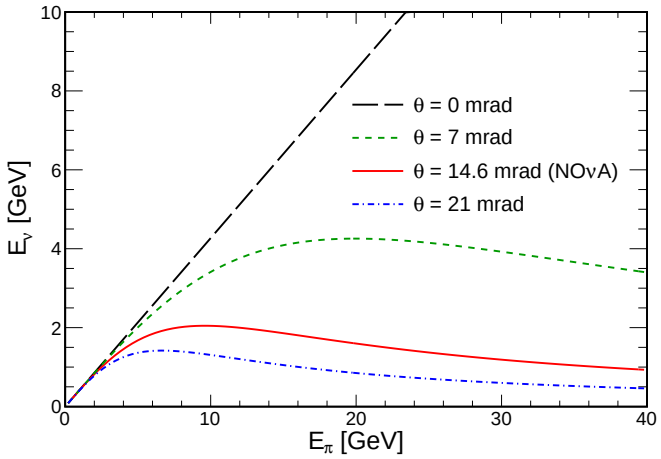

Figure 3.8: Neutrino energy as function of pion energy given by Eq. (3.7). At $\theta = 14$ mrad the pion decays yield neutrinos in the 1-2 GeV range, optimal for neutrino oscillations, compensating for the decrease in flux.

The previous equation has a critical value when $\theta = m_\pi/E_\pi = 1/\gamma_\pi$, that is

$$E \simeq 0.43 \frac{m_\pi (E_\pi m_\pi)}{2m_\pi^2} \simeq \frac{30\,\mathrm{MeV}}{\theta}. \tag{3.9}$$

As a consequence, if $\langle E_\pi \rangle$ represents the average pion beam energy, then a detector located on an angle $\theta \simeq m_\pi/\langle E_\pi \rangle$ with respect to the beam axis will receive a neutrino beam energy given by (3.9), which is independent of the pion energy. This is the essence of the off-axis concept.

The neutrino flux produced by the pion decay is given by

$$\phi = \int \frac{E_\nu^{Lab}\, dE}{dS}\, dA = \int \frac{E_\nu^{Lab}\, dE}{r^2 d\Omega}\, dA = \int E_\nu^{Lab}\, dE \frac{A}{4\pi z^2} \tag{3.10}$$

where $d\Omega = 4\pi$, A is the detector area, z is the distance between the decay point and the detector. Using the expression (3.6) we get

$$\phi = \left(\frac{2\gamma}{1+\gamma^2\theta^2} \right)^2 \frac{A}{4\pi z^2}. \tag{3.11}$$

Figure 3.9 shows the ratio $\phi(\theta)/\phi(0)$ of the neutrino flux as function of the off-axis angle for values of $\theta = 0, 7, 14, 21, 28$, with respect to on-axis $\theta = 0$. We can see that the neutrino flux suppression

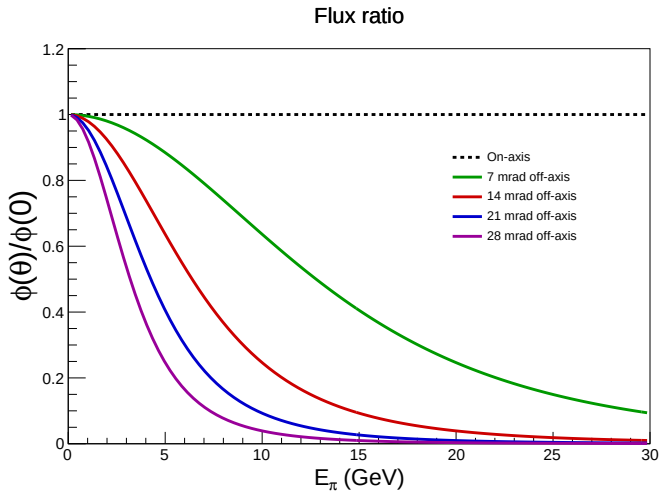

Figure 3.9: Neutrino flux suppression with respect to off-axis. Curves represent off axis values $\theta = 0, 7, 14, 21$ and 28 mrad respectively.

is considerable for off-axis detectors. To counteract this and the small neutrino cross section, a more intense beam and a detector with a large mass are needed.

The NOvA experiment uses the off-axis concept by locating the detector at $\theta = 14.6$ mrad off-axis the neutrino beam. This results in a narrow band, $\sim$ 2 GeV-peaked, quasi-monochromatic neutrino spectrum. This is fundamental, since the neutrino energy that maximizes the oscillation probability of electron neutrino appearance in a muon neutrino beam is approximately 1.6 GeV for a baseline of 810 km and $\Delta m^2_{32} = 2.3 \times 10^{-3}\text{eV}^2$. Other angle configurations are shown in Fig. 3.10 for comparison.

An off-axis configuration has important advantages [55, 128] if used for an electron neutrino appearance experiment such as NOvA. For example, the high energy tail is reduced substantially, decreasing the neutral current (NC) and tau decay backgrounds. Tau neutrinos are mainly suppressed since the peak of the beam is slightly below the threshold of tau particle production ($m_\tau = 1.78$GeV). High energy NC events can have the outgoing lepton (neutrino) carrying away most of the interaction energy, and since they are not observed, they can shift down into the signal region when reconstructed. This is a common background for both ν_μ-disappearance and ν_e-appearance analysis

in NOvA. Therefore, the off-axis configuration reduces the high energy tail, shifting most of the NC distribution to the lower energy part as shown by Fig. 3.11. Another important background is the intrinsic beam ν_e component, which comes from the kaon and muon decays after being focused by the horns and produces a broad spectrum even off-axis.

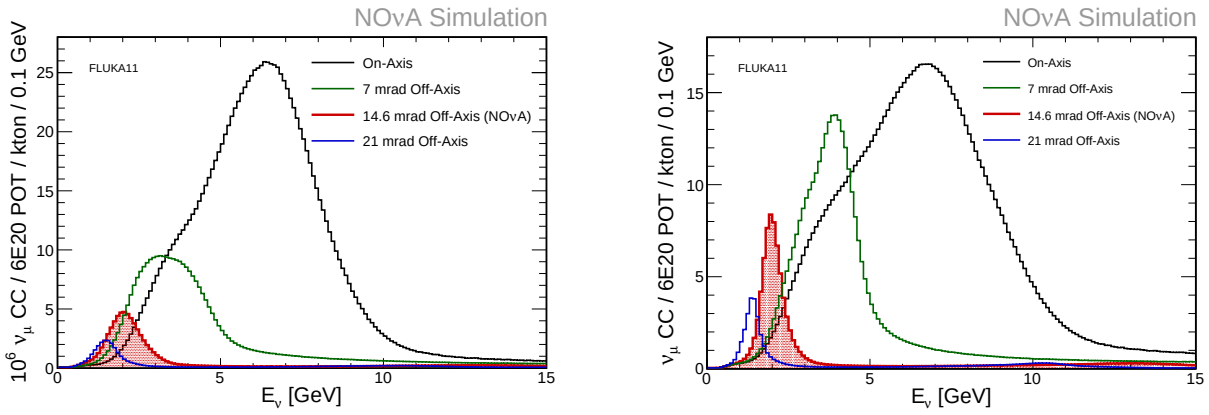

Figure 3.10: Charged-current muon neutrino energy spectra (flux times cross-section) using Fluka11 simulation software for the NOvA Near Detector (left) and Far Detector (right). Different angle configurations are shown: on-axis and at 7, 14 and 21 mrad respectively.

Figure 3.12 shows the event rate of charged current neutrino interactions in both NOvA detectors for the forward-horn current NuMI configuration. The ν_μ component shown in red is substantially larger than the wrong sign and intrinsic ν_e components. In contrast, Fig. 3.13 shows the antineutrino charged current event rate in reverse-horn current, where the $\overline{\nu}_\mu$ and wrong sign components are almost equivalent in magnitude, specially at high energies. This is a mayor difference between the two event rates.

3.4 The NOvA detectors and the physics of detection

Neutrino detection is a challenge. Due to the very small nature of the neutrino cross section when compared to other particles, neutrino detectors tend to be massive in order to collect data from interactions. For example, the cross section of a 2 GeV neutrino scattering-off a nucleon is approximately 0.8×10^{-38} cm^2/nucleon [129]. Therefore, for a 60 meter detector target filled with

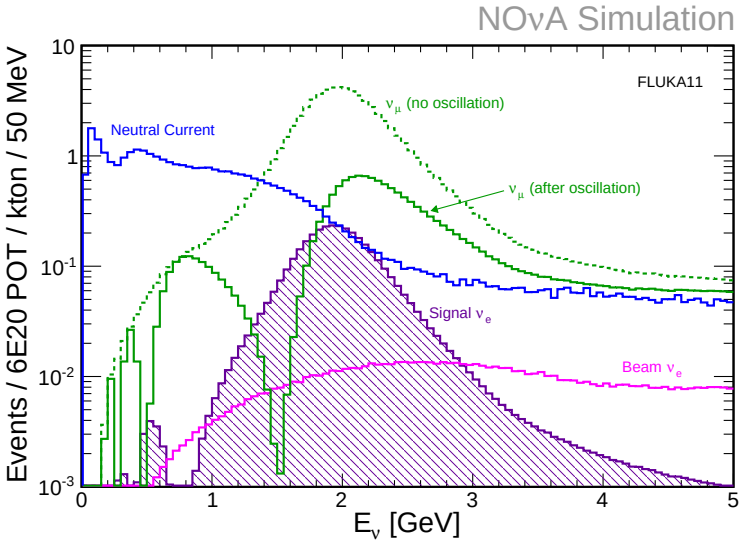

Figure 3.11: Simulated signal and background rates at the NOvA Far Detector as a function of the true neutrino energy, except for the NC (shown in blue), which are shown as function of the visible energy (e.g. the energy not carried away by the neutrino). The muon neutrino rates are shown with (green dashed) and without (solid green) oscillations applied. The light magenta curve shows intrinsic beam ν_e component. The dark violet filled histogram represents the appearance ν_e signal. Simulation parameters used $\Delta m^2_{32} = 2.32 \times 10^{-3}$ eV^2, $\sin^2(2\theta_{23}) = 1$. Source [109].

mineral oil, the interaction probability is [88]

$$R = \sigma \cdot N_A[\text{mol}^{-1}]/g \cdot d \cdot \rho$$
$$R = 0.8 \times 10^{-38}\ \text{cm}^2 \cdot 6.023 \times 10^{23}\text{g}^{-1} \cdot 6 \times 10^3\text{cm} \cdot 0.85\frac{\text{g}}{\text{cm}^3} = 2 \times 10^{-11}. \quad (3.12)$$

Therefore, is very unlikely that neutrinos interact even with massive detectors. This very small likelihood of interaction motivates high intensity neutrino beams, such as NuMI.

As mentioned earlier, NOvA uses a neutrino beam from Fermilab and two highly active, segmented, liquid scintillator off-axis detectors. They are identical in design and functionality, which significantly reduces systematic uncertainties in the oscillation analyses.

The Near Detector measures the neutrino energy spectrum close to the source and before oscillations have occurred, mitigating the significant uncertainties in the neutrino flux, cross sections, and

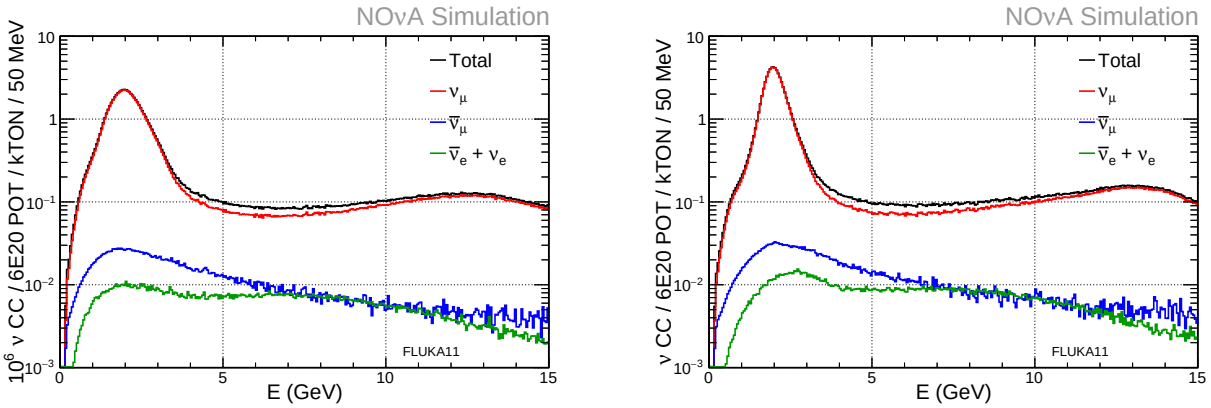

Figure 3.12: Neutrino charged-current event rate (flux times cross section) for the NOvA Near Detector (left) and Far Detector (right) using the forward-horn current (FHC) NuMI configuration. In solid black is shown the total neutrino component, in red is shown the ν_μ-only component, in blue is shown the wrong sign contamination, and green the intrinsic beam ν_e contamination. No oscillation weights applied. Source [146].

detector acceptance. Any differences between the prediction and the Far Detector data may be then associated to neutrino oscillations or some other hypothesis.

The basic unit of detection in NOvA is a rectangular cell made of polyvinyl-chloride (PVC) and filled with liquid scintillator. The cell walls are made of highly reflective by adding titanium dioxide (TiO_2) to the PVC resin. The cells have a cross section size of 3.9 cm by 6.6 cm and a length of 3.9 meters in the Near Detector and 15.5 meters in the Far Detector. Inside each cell, a 0.7 mm in diameter, Kuraray-Y11 wavelength-shifting (WLS) fiber is contained in a U-shaped fashion, with both ends terminating on a single pixel of a Hamamatsu avalanche photodiode (APD). A set of two 16-PVC cell extrusions glued together its called a module, and a custom number of modules, different for each detector, forms a plane. Planes of PVC cells with their long axis alternating 90 degrees allow three dimensional reconstruction of particles (shown in Fig. 3.14).

The Far Detector has 384 cells per plane and a total of 895 planes with a total of 344k channels. The detector dimensions are 15.5 m tall by 15.5 m wide by 59.8 m long and the total mass of 14 ktons [58]. The Near Detector is 15.3 m long and consists of an active region of 192 planes with 96 cells each. At the far end of the Near Detector, a muon range stopper is placed and consists of 11

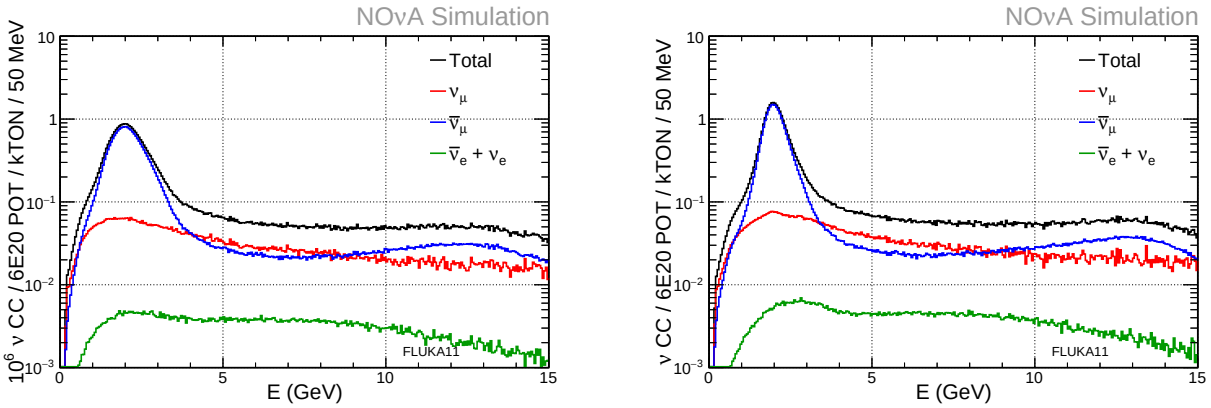

Figure 3.13: Antineutrino charged-current event rate (flux times cross section) for the NOvA Near Detector (left) and Far Detector (right) using the reversed-horn current (RHC) NuMI configuration. In solid black is shown the total antineutrino component, in blue is shown the $\overline{\nu}_\mu$-only component, in red is shown the wrong sign contamination, and green the intrinsic beam ν_e contamination. No oscillation weights applied. Source [146].

pairs of active PVC planes with a 10 cm thick steel plate between them. The muon range stopper is two thirds the height of the upstream component of the detector and its purpose is to contain muons produced in the upstream active region, as shown in Fig. 3.15. The total mass of the Near Detector is 0.3 ktons [57].

When a charged particle enters the detector, the electromagnetic field in the surroundings will interact with the liquid scintillator molecules, exciting them and releasing photons as a byproduct, photons which later will be internally reflected by the inner walls of the cell and ultimately collected by the WLS fibers.

The components of the NOvA scintillator blend are

- Mineral oil (96% by mass fraction) that serves as a mainly as solvent, with a specific gravity in the range of 0.850-0.865 and with an attenuation length at 420 nm greater than 5 meters
- Pseudocumene (4.1% by mass fraction) a benzene derivative that gets excited by traversing ionizing particles and releases photons in the UV-range, serves as the main scintillant

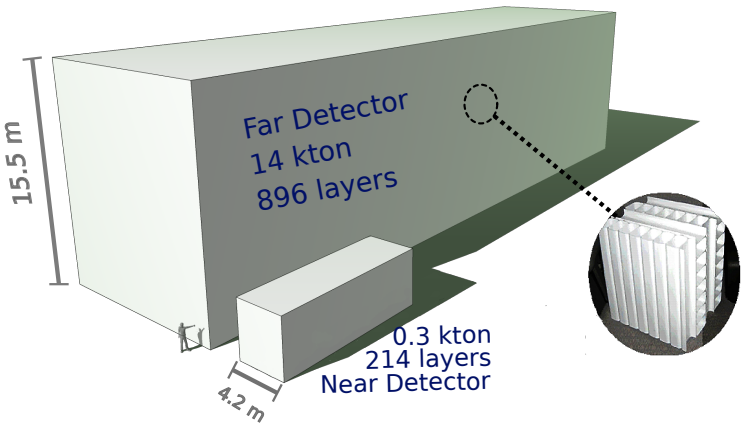

Figure 3.14: The NOvA Far and Near Detectors, at scale. Planes of PVC cells are rotated 90 degrees to allow 3D reconstruction.

- Scintillator waveshifter 1: PPO, or 2,5-diphenyloxazole (0.091% by mass fraction) takes in the UV-photons from the pseudocumene shifts them to the absorbing region of the WLS fiber
- Scintillator waveshifter 2: bis-MSB, or 1,4-di(methylstyryl)benzene (0.0013%) also shifts the UV-photons to the absorbing WLS fiber region
- Stadis-425 (0.0003%) used as antistatic agent since liquid scintillators are extremely non-conductive fluids, potentially developing charges through triboelectric effect during flow, that can lead to sparks
- Vitamin E (0.001%) used as antioxidant, preventing slow degradation of mineral oil

For the baseline scintillator, the output spectrum peaks in the wavelength range of 410 nm to 440 nm.

The plastic wavelength shift fibers are made of polystyrene in its core, with a refractive index of $n = 1.59$. Violet light ($\sim$ 425 nm) emitted by the scintillator mix, is absorbed by the commonly chosen K27 fluorescent dye imprinted in the fiber. By total internal reflection, the blue-green ($450 - 650$ nm) light emitted by the dye is trapped within the fiber. Unfortunately most of the

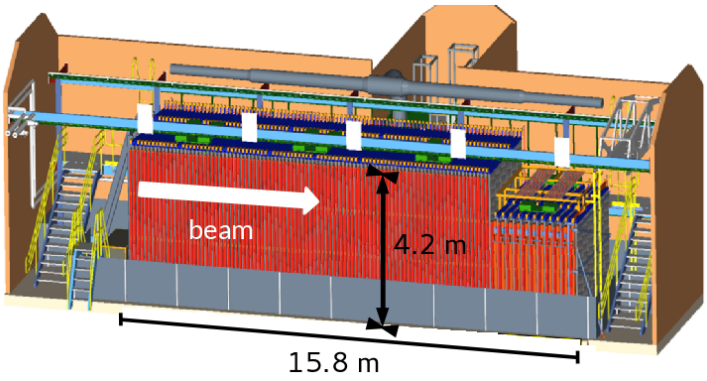

Figure 3.15: Near Detector schematics.

short wave part of the spectrum (< 520 nm) is attenuated as it travels through the entire WLS fiber. However, the longer wavelengths are only weakly attenuated. When this light signal is later registered by a APD designed with high quantum efficiency at long wavelengths, it results in a strong signal for minimal ionizing particles (MIPs) such as muons, as they travel anywhere in the cell.

After the light is collected and transmitted by the WLS fiber, the analog signal is then transmitted to the electronic readout, being the first step, the avalanche photodiode (APD), shown in Fig. 3.16. The APDs are silicon photodetectors packed in arrays of 32 pixels an mounted on a carrier board substrate using flip-chip mounting. Since both ends of a WLS fiber fit in single pixel, there is a one-to-one correspondence between a pixel and a PVC cell. After light is absorbed in the collection region, electron-hole pairs are generated and propagate towards the p-n junction due to the influence of an electric field. The electric field is so high at the junction, that avalanche multiplication occurs. One signature of silicon devices is the thermal generation of electron-hole pairs that mimic the signal. The APDs operate at a temperature of -15 °C to keep the noise contribution from the current of electrons generated at the photo-conversion region small.

One advantage that APDs have over other photodetectors is a high number of signal electrons created per incident photon, or quantum efficiency, which for NOvA is of 85% for a wavelength of

500-550 nm. Another advantage is that APDs have a uniform spectral quantum efficiency, as can be seen in Fig. 3.18.

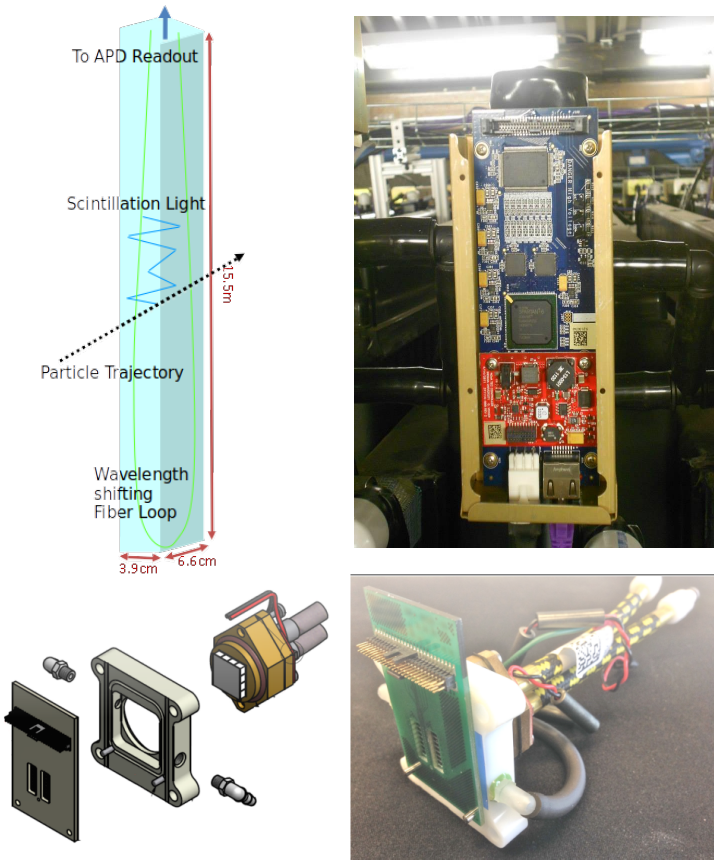

Figure 3.16: Top left: a NOvA liquid scintillator-filled PVC cell, which is the basic unit of detection. Bottom: APD module consisting of the pixel array, the carrier and the TEC. Top right: a picture of a FEB v5 installed at the sidewalk of the Near Detector. The NOvA readout electronics requires (at minimum) a 40 photoelectron signal in response to MIPs at the far end of a 15.4 meters cell, which is set by the average threshold of digital sampling oscilloscope (DSO) scans.

The APD crystal arrays are mounted on a carrier board, and the whole device is called an APD module. The APD module consists of a 32-channel APD array, a carrier printed circuit board on which the APD itself is mounted, a thermoelectric cooler (TEC), a heat sink for removal the heat from the TEC and an enclosure.

Given that each TE cooler will generate approximately 3 watts of heat per APD pixel, a water cooling system circulates water at a rate of 2 mL/s to remove this heat. In addition, dry air also

circulates through the APD modules in order to reduce any moisture that might originate in the neighborhood of the high voltage APD array, potentially causing electrical shorts.

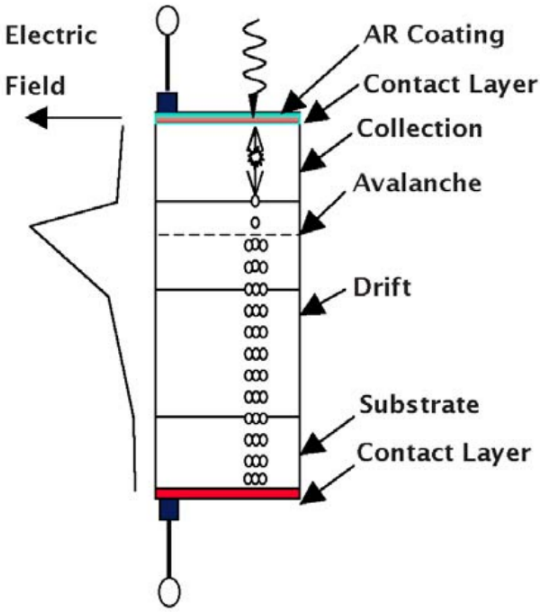

Figure 3.17: Basic diagram showing the physical process inside an avalanche photodiode (APD).

3.5 The Data Acquisition System and Data Triggers

The digitization and processing of the APD signal is dead-time free and continuous. The Front-end electronic board (FEB), is connected to the APD carrier by a ribbon cable, therefore, a one-to-one correspondence between APDs and FEBs exists. This electronics board is home to a customized application-specific integrated circuit (ASIC), an analog-to-digital converter (ADC), a carrier board connector for interfacing with the data acquisition system (DAQ), a thermoelectric cooler controller (TECC),a digital-to-analog converter (DAC), a field-programmable gate array (FPGA), and I/O functions among other general board monitoring functions. The main purpose of the FEB is to amplify and shape the discrete charge q from the signal of the APD given by

$$Q(t) = e^{-(t-t_0)/t_f} \cdot \left(1 - e^{-(t-t_0)/t_r}\right) \tag{3.13}$$

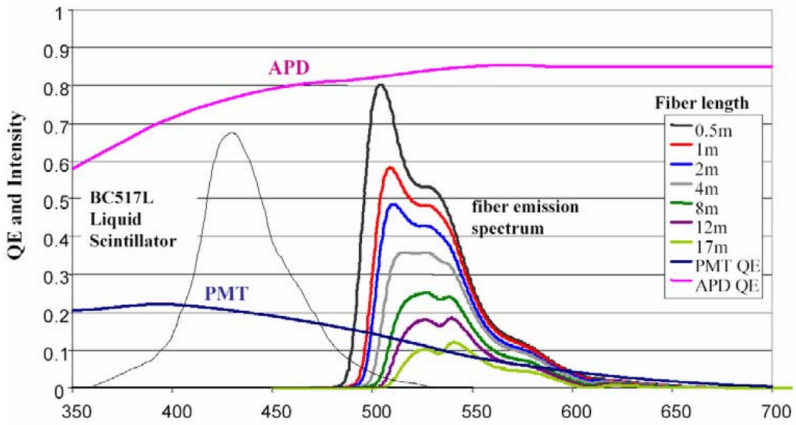

Figure 3.18: Wavelength shifting fiver emission spectrum and quantum efficiencies for avalanche photodiodes (APDs) and bi-alkali photodiodes (PMTs).

where t_f and t_r are the fall an raising times from the pulse respectively. Data from the ADC is sent to the FPGA where multiple correlated sampling is used to remove low frequency noise. This type of Digital Signal Processing (DSP) has the advantage of reducing the noise level and increases the time resolution.

The FPGA uses the DSP algorithm to extract time and amplitude signals from the APD. Any signal above the preprogrammed threshold will be time stamped and sent to the DAQ for further processing.

The waveforms from the detector cells are sampled at by the ADC at a frequency of 2 MHz (500 ns time resolution) to obtain multiple sample points along the baseline, rising edge and failing tail of the waveform. A dual correlated sampling algorithm is then used to establish a rising edge triggered threshold under which the sampling points are zero suppressed. This threshold is set independently for each channel of the detector.

A collection of 64 FEBs feeds a single data concentrator module (DCM), which aggregates and sorts data into windows corresponding to 50 μs, called microslices [173]. The DCM event builder constructs larger 5 ms long time units (millislices) which are optimized for Ethernet transmission.

The DCMs are synchronized through the use of a sophisticated timing system [123]. This system provides a stable master clock line as well SYNC and command lines, that allow the time stamp counters that are present in all the FEBs, DCMs and timing system, to be loaded and synchronized with an universal time based on GPS. Once the data streams are built by the DCMs, the 5 ms microslices of data from a specific time window are transmitted to a buffer farm in a round-robin pattern, as illustrated in Fig. 3.19.

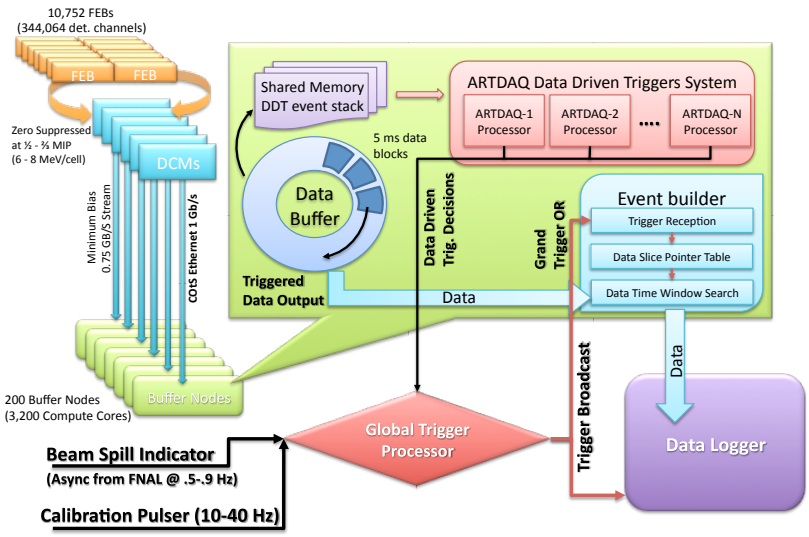

Figure 3.19: A summary of the data acquisition system for the Far Detector. The Near Detector has a similar one but in a smaller scale.

Neutrinos are sent into bunches within the NuMI spill, which extends 12 μs in time at a rate of 0.66 Hz. The NuMI beam spill trigger collects all the data within the 500 μs time window centered around the NuMI beam spill (see Fig. 3.20). There is also a $\pm 9\mu$s time relief margin centered around the beam spill, which gives a 30μs total time window ($208 - 238\mu$s) where the chance of seeing a neutrino in the NOvA detectors is high. This region is called "in-time" window and is blinded to analysis until the "box opening" (looking at our data) is done. Similarly, the time region outside the 30μs is called "out-of-time" window and is used for side-band cross check studies and to predict backgrounds for the in-time data.

Since the Far Detector is on the surface, we use the advantage of having an abundant flux of cosmic rays to generate another data set orthogonal to the neutrino sample using a periodic minimum-bias cosmic trigger. This cosmic trigger is similar in length size to the NuMI beam spill trigger and has a rate of 10 Hz. The data from the cosmic trigger is used for training and testing the boosting decision tree algorithm used for cosmic rejection of the sample for this thesis, and also to understand the performance of the Far Detector (e.g. calibration purposes). For the Near Detector, the all activity trigger collects data (mostly muons originated by the rock material outside the active volume) that also helps understand its performance.

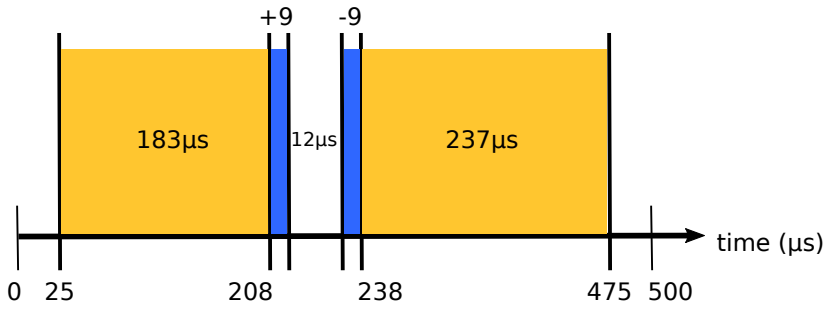

Figure 3.20: Neutrinos come in bunches within the NuMI spill, which spans 12 μs in time at a 0.66 Hz rate. The NuMI beam spill trigger collects the data from a 500 μs time window centered around the neutrino beam spill.

In the next chapter we will discuss the steps involved in the NOvA simulation of neutrino events, and how the NOvA detectors are calibrated using some of the features described in here.

CHAPTER 4. SIMULATION AND CALIBRATION

This chapter describes the steps involved in the simulation and calibration of the NOvA data. Monte Carlo (MC) simulation is key to understand the physics of particle interactions with the materials in the NOvA detectors. Simulating the production of neutrinos, their propagation and interaction allow us to optimize selection cuts, tune particle identification algorithms and compare reconstruction metrics with data. The calibration process serves as the connection between the hardware and the physics analysis worlds. These processes are discussed in detail in the following sections.

4.1 Simulation modeling

The simulation of the neutrino interactions and the backgrounds in the NOvA detectors is divided in three main stages (see Table 4.1). The first stage is the simulation of neutrino beam and flux through the NOvA detectors. This consists of simulating the hadron production within the target and the propagation through the horns and other beam components until the final meson decay. The second stage uses the previous information and simulates neutrino interactions in the detectors, taking into account initial and final-state interactions involving nuclear models. Finally, the third stage simulates the passage of final-state particles through the detectors, and the electronic response of the readout, including detector features like generation and propagation of scintillation light through the fiber, APD response and electronic noise.

Table 4.1: Stages of simulation for the NOvA experiment.

Step 1:	Beam simulation (G4NuMI/PPFX/FLUKA)
Step 2:	Neutrino interactions (GENIE)
Step 3:	Detector simulation (GEANT4)

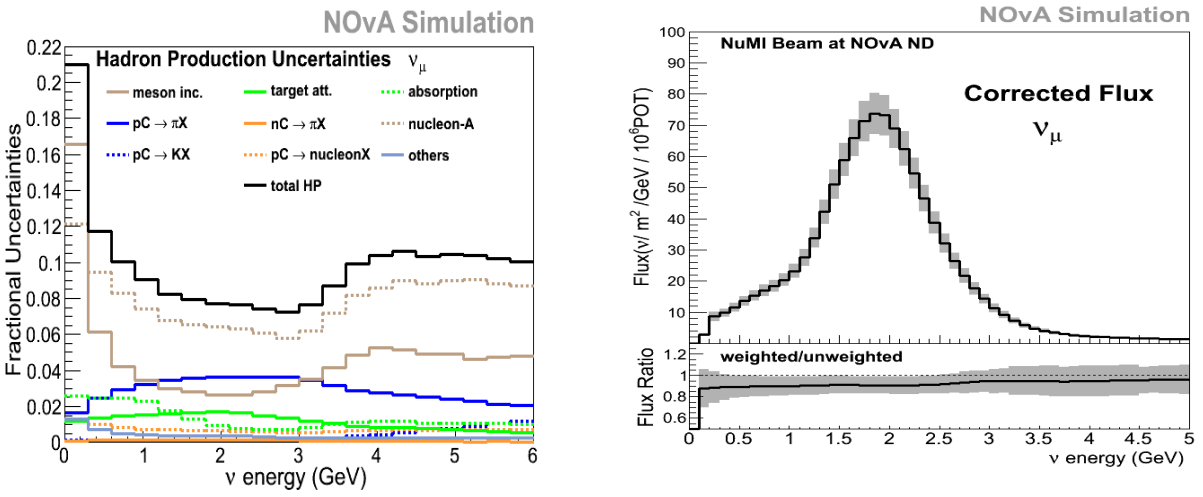

(a) (b)

Figure 4.1: (a) Hadron production fractional uncertainties. Solid black line represents the total, calculated in quadrature for each interaction type. At the oscillation peak (1-3 GeV) the fractional uncertainty is around 8%. The pion flux component uncertainty is around 4% in the oscillation peak, whereas the kaon flux component is $\sim 1\%$ at higher energies. PPFX assumes high uncertainties for low energy interactions. (b) ν_μ flux spectrum integrated over the ν_μ cross section fiducial volume in the Near Detector. Grey band corresponds to the total beam uncertainty (hadron production plus focusing) added in quadrature. The ratio between the simulation output and the total beam uncertainty is shown on the bottom.

4.1.1 Beam simulation

The beam neutrino flux produced by the NuMI beamline is based on the recently developed G4NuMI [72], which uses GEANT4 [12] with a detailed description of NuMI beamline materials and geometry. When the high energy proton beam interacts with the NuMI target, it generates a cascade of pions, kaons, protons and other particles (hadronic production for short). They might interact again within the target producing a reaction chain or travel further and get focused (defocused) by the magnetic horns depending on their charge. The simulation tracks every particle through the target, horn and decay pipe until they lose all their energy or decay into neutrinos. G4NuMI records parent and grandparents information along the way so that, for example, one knows if a neutrino came from a pion of kaon decay.

A correction to the G4NuMI hadron production is made using the customized Package to Predict the Flux or PPFX [18]. This package calculates the corrections and their uncertainties using measurements from dedicated hadron-nucleus collision experiments. PPFX corrects the FTFP_BERT hadronic model of GEANT4, which is the recommended reference physics list for high energy physics, and uses FLUKA [48, 75] to remove residual energy dependencies of data for NuMI. There are two types of output corrections (weights) produced by PPFX: one for the probability that an interaction happened (attenuation correction) and one for the production of the particle with the right yield, given an interaction (interaction correction). These corrections when applied to the simulation stage are of the order of 7-10% for both ν_e and ν_μ flux predictions, with uncertainties in the peak of about 8%. The pion flux component uncertainty is around 4% in the oscillation peak, whereas the kaon flux component is $\sim 1\%$ at higher energies (see Fig.4.1).

4.1.2 Neutrino and particle interactions simulation

The simulation of neutrino interactions in the NOvA detectors and the surrounding rock material was achieved by using GENIE [23]. This neutrino event generator uses the flux produced in the previous stage and models the primary interaction inside the nucleus, the production of all the final state particles in the nucleus (process known as hadronization), and the transport and rescattering of the final state particles through the nucleus (or intranuclear transport).

This analysis uses GENIE v2.12.2 with some modifications in physics modeling. These modifications include an updated multi-nucleon ejection weight (or 2p2h, two-particle, two-hole) via meson exchange currents (MEC), and a nuclear charge screening correction, technically described as the Random Phase Approximation (RPA). From the theoretical point of view, modeling the interaction scattering from correlated nucleon-nucleon pairs, where both nucleons are ejected from the nucleus, is called two-particle, two-hole (2p2h). The most heavily researched subset of these reactions arise from the exchange of mesons (mostly pions) between the nucleons to bind them into pairs. The models describing this are referred as MEC models. This analysis uses an empirical MEC model,

which assumes a Gaussian shape in W, the reconstructed invariant mass given by the expression

$$W = \sqrt{M_p^2 + 2M_p(E_\nu - E_\mu) - Q^2},$$

with the four momentum transfer Q^2 as

$$Q^2 = -q^\mu q_\mu = 2E_\nu(E_\mu - p_\mu \cos\theta_\mu) - m_\mu^2,$$

where E_ν is the energy of the neutrino, E_μ the muon energy, θ_μ the angle between the incoming neutrino and the outgoing muon, and E_{had} the calorimetric hadronic energy. We can rewrite in terms of the magnitude of the three-momentum transferred to the nucleus from the neutrino as

$$|\vec{q}| = \sqrt{Q^2 + q_0^2},$$

with

$$q_0 = E_{\text{had}}.$$

In our model, W is distributed between the quasielastic and Δ-resonance peaks. This empirical MEC model derives its normalization based on the difference between MiniBooNE's data for QE scattering and free electron scattering [163]. The global Fermi gas model was used as the nuclear model, which assumes all nucleons exist in a simple, non interacting gas. Overall, this correction results in a 20% increase in the yield of events from GENIE's empirical MEC model (see Fig. 4.2).

Evidence from the MINERvA experiment [141] suggests the need for a correction to the quasielastic scattering prediction to account for a weak charge screening effect that modifies the response of the nucleus to a weak probe (e.g. a neutrino), particularly at low Q^2 values. This correction is based on the long-range nuclear correlation effects computed with the RPA method. Our implementation of this correction is based on the work of the IFIC Valencia group and Rick Gran [86] mainly by correcting the energy and momentum transfer variables. Some features of this correction include a reduction of the cross section at lower values of Q^2 and a broad enhancement of the charged-current quasielastic cross section across most values of Q^2.

The region of interest in which the work on this thesis was focused corresponds to neutrino interactions with reconstructed neutrino energy $E_\nu^{\text{reco}} > 5$ GeV. This implies a transition region

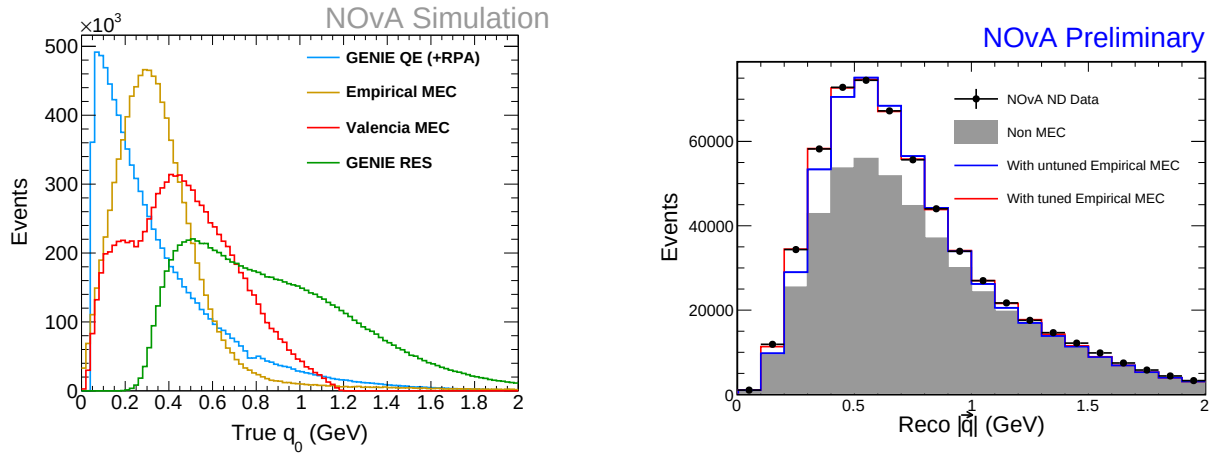

(a) (b)

Figure 4.2: (a) Distributions in true energy transfer q_0 for various models in GENIE. (b) Before and after comparison of the muon neutrino energy spectrum illustrating the effect of tuning Meson Exchange Current component in bins of true momentum transfer $|\vec{q}|$, which after being fit, matches the ND data.

where baryon resonant production (RES) and non-resonant inelastic scattering (DIS) events take a natural place. But also where development in neutrino interaction modeling is taking place. GENIE considers the neutrino-nucleon charged current cross section as the direct sum of individual contributions

$$\begin{aligned}\sigma^{tot} &= \sigma^{QE} \oplus \sigma^{1\pi} \oplus \sigma^{2\pi} \oplus \cdots \sigma^{n\pi} \oplus \sigma^{1K} \oplus \cdots \oplus \sigma^{DIS} \\ &\approx \sigma^{QE} \oplus \sigma^{RES} \oplus \sigma^{DIS}.\end{aligned} \tag{4.1}$$

Thus, the total inelastic differential cross section is modeled as

$$\frac{d^2\sigma^{inel}}{dQ^2dW} = \frac{d^2\sigma^{RES}}{dQ^2dW} + \frac{d^2\sigma^{DIS}}{dQ^2dW}, \tag{4.2}$$

where the first term represents the contribution from all low multiplicity inelastic reactions via resonance production, as prescribed by the Rein-Sehgal model [140] and the Feynman-Kislinger-Ravndal (FKR) relativistic quark model of baryonic resonances [76]. The second term represents the DIS contribution as predicted by the Bodek-Yang model [46] and tuned in the resonance dominance

region with $W < W_{cut}$ (W_{cut} being a configurable parameter in GENIE), making the RES and DIS components agree with experimental data [24].

The final stage of the simulation takes in all the particles generated by GENIE and propagates them through the detector geometry model. The interactions and decays of final state particles in addition with their trajectories and energy loss within the boundaries of the detector are simulated by GEANT4, producing a list of Fiber-in-Liquid-Scintillator-Hits (FLSHits) as output and representing the true energy deposited by the particle in the active (scintillator) volume of the detector.

4.1.3 Detector response simulation

The last stage in our simulation deals with modeling the scintillation light production, transport and conversion to electrical signals.

High energy particles interacting with organic scintillator materials have a non-linear response of the energy loss per unit length, dL/dx, due to recombination and quenching effects. This is described by Birk's law, which is a first order correction given by [44]

$$\frac{dL}{dx} = \frac{L_0 \frac{dE}{dx}}{1 + k_B \frac{dE}{dx}} \tag{4.3}$$

where k_B is the measured Birk's constant. Birk's law can include a second order correction term, and this is known as Birks-Chou law [52]

$$\frac{dL}{dx} = \frac{L_0 \frac{dE}{dx}}{1 + k_B \frac{dE}{dx} + k_C \left(\frac{dE}{dx}\right)^2} \tag{4.4}$$

with k_C being the Chou constant. Both k_B and k_C constants were obtained by first selecting Near Detector events with exactly two reconstructed tracks (muon and proton) and comparing data versus Monte Carlo simulation distributions of dE/dx as a function of the number of planes from the end of the track [133]. But even after the tuning, data/simulation differences persisted for protons and muons, requiring a much larger Birks constant that reported by scintillator experiments (e.g. Kamland and Borexino [31]). It was also necessary to use a negative Chou term, which combined caused the quenching factor to reach large nonphysical values at $\beta\gamma \approx 0.1$

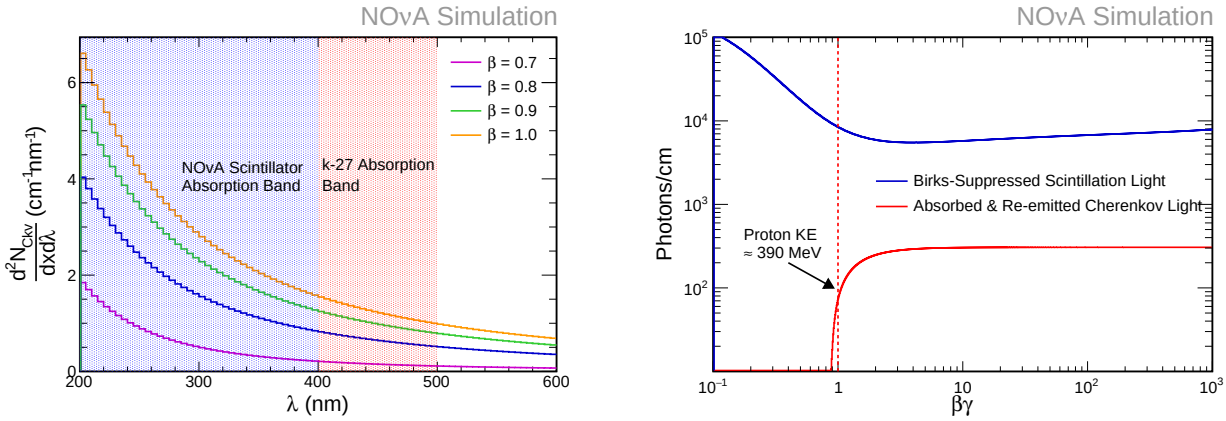

(a) (b)

Figure 4.3: (a) The Cherenkov light emitted for particles of various β as a function of wavelength. Very few photons are emitted in the k-27 dye absorption band of the NOvA wavelength shifting fibers. Instead, photons emitted at short wavelengths are absorbed by the scintillator and re-emitted in the absorption band. (b) The number of scintillation photons/cm (after Birks suppression) and the number of Cherenkov photons/cm absorbed and re-emitted in the k-27 dye absorption band as a function of $\beta\gamma$.

Including Cherenkov light modeling in the NOvA scintillation process improved substantially the simulation of the hadronic system and helped to remove the nonphysical Birks-Chou constants. The number of Cherenkov photons produced per distance traveled at a given wavelength is given by the Frank-Tamm formula [95]

$$\frac{d^2N_\gamma}{dxd\lambda} = \frac{2\pi\alpha z^2}{\lambda^2}\left(1 - \frac{1}{\beta^2 n_\lambda^2}\right) \tag{4.5}$$

where n_λ is the refractive index, $\beta = v/c$ is the particle velocity, N_γ is the number of photons, z is the electric charge and α is the fine structure constant.

We can see from Fig. 4.3(a) that very few Cherenkov photons are produced in the 400-500 nm region where the k-27 dye in the NOvA wavelength shifting fibers can absorb. In contrast, a large amount of these photons are produced in shorter wavelengths. Hence, integration over wavelengths that can be absorbed/reemitted at wavelengths that can be captured by the WLS fiber must be performed. The caveat here is that most of the 200-400 nm wavelengths are absorbed instantly.

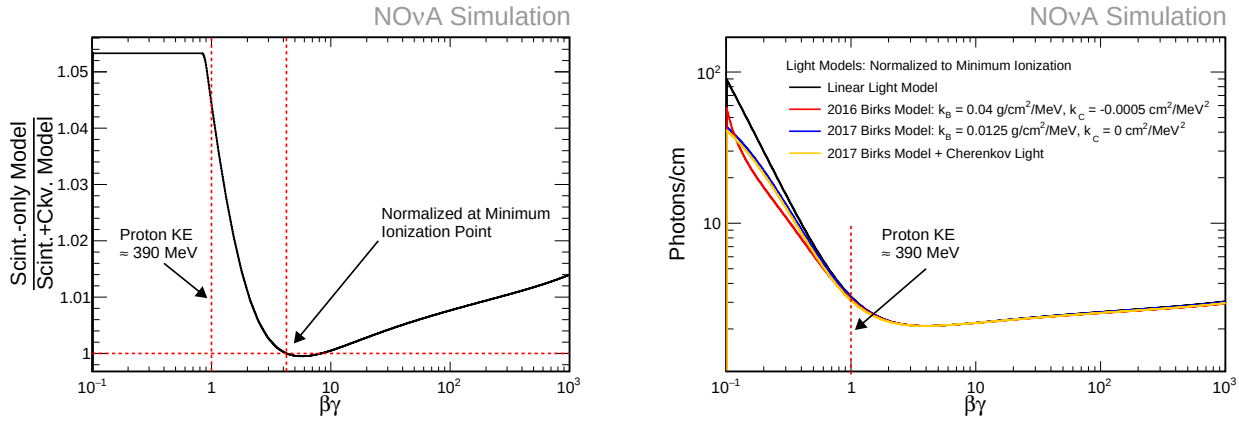

(a) (b)

Figure 4.4: (a) Comparisons between scintillation only and scintillation + Cherenkov light models. Since the calibration procedure fixes the scale at the minimum ionization point regardless of the light model, the ratio is fixed to 1 at that point. Assuming a scintillation only light model produces an 5% energy bias for low $\beta\gamma$ particles. (b) Comparisons of the 2017 scintillation + Cherenkov light with the linear light model, the 2016 light model using Birks-Chou suppressed scintillation, and the 2017 light model using scintillation only.

The number of Cherenkov photons emitted per centimeter is shown in Fig. 4.3(b). Since Cherenkov light depends on the velocity, only high energy protons emit Cherenkov light.

The impact of the inclusion of this Cherenkov light in our simulation is shown in Fig. 4.4(a). The figure shows the ratio between the number of photons produced by the 2017 model neglecting the addition of Cherenkov light (scintillation only model) and the full 2017 model (scintillation plus Cherenkov). If no Cherenkov light is modeled in the simulation, that leads to an over-estimate of the energy deposited by slow protons and pions. A comparison of the number of photons per centimeter from a variety of light models is shown in Fig. 4.4(b). After implementing Cherenkov light in the simulation we obtain $k_B = 0.01$ g/cm^2/MeV and $k_C = 0.0$ cm^2/MeV^2 [33] consistent with the results from KamLAND and Borexino.

Some WLS fibers attenuate light more than others. This 20-30% variation in the average light output has a significant effect on signals that are close to the threshold. This fiber brightness variation found only in the Far Detector is added to the NOvA simulation.

Since it is located on the surface, energy depositions from cosmic rays are a significant background that must be well understood. Therefore, the Far Detector Monte Carlo contains cosmic ray data combined with the simulated beam neutrinos [67]. This procedure accounts for the loss of efficiency due to neutrinos events overlapping in space and time (pile-up) with cosmic ray muons. It also helps to better understand the detector noise and requires no modeling of neutrons and Michel electrons produced by cosmic rays.

A run-by-run beam intensity is included in the simulation in order to model the significant power increase of the NuMI since NOvA started taking data. We would expect multiple neutrino interactions per beam spill[1] in the Near Detector as well in the rock material surrounding it. Pile-up can reduce the expected number of neutrino interactions per protons-on-target (POT) and shift the reconstructed energy spectrum to higher values. The average POT/spill included in the simulation comes from the calculated total POT/run and number of spills stored in the NOvA runs database.

All pixels in the NOvA detectors share a common voltage source. When a large deposit of energy occurs in one pixel, the baseline current of the others momentarily "sag". This sag effect is included in the simulation if the total amount of light captured by all pixels of an APD is greater than 5000 ADC counts in any 15 ns window.

4.2 Calibration

The calibration of the NOvA detectors can be divided in two main parts: energy and timing calibration. The purpose of the energy calibration is to relate the recorded digitized amplitude of the light in any cell to an energy deposition in physical units. The purpose of the timing calibration is to correct for any time offsets between the data concentrator modules (DCMs) so that energy depositions in different cells from the same particle are property correlated in time.

Cosmic ray muon data is used for the energy calibration. For clarification purposes, a brief description of the energy calibration units used in subsequent sections is as follows:

[1] Also refers to the 500μs of detector readout around the neutrino beam.

- ADC: the peak of the dual correlated sampling value from raw data
- PE: a simple uncalibrated scaling of the ADC value to approximate the number of photoelectrons
- PECorr: the number of photoelectrons after threshold, shielding, fiber brightness and attenuation corrections
- GeV: estimated energy deposited in the active material (scintillator)

In terms of offline coordinates, the z-axis is along the detector in the beam direction, x-axis horizontally and y-axis vertically. The coordinate W represents the distance along the cell length, therefore $W = 0$ is at the center of the detector and more positive values of W are closer to the readout.

4.2.1 Attenuation calibration

The first step of the energy calibration is to correct for the attenuation of light in the WLS fiber, which is performed on a cell-by-cell basis. We start by converting the ADC pulse height to uncorrected PE by multiplying a 0.5 scale factor, which is an approximation to the effect of the FEB electronics. Then we select hits from cosmic ray tracks and then make distributions of uncorrected photoelectrons by path length through the cell, PE/cm, as a function of the distance along the cell, W. The distance along the cell (W) is calculated for each track by taking the position of the straight line defined by the two neighbouring trajectory points at the z-coordinate of the cell. Since we require a reliable estimate of the path length, not all the hits from the muon track are suitable. If a cell has its neighbors in the same plane, then we can assure that, for an Y-view cell, the track entered through the upper wall and exited through the lower one, striking the neighbor cells as show in Fig. 4.5. The path length is just the width of the cell divided by the direction cosine C_y. This selection is known as tricell hit selection, since it requires hit neighbors in the x or y-axis and has the property of reducing the chance of noise hits.

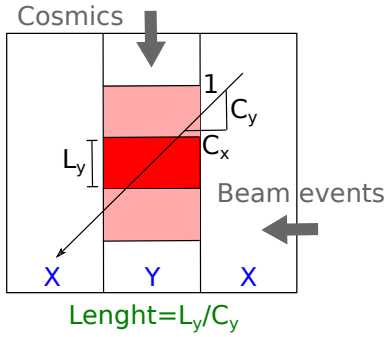

Figure 4.5: The tricell hit criteria requires a selected hit to be surrounded by two hits on both adjacent same-plane cells, ensuring a well reconstructed hit path length.

Tricell hits are used to calibrate both real and simulated data in the Near and Far Detectors. Once we have the selected sample of hits, we determine the average PE/cm vs W for each cell and view. At this point we are now ready for the next stage in the calibration.

4.2.1.1 Threshold and shadow corrections

It was noted that the Far Detector data and MC simulation had discrepancies between the calibrated and true energies as function of W [34]. Two effects were considered mayor players for this: threshold and shadowing or self-shielding. The number of photoelectrons (PE) generated in an APD follows a Poisson distribution. As an ADC threshold cut is applied (usually 43 ADC for Far Detector), it truncates the lower part of the Poisson distribution and it shifts the mean of the PE distribution to higher values. On the other hand, as a charged particle deposits energy during its propagation in the detector, the momentum changes and therefore the spectrum of dE/dx energy deposition (PE/cm) changes. These two effects add a bias to the hits used for the attenuation calibration, which implies an overestimate of the light-level and an under-estimate of the real hit energies. The way to correct these effects has recently two approaches: a simulation-driven approach [153], currently used as part of the official NOvA calibration process, and data-driven [166], currently in development.

The simulation-driven approach computes a combined correction factor that is a function of view, cell, W and fiber brightness (for Far Detector only). This correction is given by

$$Corr = Corr_{\text{Thresh}} \times Corr_{\text{Shadow}} = \frac{PE}{\lambda} \cdot \frac{E_{\text{True}}}{E_{\text{MIP}}}, \tag{4.6}$$

where $Corr$ is the combined threshold-shadow correction factor, PE is the simulated number of photoelectrons at the readout, λ is the number of expected photons in the readout in the absence of fluctuations, E_{True} is the true energy deposited in the cell and E_{MIP} is the reconstructed expected energy based on the path through the cell. A separate threshold and shadow correction is calculated for each sample of fiber brightness according to a fiber brightness map [49]. This correction is applied to the PE/cm distribution of each cell just before attenuation fits.

The data-driven correction approach was initially developed in late 2014 [167, 168, 166]. The idea was to follow the same definition of the simulated driven corrections and replace the true variables with reconstructed ones.

We started by selecting a sample of hits coming from cosmic muons. We then loop over the hits in the muon track and select all the hits that are within a range of 100-300 cm from the detector end point. This defines our core sample of hits. This range was subject to study and tuning. Original work [166] used the 100-200 cm region instead based on the flat profile of the distance to track end versus PECorr/cm distributions. Increasing the region from 200 to 300 cm was motivated again by increasing the sample size of hits selected.

We then divide the sample of hits coming from stopping muons within a window from the end in four categories, in principle overlapping as follows. The first category is from the sample of hits that come from stopping muon tracks, which we labeled as minimal ionizing particle (MIP) hits. Second, the sample of hits that do not follow this criteria are labeled as Non-MIP. The fiducial boundary was subject to study. While the original of 50 cm from the detector edge was used at the beginning, other fiducial definitions were studied through the development stage, in particular, in terms of projected cells and planes to the edge of the detector, in order to increase the size of the selected muon sample. Now, if the path length within the cell exceeds the width of the cell for each

view (e.g. 6 cm for X-view and 4.5 cm for Y-view) then that hit is labeled as "long" and defines the third category. The fourth category corresponds to the hits with no restriction of path length.

With these criteria in mind, for each cell and for each view we create PE/cm vs W distributions and compute each data driven shadow ($Corr_{DDShadow}$) and threshold ($Corr_{DDThresh}$) corrections as the ratio

$$Corr_{\mathrm{DDShadow}} = \frac{\mathrm{Mean}[(PE/cm)_{\mathrm{(MIP+NonMIP)\&Long}}]}{\mathrm{Mean}[(PE/cm)_{\mathrm{MIP\&Long}}]} \tag{4.7}$$

$$Corr_{\mathrm{DDThreshold}} = \frac{\mathrm{Mean}[(PE/cm)_{\mathrm{MIP\&AllLength}}]}{\mathrm{Mean}[(PE/cm)_{\mathrm{MIP\&Long}}]} \tag{4.8}$$

where the common denominator requires the sample of hits be part of a stopping muon (MIP), thus avoiding the impact of shadow effect by construction, and have a long path length (Long), which assumes same path length shape when no threshold cut is applied. The shadow correction numerator requires hits also having long path length, independently of coming from a stopper, and the numerator of the threshold requires hits stopping muons independently of their path length.

A combined correction is simply given by the product

$$Corr_{\mathrm{DD}} = Corr_{\mathrm{DDThresh}} \times Corr_{\mathrm{DDShadow}} \tag{4.9}$$

in analogy to the simulation driven approach. The final correction to the number of photoelectrons is implemented as $PECorr = PE/Corr_{DD}$.

A comparison of the simulated and data-driven approaches is shown in Fig. 4.6. For each view, a combined correction is shown against the distance along the cell (W) for all cells in the detector. The red points represent the simulation-driven correction given by Eq. 4.6 and currently used in the calibration procedure. The blue points represent the data driven approach using Eq. 4.9 and the standard tricell hits, in analogy to the simulation driven. The green points also represent the data driven approach using Eq. 4.9 but using a different instance of reconstruction hits more related to the track itself, called trajectory points. The trajectory point study was used in order to investigate potential biases of the tricell selection itself. As we can see, agreement in the central region of the

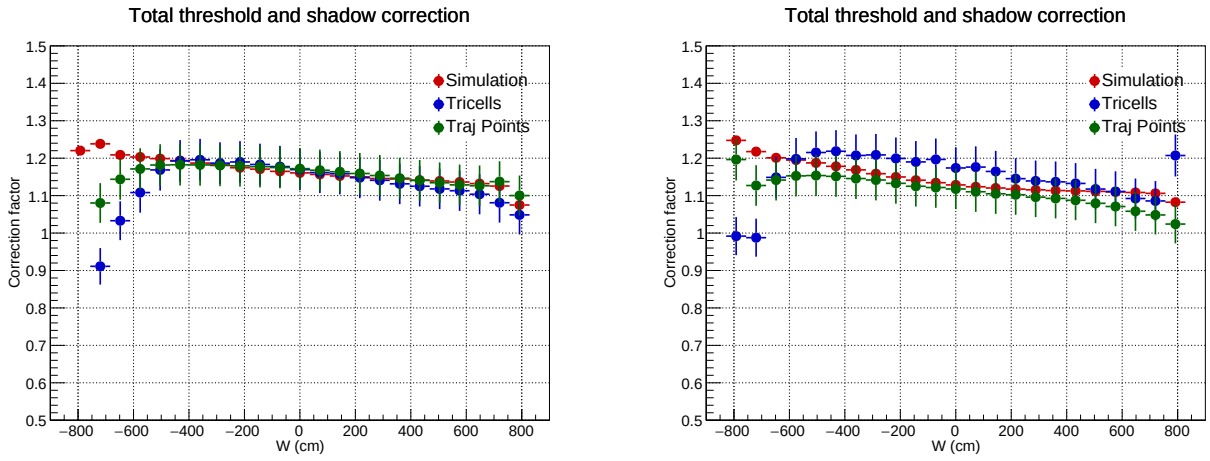

(a) (b)

Figure 4.6: Combined data driven shadow and threshold corrections using tricells (blue), trajectory points (green) compared with simulation driven (red) for all X-view cells (a) and Y-view cells (b). Images from [147].

detector for the X-view cells is within error bars for both data driven approaches except at the edges, due to the low efficiency in the number of hits selected. In contrast, there is a slight over estimation of the correction for central values in the Y-view for the tricell data driven approach, whereas for the trajectory points it seems to under compensate.

Once the simulation-driven threshold and shadow corrections are applied, the next step is to determine the attenuation calibration constants, which will be discussed in the following part.

4.2.1.2 Attenuation fits

The attenuation fit for the profile of each cell is mathematically defined using the following expression

$$y = C + A\left(exp\left(\frac{W}{X}\right) + exp\left(-\frac{L+W}{X}\right)\right) \tag{4.10}$$

where y is the sum of the response at the two fiber ends, W the distance along the cell, L is the cell length and C, A and X are free parameters in the fit, with the latter giving the attenuation length as well. This function describes the response in the center of the cell for both NOvA detectors.

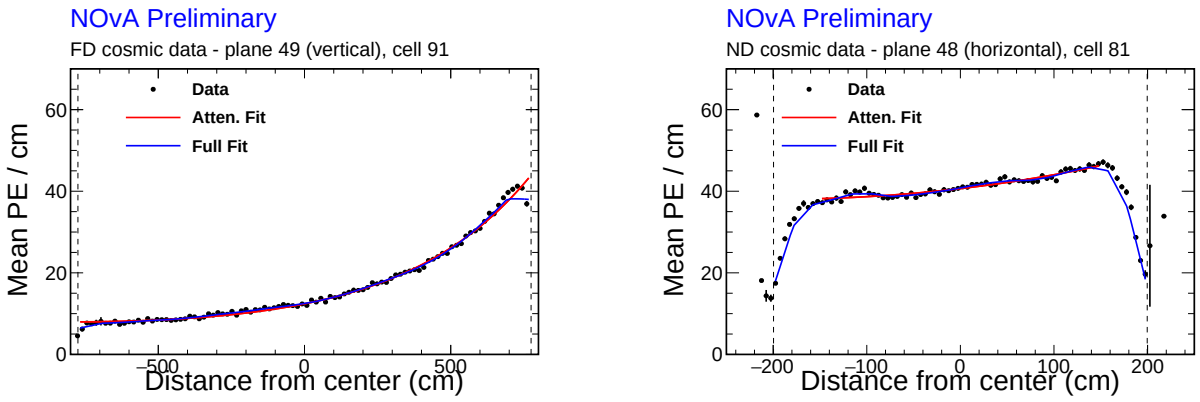

(a) (b)

Figure 4.7: Examples of attenuation fits before (red) and after (blue) LOWESS corrections for a Far Detector vertical X-view cell (a) and for a Near Detector horizontal Y-view cell (b).

An interesting effect found in data shows pronounced "roll-offs" of the attenuation fit at the end of the cells which are absent or less pronounced in simulation. This feature can be explained by the behaviour of reflected light given the geometric constraints of the edges and the uncertainty of the varying fiber position within the cell. For this analysis we use the non-parametric regression LOWESS[2] fit method in order to capture this behaviour. The LOWESS curve at each point is formed from the weighted mean of deviations, given by the weighted function

$$w_i = \begin{cases} \left(1 - \left|\frac{W - W_i}{3}\right|^3\right)^3 & \text{for } |W - W_i| < \sigma \\ 0 & \text{for } |W - W_i| \geq \sigma \end{cases} \tag{4.11}$$

where W_i is the i^{th} neighbor point around W in the range given by σ on the LOWESS curve, w_i is the local weight on W_i and W is the distance from the readout. A typical value for the length scale σ is 30 cm. There might be instances of cells that deviate from the norm even though have a successful LOWESS fit. To prevent this cases, the mean fractional deviation of the data from the fit in quadrature is monitored and serves as metric that asses the quality of the fit. If this metric exceeds the 0.2 value, the cell is marked as uncalibrated, representing an average 0.9% and 1.7%

[2]Locally Weighted Scatterplot Smoothing

from the total for the Far and Near Detectors respectively [152]. The result of the fit in Eq. 4.10 in addition with the LOWESS correction is shown for two cells in Fig. 4.7.

4.2.2 Drift calibration

The drift calibration applies corrections for changes in the detector response over time. These changes could be from the degradation in the composition of the liquid scintillator, aging of the detector components or in the electronics response. The energy deposited by cosmic rays passing through the detector are used to track the detector response over time. The drift calibration is computed at the front-end board (FEB) level [42, 157]. The procedure starts by selecting the hits from cosmic muons in a similar fashion to the ones selected by the attenuation correction. The information is stored in 2D histograms containing information about the FEB and their corrected photoelectron (PECorr) hits combined across all the subruns in a run. The mean PECorr RMS and their errors are determined for each FEB in each run. The drift correction factor is computed as

$$Corr_{\text{Drift}} = \frac{\text{Average PECorr value for a week of combined data (fit to constant)}}{\text{Average PECorr value for all combined data (fit to constant)}} \tag{4.12}$$

where the numerator is the average $PECorr$ over approximately one week of data, or 51 runs, and the denominator is the average $PECorr$ in all the runs in the subset of data. The drift scale factor is given by $1/Corr_{\text{Drift}}$ [42]. A before and after comparison including drift calibration in a subsample of data is shown in Fig. 4.8.

The drift calibration is shown to be a very small component. This correction has been developed and validated and it is expected to be applied to the calibration chain for future analysis.

4.2.3 Absolute energy calibration

The final step in the energy calibration chain comes from determining absolute energy scales that allow to convert PECorr measurements into GeV in data and simulation for both detectors. This is

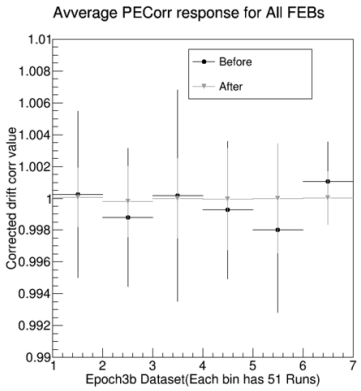

Figure 4.8: Before and after comparison of the drift correction applied to a sample of Far Detector data. The corrected drift correction value shows a $\sim 0.4\%$ variation for the period shown. Image from [42].

done by using stopping muons and the Bethe-Bloch formula. The Bethe-Bloch formula describes the rate of energy loss of muons passing through matter in the range $0.1 < \beta\gamma < 1000$ as follows [129]

$$\left\langle -\frac{dE}{dx} \right\rangle = Kz^2 \frac{Z}{A} \frac{1}{\beta^2} \left[\frac{1}{2} \ln \frac{2m_e c^2 \beta^2 \gamma^2 W_{\max}}{I^2} - \beta^2 - \frac{\delta(\gamma\beta)}{2} \right] \tag{4.13}$$

where $K = 4\pi N_A r_e^2 m_e c^2$ includes Avogadro's number N_A, the classical electron radius r_e, and the rest mass of the electron $m_e c^2$, $W_{\max}$ is the maximum energy transfer in a single collision, Z/A is the ratio of the atomic number to the mass number, I is the mean excitation energy, $\delta(\gamma\beta)$ is the density effect correction to ionization energy loss, z is the incident charge, and β and γ the relativistic velocity and gamma factors of the incident particle. From Eq. 4.13 we can see that the energy loss rate depends on the material as well as the incident particle's mass and momentum. Therefore, we can use the Bethe-Bloch equation to calculate dE/dx if we have muons that stop inside the detector, since we have access to the energy at any point. In NOvA, the energy that a muon deposits within each cell is estimated using GEANT4 and stored in Fiber-in-Liquid-Scintillator-Hits (FLSHits), which represent that deposition in the active material (scintillator) only. The minimum dE/dx for a muon passing through mineral oil (polyethylene) in the NOvA

detectors is [87]

$$\left(\frac{dE}{dx}\right)_{MIP} = 2.079 \text{ MeV cm}^2/\text{g}.$$

The linear stopping power, in MeV/cm is given by $\langle -\frac{dE}{dx} \rangle \cdot \rho$, where ρ is the density in g/cm^3, which for the liquid scintillator in NOvA is (0.8617 ± 0.0017)g/cm^3 at 15.6 °C [117], which translates in a value of

$$\left(\frac{dE}{dx}\right)_{MIP} = 2.079 \times 0.8617 = (1.7915 \pm 0.0035) \text{ MeV/cm}. \tag{4.14}$$

This calculation gives an estimate of the minimum dE/dx deposited in liquid scintillator by muons stopping in the NOvA detectors. The calorimetric energy scale calibration will be described below.

We started by selecting contained stopping muons by either looking at the tracks whose reconstructed end point is contained within the detector or by looking at the tracks that have a Michel electron associated at one end. A Michel electron is an electron produced when the muon decays. We then select all the hits in those tracks that are tricell hits and are between 100 and 200 cm from the end of the track. Two new additional cuts, one for each detector, have been implemented in the lates analysis. The first one (Near Detector) selects hits in the range $-100 < W < 100$ cm along the position in the cell in order to remove edge effects from relative calibration (differences between detectors). The second one (Far Detector) selects hits in the range $200 < W < 600$ cm along the position in the cell in order to remove edge effects and threshold bias. The selected hits produce distributions of Muon Energy Units (MEUs) for each detector and for data and MC simulation. The MEU is defined as the mean detector response in units of PECorr of a stopping muon tricell within the track divided by the length of the track inside the cell. A calorimetric energy scale factor that converts PECorr to GeV is found from the ratio [161, 112]

$$\text{calorimetric energy scale} = \frac{\text{MEU}_{\text{Truth}}}{\text{MEU}_{\text{Reco}}} \tag{4.15}$$

where $\text{MEU}_{\text{Truth}}$ is the mean of the simulated MeV/cm distribution, whereas MEU_{Reco} is the mean of the $PECorr/cm$ in both data and simulation. Each view is calibrated separately to avoid biasing. The resulting differences in the averaged scale factors per view were around $\sim 1\%$ for Far Detector data [20]. Figure 4.9 shows some results after applying the absolute energy calibration correction.

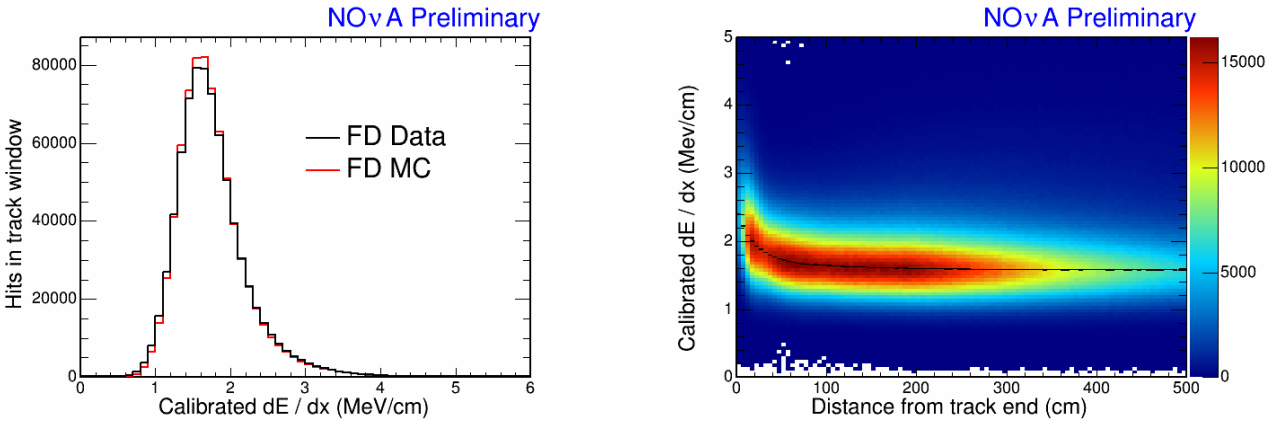

(a) (b)

Figure 4.9: (a) Calibrated dE/dx distribution versus tricell hits on a stopping muon track for Far Detector data (black) and Monte Carlo simulation (red). (b) Distance to the end muon track point versus calibrated dE/dx. The black solid line represents the mean of a fit to the peak of the calibrated dE/dx for a given distance from the track end point.

The substantial results in Fig. 4.10 show the comparisons before and after the calibration is applied to both detectors.

After the complete calibration the residual disagreement between data and MC simulation in the muon response using beam muons is 3.1%. For protons, there is a 5% dE/dx difference between Near Detector data and MC simulation that is interpreted as the absolute calibration uncertainty [84].

4.2.4 Timing calibration

The recorded hits in each detector must be synchronized in order to temporally identify interactions within them and correlate them with the neutrino beam. The beam is pulsed and delivers a 10 μs spill of neutrinos every 1.33 seconds. It is not possible to know the arrival time of a spill because its frequency changes depending on accelerator operating conditions and the number of experiments running on campus. Due to the overwhelming 140 kHz cosmic muon background at the Far Detector compared to the few contained neutrinos expected per week, activity based triggers are not an option for selecting signal events. This motivates a software driven trigger, with 100%

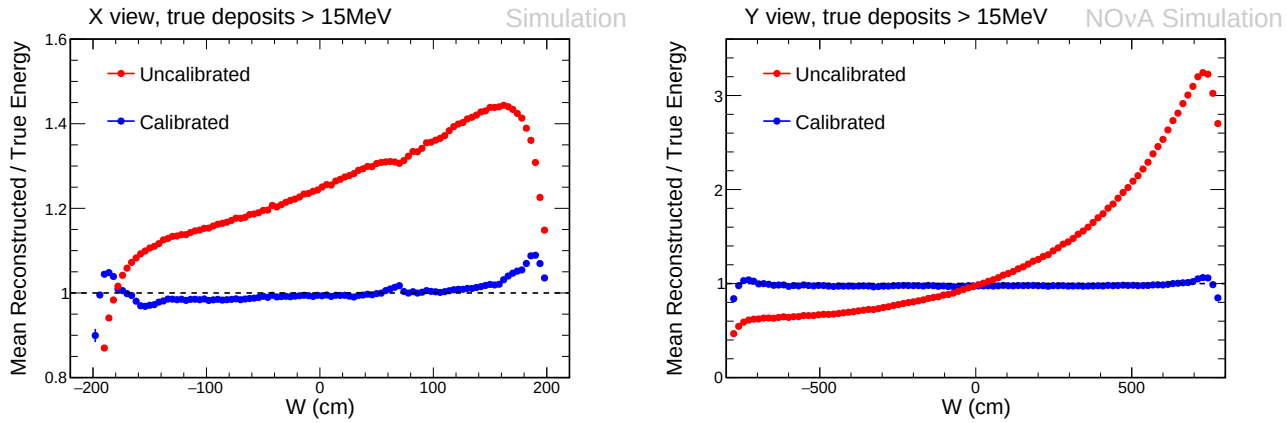

(a) (b)

Figure 4.10: Profiles of the reconstructed and true energy ratios as a function of W for the Near Detector X-view cells (a) and for the Far Detector Y-view cells (b) comparing before and after calibration is applied.

of the data stored in a buffer for up to minutes before a decision is made to readout data. When a neutrino spill is generated at Fermilab, it gets time stamped by the NOvA clock and a message is sent to both detectors to readout data from from the corresponding time window in the buffer. This requires both detectors synchronized to an absolute wall clock that also records spill triggers. The NuMI beam spill trigger initiates a readout of 500 μs of data centered at the beam spill. The extra readout window allows for side-band analysis of backgrounds. For the Near Detector it is required that all readout channels be in sync with the global clock within 10 ns in order to reduce event pile-up.

Figure 4.11 shows the schematics of the timing system used in NOvA. A Master Timing Distribution Unit (MTDU) interfaces with a GPS receiver and sends signals to the slave units, one per diblock. Each slave unit transmits commands to DCMs and they transmit back with a loop-back connector for calibration purposes and to the 64 FEBs (Far Detector) where the sync return line is exchanged for the data link[120].

The timing calibration was determined using data in both NOvA detectors. Neutrino interactions are separated in space and time by an algorithm that creates groups of hits, known as slices. A

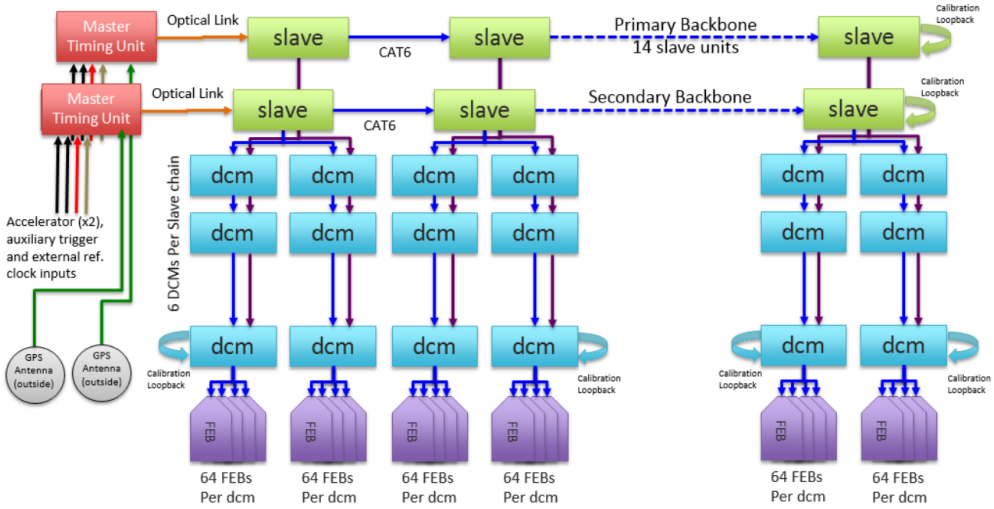

Figure 4.11: Schematics of the timing system used for the NOvA Far Detector (for Near Detector similar layout at lower scale). Image from [125].

series of customized quality cuts is used to select cosmic ray muons or muons induced from neutrinos interacting with the rock outside the Near Detector. After the hits from these tracks are selected, the hit times get corrected for the time-of-flight along the muon path and for the distance of hit to APD readout. Later, the time difference between all pairs of hits within a DCM on the track is calculated. A two dimensional histogram is filled with this information versus the number of uncorrected photoelectrons (PE). The resolution was fit to a function given by

$$\sigma_t = \frac{p_0}{p_1 + n_{pe}^{p2}} + p_3 \tag{4.16}$$

where n_{pe} is the number of photoelectrons, σ_t is the timing resolution, and $p_0, \ldots, p_3$ are fit parameters. The actual timing resolutions is 5 ns for the Near Detector and 10 ns for the Far Detector.

An absolute timing offset calibration between DCMs is also performed. First, the time t_i' of each selected hit in DCM is taken after fitting readout samples from the ADC pulse-shape curve. This time has time-of-flight correction but it does not include corrections for fiber speed variations or the time to takes to the scintillator light to be absorbed. It is intended that t_i' represents simultaneous readout time of each hit on a track within one DCM. Second, a weighted average of the time of each DCM on a track is computed. Third, the relative timing offsets between pairs of DCMs on a track

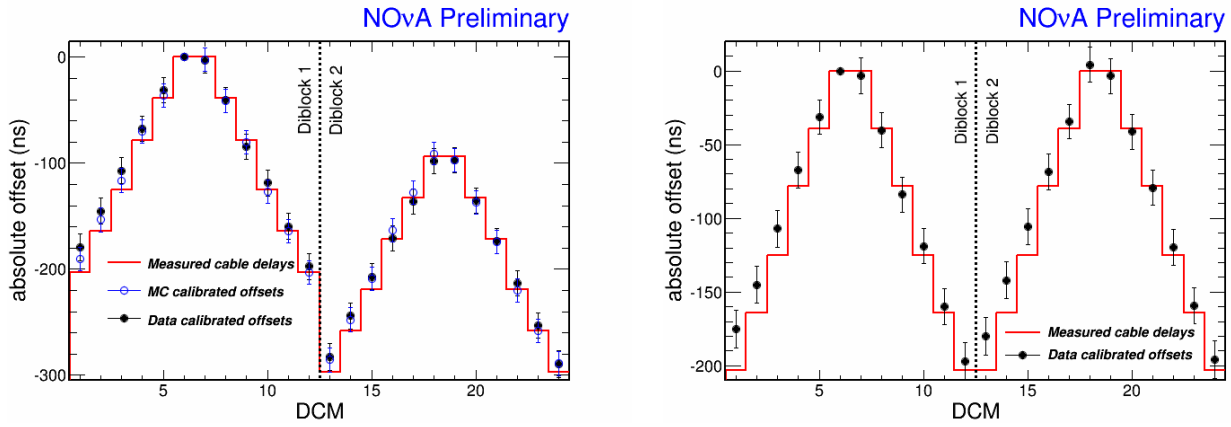

(a) (b)

Figure 4.12: The absolute DCM timing offsets for the first two diblocks at the Far Detector. The red line is the measured DCM offset based on cable delays from a calibration pulse issued by the master timing unit. (a) The black points represent data from early 2014. The blue points represent MC simulation to mimic data conditions and the offset for DCM 6 was fixed at zero when solving the matrix of relative offsets for the absolute values (pre-sync). (b) The black points represent data from early 2014 after cable delay between diblocks was corrected. That is why there is a shift in diblock 2 delays compared to (a) (post-sync).

are also computed. This creates a matrix of relative offsets. Finally, the matrix of relative offsets is solved for the absolute timing offsets between DCMs. One DCM is picked as a reference with a fixed time and and all other DCMs will be solved for the time difference between hits in it and the reference DCM. An example of the results of this time offset calibration is shown in Fig. 4.12.

CHAPTER 5. EVENT RECONSTRUCTION AND PARTICLE IDENTIFICATION

After data has been collected (or neutrinos simulated) and detector response properly calibrated, the next step is to use single channel readout quantities to fully characterize particles interacting in the detector. In this chapter we explain how this reconstruction process is implemented in the NOvA experiment. We describe the algorithms and methods that create reconstructed objects, such as tracks and vertices, and particle identifiers in a preamble for oscillation analysis.

5.1 Interaction separation using slicing algorithm

The basic unit of detection in the NOvA framework is the cell hit. Each cell hit by construction has information from only two spatial coordinates, XZ or YZ. Each hit contains the plane and cell number of that channel, the total charge in terms of ADC counts and time information such as the hit time and hit resolution. In order to have three dimensional reconstructed objects, we must be able to combine sets of hits that are correlated spatially and temporally to the same physics interaction. A NOvA event is a collection of hits that occur within the NuMI beam trigger window of 550 μs. All hits in an event can be divided in two categories: signal hits and noise hits. Signal hits come from interactions of charged particles traversing the cell, and are usually correlated by time. Noise hits come from the electronics, are uncorrelated by time and do not deposit energy. Separating hits into sets of correlated groups, called clusters, is referred as "slicing". The plan is to be able to separate noise hits from signal hits and the signal hits into clusters coming from the same physical source (one slice per neutrino interaction, or cosmic ray).

The slicing algorithm implemented in NOvA is based in the Density-Based Clustering algorithm (DBSCAN) [69]. It uses space and time information to separate clusters using regions where the

density of points in some parameter space drops below a threshold. The clusters made by this algorithm contains two types of points: core and border points. Core points have at least the minimum number of nearby hits within a critical distance from each of them. Border points have less than the minimum number of neighbors and are included to a given cluster as long as they are the neighbor of a core point. Clusters are made by adding points around core points until all expanding branches are border points. Any point not assigned to a cluster is labeled as noise.

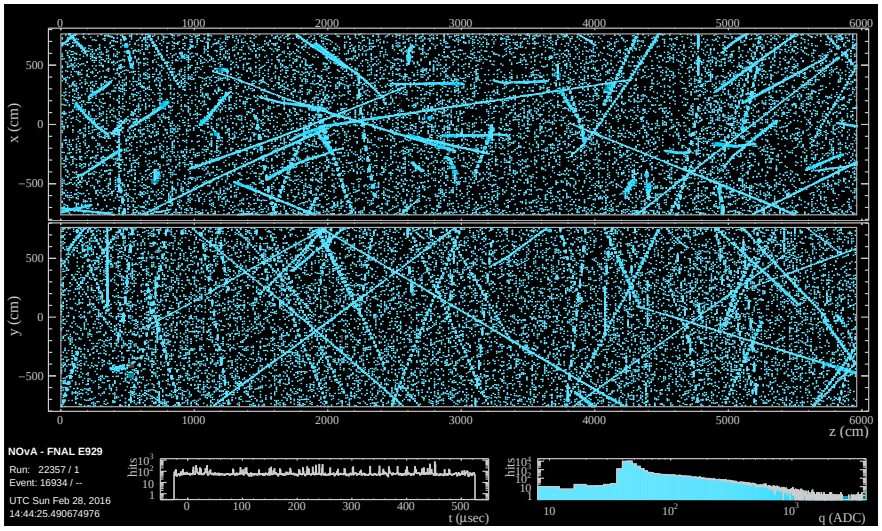

Figure 5.1: NOvA event display showing the 550μs NuMI beam spill trigger window in the Far Detector. The charge distribution of raw hits in shown in cyan color at the bottom right.

A local density is constructed for each hit by counting the number of nearby hits within a given distance of that hit. This distance is parametrized in terms of a custom neighbor function (NS), that includes a causality term, two terms that penalize hits far in space and a term that penalizes low energy hits [39]

$$NS = \left(\frac{|\Delta T| - |\Delta \vec{r}|/c}{T_{res}}\right)^2 + \left(\frac{\Delta Z}{D_{pen}}\right)^2 + \left(\frac{\Delta XY}{D_{pen}}\right)^2 + \left(\frac{PE_{pen}}{PE}\right)^5, \tag{5.1}$$

where T_{res} is the timing resolution of the two hits added in quadrature, D_{pen} is the distance penalty, PE_{pen} is the uncorrected number of photoelectrons, PE is the number of photolectrons (PE) for both hits added in quadrature, ΔT is the time in nanoseconds between the hits, and

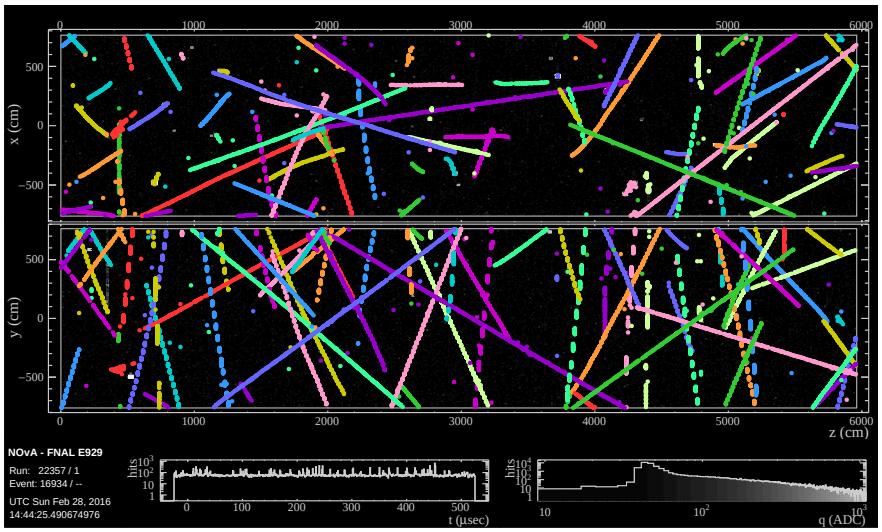

Figure 5.2: NOvA event display showing the 550μs NuMI beam spill trigger window in the Far Detector. The reconstructed slices using the DBSCAN-inspired slicing algorithm are shown in both views. Each color represents an interaction. Matching colors in each view represent the same interaction.

ΔXY, ΔZ are the distances in centimeters between hits in each view. For hits in the same view $|\Delta\vec{r}| = \sqrt{\Delta Z^2 + \Delta XY^2}$, whereas for hits in opposite views $|\Delta\vec{r}| = \Delta Z$.

The parameters in the NS function were tuned using a data-driven method and optimized using two metrics: the efficiency or completeness defined as

$$\text{Completeness} = \frac{\text{Energy from interaction deposited in the slice}}{\text{Total energy from interaction deposited in the detector}}, \tag{5.2}$$

and the purity,

$$\text{Purity} = \frac{\text{Energy from interaction deposited in slice}}{\text{Total energy in slice}}. \tag{5.3}$$

Using Far Detector cosmic simulation, slicing had a completeness and purity of 99.3%. Near Detector neutrino simulation predicts a completeness of 94.4% and a purity of 98.5% [38].

5.2 Lines found with Multi-Hough transform

After a physics interaction has been sliced, the next step is to identify converging lines in order to find the vertex, which is the point where the primary neutrino interaction occurred in the detector.

This is performed in NOvA by using the Hough transform algorithm [74]. It starts by taking pairs of hits in each detector view (XZ, YZ) separately to later calculate the line that passes through the hit pair using polar coordinates. For each of these lines, a "vote" metric is created

$$\text{Vote}(\rho,\theta) = exp\left(-\frac{\rho-\rho_0}{2\sigma_\rho^2}\right) \times exp\left(-\frac{\theta-\theta_0}{2\sigma_\theta^2}\right), \tag{5.4}$$

where the uncertainties are given by $\sigma_\rho = \frac{3}{\sqrt{12}}$, $\sigma_\theta = \frac{3}{d\sqrt{6}}$, d is the distance between the two points, determined by the NOvA cell size, ρ is the perpendicular distance from the line to the origin and θ is the angle between ρ and the x-axis. The vote metric populates a (ρ,θ) phase space. Accumulations in this "Hough map" are associated to the coordinates of the line of interest in a given event.

Once the Hough map is created, it is smoothed by averaging hits using a Gaussian smoothing weight. The peaks in the parameter space need to be above a threshold, which is determined by the number of hits in the event, in order to be considered a valid line. To create new lines, the algorithm removes all the hits from the tallest peak associated to the dominant line, and looks again for new peaks associated with new lines in the new parameter map. This "Multi-Hough" procedure [37] is iterated until no more peaks above threshold are found. In terms of performance, the key feature is checking if the dominant Hough lines form intersections and if so, check they are near the primary interaction point of the slice. Results showing the average distance to the vertex using Far Detector simulation are shown in Table 5.1.

Table 5.1: Average distance from the vertex in centimeters by interaction type of primary and secondary Hough lines using simulation Far Detector events.

Interaction	ν_e CC	ν_μ CC	NC
Primary line	2.7 cm	4.1 cm	6.9 cm
Secondary line	8.8 cm	8.2 cm	9.9 cm

5.3 Vertex finding using elastic-arms

Once we have a cluster of hits sliced and a set of valid lines produced by the Multi-Hough algorithm, the NOvA reconstruction chain uses this an input to find the primary neutrino interaction point and a set of "arms" emanating from that point in the detector. A simple description of an arm a is in terms of a straight line described by parametric equations

$$\begin{aligned} x(s) &= x_0 + s(\sin\theta_a)\cos\phi_a \\ y(s) &= y_0 + s(\sin\theta_a)\sin\phi_a \\ z(s) &= z_0 + s(\cos\theta_a) \end{aligned} \tag{5.5}$$

where (x_0, y_0, z_0) is the spatial location of the arm origin, θ_a the polar and ϕ_a azimuthal angles as function of the distance s. The goal of the elastic arms algorithm [126] (also known as deformable templates) is to find the parameters $(x_0, y_0, z_0, \vec{\theta}, \vec{\phi})$ which best describes the interaction. In most applications the vertex is known and highly constrained. In the NOvA implementation [124], that is not the case which requires custom tools outlined below.

The algorithm looks for the optimal vertex and M arms which describe the N hits recorded in the event. The parameters are considered optimal if they minimize the energy cost function

$$E = \sum_{i=1}^{N}\sum_{a=1}^{M} V_{ia}M_{ia} + \lambda\sum_{i=1}^{N}\left(\sum_{a=1}^{M} V_{ia} - 1\right)^2 + \frac{2}{\lambda_v}\sum_{a=1}^{M} D_a \tag{5.6}$$

where M_{ia} is the distance between the hit i projected into the arm a in the XZ or YZ view, V_{ia} is the strength of the association between hit i and arm a, and D_a is a distance measure from the vertex to the first hit on arm a. The first term quantifies the goodness of fit between the arms and the hits and its minimum is reached when the arms pass through the hits. The second term penalizes hits that are not associated to any arm. The third term is also a penalty term but for the arms whose first hits are located far from the vertex location. This is important when finding a vertex for the NC events in NOvA, where two photons produced by the decay of the π^0 travel some distance . In fact, the likelihood for a photon to travel a distance d before converting is

proportional to $e^{-d\lambda_v}$, where $\lambda_v = (7/9)X_0$ or ~ 30 cm, which leads to a penalty term factor of

$$\chi^2 = -2\ln L = 2\frac{d}{\lambda_v}.$$

Hence, λ and λ_v regulate the strength of these penalty terms [116, 43]. The explicit form of the parameter M_{ia} is given by

$$M_{ia} = \left(\frac{d_{ia}^{\perp}}{\sigma_i}\right)^2, \tag{5.7}$$

with the spatial resolution σ_i being half cell depth over $\sqrt{12}$ or $\sigma_i \simeq 3\text{cm}/\sqrt{12} = 0.9$ cm. The strength of the association between hit i and arm a is computed from the Potts factor [116],

$$V_{ia} = \frac{e^{-\beta M_{ia}}}{e^{-\beta\lambda} + \sum_{b=1}^{M} e^{-\beta M_{ib}}}, \tag{5.8}$$

with $e^{-\beta M_{ia}}$ being the likelihood that hit i is associated with arm a, and the constant term $e^{-\beta\lambda}$ the likelihood that a hit is noise. The parameter β is the range of influence of each arm and λ is the distance at which a noise hit has a 50/50 chance of being associated with an arm or being noise.

For all the vertex candidates, arms are seeded and the directions are scanned in order to minimize the energy cost function Eq. 5.6. The minimization, performed by the MINUIT class in ROOT, depends in great part on the performance of the Multi-Hough input. The fit is initialized using low values of β to avoid local minima in the energy lost function, and then β is gradually tuned until it reaches the final 3D vertex point in the slice. When combined, Multi-Hough and Elastic Arms algorithms achieve vertex resolutions of 11.6 cm for ν_μ-CC events, 10.9 cm for ν_e and 28.8 cm for neutral currents [124]. This translates in a reconstructed vertex for charged-current interactions within 2 cell widths of the true vertex on average. Figure 5.3 shows a NOvA event display with and isolated slice associated to a neutrino interaction. In golden are the Multi-Hough lines and the red cross shows the reconstructed vertex.

5.4 Prongs and the Fuzzy-K algorithm

After the global vertex candidate has been reconstructed by the Elastic Arms method, the next stage is to assign a group membership to each cell within the event. We call this group of member

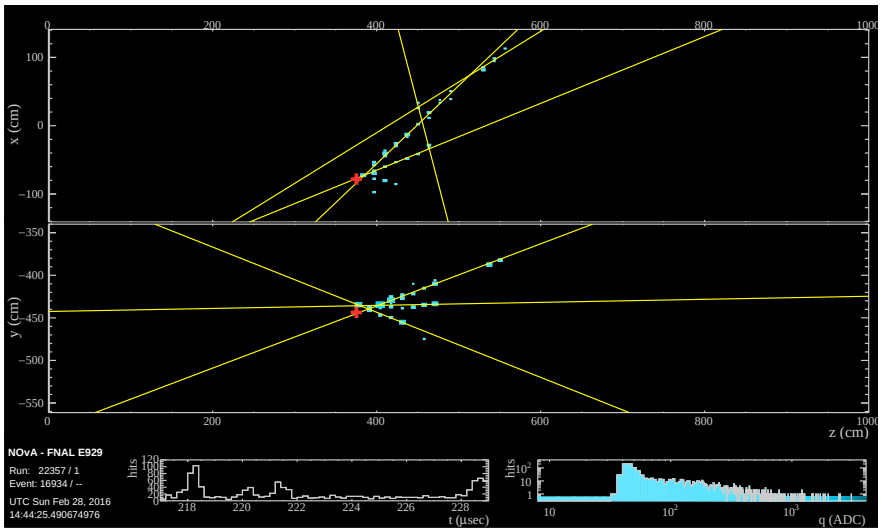

Figure 5.3: NOvA event display showing a selected neutrino interaction filtered by the DBSCAN-inspired slicing algorithm. The golden lines the reconstructed Hough lines. The red cross at the center left represents the vertex reconstructed by the elasticarms algorithm.

hits a prong. A prong is a cluster of hits with a well defined starting point and direction. Each prong is intended to represent hits from a single particle track or shower. This is accomplished with a "possibilistic" Fuzzy-K Means algorithm [105, 169, 121]. Possibilistic means the sum of the membership of each hit across all prongs is not forced to be one, allowing isolating hits be treated as noise. "Fuzziness" allows a particular hit to belong to more than one prong.

The general idea is that when at the reconstructed vertex and for each cell view, the cell hits in the slice should appear as peaks of deposited energy in a 1D-angular space around that vertex. The Fuzzy-K algorithm determines how many prong peaks (centers) are present and assigns a prong membership value to the hits in the slice. Each hit is converted to an angle with respect to the vertex, in a range $[-\pi, \pi]$ with zero being the Z-axis. The uncertainties were assigned empirically from simulation to incorporate multiple scattering effects. An iterative process finds the prong centers and determines the membership for each cell. It begins by assuming one prong is centered on the region of highest density in the 1D-hit angular space. A metric that computes a degree of

membership U_{ij} for each hit θ_j in each prong center θ_i is computed using

$$U_{ij} = exp\left(-\frac{d_{ij}m\sqrt{c}}{\beta}\right), \tag{5.9}$$

where d_{ij} is the distance to prong centers given by

$$d_{ij} = \left(\frac{\theta_j - \theta_i}{\sigma_j}\right)^2, \qquad -\pi \leq (\theta_j - \theta_i) \leq \pi. \tag{5.10}$$

In this case, σ_j is the angular uncertainty, m is the degree of "fuzziness" which allows hits to retain partial membership in multiple prongs, c is the number of prong centers, and β is a normalization term that represents the expected spread of the hits around a normal prong center. Later, the prong centers are updated to a new θ_i' value according to [38]

$$\theta_i' = \theta_i + \frac{\sum_{j=1}^{n} A_{ij}(\theta_j - \theta_i)}{\sum_{j=1}^{n} A_{ij}} \tag{5.11}$$

where $A_{ij} = U_{ij}^m/\sigma_j^2$ and the process is repeated until the difference $\Delta\theta = |\theta_i' - \theta_i|$ is below a tolerance value for all centers.

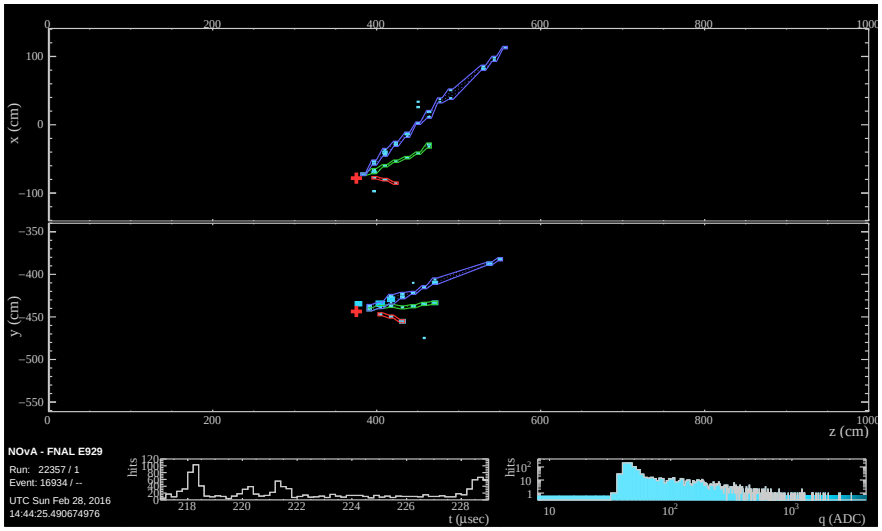

Figure 5.4: NOvA event display showing a selected neutrino interaction filtered by the slicing algorithm. The blue, green and red regions are the reconstructed 3D Fuzzy-K prongs. The red cross is the Elastic Arms based reconstructed vertex.

Additional prongs are created until all cell hits have at least 1% membership to a prong or the maximum number of prong seeds has been reached. Prongs with significant membership overlaps

are merged, whereas prongs with large spatial gaps that indicate two collinear particles are split. Since this process is performed for each view, the last step is to match 2D prongs between views in order to form 3D prongs. This matching involves comparing the energy profile of a prong in each view [43]. A Kuiper metric $K = D^+ - D^-$, based on a modified Kolmogorov-Smirnov test [106, 124], is used to find the best match for the prong, where $D^{+/-}$ is the sum of the largest absolute positive (negative) vertical distances between profiles. The view matching pairs together clusters from each view best matched by the Kuiper metric, and continues until all clusters are matched. In terms of performance [38], the metric used is the completeness for hits produced in the primary lepton in charged-current interactions shown on Table 5.2.

Table 5.2: Average hit completeness for the Fuzzy-K algorithm by interaction type.

Interaction	Charged Current	Quasielastic	Non-Quasielastic
ν_e completeness	88%	95%	86%
ν_μ completeness	93%	98%	92%

The 3D matched prongs will keep the membership information for the cells and become a useful starting point for other reconstruction algorithms that make high level reconstruction objects such tracks and showers as well as particle identifiers (PIDs). Figure 5.4 shows the 3D reconstructed prongs associated to an interaction in the Far Detector.

5.5 Tracking

Let us now discuss the steps to recreate the tracks associated to the final state particles that interact in the NOvA detectors. The tracks are reconstructed using individual slices (interactions). We are interested in methods that reconstruct the tracks of particles that do not create large electromagnetic or hadronic showers, like muons and protons. The first class of tracks that we will discuss in this section are the ones based on the Kalman filter, namely Kalman tracks.

5.5.1 Kalman Filters

A Kalman filter [102] is an optimization algorithm that can estimate a system state when the variables of interest can only be measured indirectly or when the measurements are available from various sources (sensors) but might be subject to noise. In general, they solve the problem of estimating the true value of a real n dimensional state x at discrete k-steps with z measurements. The relationship between the step k and the previous $k-1$ is given by

$$x_k = A \cdot x_{k-1} + B \cdot u_{k-1} + w_{k-1}, \tag{5.12}$$

where u represents any input into the system and w represents the inherent noise in the system process. The matrices A, B transform the state and input at step $k-1$ to k, respectively. Similarly, the relationship between the measurements of the system and its true state is given by

$$z_k = H \cdot x_k + v_k, \tag{5.13}$$

where v_k represents the noise inherent in the measurements and the matrix H defines how the measurement of the system relates to the true state of the system [138].

The Kalman filter determines the best estimate of a state x_k assuming a linear system, with noise and measurement independent of each other and their probability following a normal distribution. The estimate $\hat{x}_k$ of the state at step k is computed such that minimizes the mean square error between the estimated and true states.

An early example on the application of the Kalman filter algorithm in particle physics was implemented in the data analysis program of the DELPHI experiment [79]. In NOvA, a Kalman filter based tracker algorithm is used to reconstruct long single tracks associated to charged particles traversing the detector. It was optimized for muons produced in charged current muon neutrino interactions.

In the context of tracking, the Kalman filter is used to reconstruct the true position of a final state particle given the measurements of the cell hits in the data. The true position and direction

represent the state of the system and the noise associated with the system is the noise originated from the detector cells having finite dimensions. The process noise is the noise originated from the chance that a particle scatters off between measurements that modify the true particle position from the one expected. Non-showering charged particles are expected to follow a straight line in the NOvA detectors due to energy loss by ionization and the lack of an external magnetic field. Any deviations from the straight line assumption are taking into account by multiple scattering, which can be approximated as a normal distribution with a width given by

$$\theta_0 = \frac{13.6 \text{ MeV}}{\beta p} z \sqrt{\frac{x}{X_0}} \left[1 + 0.0038 \ln \left(\frac{x}{X_0} \right) \right], \tag{5.14}$$

that for the case of 2 GeV muon in NOvA, $\theta_0 = 5.4 \times 10^{-3}$ radians.

The Kalman filter applied to NOvA is divided in three steps: track finding, track fitting and view matching. Track finding sorts out which hits in a slice belong to a single track per view. First the algorithm finds segments of tracks called seeds, which are formed from combinations of two hits separated by less than 4 cell from each other. These pair of hits are used to estimate position and slope of the track. The location of the adjacent hits is predicted using the estimated position and direction of the track assuming a linear fit, process errors coming from scattering, and the measurement errors from the uncertainty of the particle location within the cell [137]. Hits that are less than eight χ^2 units away from the track prediction are added the track. Once a new hit is added, the track position and direction are updated given the measurement and the process continues until no more track hits can be added. The propagation process starts from high Z-axis values to low Z-axis values of the detector, since it is assumed that in that region particles emerging from a neutrino interaction will be the most separated from each other. Once the tracks are propagated to the point where no other hits are found to be added to the track, propagation is switched in direction to go to high Z-values, picking up any missing hits. One third final propagation is repeated to go to low Z-values again to separate tracks near the interaction vertex.

Track fitting is the process of determining the best particle trajectory to all the hits in a single track view using the Kalman filter algorithm. At any given location along the track, the fit is determined

from a step-wise forward (backward) propagation of all the hits that came before (after) the current location. A weighted sum of the forward (backward) location and direction is used to fit the final trajectory.

Finally, view matching gets the 2D tracks found in each view, if any, and combines them into a single 3D track. The only dependence in location and direction of the 2D tracks comes from the Z-axis. Therefore, they are matched based on a scoring metric, S, that measures the degree of overlap between the two dimensional tracks in the Z direction

$$S = \frac{\text{Start}_{diff} - \text{Stop}_{diff}}{\text{Overlap}}, \tag{5.15}$$

where Start_{diff} is the difference in planes between the starting point of the tracks in the two views, Stop_{diff} is the difference in planes between the stopping point of tracks in the two views

$$\text{Start}_{diff} = |Z_{\text{low XZ view on track}} - Z_{\text{low YZ view on track}}|$$

$$\text{Stop}_{diff} = |Z_{\text{high XZ view on track}} - Z_{\text{high YZ view on track}}|$$

and *Overlap* is the number of planes that overlap each other over the length of the two tracks in the z-direction. Combinations of 2D tracks are ranked against each other and the combination with the lowest value of S are matched together as 3D reconstructed kalman tracks. Once a match is found, the corresponding 2D tracks are removed from the pool and the matching continues until no more 2D tracks are available. In terms of performance, the kalman filter tracking algorithm completeness and purity results are shown in Table 5.3.

5.5.2 Cosmic tracker

The rate of cosmic ray induced muons at the surface of the Far Detector in the NOvA experiment is approximately 140 kHz. A computationally fast and simple tracking algorithm that models the trajectory of long muons is performed by the cosmic tracker [139]. The cosmic tracker algorithm is a basic straight line-type fitter. It finds the best fit line to a collection of points in each of the cell views by minimizing the squared perpendicular distance from the points to the line. The algorithm

Table 5.3: Performance of the Kalman filter based tracking algorithm by interaction type for both Near and Far Detectors. Numbers taken from [138].

Interaction	CC-Quasielastic	CC-Resonance	CC-Deep Inelastic
FD ν_μ completeness	97%	97%	92%
ND ν_μ completeness	95%	95%	88%
FD ν_μ purity	99%	98%	90%
ND ν_μ purity	97%	95%	85%

takes in the slices as input and loops over all the hits in it, fitting using the X and Y positions in each view, including a weight proportional to the number of hits in each view. After that, the algorithm looks for hits furthest to the fit. It such hit happens to be more than 10 cm (2 cells), its weight is set to zero and the hit is dropped, moving on to the next furthest hit. Before the final fit, the algorithm loops back over dropped hits to see if they can be added back to the track. In case they are not, a linear fit on the final collection of hits is performed. The output corresponds to the start and end points for each line for each view. There is a swap between the start and end points in case the timing of these points indicate that the 2D track goes upstream (slope is positive if time increases with high values of z-axis, negative otherwise) [65]. Performance results of the cosmic tracker algorithm show an efficiency of 98% and purity of 99% where efficiency is defined as

$$\text{Efficiency} = \frac{N_p}{N_u},$$

and purity

$$\text{Purity} = \frac{N_p}{N_v},$$

with N_p being the number of cell hits in the track that belong to the particle, N_u the number of cell hits that belong to a particle and N_v the number of cell hits in the track [66, 27].

5.6 ReMId and CVN classifiers

After vertices and particle trajectories have been reconstructed, the next step is to use data driven algorithms that exploit the interaction topologies of signal and background like events in order to classify particles, and ultimately, neutrino interactions. A particle identifier (PID) is a classifier metric constructed upon trained and tested data whose output helps discriminate between signal and background. Specifically for the muon neutrino disappearance analysis, two PIDs are used in order to select neutrino interactions (slices) with a muon-like particle in the final state, which is the label of a muon neutrino interaction. The first one to describe is the Reconstructed Muon Identifier (ReMID) classifier, which uses the k-nearest neighbors algorithm [59] and four variables to produce an output metric that discriminates between muon tracks coming from ν_μ charged current interactions and background tracks coming from other charged current and neutral current interactions. Later, we will discuss the Convolutional Visual Network (CVN) classifier, which uses pattern recognition, neural network and deep learning techniques.

5.6.1 The Reconstructed Muon Identifier (ReMId) classifier

The signal for the ν_μ disappearance analysis is a muon neutrino interacting in the detector producing a muon particle in the final state in addition to one or more hadrons via a charged-current process. Therefore, proper observation of the outgoing lepton categorizes the interaction as a ν_μ-CC interaction. The principal background component comes from neutral current (NC) interactions, where one of the outgoing particles is a $\pi^\pm$, which could have features similar to muons in a ν_μ-CC interaction. About 10% of the ν_μ-CC events have a final state muon with a track length shorter than other final state particles. Therefore, track length is an important feature but could be misleading. Another potential background to ν_μ-CC events are the ν_e-CC interactions, which result in a electron in the final state. This electron results in an electromagnetic shower which most of the time can be easily distinguished from muons using proper variables.

The ReMId classifier [138] uses four variables as input in order to classify the ν_μ-CC muon-like track: the dE/dx log-likelihood (LL), scattering log-likelihood (LL), track length, and the non-hadronic plane fraction. A brief description of each one is as follows:

dE/dx log-likelihood Charged particles deposit energy in the NOvA detectors according to the Bethe-Bloch equation. Pions lose energy through hadronic scattering. Since the interaction length for a charged pion is 82 cm [115], by using the shape of the dE/dx distribution is possible to distinguish between muons and pions. The dE/dx is measured at plane by plane basis, by adding the total calorimetric visible energy associated to the reconstructed track in the plane and dividing by the total path length in active material that the track goes through in that plane. Using planes instead of cells avoids potential issues with the calculation of the active path length, due to missing cells, resulting in unnecessary uncertainties. To characterize the dE/dx, the log-likelihood (LL) that a particle of type i created the energy deposition profile of the track is defined as

$$LL_i^E = \frac{1}{N_{plane}} \sum_j P_j^i, \tag{5.16}$$

where the rate of energy loss dE/dx is measured at plane j and the probability $P_j^i$of the particle of type i to have the measured dE/dx is calculated as a function of the distance from the track end. The number of planes N_{plane} normalizes the LL among tracks of different lengths. The planes that go into the sum in Eq. 5.16 are all the planes in which the track has deposited energy and does not have energy contamination from vertex activity. In case they have, the planes with energy contamination are determined from an algorithm designed to look for excess energy [144]. The difference in the dE/dx LL between the muon and pion assumptions, $LL_\mu^E - LL_{\pi^\pm}^E$ forms the final variable used as input into the ReMId classifier. The difference is used since both muon and pion energy deposition distributions look alike thus the difference measures the likelihood a track is a muon compared to a charged pion.

Scattering log-likelihood The scattering LL looks at the scatter of the reconstructed track as a function of the distance measured from the end of the track, similarly to the dE/dx LL. The

NOvA detectors have no magnet, therefore any deviation from straight line in the reconstructed tracks is linked to scattering. Muons get this curvature from multiple scattering at small angles and occasionally hard Coulomb scattering. Charged pions experience the same Coulomb scattering with the addition of hadronic interactions due to the strong force. To characterize the scattering of a reconstructed track, the scattering LL is defined as

$$LL_i^S = \frac{1}{N_S} \sum_j P_j^i, \tag{5.17}$$

where P_j^i is the probability of the particle of type i to have a measured scatter value at position j as a function of the distance from the end of the track. The factor N_S normalizes the LL among tracks of different lengths. The amount of scattering is measured as

$$s = \frac{\theta^2}{d}, \tag{5.18}$$

where θ is the scattering angle and d is the distance from the last scatter. The scattering measurements are made at every trajectory point along the track, except at the start and end points. As in the previous variable, the difference between the scattering LL of the muon and the pion, $LL_\mu^S - LL_{\pi^\pm}^S$ is used as input in the ReMId classifier.

Track length The track length of the reconstructed Kalman track is another input to the ReMId classifier. By construction, hadronic showers produce several short-length reconstructed tracks, whereas muon-like particles produce long single tracks. This metric thus provide with discrimination power between tracks from muons and hadronic showers.

Non-hadronic plane fraction Also by construction, the dE/dx LL is computed using a limited range of planes where the track is free of contamination from activity around the vertex. By excluding the planes with contamination, information about the hadronic energy deposition in the track is lost. Muons tend to have very little hadronic contamination as they travel inside the detector. Therefore, in order to recover the information about the hadronic energy deposition, the

fraction of planes used in the dE/dx LL out of the total number of planes in the track with energy deposition is used as input to the ReMId classifier.

The sample of simulated events used for the ReMId classifier use muon tracks from ν_μ-CC interactions and pions from NC events. The reconstructed tracks used have both the starting and ending points at least 50 cm away from the detector edges. Tracks are associated to particles based on the particle type that is most pure according to the hits contained in the track.

5.6.2 The k-nearest neighbors algorithm

The ReMId classifier is built upon a k-nearest neighbor (kNN) classifier algorithm [59], that uses the four input variables described above and outputs an overall score that characterizes a track likeness to a muon coming from a ν_μ-CC interaction. The kNN method is implemented as part of the TMVA [1] or Tool for Multivariate Data Analysis with ROOT[2]. The kNN algorithm works by sampling a training set that includes signal and background events, and uses the input distributions to create weights in a multidimensional parameter space that measure how signal-like and event is. The kNN algorithm searches for k-nearest training events around a query test point

$$k = k_S + k_B \tag{5.19}$$

where $k_{S(B)}$ is the number of signal (background) events in the training sample. How close they are is measured by the multidimensional Euclidean distance

$$R = \left(\sum_{i=1}^{n_{var}} |x_i - y_i|^2 \right)^{1/2}, \tag{5.20}$$

where n_{var} is the number of input variables used for classification (four in our case), x_i are the coordinates from the training sample and y_i are the variables of the observed event. The probability that the input event is signal-like is

$$P_S = \frac{k_S}{k_S + k_B} = \frac{k_S}{k} \tag{5.21}$$

[1] Official website http://tmva.sourceforge.net/
[2] Official website http://root.cern.ch/

The ReMId score of a reconstructed track is set as P_S. The value of k determines the size of the neighborhood for which the probability density function is evaluated. Large values of k do not capture local behavior whereas small values of k cause statistical fluctuations. The ReMId classifier uses $k = 80$ and the score goes from 0 to 1, with values close to 1 indicate high chance of being a muon and values close to 0 indicate the opposite. The value of k was chosen as the lowest value that maximized the figure of merit (FOM) given by

$$FOM = \frac{S}{\sqrt{S+B}} \tag{5.22}$$

with S is the number of signal events and B is the number of background events.

The efficiency and purity at which the ν_μ-CC events can be identified is estimated from all the events that have a higher than threshold ReMId score, relative to the total events. For a ReMId score of 0.50, the selection efficiency 86% is and purity is 95% [138]. Figure 5.5 shows comparison of the predicted and data distributions of the ReMId score variable in the NOvA Near Detector, which for this analysis, the optimal cut was set to $ReMId > 0.5$ for events with muon like tracks.

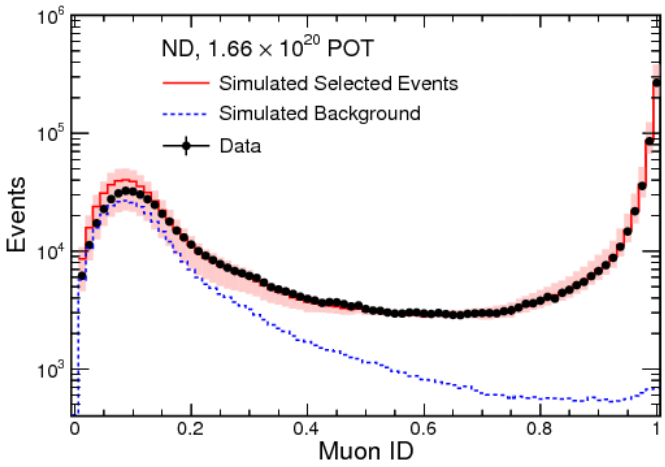

Figure 5.5: The reconstructed muon identifier (ReMId) variable in the Near Detector for contained neutrino interactions.

5.6.3 The Convolutional Visual Network (CVN) classifier

The most recent event classification method used in NOvA uses a machine learning algorithm known as a convolutional neural network (CNN). CNNs extract features of varying levels of complexity by using kernels, filters and convoluted layers, in order to learn correlations. The inputs are image representations of the physics interactions in our detectors, using calibrated hit information only, which means it does not require track or vertex reconstruction. The Convolutional Visual Network classifier, which is a specific application of the CNN technique, is combined with the ReMId classifier in order to select muon neutrino events for the disappearance analysis in NOvA.

This technique was inspired by the studies of the visual cortex of animals [92] in which simple cells are sensitive to edge-like features within the retina, and complex cells are sensitive to position independent edge-like features. CNNs mimic this structure using a series of convoluted layers that extract sets of features from the input image, and pooling layers that perform dimensionality reduction and add translational invariance. The data passed from layer to layer in a CNN has a three dimensional structure (height, width and channel number) in analogy to the RGB channels of color images. For an $n \times m$ convolutional layer, the input data is transformed according to [32]

$$(f * g)_{p,q,r} = \sum_{i=1}^{n} \sum_{j=1}^{m} \sum_{k=1}^{c} f_{i,j,k,r} \cdot g_{p+1,q+j,k}, \tag{5.23}$$

where $(f * g)_{p,q,r}$ refers to the (p, q) pixel of the r channel of the transformed image, n and m are the height and width of the convolutional kernel, c is the number of channels of the input image, f is a filter and g is an array of pixel intensities of the input image. The filter f is a 4D tensor trained to identify features within the image, where i, j are the height and width of the filter, k is the input channel and r is the output channel.

The application of CNN to NOvA event classification was performed after developing and further training a convolutional visual network (CVN).The CVN classifier was constructed to characterize neutrino events into one of the following interaction types:

- ν_μ CC - a muon with a hadronic component,

- ν_e CC - an electron with a hadronic component,
- ν_τ CC - a tau particle with a hadronic component,
- ν NC - only hadronic component.

The input to the CVN classifier consisted in slices of hits separated in space and time, associated to neutrino interactions and with almost zero noise. Grids of 100 planes deep and 80 cells wide are chosen as containers of the slice, one for each XZ and YZ views. This grids correspond to a 14.52 m deep and 4.18 m wide windows of detector, representative of the typical muon neutrino interaction dimension. The intensity of each pixel is proportional to the calibrated energy deposition, allowing these projections to be interpreted as "grayscale" images. An example of this with signal and background like events is shown in Fig. 5.6.

The implementation of CVN was developed using Caffe [98], which is an open source framework for deep learning applications. The CVN was trained using 4.7 million simulated events approximately including cosmic ray interactions coming from Far Detector data. A 15 hit event requirement was imposed for the training events. The CVN architecture initially uses two separate branches, one for each of the cell X-view and Y-view respectively. The branches are later merged to a single convoluted output, which is normalized to one and can be loosely interpreted as a probability of falling in each of the training categories. In that sense, a value of zero is more likely be background whereas a value of one is signal. Distributions of the CVN classifier for ν_e-CC and ν_μ-CC events with NuMI backgrounds are shown respectively in Fig. 5.7.

Implementation of the CVN classifier in the NOvA experiment resulted in an increase exposure of 30% compared to the previous classifier method used for the ν_e appearance analysis [43]. It is also the first reported case of a CNN used in a high energy physics result.

Efficiency, purity and the FOM give all a general insight of the performance of the ReMId classifier. But these metrics where not used to determine the optimal selection cut for this variable. Instead, a combination of the ReMId classifier with a Convolutional Visual Network (CVN) algorithm was

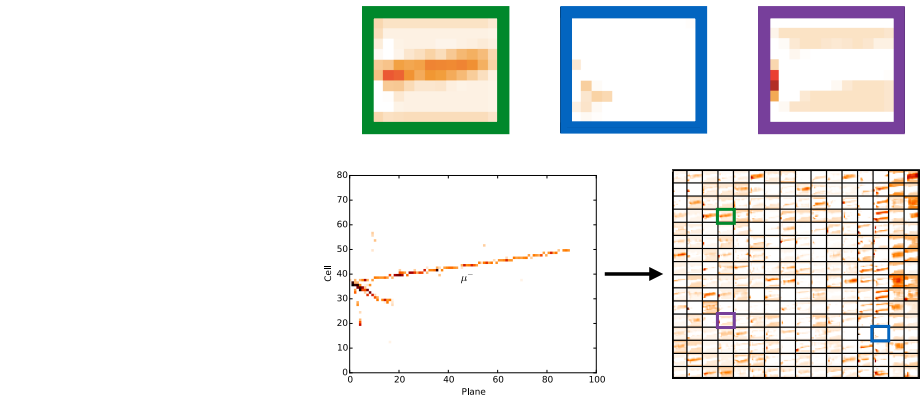

(a) ν_μ-CC

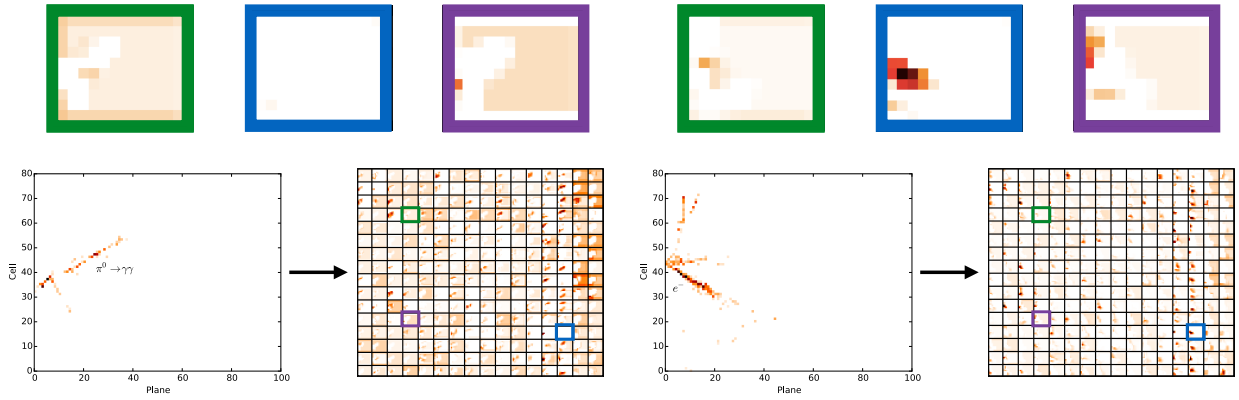

(b) NC (c) ν_e-CC

Figure 5.6: (a) A Y-view example of a true ν_μ-CC interaction in the cell-plane space next to the feature maps extracted from that event by the end of the first inception module in the CVN network, and the three highlighted feature maps from the ensemble, which appear to have become sensitive to muons (green square), electromagnetic showers (blue square) and hadronic activity (purple square) respectively. For comparison, an example of neutral current (b) and ν_e-CC (c) events, both backgrounds to our signal, are also shown.

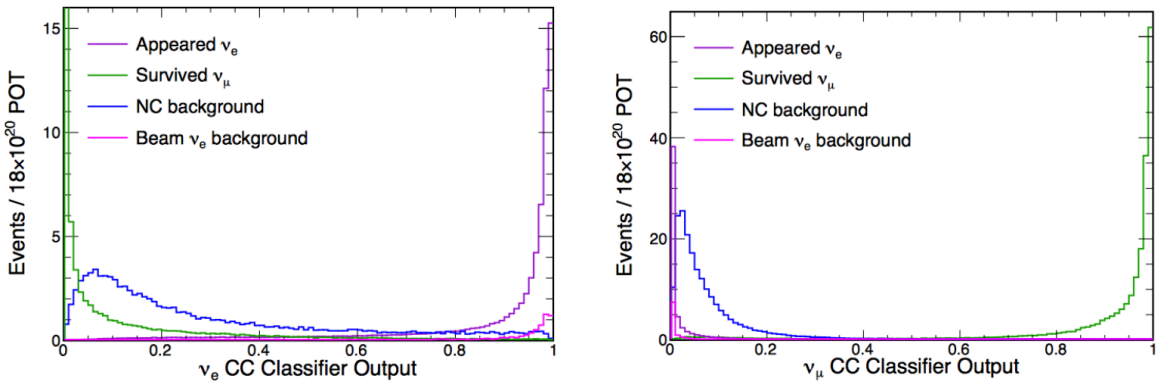

Figure 5.7: The CVN classifier score distribution for ν_e-CC (left) and ν_μ-CC (right) simulated events. Distributions scaled to a NuMI exposure of 18×10^{20} protons on target and a full 14-kton Far Detector. Images from [32].

performed in order to determine the best cut value at which the maximal mixing rejection of $\sin^2 2\theta_{23}$ could be determined under different assumptions [113].

With the reconstruction and particle identificiation details covered, in the next chapter we will describe all the steps involved in the muon disappearance analysis in NOvA.

CHAPTER 6. THE ν_μ DISAPPEARANCE ANALYSIS IN NOvA

This chapter describes an overview of the steps used to produce the 2017 NOvA ν_μ disappearance analysis, corresponding to 9.38×10^{20} POT. The ν_μ disappearance measurement is performed by comparing the reconstructed energy distribution of the selected ν_μ-like candidate events from data to the predicted energy distribution of ν_μ-like events in the Far Detector. Details on the analysis framework, event selection, energy reconstruction and event rate predictions will be presented in the following sections.

6.1 Analysis Software

The ν_μ disappearance analysis presented herein used Common Analysis Format (CAF) files [122], which only contain the final stage variables needed to perform fits and plots of interest. CAF files have a tree structure in which each branch groups variables alike (e.g. header information, energy, simulation) and each leaf represents that variable. Each tree entry corresponds to a reconstructed slice, which as discussed in previous chapters, is a collection of correlated hits in space and time. CAFAna [35] is the software framework in which CAF files are interpreted and actual analysis constructed. By design, CAFAna is histogram-based and flexible. It facilitates the creation of custom cuts and variables, implements classes that predict the estimation of events under different oscillation assumptions, enables the inclusion of systematics uncertainties and computes the fit to the data using MINUIT [96], among others.

6.2 Event selection and analysis improvements

The first step in the ν_μ disappearance data analysis is to select, measure and characterize the ν_μ CC events in both NOvA detectors. The collection of cell hits that have an APD signal above threshold get selected. They are later clustered in space and time using the slicer algorithm [39] in order to obtain individual neutrino candidate interactions. Charged particles leaving trajectories in the detectors are reconstructed using the Kalman-filter inspired tracking algorithm [138]. An example typical neutrino interaction topologies is shown in Figure 6.1. The top rectangle shows a quasielastic ν_μ CC interaction with a muon neutrino incoming and interacting with a nucleus producing a short track associated with a proton and long track associated with a muon, with the distinction that both particles are attached to the same vertex. The color is proportional energy deposited. This is an example of a signal event for the ν_μ disappearance analysis.

Two main background sources are associated to the ν_μ CC disappearance signal: beam-induced backgrounds inside the fiducial volume, including ν_e (ν_τ) CC interactions (center rectangle of Fig. 6.1 shows a ν_e CC event) and neutral current interacions (e.g. bottom rectangle of Fig.6.1), and backgrounds induced by particles from outside the fiducial volume. The latter arise from cosmic ray interactions and neutrino interactions that occur in the material outside the detectors. A set of selection algorithms have been developed in order to identify signal candidates while rejecting background events.

6.2.1 Basic data quality and preselection

A good data quality selection is responsible to account for any potential problems related to the electronics, data acquisition system, timing and/or the NuMI beam that could impact the analysis. It consists of three parts [156]. The first looks at the detector condition over a subrun, where a subrun is about 2 minutes of data taken at the Far Detector (1 hour at the Near Detector). It mainly uses instrumentation and timing information of the detectors to ensure its good performance [143]. Second, metrics constructed to look for short lived transient issues in a spill-by-spill basis were

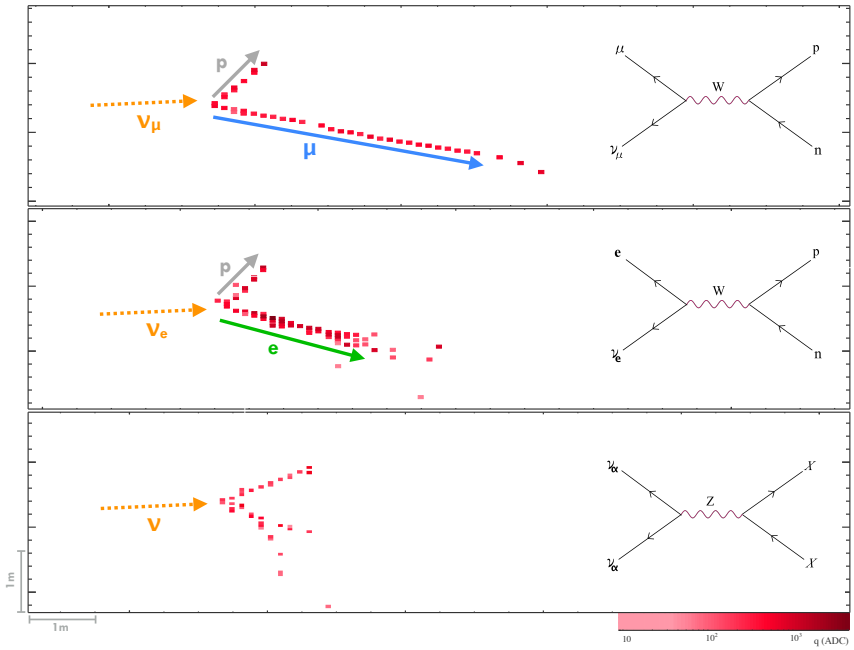

Figure 6.1: Typical neutrino interaction topologies in the NOvA detectors. Each point represents a detector cell and the color is proportional to the charged deposited. Top: a quasielastic ν_μ-CC interaction, with a muon neutrino coming from the left producing a short track associated to a proton and a long track associated to the muon, and both particles attached to the same vertex. Middle: a quasielastic ν_e-CC interaction, with an electron neutrino coming from the left and also producing a low-range track associated with the proton, and an electromagnetic shower associated to the outgoing electron, with both particles attached to the same vertex. Bottom: a neutral current neutrino interaction ν-NC, with an incoming neutrino producing no final lepton but energy deposits through hadronization.

developed. In particular, the selection requires zero DCMs missing during a spill, and that there is no excess of tracks stoping at the DCM edge boundaries, which indicates an out-of-sync detector [104]. Third, we monitor the condition of the NuMI beam spill and apply a selection on those events with sufficient beam quality parameters. These include spills within acceptable time ranges, number of protons on target, horn current, beam position on target, and beam width [134].

After the events have passed the good data quality selection, a preselection is applied requiring basic reconstructed objects to be present, such as a minimum non-zero number of cell hits, tracks and continuous planes. It is at this stage where events with reconstructed neutrino energy less than 5 GeV are selected for further analysis.

6.2.2 Containment

A containment cut is applied to events that pass the previous stage. A neutrino interaction is said to be contained if such interaction has both the vertex and all the final state particles contained within the detector. This is in order to reduce the background due to rock muons and cosmic rays, and to improve the accuracy of the reconstructed energy of neutrino interactions. The selection requires that the projected forward (backward) end (start) of the Kalman track passes through at least 6 cells before exiting the Far Detector; that the projected forward (backward) end (start) of the Cosmic track passes through at least 0 (7) cells before exiting the Far Detector; a two (first, last) plane gap between the interaction and the detector edge; and that the distance of all reconstructed prong objects to be inside a fiducial volume with respect to the detector edges. The containment criteria for the Near Detector is slightly different since includes the muon catcher, which is around 2/3 the height of the active region. First, it requires that all the reconstructed shower-like objects within the slice are contained, that is, that the starting and ending points are well within the fully active volume; that if a particle reaches the muon catcher, such particle is associated to the muon-like track; a two (first, last) plane gap between the interaction and the detector edges of the

active region with a muon-like track starting also in the active region; and that the interaction vertex occurs upstream of the muon catcher.

6.2.3 Muon particle identification

After containment, a particle identifier is applied to the event in order to determined the likelihood of being a ν_μ CC interaction. This translates into finding a muon candidate within the particles in the slice. As discussed previously, the track reconstruction is performed using a Kalman-filter-inspired algorithm [137], whereas track identification is achieved by using ReMId, a kNN-based classifier [138]. A new addition to the analysis has been the inclusion of a Convolutional Visual Network (discussed also in previous chapter) to increase the selection efficiency, specially at low track lengths. The CVN classifier identifies muon neutrino candidate interactions based on event topology (see Fig. 6.1). Both ReMId and CVN classifiers range from 0 (less muon-like) to 1 (more muon-like), as shown in Figures 5.5 and 5.7. For this analysis, if a neutrino interaction has a ReMId value greater than 0.5 and a CVN value greater than 0.5, such event is cataloged as ν_μ CC and selected for further analysis.

6.2.4 Cosmic Rejection

The NOvA Far Detector is located on the surface 810 km away from the target where protons collide at an energy of 120 GeV producing neutrinos. The expected rate of cosmic-ray induced muons is about 140 kHz. The length of the NuMI beam window is 10 μs every 0.75 Hz. The expected number of cosmic-ray induced muons per day that will be inside the NuMI beam window is given by

$$(64,800\ \text{spills/day})\cdot(365\text{day/year})\cdot(1.4\ \text{cosmics/spill}) \approx 3.3\times10^{7}\ \text{cosmics/year} \qquad \text{(in NuMI spill)},$$

where

$$(86,400\ \text{s/day})\cdot(0.75\ \text{spills/s}) = 64,800\ \text{spills/day},$$

and

$$(1.4 \times 10^5 \text{ cosmics/s}) \cdot (10 \times 10^{-6} \text{ s/spill}) = 1.4 \text{ cosmics/spill.}$$

Compare the previous numerical value with the number of neutrino events given by the expression [115]

$$N_{obs} = \left[\int \Phi_\nu(E_\nu) \cdot \sigma(E_\nu) \cdot \epsilon(E_\nu, \cdots) dE_\nu d\cdots \right] \frac{M}{A \cdot m_N} \cdot T$$

where Φ_ν is the flux of neutrinos (e.g. $1/cm^2/s$ for a super beam at 1000 km), σ is the neutrino cross section per nucleon (e.g. $\simeq 0.7 \cdot (E_\nu/[\text{GeV}]) \times 10^{-38}$ cm^2), ϵ is the detection efficiency, M is the total detector mass (kg), A is the effective atomic number of detector, m_N is the nucleon mass and T is the exposure time (2×10^7 s typical accelerator up-time in one year). Computing the estimate gives

$$N_{obs} = \left[\frac{1}{\text{cm}^2 s} \right] \left[0.7 \times 10^{-38} \frac{E_\nu}{\text{GeV}} \text{ cm}^2 \right] [\epsilon] \, [1 \text{ GeV}] \left[\frac{M}{20 \cdot 1.67 \times 10^{-27} \text{kg}} \right] \left[2 \times 10^7 \text{s} \right]$$

$$N_{obs} = 4 \times 10^{-6} \frac{E_\nu}{\text{GeV}} \cdot \epsilon \cdot \frac{M}{\text{kg}}.$$

Assuming a 14 kton detector with organic scintillator being 62% of the fiducial mass and a 62% efficiency for selecting contained ν_μ-CC interactions, the number of observed neutrinos at say, $E_\nu = 2$ GeV per year, is

$$N_{obs} = 4 \times 10^{-6} \cdot 2 \cdot (0.62) \cdot 14 \times 10^6 \cdot (0.62) \approx 43 \text{ neutrinos/year.}$$

Cosmic rejection is of vital importance for reducing the number of background events that mimic our signal at the Far Detector. A boosted decision tree (BDT) algorithm was trained and tested using 7 input variables whose output, when applied to events within the beam spill, classifies between signal and background [40]. The cosmic rejection BDT uses the cosine of the angle between the lepton and the neutrino, the reconstructed y-direction of the muon, the reconstructed muon-like track length, the largest y-position of either the start or the end of the muon-like track (whichever is larger), the cosmic PID output of the CVN algorithm (included in order to make the BDT less susceptible to calibration uncertainties), the ratio between the number of hits in the Kalman track and the number of hits in the slice (hadronic energy fraction), and the projected distance from

both track start and end points to the detector edges. The optimal cut for the cosmic rejection PID was set to a score of 0.5 and larger as shown in Figure 6.2.

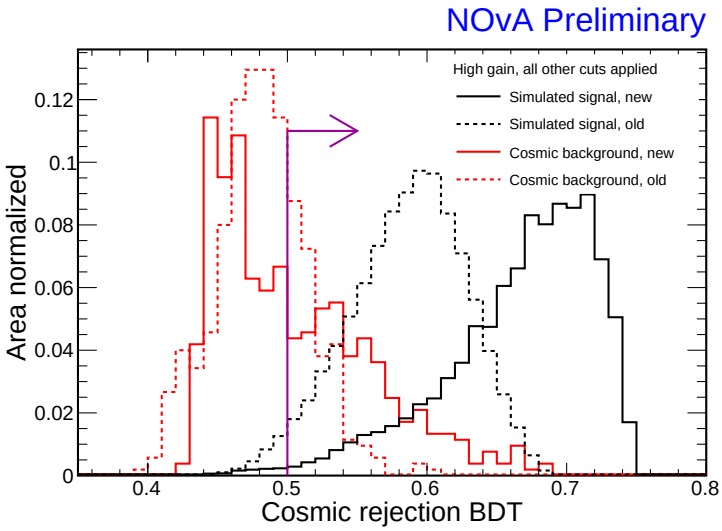

Figure 6.2: Area normalized distributions showing the cosmic rejection PID output for simulated signal (solid black) and cosmic background (solid red). The dashed distributions show a comparison with the previous tuning. The purple arrow at 0.5 shows the optimal cut value [40].

Overall, an increase of 17% in the efficiency with respect to previous analysis was achieved with the improvements in the muon and cosmic rejection PIDs. Is important to note that the optimal cut values for ReMId, CVN and the cosmic rejection were chosen based on the sensitivity to maximal mixing [114].

6.2.5 Beam and cosmic background estimation

The beam induced backgrounds are estimated directly from simulated events in the detectors. If an interaction that passes the selection does not have a true muon associated to it, such interaction is labeled background. The Far Detector cosmic ray background is estimated using two samples of data. The first corresponds to the events selected using the timing sideband region, just outside the 10 μs NuMI beam spill window. This sample has the advantage of having the same detector exposure to the NuMI beam, but given that our entire chain of selection has been optimized to

reject cosmic ray events, the sample is statistically limited. The second sample corresponds the events selected using the cosmic data trigger during a 500 μs window that does not include the NuMI beam spill. Given the high rate of cosmic rays in the surface of the Far Detector (140 kHz), the events on this sample are enough to produce a continuous and well populated distribution, whose shape is used to fit the sideband sample. After converting to the same exposure, the total count of this shape-fitted distribution is used as the estimate of the cosmic background. Figure 6.3 shows the number of signal and background events after each stage of selection. The optimization of the selection reduces the cosmic background by six orders of magnitude, representing a $\sim 5\%$ from the total selected beam signal.

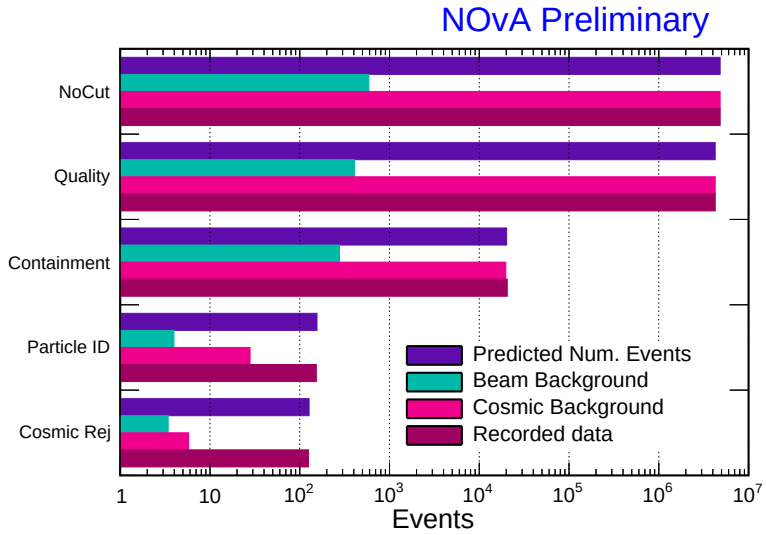

Figure 6.3: Cut flow chart showing the number of events after each selection has been applied. Recorded data corresponds to NuMI events, along with estimates from simulation and cosmic sidebands.

6.2.6 Energy estimation

After a contained ν_μ CC interaction has been identified and reconstructed, the next step is to reconstruct its energy. The muon neutrino energy E_{ν_μ} is estimated as the sum of the reconstructed

muon energy and the energy of the hadronic system,

$$E_\nu = E_\mu + E_{\text{Had}}. \tag{6.1}$$

The muon energy is reconstructed from the range of contained tracks, adjusted to true muon energy using piecewise linear (spline) fits from simulation. The hadronic energy is estimated using calorimetry by adding up all the visible energy from cell hits not associated to the muon. A piecewise linear fit is also used to map the summed visible energy to the total hadronic energy [107]. The muon energy resolution is about 3% in the Far Detector and 3.2% in the Near Detector due to the contribution from the muon catcher. The hadronic energy resolution is about 24% for the Far Detector and 28% for the near detector. Finally, the overall neutrino energy resolution is 6.6% for the Far Detector and 6.8% for the Near Detector [158].

6.2.7 Energy binning

The main goal of the ν_μ disappearance analysis is to optimize the sensitivity to $(\sin^2\theta_{23}, \Delta m^2_{32})$. One strategy is to separate the neutrino events by energy resolution. Neutrino interactions with well defined energy resolutions are less likely to migrate across bins of reconstructed neutrino energy, which is of special importance for events within the oscillation region. We already showed that at the Far Detector, the muon energy resolution is about 3%, whereas the hadronic energy resolution is about 24% (slightly larger for events at the Near Detector). This implies that events with a large fraction of hadronic activity will have a worse energy resolution, becoming susceptible to bin migration. The ratio between the reconstructed hadronic energy and the reconstructed neutrino energy,

$$\text{hadronic energy fraction} = \frac{E_{\text{Had}}}{E_{\nu_\mu}} = \frac{E_{\text{Had}}}{E_\mu + E_{\text{Had}}} \tag{6.2}$$

or hadronic energy fraction, was the metric used to estimate the neutrino energy resolution. A map between the reconstructed neutrino energy and the hadronic energy fraction is shown in Figure 6.4. Using that map, the selected sample is divided into "quantiles" of equal number of events, shown by the solid black line boundaries. These quantile boundaries are defined in a period by period

scheme in order to incorporate any change in performance that affected the detectors. The number of quantiles was determined by studies where the sensitivity to maximal mixing rejection and the computational resources required to make the final fit were optimized [159].

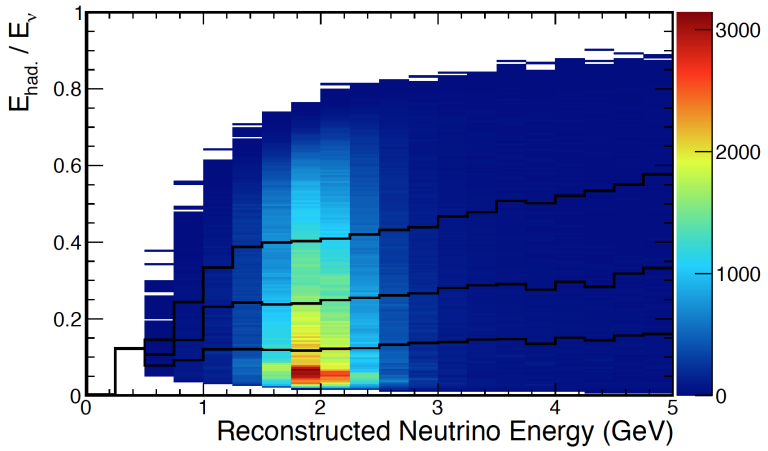

Figure 6.4: Hadronic energy fraction versus reconstructed neutrino energy for selected simulated events at the Far Detector for a subset of data (Period 2). The solid black lines show the quantile boundaries for each neutrino energy bin using the 4-hadronic bin strategy.

The left plot on Figure 6.5 shows the sensitivity to maximal mixing rejection versus the number of quantiles on the left and the distribution of hadronic energy fraction for selected events with four boundaries on the right, both for a subset of the total data taken (Period 2). When comparing with the no-quantile division approach, the improvement is increased by roughly $\sim 16\%$. After four quantiles, the rejection sensitivity is low compared to the memory print and computational resources used, therefore, 4 quantiles were chosen. The quantile with the lowest hadronic energy fraction contains the 25% of the sample with best neutrino energy resolution, whereas the quantile with the highest hadronic energy fraction contains the 25% with the worst neutrino energy resolution.

Another improvement to the sensitivity for the disappearance analysis was optimizing the binning of the reconstructed neutrino energy. Previously, a 20 bin template in the range from 0-5 GeV with constant bin size of 0.25 GeV was used. A binning wider than the energy resolution of the event will diminish any relevant information on the shape of the oscillated spectrum. A smaller

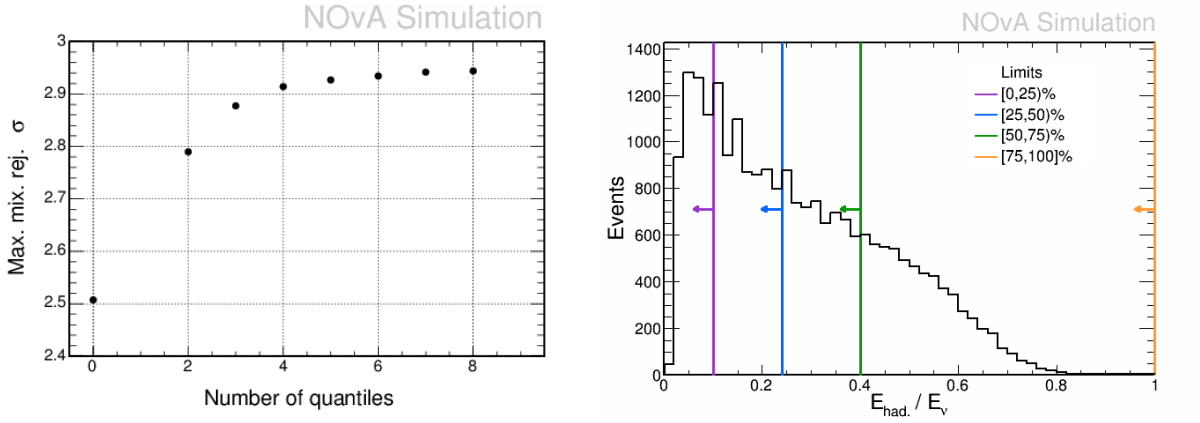

Figure 6.5: Left: Maximal mixing rejection significance ($\sin^2\theta_{23} = 0.5$) versus the number of hadronic energy fraction quantiles. Comparison with the no-quantile division approach shown in the first bin. Right: hadronic energy fraction for selected simulated events in the Far Detector for a subset of data (Period 2). Vertical lines determine the limits for each of the four quantiles dividing the sample evenly.

binning will increase the number of bins used in the fit and ultimately, computational resources. An optimal binning, specially in the region of 1-3 GeV (maximal oscillation) could increase our ability to extract information of the oscillation parameters. Several binning schemes were studied [159] and at the end, the one that gave a better maximal mixing rejection sensitivity was a scheme with 19 bins $(0, 0.75, 1, 1.1, 1.2, 1.3, 1.4, 1.5, 1.6, 1.7, 1.8, 1.9, 2, 2.25, 2.5, 2.75, 3, 3.5, 4, 5)$.

6.3 Extrapolation

After the events have been selected the next step is to make a prediction of the number of selected interactions in the Far Detector. The process of predicting the Far Detector spectrum using the Near Detector data is called extrapolation [7]. NOvA uses Monte Carlo simulation to derive a transfer method that extrapolates the neutrino energy spectrum measured in the Near Detector to the Far Detector. This method [101, 108] extrapolates the Near Detector measurement in three steps, starting from a selected charged-current-like reconstructed energy spectrum:

1. A Near Detector conversion from reconstructed to true signal neutrino energy spectrum

2. Conversion from Near Detector true energy to Far Detector true energy using Far-over-Near ratio and neutrino oscillations applied

3. Conversion from true neutrino energy to reconstructed energy spectrum, and adding backgrounds

In the first step, signal channel events ($\nu_\mu \rightarrow \nu_\mu$ and $\overline{\nu}_\mu \rightarrow \overline{\nu}_\mu$) are selected from Near Detector data, $N^\mu(E_i^{reco})|_{data}$ where i represents the bin index of reconstructed energy and μ represents the $(\nu_\mu + \overline{\nu}_\mu)$-CC selection. Background are subtracted from the Near Detector data spectrum using simulation

$$N^\mu(E_i^{reco})|^*_{data} = N^\mu(E_i^{reco})|_{data} - N^{bkg}(E_i^{reco})|_{sim}. \tag{6.3}$$

The resulting spectrum represents the reconstructed energy of charged current events, $N^\mu(E_i^{reco})|^*_{data}$ with no backgrounds. A reco-to-true migration matrix from simulation, $M^{\mu,ND}$, is used to convert the reconstructed energy spectrum (X-axis) to a true neutrino energy spectrum (Y-axis) using the signal ν_μ selection. The matrix must encode the probability that a neutrino with reconstructed energy E_i came from a neutrino with true energy E_j (where j is the index over true energy) [108]. Therefore, each column of reconstructed energy is normalized to one. The predicted Near Detector true energy spectrum becomes

$$N^\mu(E_j^{true})|_{pred} = \sum_i \frac{N^\mu(E_i^{reco})|^*_{data} \times M^{\mu,ND}(E_i^{reco}, E_j^{true})|_{sim}}{N^\mu(E_i^{reco})|_{sim}} \tag{6.4}$$

where the data/simulation ratio per bin helps to correct the Near Detector prediction. In the second step, a far-over-near (F/N) ratio is later applied to each bin of true energy to predict the number of events at the Far Detector. The advantage of this approach is that many systematic uncertainties that affect both detectors cancel out in the far-over-near ratio, resulting in a smaller error on the measurement. For example, major sources of relative near to far differences in the neutrino flux (and hence, neutrino energy) are due to angular acceptance, decay kinematics, beamline geometry and focusing of the particles. The ratio is created using the simulated events that have passed the same selection, with no oscillations applied, and defined as $F^{\mu,unosc}(E_j^{true})|_{sim}/N^\mu(E_j^{true})|_{sim}$. The

number of predicted unoscillated Far Detector events for each bin j becomes

$$\begin{aligned} F^{\mu,unosc}(E_j^{true})|_{pred} &= \frac{N^{\mu}(E_j^{true})|_{pred} \times F^{\mu,unosc}(E_j^{true})|_{sim}}{N^{\mu}(E_j^{true})|_{sim}} \\ &= N^{\mu}(E_j^{true})|_{pred} \times \frac{F^{\mu,unosc}(E_j^{true})|_{sim}}{N^{\mu}(E_j^{true})|_{sim}} \\ &= \frac{N^{\mu}(E_j^{true})|_{pred}}{N^{\mu}(E_j^{true})|_{sim}} \times F^{\mu,unosc}(E_j^{true})|_{sim} \end{aligned} \tag{6.5}$$

Note that the second expression describes a reweighting of the Near Detector prediction by a Far-over-Near ratio (hence the name) whereas the third expression describes a reweighting of the Far Detector simulation by a Near Detector data (prediction) over MC ratio [108]. The survival three-flavor neutrino oscillation probability $P_{\nu_\mu \to \nu_\mu}(E_j^{true}; \vec{\theta})$ for a given set of oscillation parameters, including matter effects

$$\vec{\theta} = \{\theta_{12}, \theta_{23}, \theta_{13}, \Delta m^2_{12}, \Delta m^2_{32}, \delta_{CP}, \rho, L\}$$

is applied to the corrected Far Detector true energy spectrum by the product

$$F^{\mu,osc}(E_j^{true})|_{pred} = F^{\mu,unosc}(E_j^{true})|_{pred} \times P_{\nu_\mu \to \nu_\mu}(E_j^{true}; \vec{\theta}). \tag{6.6}$$

In the third step, the Far Detector oscillated true energy spectrum is migrated back to bins of reconstructed energy using the migration matrix $M^{\mu,FD}$, where the rows of true energy are normalized to one, making the probability that a neutrino of true energy E_j leaves a reconstructed energy E_i

$$F^{\mu,osc}(E_i^{reco})|_{pred} = \sum_j F^{\mu,osc}(E_j^{true})|_{pred} \times M^{\mu,FD}(E_j^{true}, E_i^{reco})|_{sim}. \tag{6.7}$$

This spectrum is later combined with the trivially extrapolated beam-induced backgrounds (ν_e-CC, ν_τ-CC),

$$F^{Beam}(E_i^{reco})|_{pred} = \sum_j F^{Beam}(E_j^{true})|_{sim} \times M^{Beam,FD}(E_j^{true}, E_i^{reco})|_{sim} \tag{6.8}$$

and the neutral current background, which gets reweighted by reconstructed energy

$$F^{NC}(E_i^{reco})|_{pred} = N^{NC}(E_i^{reco})|_{data} \times \frac{\sum_j F^{NC}(E_j^{true})|_{sim} \times M^{NC,FD}(E_j^{true}, E_i^{reco})|_{sim}}{N^{NC}(E_i^{reco})|_{sim}}, \tag{6.9}$$

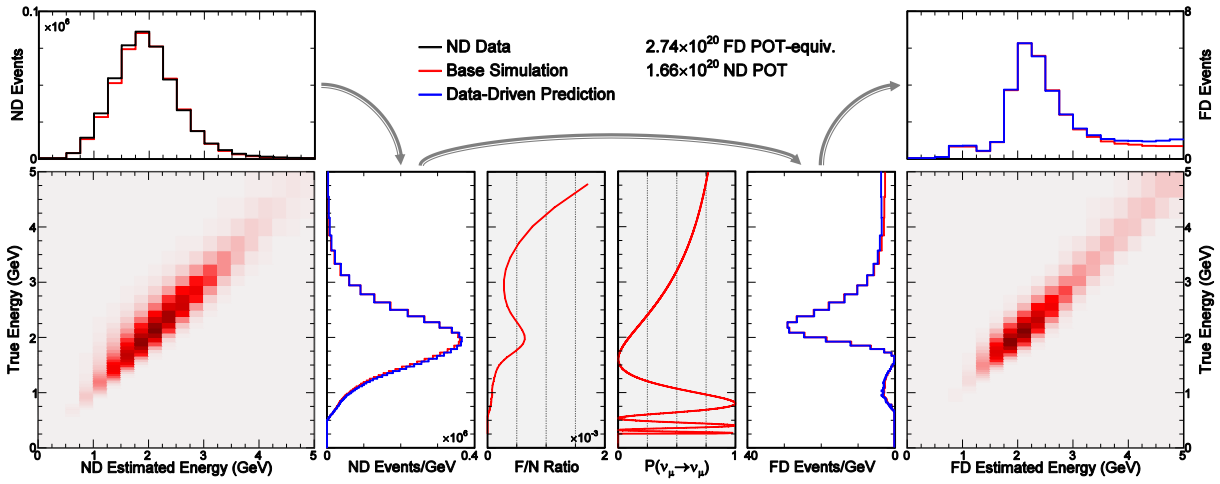

Figure 6.6: Schematics of the ν_μ extrapolation procedure for the NOvA disappearance analysis. First, the Near Detector background-subtracted neutrino energy spectrum from data is converted into a true energy spectrum via a migration matrix. Then, this true energy spectrum is multiplied by a Far-to-Near Detector ratio, that takes into account flux, acceptance and converts it into a Far Detector spectrum. In addition, it is multiplied by an oscillation probability assuming a set of parameters and mapped into a reconstructed neutrino energy spectrum using a Far Detector migration matrix from simulation. At the end, the cosmic a beam induced backgrounds are added completing the extrapolated Far Detector prediction [130].

and finally, the cosmic ray induced muon background selected from outside the 10 μs beam spill window. A schematic diagram of the extrapolation method used in NOvA is shown in Fig. 6.6.

With all the improvements in the event selection from the cosmic rejection and hybrid PID, and the use of quantiles of hadronic energy fraction with optimized binning described in early sections, a Far Detector prediction is shown in Figure 6.7. The solid purple line represents the extrapolated neutrino energy prediction, with the cosmic in and beam expected backgrounds shown.

6.4 Systematic Uncertainties

Systematic errors are defined as having a nonzero mean, affecting the accuracy of a measurement by shifting away from the correct value, in a reproducible fashion independently of the number of trials. They are related to measuring devices (such as a neutrino detector) or measuring methods

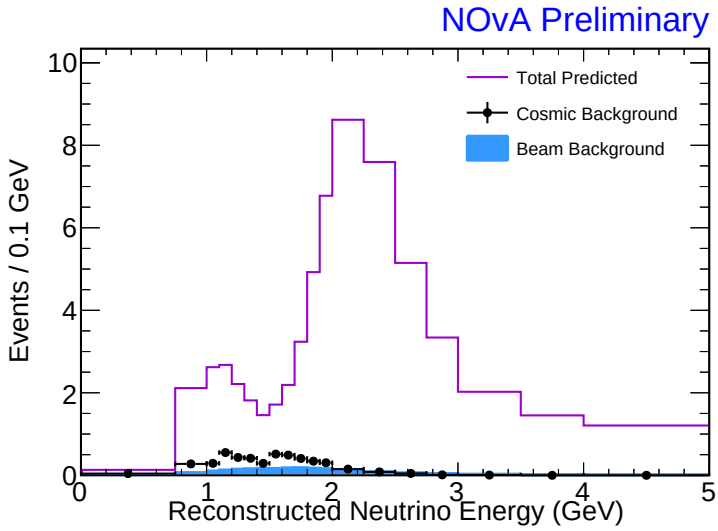

Figure 6.7: Far Detector prediction showing the total number of events that have passed the Numu2017 selection criteria (solid purple), beam-induced (light blue) and cosmic sideband (black dot) events also shown. No NuMI data included.

(such as the energy of a muon-like event). The two detector design of the NOvA experiment allows for a reduction or cancellation of the systematic errors in the Far-over-Near ratio step. The assessment of the oscillation parameters $\sin^2\theta_{23}$ and $\Delta m^2_{\theta_{32}}$ takes into account remainder systematic uncertainties in the neutrino flux, calibration, energy scale, neutrino cross sections, final state interactions, scintillator light modeling, and energy independent scale factors. These systematic uncertainties can be absolute, in the sense that affect both detectors in the same way, or relative, contributing differently depending on the detector due to differences between them. To study the effects of systematic uncertainties, two procedures are used. A direct approach, in which events are reweighted in order to quantify the effect of an uncertainty, for example, on a particular interaction type. An indirect approach, in which the reweighting is not possible, motivates the generation of a new sample of simulated events with shifts applied. In these shifted samples which may affect reconstruction, the central value becomes the $\pm 1\sigma$ bound on the uncertainty. For systematic uncertainties due to different models, such as the light modeling, a new simulation sample is created assuming different parameters. In the end, the effect of each source of systematic uncertainty is included into the analysis by shifts and normalization reweights to the neutrino energy spectrum

from simulation. This section describes the errors incorporated in the official ν_μ-disappearance analysis that uses contained events.

6.4.1 Calibration Uncertainties

A study on proton energy in Near Detector data and MC simulation found that the calorimetric detector in data is 5% lower than the MC simulation [84]. This is interpreted as a 5% absolute calibration uncertainty. The effect of this uncertainty is evaluated by generating two simulation sample sets with a +5% or a −5% shift applied and known as "XY" shifted samples, corresponding to different calibration constants, before the reconstruction and particle identification stages. Since the proton study was only performed in the Near Detector, a 5% discrepancy is assumed to be present in the Far Detector as well. A reconstructed versus true energy comparison of simulated cosmic hits as function of their position along the length of a cell (W) shows a residual disagreement after calibration corrections where applied [19]. This disagreement arises when all cell hits with energy > 15 MeV are used, instead of the standard "tricell" hits used for calibration [19]. A polynomial was fit to the ratio and the resulting function was used to change the calibrated "shape" response versus W. This sample is known as the "func" shifted sample and also was used in extrapolation in place of the nominal to gauge the impact on the predictions.

6.4.2 Beam Uncertainties

Both NOvA detectors are exposed to the neutrino flux of the NuMI beam. Systematic uncertainties associated to this flux can be divided in two components: hadron production and beam transport uncertainties. The uncertainties of the hadronic production are related to the modeling of the production of pions and kaons in the target and horns, whereas the beam transport uncertainties refer to the specifications of the proton beam, the simulated beam geometry and the focusing horns and magnetic fields. Assessment of the hadron production uncertainty used the PPFX method [18] recently implemented in NOvA. It constraints the GEANT4 flux simulation by generating a number

of alternative weights where hadron production cross-section assumptions are varied within their uncertainties. A covariance matrix describing the uncertainty in the NuMI flux is generated using these alternative weights. A principal component analysis (PCA) disentangles these correlations and re-arranges the components based on the largest impact to the oscillation fit [118], which are set to $\sim 3\%$ signal and $\sim 6\%$ background uncertainties. Beam transport uncertainties, including horn current miscalibrations, horn position, beam position on target, horn geometry and water layer, target position, beam divergence, and magnetic field a the decay pipe uncertainties, are motivated by data from beam monitoring devices [61]. For each beam parameter described above, neutrino fluxes were calculated from simulation for each detector. The ratio of each variation with respect to the nominal were converted into weights in true energy bins. These weights were applied to the nominal simulation spectrum for both detectors when using the extrapolation method. A conservative overall effect was computed by adding each component in quadrature, which showed that all the components contributed below 5%, except the ± 3 mm uncertainty in the horn 1 X-position, which has an effect of 10% at 3.5 GeV [61].

6.4.3 Neutrino Interaction Uncertainties

Another source of systematic uncertainty is how well we are able to model neutrino interactions in our detectors. A way quantify this is by evaluating the uncertainties due to cross sections, final state interactions and hadronization models using GENIE's reweighting tools which are applied to simulated events. The modeling of the interactions depends on different parameters, or "knobs", which can be tuned to enhance/suppress cross sections and final-state particle kinematics. A $\pm 1\sigma$ reweight variation for a subset of GENIE knobs is determined after a careful revision of the interaction model and inputs from other experiments, such as MINERvA. These one-sigma variations are propagated in the analysis using the extrapolation method and compared to an unshifted nominal prediction, for both signal and background. For this latest analysis, the uncertainty in the shape of the 2p2h cross section is decribed using three degrees of freedom. First, use the empirical MEC with the energy transfer (q_0) reshaped in such a way that the $\pm 1\sigma$ errors match the GENIE QE

and RES predictions. Second, the neutrino energy cross section dependence, whose ±50% impact events with $E_\nu^{true} \sim 0.2$ GeV, but monotonically aproaches to ±10% for $E_\nu^{true} \sim 4$ GeV. Third, the nn/np composition of the scattering off initial-state nucleon pair, set at a central value of 80%, with a $\pm 1\sigma$ set to 10%. A one-sided $+1\sigma$ effect for the RPA correction on the resonant pion production is applied as function of true Q^2 in a range of −30% to 15%. Based on Near Detector data/simulation discrepancies, a 50% uncertainty is applied to the non-resonant pion production with invariant hadronic mass $W < 3$ GeV, and a 5% for $W \geq 3$, for 1−, 2− and +2−pion cases. The full list of uncertainties used in the latest official NOvA analysis can be found in [163]. Considering all quantiles in the oscillated Far Detector, the yield shifts with larger effects were of the order of ∼ 4%, corresponding to the knobs affecting the axial mass for resonant pion production M_A^{RES}, the MEC transfer q_0 shape, and resonant production RPA correction. The next eight had a contribution of $\simeq 0.5\%$, whereas the vast majority of the ∼ 70 knobs, when combined in quadrature, had a impact of ∼ 1% [56].

6.4.4 Light yield modeling

Three special datasets were produced to account for the uncertainty in modeling light yields in the liquid scintillator. In the first one, both Cherenkov and Birk's suppression are tuned in such a way that Cherenkov light efficiency increases but standard scintillation light production is reduced, in order to make muons match data and simulation. By doing this, the 2% dE/dx discrepancy observed in Near Detector data versus MC simulation proton and muon comparisons is removed. The other two samples were created with Birk-Chou constants set to alternative values. These were motivated by disagreements between PE/cm distributions in data and MC event after a ∼ 10% tune and a similar sized systematic in the overall light model normalization when looking at the distribution of fiber brightness values [31]. But since a change in the normalization of the light model would be removed by an absolute calibration scale, when the scintillation light levels are shifted ±10%, the absolute calibration needs to be shifted by 10% in the opposite direction, which

occurred for this two datasets. They were used to evaluate the effect of hits rising above or falling below the readout threshold.

6.4.5 Muon Energy scale

The full uncertainty in the muon energy scale was constructed by including all the individual uncertainties in the simulation of the muon energy loss. The uncertainties in the composition and mass of the detectors, including the muon catcher, were taken into account [155]. The relative muon energy scale uncertainty is applied by shifting events in both detectors by half the amount in opposite directions, e.g. for a $+1\sigma$ shift, the Near Detector is shifted by $+0.5\sigma$ and the Far Detector by -0.5σ. Since we use a function to map track length onto energy, the shifts are applied to the track length instead before the energy is calculated. The relative (uncorrelated component) muon energy scale uncertainty is set to 0.27%. The absolute muon energy scale is fully correlated between the Near and Far Detectors and is set to 0.94% [155].

6.4.6 Hadronic Energy scale

Relative and absolute hadronic energy scale uncertainties were motivated by a 5% data/simulation discrepancy in the response to protons at the Near Detector [84] and by comparing different hadronic interaction models in our simulation [119]. Since the study on protons was only performed in the Near Detector, it was cautiously assumed that the same 5% discrepancy occurs at the Far Detector. For the absolute scale, the uncertainty is applied to the reconstructed hadronic energy (both in the hadronic system and in the hadronic hits on the muon-like track). For the relative scale, the scale is also applied to the reconstructed hadronic energy but as a positive scale in the Near Detector and as a negative scale at the Far Detector.

6.4.7 Other systematic uncertainties

The uncertainty on the neutral current background is obtained for the GENIE cross section uncertainties, motivated by the validation of the simulated NC contamination in the Near Detector [154]. The constraint of the NC contamination comes from the differences in neutron production from stopped muons and pions. Simulated neutrinos interacting with material outside the detector in conjunction with cosmic activity originated outside the detectors were studied under the assumption that pile-up with contained events occur, causing them to fail selection and therefore, creating acceptance differences. It was found that the effect is negligible at the Far Detector [150] but a 3% Near Detector normalization uncertainty is required [160]. The uncertainty on ν_τ is taken as 100%, and is not included as a systematic since has negligible impact on the analysis. Beam intensity effects are negligible since our Near Detector simulation matches the intensity of the data in a run-by-run basis. Detector alignment was shown to also be small [171] and not included. The uncertainty due to the noise model is estimated by comparing two noise models (versions 1 and 2). Studies show that the effect is negligible [30, 162].

6.4.8 Summary of systematic uncertainties

The list of systematic uncertainties for this round of the disappearance analysis and their contribution to the measurement of the mixing parameters $\sin^2\theta_{23}$ and $\Delta m^2_{\theta_{32}}$ are shown in Fig. 6.8. The bottom two rows show the total systematic error added in quadrature, and the total statistical error in light red. We can notice that calibration is the largest contribution for both parameters, followed by cross section systematic uncertainties, and that the analysis is statistically limited.

6.5 Discussion of official analysis results

In this final section we will discuss the NOvA 2017 ν_μ CC disappearance results. This analysis uses the Near and Far Detector data sets from February 6th, 2014 to February 20th, 2017. This is

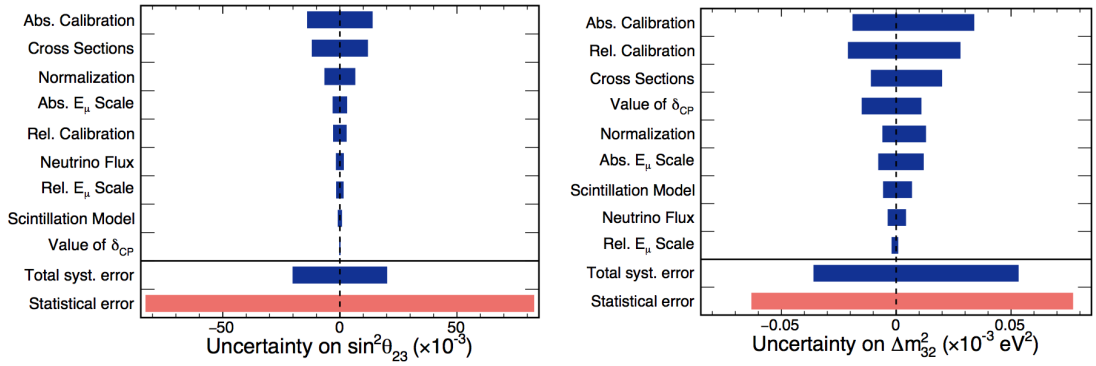

Figure 6.8: Systematic uncertainties for each mixing parameter for the 2017 analysis. Largest contribution are the calibration and cross section systematics. Both analysis are statistically limited.

equivalent to 8.85×10^{20} protons on target (POT) on the full 14 kton NOvA Far Detector, a 46% increase since the last analysis.

Figures 6.9, 6.10, and 6.11 show data and simulation comparisons for the reconstructed muon, hadronic and neutrino energies in the Near Detector for each of the hadronic energy fraction quantiles. These Near Detector comparisons where used to validate the agreement between data and MC before looking at the Far Detector data. The data, represented by the black dots, is shown with the simulated selected events (solid red) and the 1σ systematic uncertainties (shaded red). The simulated background that passes the selection is shown in solid blue.

For the reconstructed muon energy, the agreement between data and simulation is within expectations for all the quantiles of hadronic energy fraction. But the first quantiles have a data mean and simulation mean difference of around 0.02 GeV, whereas for the last two quantiles and the all-quantiles combined, such difference is of 0.01 GeV. In interest to see that the majority of the simulated background is located in the quantile with higher hadronic energy fraction. Similarly, for the reconstructed hadronic energy, the agreement across the four quantiles is within expectations. But all except one quantile have a data mean and simulation mean difference of 0.01 GeV, including the all-quantiles combined distributions. Finally, the reconstructed neutrino energy shows

0.01 GeV data mean and simulation mean differences in all quantiles except the one with highest hadronic energy fraction, and the all-quantiles combined.

When looking at the Far Detector, a spectrum prediction is created by extrapolating the Near Detector data distribution (with simulated background subtracted), with a 3-flavor neutrino hypothesis applied. In order to extract the oscillation parameters $\vec{\theta}$, this predicted Far Detector spectrum is fitted to the measured data by minimizing

$$-2\log\lambda(\vec{\theta}) = 2\sum_{i}^{bins}\left[e_i(\vec{\theta}) - o_i + o_i\cdot\ln\frac{o_i}{e_i(\vec{\theta})}\right] \qquad \text{(stats only)} \tag{6.10}$$

where o_i is the number of observed events in each bin, and $e_i(\vec{\theta})$ is the number of events expected at these oscillation parameters. In the large sample limit, the minimum of $-2\ln\lambda$ given by Eq. 6.10 follows a χ^2 distribution [129]. For the general case of including systematics uncertainties, the minimization is taken with respect to the systematic parameters with the addition of a penalty term,

$$-2\ln\lambda(\vec{\theta}) = 2\sum_{i}^{bins}\left[e_i(\vec{\theta}) - o_i + o_i\cdot\ln\frac{o_i}{e_i(\vec{\theta})}\right] + \sum_{j=1}^{systs}\frac{\Delta s_j^2}{\sigma_{\alpha_j}^2} \qquad \text{(with systematics)} \tag{6.11}$$

where Δs_j is the difference from the nominal value for the systematic parameter s_j, and σ_{s_j}, treated as the penalty term which is the estimated 1σ uncertainty on s_j.

For this analysis we observed a total 126 candidate events, with an expected prediction of 129.20 at best fit point, and a total expected background of 9.24 events, of which 5.82 are cosmics, 2.50 neutral currents and 0.96 beam induced events. Figure 6.12 shows the Far Detector reconstructed neutrino energy spectrum with the data (black points), best fit prediction (solid red) and the $\pm1\sigma$ systematics band, with beam induced and cosmic background for each and all quantiles of hadronic energy fraction.

In the absence of neutrino oscillations, a total of 763 are expected in the Far Detector. The left side of Figure 6.13 shows the reconstructed neutrino energy distribution of data (black points), the oscillated prediction (solid red) with its total background (dashed blue) and the unoscillated prediction (dashed blue). This shows a remarkable evidence for muon neutrino disappearance at

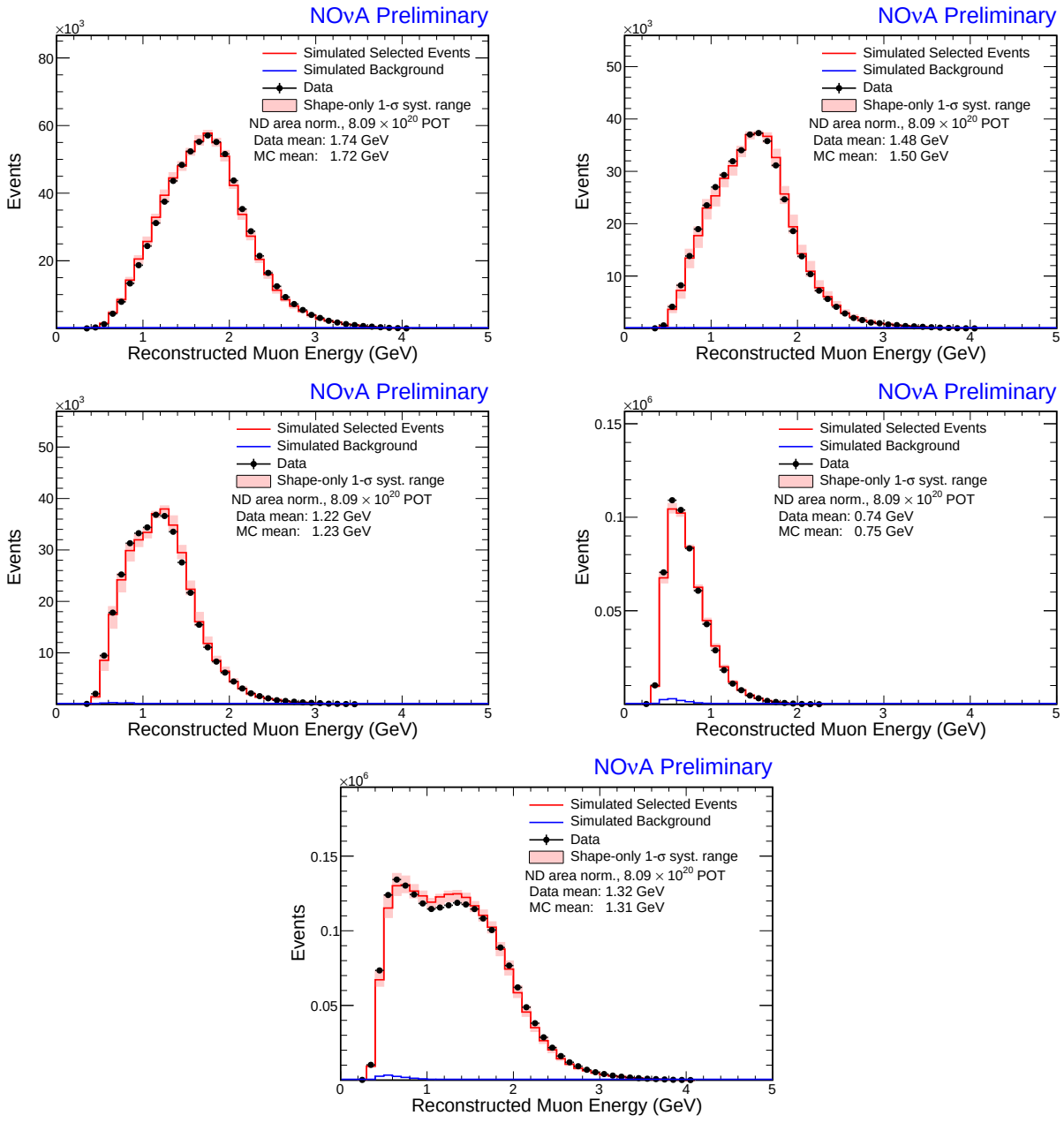

Figure 6.9: Numu 2017 analysis Near Detector area normalized reconstructed muon energy spectrums showing data, simulated selected events with $\pm 1\sigma$ systematics band and simulated background for quantile 1 (top left), quantile 2 (top right), quantile 3 (center left), quantile 4 (center right) and all quantiles combined (bottom).

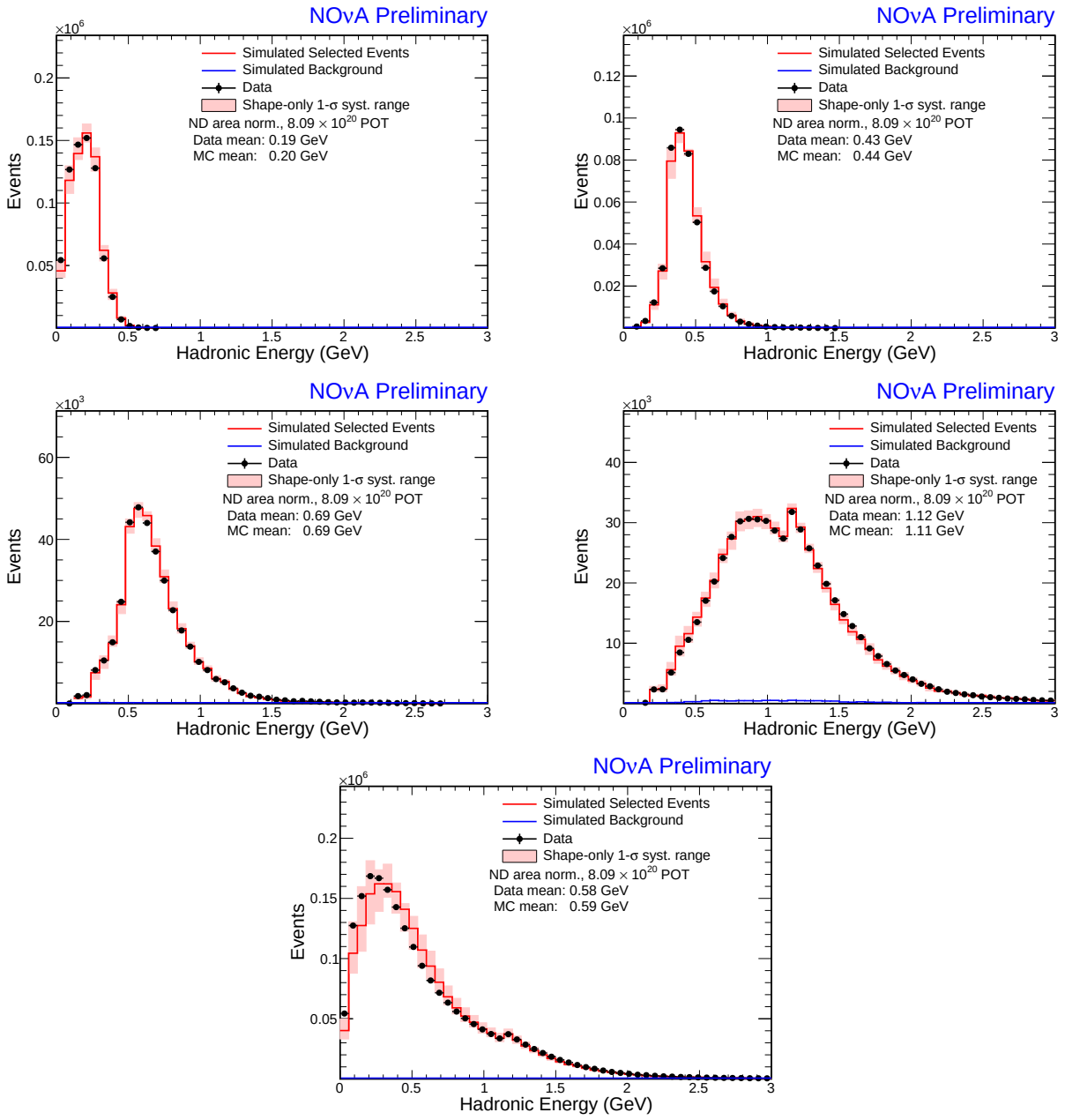

Figure 6.10: Numu 2017 analysis Near Detector area normalized reconstructed hadronic energy spectrums showing data, simulated selected events with $\pm 1\sigma$ systematics band and simulated background for quantile 1 (top left), quantile 2 (top right), quantile 3 (center left), quantile 4 (center right) and all quantiles combined (bottom).

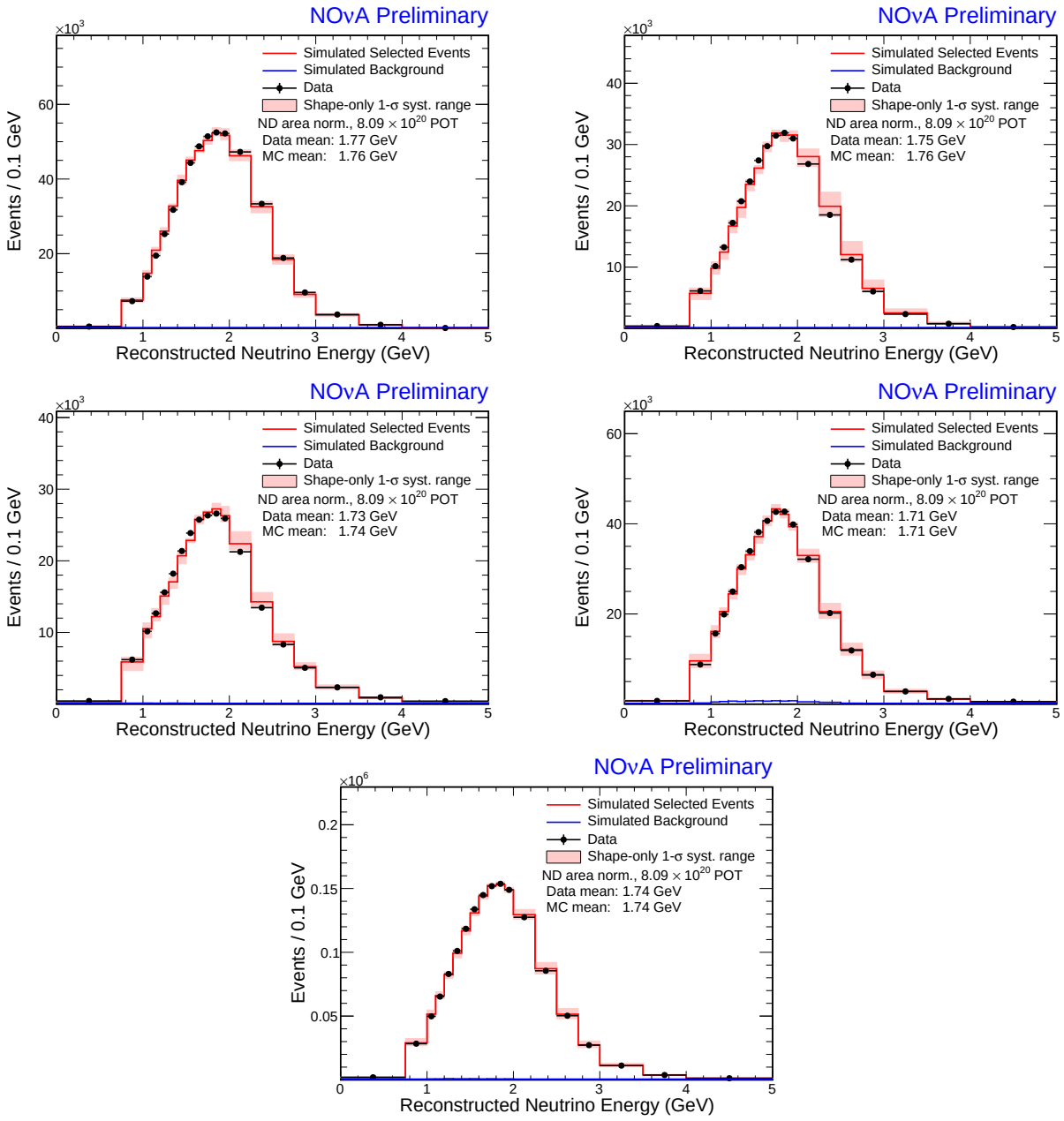

Figure 6.11: Numu 2017 analysis Near Detector area normalized reconstructed neutrino energy spectrums showing data, simulated selected events with $\pm 1\sigma$ systematics band and simulated background for quantile 1 (top left), quantile 2 (top right), quantile 3 (center left), quantile 4 (center right) and all quantiles combined (bottom).

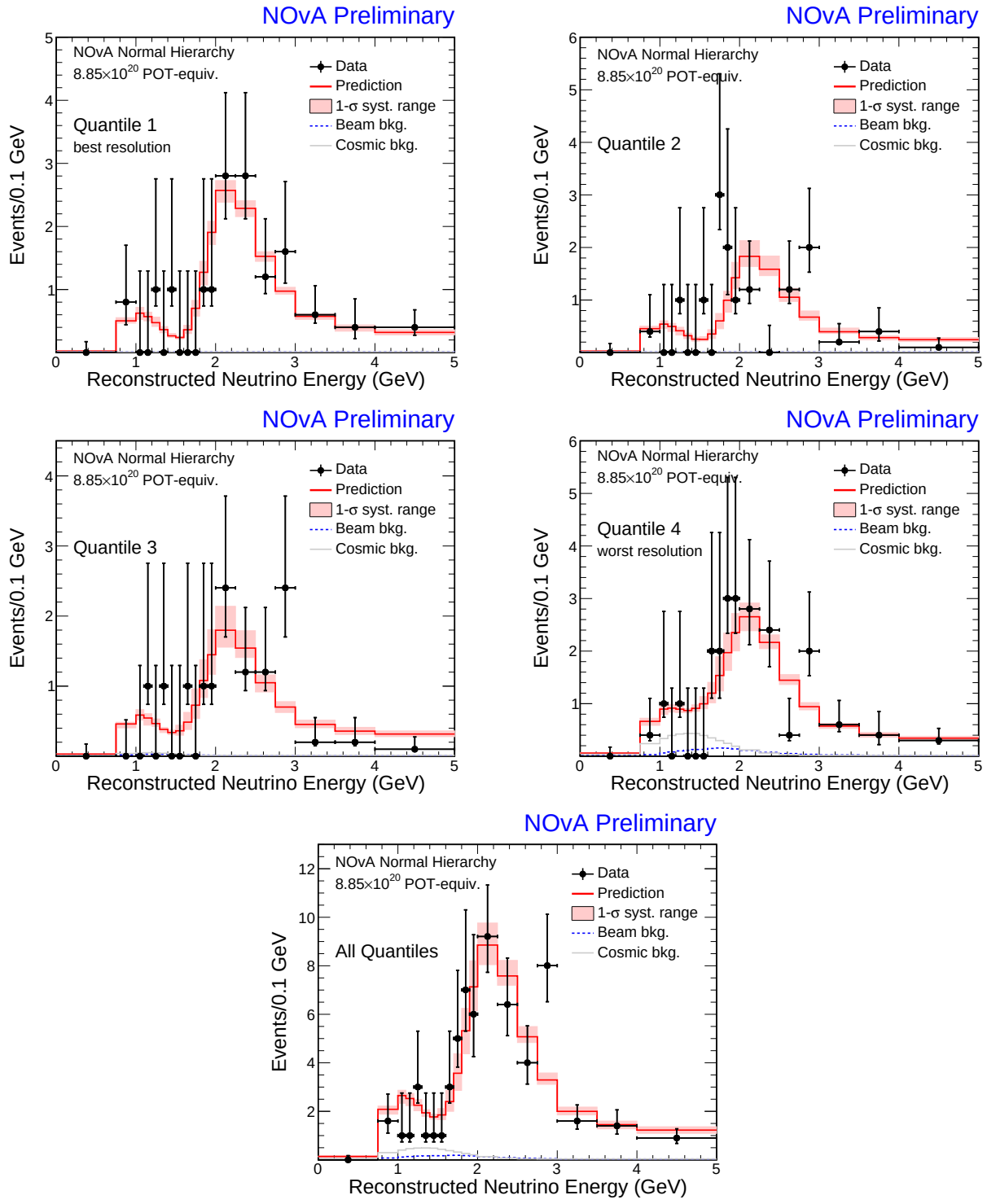

Figure 6.12: Numu 2017 analysis Far Detector reconstructed neutrino energy spectrums showing data, best fit prediction with $\pm 1\sigma$ systematics band, beam-induced and cosmic backgrounds for quantile 1 (top left), quantile 2 (top right), quantile 3 (center left), quantile 4 (center right) and all quantiles combined (bottom). A total of 126 events were observed from data, with 129 expected events at the best fit, and a total of 9.24 background events, including 5.82 cosmics, 2.50 neutral current and 0.96 beam-induced events.

the NOvA Far Detector. The right side shows the ratio to no oscillations for data and simulation (all quantiles) after background has been subtracted.

The oscillation parameters Δm^2_{32} and $\sin^2\theta_{23}$ are varied in a 2-dimensional parameter space. Confidence limit contours $\Delta\chi^2 = \chi^2\vec{\theta} - \chi^2_{best}$ are used to show the $(\Delta m^2_{32}, \sin^2\theta_{23})$ regions allowed by the fit to the data. The best fit point is determined by a χ^2 statistic similar to Eq. 6.11.

The best fit to the data gives $\Delta m^2_{32} = 2.431^{+0.079}_{-0.070} \times 10^{-3}$ eV^2 and $\sin^2\theta_{23} = 0.466$ or 0.562 $(0.428 - 0.598)$. Figure 6.14 shows the sensitivity contours from the fit to the data with systematics. The solid black line represents the 90% confidence level using the best fit ν_μ disappearance results for NOvA. A comparison with combined ν_μ and $\overline{\nu}_\mu$ oscillation results from 2016 T2K analysis [3] and from the combined ν_μ disappearance and ν_e appearance 2014 MINOS analysis [8] are shown in dotted blue and dashed red at the 90% C.L. respectively.

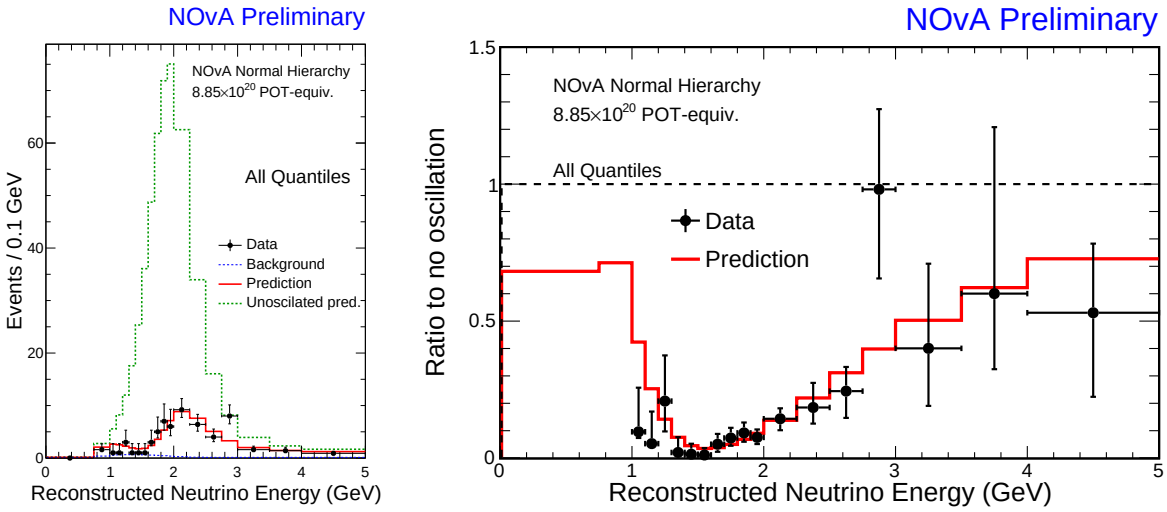

Figure 6.13: Left: Reconstructed energy spectrums of the unoscillated prediction (dashed green), data, best fit prediction with no systematics, and backgrounds for selected events for all quantiles combined. In the absence of oscillations, a total of 763 events are expected. Right: Reconstructed energy spectrum showing the ratio of data over unoscillated prediction and best fit prediction over unoscillated prediction. Backgrounds from predictions have been subtracted before taking the ratio.

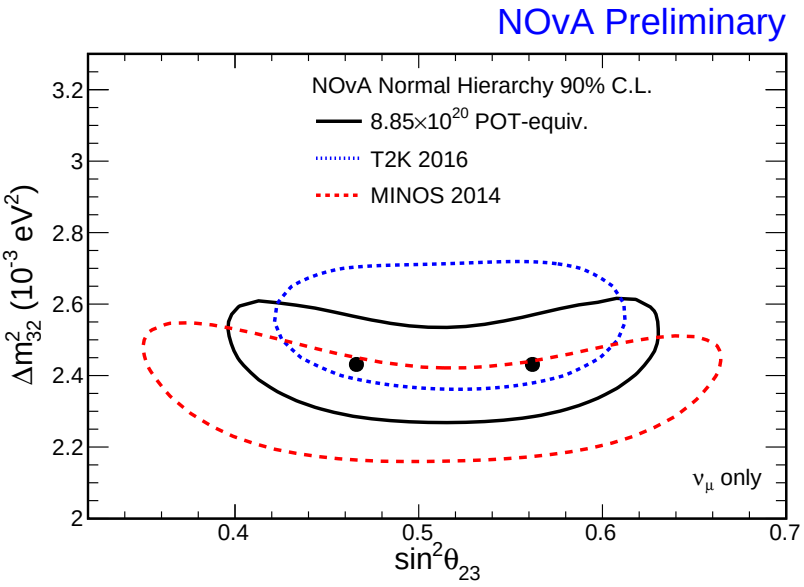

Figure 6.14: Sensitivity contours showing 90% confidence levels for the NOvA disappearance analysis result with systematics and overlayed with T2K 2016 and MINOS 2014 results for comparison. Maximal mixing rejection is 0.47σ and best fit value is at $\Delta m^2_{32} = 2.431^{+0.079}_{-0.070} \times 10^{-3}$ eV^2 and $\sin^2\theta_{23} = 0.466$ or 0.562 $(0.428 - 0.598)$.

CHAPTER 7. UNCONTAINED EVENTS AND THE KAON PRODUCTION MEASUREMENT

Precise knowledge of the neutrino flux, produced by the decay of pions and kaons during proton collisions in the NuMI target, is required for long-baseline neutrino experiments. In NOvA, the flux is used to measure neutrino cross sections at the Near Detector, whereas at the Far Detector it provides an estimate of the expected number of events for oscillation analysis. Understanding the kaon component of the NuMI beam is key for accurately predicting the NOvA neutrino flux. In addition to decay into muon neutrinos, kaons also decay into high energy electron neutrinos, which form a major background for the ν_e appearance measurement in NOvA (see Figure 7.1).

As shown in the previous chapter, NOvA has used only events with an interaction vertex and all secondary particles fully contained in the detectors. We found that the kaon component of the NuMI beam can be studied using high energy Far Detector uncontained ν_μCC neutrino interactions. This chapter is devoted to present and explain the measurement of the kaon production normalization using uncontained events in the 10-20 GeV energy range at the Far Detector. In particular, we will discuss the custom event selection based on the event topology with $\nu_\mu + X \rightarrow \mu + X'$, where the muon is uncontained but the hadronic system is contained. We will show how multivariate techniques (such as boosted decision trees) were used to develop a cosmic rejection classifier and a muon energy estimator using regression for these type of events.

7.1 Cosmic rejection tuning

As discussed in Section 6.2.4, because the Far Detector is on the surface and the cosmic rate is about 140 kHz, we would expect ~ 1.4 cosmics/spill. In order to reduce such amount of background, all previous analysis have used neutrino events that are contained, meaning all the final state particles

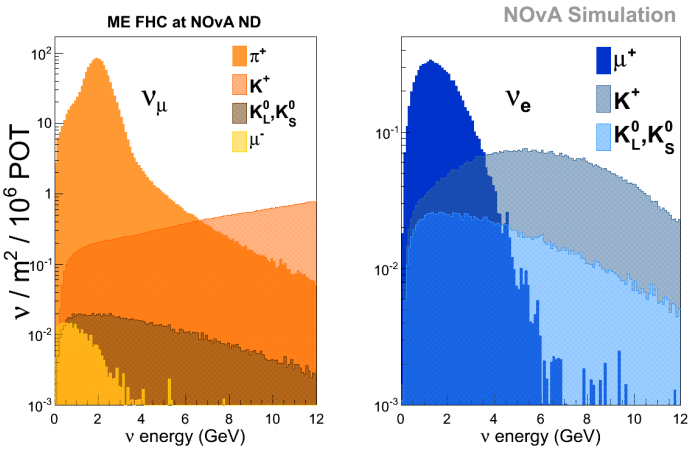

Figure 7.1: Distribution of parent particles of ν_μ (left) and ν_e (right) for the forward horn current mode in the NOvA Near Detector. Neutrinos coming from kaons become a significant component at higher energies.

are within the boundaries of the PVC detector. Our goal is to look now at the sample of events that have the muon-like particle in the final state leaving the detector, but having the hadronic component and the vertex contained. We call this specific set of events the **uncontained sample**. Figure 7.2 shows the neutrino energy distribution of events failing containment when compared with other samples not currently used for analysis. We noted that this sample contains a well defined, broader high energy peak at around 13 GeV and that its shape does not change much when requiring a muon-like particle in the final state. The situation becomes extremely challenging when trying to separate an uncontained muon from a neutrino interaction from a stopping muon of cosmogenic origin in the Far Detector. Therefore, in order to explore in more detail this sample, a tuned cosmic rejection discriminator, in the form of a boosted decision tree classifier (BDT) has been developed, inspired by previous works on this subject [41].

The training and testing of the cosmic rejection classifier used Far Detector NuMI GENIE simulation files with cosmic ray induced muons overlaid with the neutrino interactions as signal files, whereas actual data files from cosmic-ray induced muons were used as background input. Our first step was to process all the cosmic data available at the time, in order to gain enough statistics.

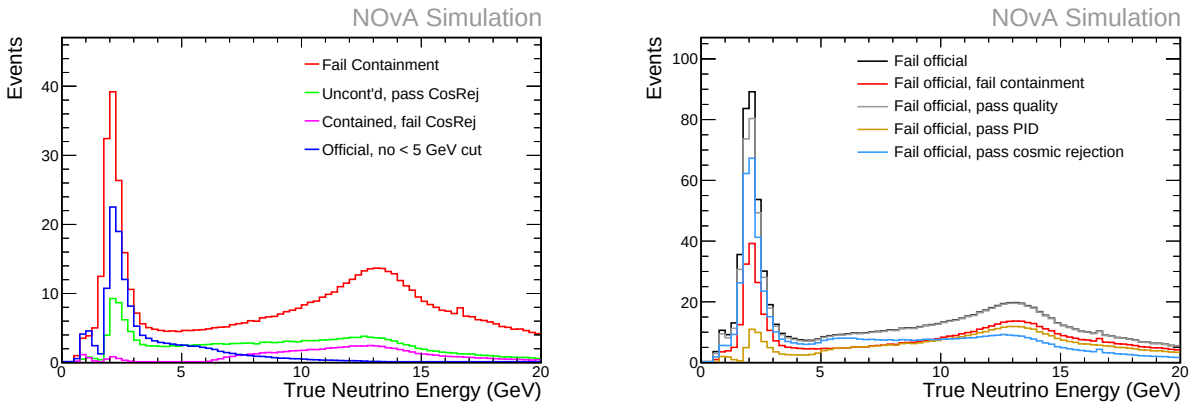

Figure 7.2: True neutrino energy spectrum for events not used in analysis at the Far Detector in the range 0-20 GeV. The solid red distribution shows events that have failed the official disappearance analysis selection because they have failed containment. Left: comparison of the uncontained sample (red) with other samples. The light green shows the distribution of events failing containment but pass all the other criteria, including cosmic rejection tuned for contained events. The magenta distribution shows events that have passed all the other official selection criteria except cosmic rejection. The solid blue is the distribution of events that are contained when looking at $E_\nu > 5$ GeV range. Right: comparison of the uncontained sample (red) with complementary samples. We can infer that if we combine uncontained events with events that have a muon in the final state (dark yellow), its number in the oscillation region $(0 - 5$ GeV) will be decreased, but the high energy tail remains mostly unchanged.

But due to the nature of our uncontained sample, file size will become an issue since containment selection removes nearly 98% of cosmic events and large files are not optimal when training/testing. Therefore, a quick study on preselection was performed [151] in order to look for a few set of variables that help remove cosmic events without compromising our signal. This preselection consists in selecting well behaved and properly reconstructed Far Detector events that have failed the current official ν_μ-analysis criteria by failing the ν_μ-analysis contained selection (in order to potentially recover them), that have passed a basic quality selector (which establishes the minimal required for well-reconstructed events), and that have a reconstructed muon-like particle in the final state. This sets the stage for a tuned cosmic rejection.

7.1.1 Boosted decision tree: training and testing

A decision tree is a set of questions organized in hierarchical manner and represented graphically as a tree, which is a collection of nodes and edges [62]. It has been shown that by combining ensembles of weak learners (or models) with low correlation among them, it is possible to produce a stronger one with greater accuracy and generalization power. By combining the ideas of decision trees and ensemble methods resulted in decision forests, that is, the ensembles of randomly trained decision trees.

In the boosting algorithm [77], iterative re-weighting of training data can be used to build strong classifiers as linear combination of many weak ones. In particular, the adaptive boosting (AdaBoost) penalizes a correctly classified event but enhances the weight of a misclassified event using an exponential form.

The cosmic rejection problem for uncontained events is a classification problem: given an event that has passed our basic preselection, we want to know if it is a signal (charged current ν_μ) event originated from a neutrino interaction or if it is a background (cosmic-ray induced) event. We will

use the method of boosted decision trees implemented in the ROOT Toolkit for Multivariate Data Analysis (TMVA) framework[1] to develop a classifier that help us answer those questions.

7.1.1.1 Input variables

A set of eleven input variables gave the best overall performance when tested on uncontained Far Detector events. Such variables were inspired by the topology of the events and by previous results. Below is a description of each of them and its purpose:

- **anglekal:** this variable was inspired by the quasielastic energy formula and is the cosine of the angle between the reconstructed muon-like kalman track and the incoming beam direction,
- **kaldiry:** the Y-axis component of the cosine direction of the reconstructed muon-like kalman track, used due to its discrimination power during the test phase,
- **tracklen:** track length (in cm) of the reconstructed muon-like kalman track; without it classifier performance is substantially damaged,
- **nhitcos/nhit:** ratio of the number of hits from the reconstructed cosmic track and the total number of hits from the interaction (slice); a truly cosmic-ray induced interaction should have this ratio close to one,
- **max(vty,endy):** maximum position value (in cm) between the Y-axis projection of the starting point of the reconstructed muon-like kalman track and its end Y-axis projection; discriminates between incoming cosmic-ray induced muons from the top of the detector,
- **cvncosmic:** Convolutional Visual Network (CVN) particle identifier (PID) output for cosmic-like events; state of the art PID, discriminates between cosmic and non-cosmic-like events,
- **hadEPerNHit:** ratio between the hadronic calorimetric energy and the number of hits in the hadronic system; for cosmic-like events, a low hadronic activity is expected, so the ratio should tend to zero,

[1] Visit https://root.cern.ch/tmva

- **slcCalEPerNHit:** ratio between the calorimetric energy in the slice and the number of hits in the slice; similar philosophy as above,
- **trkEPerNHit:** ratio between the calorimetric energy in the reconstructed muon-like kalman track and the number of hits of such track; similar philosophy as above,
- **vetoangl:** product between the absolute value of the cosine of the reconstructed muon-like kalman track vs NuMI beam times the Y-axis projection of the track direction plus one,
- **scatt/tracklen:** the scattering angle of the reconstructed muon-like kalman track (cumulative sum of angular changes, in degrees) normalized by the track length; experimental use based in overall performance

The distributions of the input variables are shown in Fig. 7.3 and Fig. 7.4. Both signal and background distributions are normalized according to the scale factor:

$$\text{scale} = \frac{1}{N \cdot dx}, \tag{7.1}$$

where N is the sum of weights or the total sum of all the content in each bin of the distribution (integral) whereas dx is the optimal width given by

$$dx = \frac{\text{Max. value in axis range} - \text{Min. value in axis range}}{\text{Number of bins in histogram}}. \tag{7.2}$$

Some benchmark quantities give some guidance when assessing the performance of a given set of inputs for a given classifier algorithm. For example, the separation $\langle S^2 \rangle$ of a classifier y, defined by the integral [2] of

$$\langle S^2 \rangle = \frac{1}{2} \int dy \frac{(\hat{y}_S(y) - \hat{y}_B(y))^2}{\hat{y}_S(y) + \hat{y}_B(y)}$$

where $\hat{y}_S$ and $\hat{y}_B$ are the signal and background probability density function (PDF) of y, respectively. The separation is zero $\langle S^2 \rangle = 0$ for identical signal and background shapes, and $\langle S^2 \rangle = 1$ for shapes with no overlap.

[2] TMVA User's guide http://tmva.sourceforge.net/docu/TMVAUsersGuide.pdf

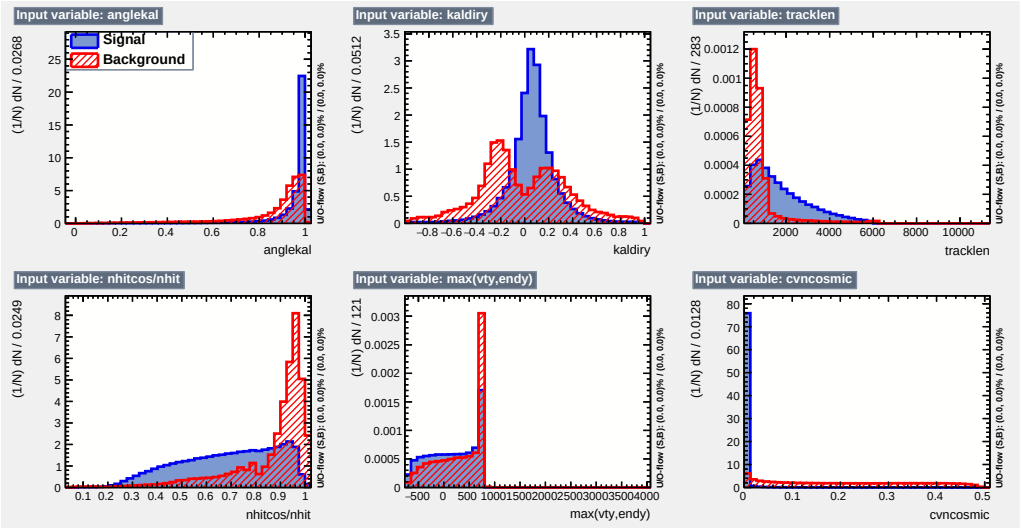

Figure 7.3: First set of input variables for the tuned cosmic rejection PID for uncontained events: `anglekal`, `kaldiry`, `tracklen`, `nhitcos/nhit`, `max(vty,endy)`, `cvncosmic`.

Table 7.1 summarizes the separation value (shown in percentage) for the input variables of the tuned cosmic rejection classifier for uncontained events.

For the specific case of a BDT, the TMVA framework provides a ranking of the variables after training and testing. The method is described as a combination of counting how often such variables are used to split decision tree nodes, and similarly, by weighting each split occurrence by the separation gain-squared it has achieved and by the number of events in the node. Table 7.2 shows the ranking by importance (in percentage) of the input variables for the cosmic rejection of the classifier for uncontained events.

After training and testing, the TMVA framework gives the linear correlation coefficients (shown also in percentage) among the input classifier variables for both signal and background. For example, the top of Fig. 7.5 shows the 11×11 matrix where the lighter color represent the value of positive correlation whereas darker colors represent a negative correlation. From there we can clearly observe a cluster of correlation among the hadronic, slice, and track energy per hit variables at the upper left, that is explained by the own nature of their definition but necessary for the sake of overall performance. A similar trend is observed in the bottom of Fig. 7.5.

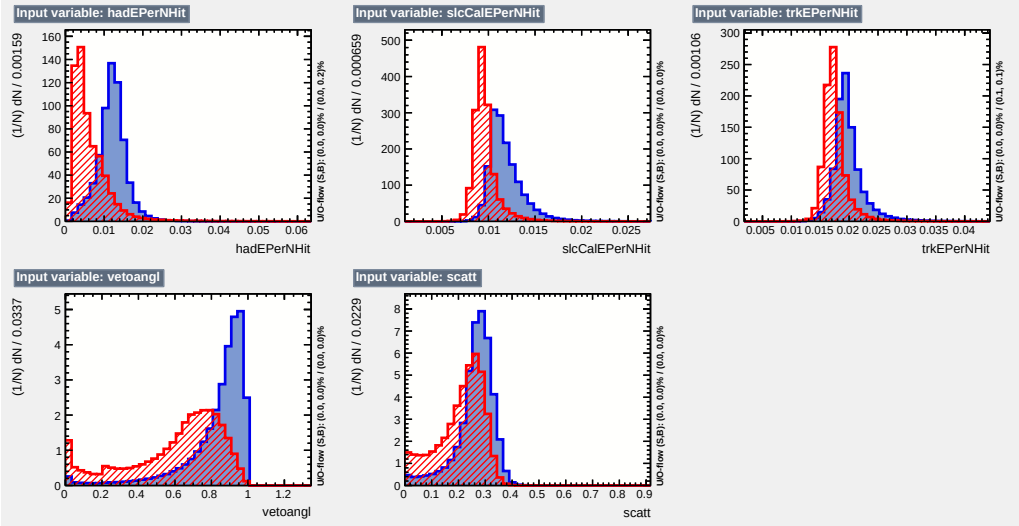

Figure 7.4: Second set of input variables for the tuned cosmic rejection PID for uncontained events: `hadEPerNHit, slcCalEPerNHit, trkEPerNHit,vetoangl, scatt/tracklen`.

7.1.2 Performance

Given the input variables described in earlier sections, a BDT with 700 trees and adaptive boosting (AdaBoost) was implemented over more than 7 million events (slices), including signal and background (see Table 7.3).

The results after the training/testing phase of the tuned CosRej classifier and the type of events selected are shown in Fig. 7.6. The data points in the top image represent the output distribution during the training phase whereas the color-filled histogram shows the output of the testing sample. The fact that both distributions are superimposed indicates that there is no substantial sign of over-training. The author believes the values for the Kolmogorov-Smirnov test [3] for signal (0.793) and background (0.784) probabilities can be improved but that is left for future studies. Bottom image of Figure 7.6 shows the result of the PID classifier divided by interaction type from simulation. The red arrow indicates events are selected to the right of the optimal cut value. As expected, at higher neutrino energies, most selected events will be produced from deep-inleastic (DIS) and baryonic resonant (RES) interactions.

[3] Statistical test of compatibility in shape between two distributions

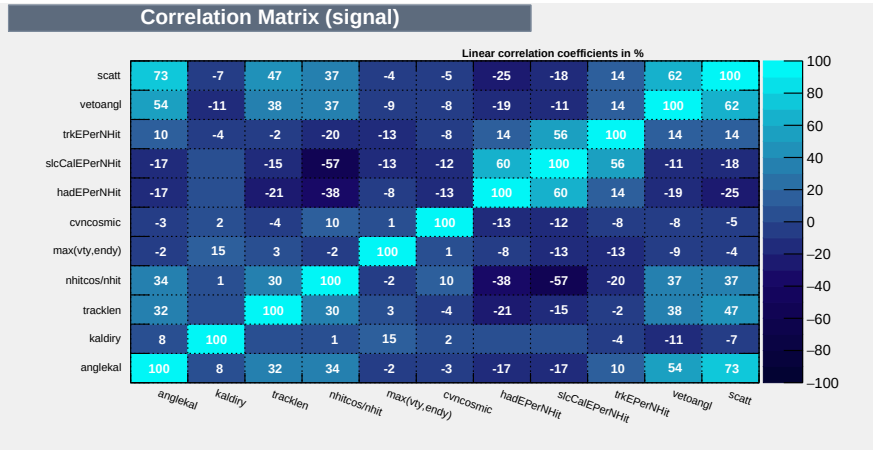

(a)

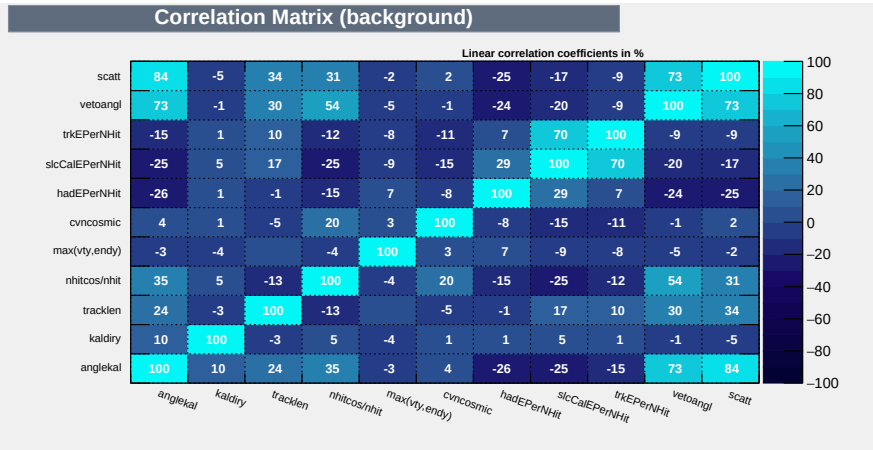

(b)

Figure 7.5: Correlation among input variables in the case of signal events (a) and background events (b). Empty values refer to correlation of the order of 0.

Table 7.1: Ranking of variable separation for our BDT classifier.

Rank	Variable name	Separation (%)
1	`cvncosmic`	79.73
2	`slcCalEPerNHit`	48.86
3	`hadEPerNHit`	44.57
4	`vetoangl`	29.92
5	`trkEPerNHit`	29.87
6	`tracklen`	28.46
7	`nhitcos/nhit`	27.06
8	`kaldiry`	23.70
9	`anglekal`	22.68
10	`scatt/tracklen`	12.20
11	`max(vty,endy)`	3.77

Finally, efficiency performance is shown in Fig. 7.7. Given the values used for testing in Table 7.3 the figure of merit (FOM) is computed using the expression $s/\sqrt{s+b}$, focusing on reducing the amount of cosmic ray induced muons classified as signal. The optimal cut for the cosmic rejection classifier is set where the maximal FOM is computed, that is, at **0.5184** that translates in a signal efficiency of roughly 96%.

7.2 Event selection

The next step after tuning the cosmic rejection was to construct a selection criteria that filters out the background and selects well-reconstructed signal events with the interaction vertex within an optimal fiducial volume, the hadronic component contained and the final state muon leaving boundaries of the Far Detector.

7.2.1 Fiducial selection

From the subset of events that have passed the optimal cut of the tuned cosmic rejection, we focused on the distributions for the interaction vertex in the three spatial coordinates. For a

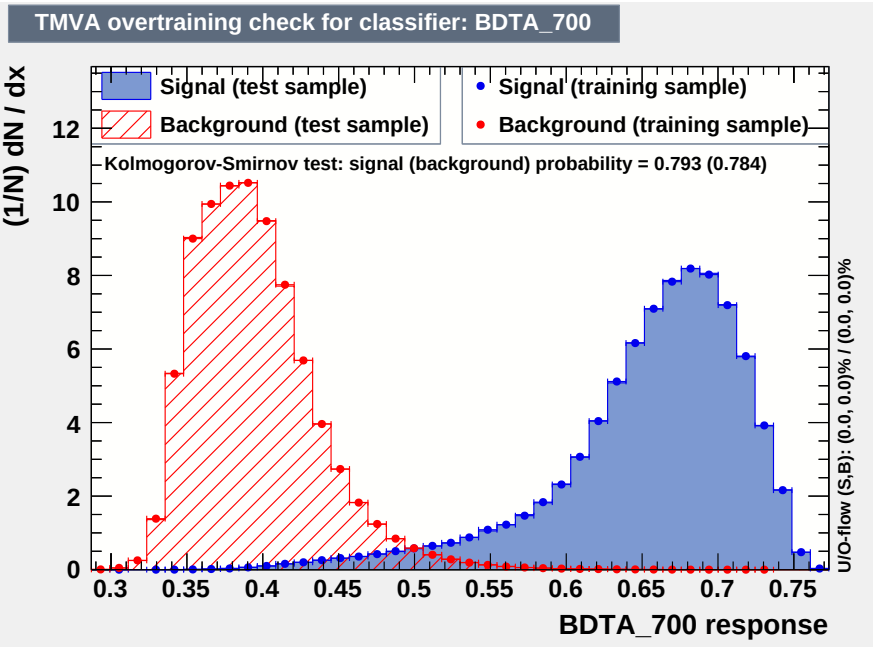

(a)

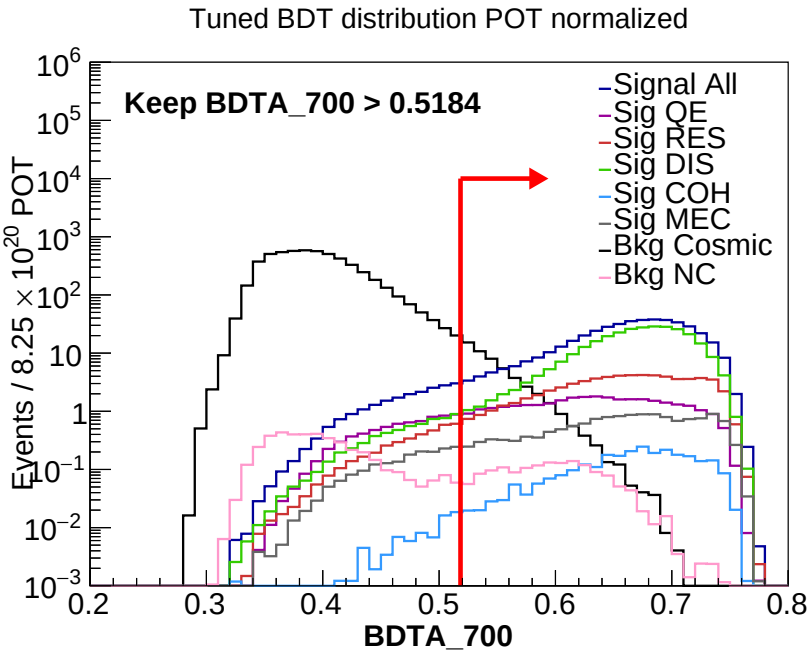

(b)

Figure 7.6: (a) Distribution of the cosmic rejection classifier area normalized. (b) Distribution of the cosmic rejection classifier normalized by POT.

Table 7.2: Ranking of variable importance for our BDT classifier.

Rank	Variable name	Importance (%)
1	`cvncosmic`	18.75
2	`max(vty,endy)`	15.79
3	`tracklen`	11.00
4	`kaldiry`	8.60
5	`hadEPerNHit`	8.07
6	`vetoangl`	7.95
7	`nhitcos/nhit`	7.67
8	`anglekal`	6.44
9	`slcCalEPerNHit`	5.96
10	`trkEPerNHit`	5.49
11	`scatt/tracklen`	4.25

Table 7.3: Description of the sample of raw events used for training and testing. These numbers have neither POT normalization nor oscillation probabilities applied.

	Signal	Background	Total
Training	639 430	1 368 317	2 007 747
Testing	639 430	1 368 317	2 007 747
Total	1 278 860	2 736 634	4 015 494

charged-current muon neutrino interaction, the vertex is defined at the starting point of the muon-like reconstructed track, with some hadronic activity attached in the neighbor cells. One would expect that such neutrino interactions occur inside the boundaries of the detector, therefore any indication of a reconstructed vertex at these boundaries or outside, will be inferred as non-physical and rejected. An example of this situation is shown in Fig. 7.8, where a long muon-like track has its vertex right at the corner in the side view, and traveling all the way in crossing the entire detector. The problem with this event is that we do not know how much energy hadronic energy was deposited outside the detector. In addition, we do not know how long the reconstructed track is. The solution is to apply an optimal fiducial cut that deals with this sort of topologies.

Table 7.4: Efficiency values for the tuned cosmic rejection classifier based on BDT with 700 trees and AdaBoost. Raw numbers with neither POT nor oscillation probability applied.

	Optimal cut	FOM	NSig	NBkg	EffSig	EffBkg
BDTA_700	0.5184	772.347	610 895	14 721	0.9554	0.01076

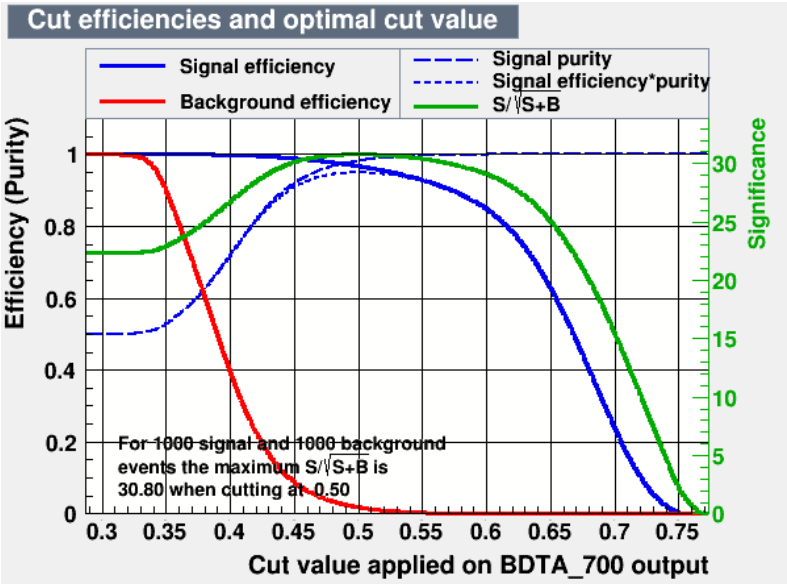

Figure 7.7: Performance of the cosmic rejection classifier.

Figure 7.9 shows the distributions of the vertex of the neutrino interactions after passing cosmic selection for different metrics. On the left column, we present the area normalized distributions for each coordinate. As expected, most of the events occur near the edges. The central column shows the efficiency of the cosmic rejection cut versus each coordinate. The efficiency is defined as the ratio between all the events being signal (background) and passing the cosmic rejection optimal cut, divided by all the events left (that is, the union of the events passing the BDT cut and the events that fail the BDT cut),

$$\text{Efficiency(signal)} = \frac{\text{Signal AND passes BDT cut}}{\text{Total events left}},$$

and in similar way for background. This metric shows a remarkable drop around the values of vertex x,y-axis positions $(-800, 800)$ and for vertex z-axis position $(0, 6000)$, clearly indicating detector

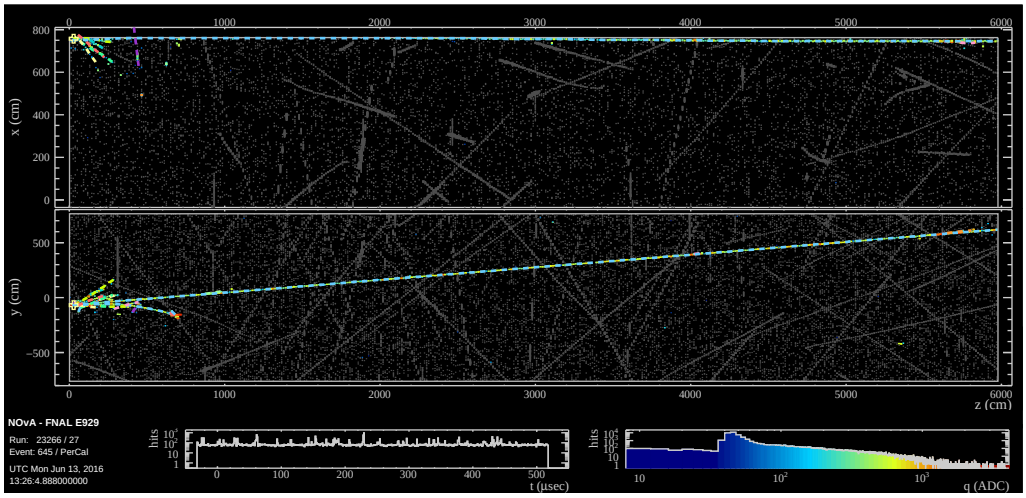

Figure 7.8: Run 23266, subrun 27, event 645, slice 48 from simulation. Vertex (indicated by a cross) and muon-like track close to detector edges.

edges. Flat behavior indicate invariance along the coordinate. There seems to be an excess of interactions in the lower part of the detector, as indicated by the middle-central figure. The drops within the middle of the detector shown by the middle-bottom figure (Vertex Z position) show partial detector configurations applied (e.g. the final diblock is different or less than the 14th diblock).

Finally, the right column shows the purity of the cosmic rejection versus interaction coordinate. This metric is defined as

$$\text{Purity(signal)} = \frac{\text{Signal AND passes BDT cut}}{\text{Signal}},$$

and in similar fashion for the background. We expect most of the time the signal events get selected by the cosmic rejection criteria. Once again, the drops indicate detector boundaries.

The method for finding the optimal vertex fiducial volume for uncontained events used the distributions showed before as a starting point in addition to an iterative method that maximizes the figure of merit (FOM) given by $s/\sqrt{s+b}$. By keeping parallel sides of a two-dimensional box fixed, while leaving the others as parameters, we loop over cell-size incremental steps and set the limits where FOM reached the largest value. Once the parameter sides were found optimal, they become

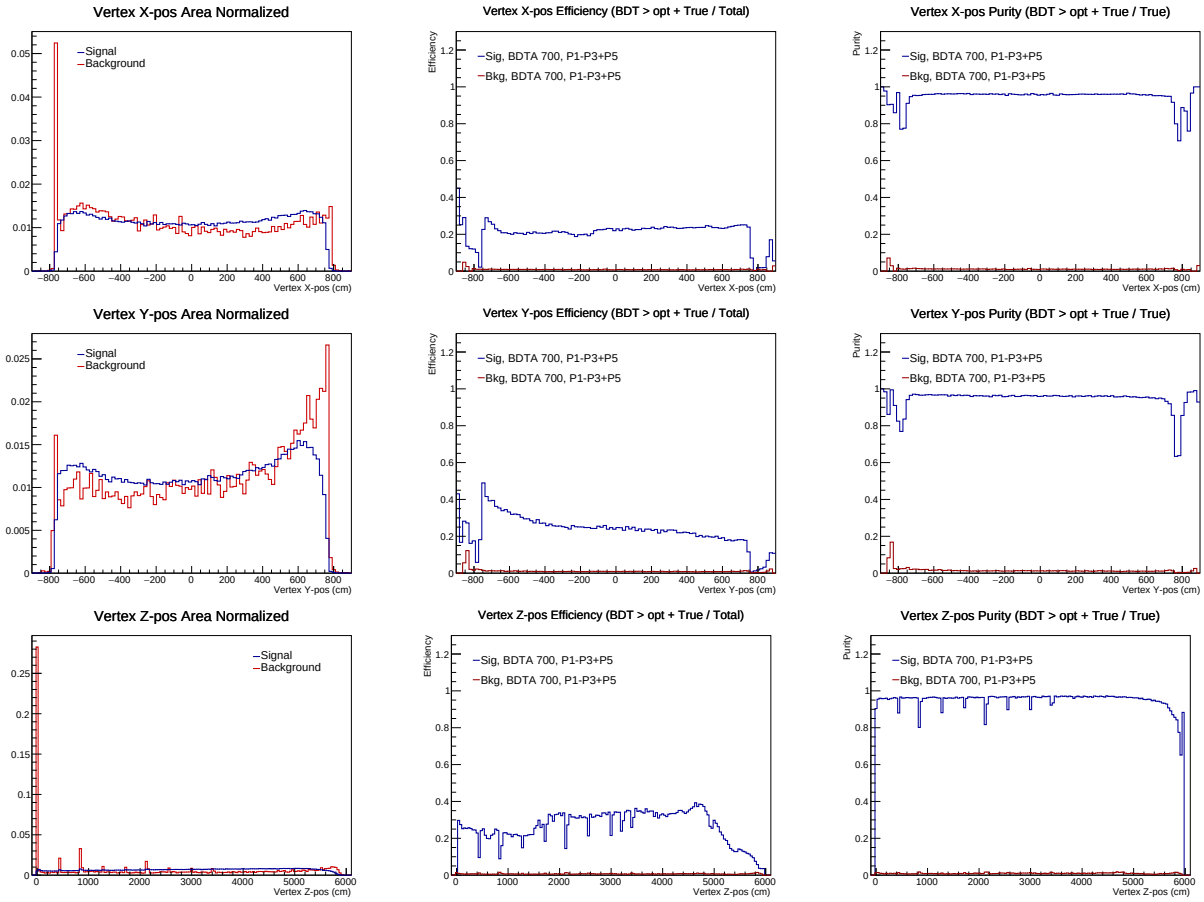

Figure 7.9: Distributions of the vertex position projected on each coordinates for signal (blue) and background (red) for selected events (left side); efficiency of vertex position spectrum for selected events (center); purity of vertex for selected events (right).

fixed and moved to the next orthogonal dimension. In the end, the optimal vertex fiducial values were set as the ones indicated by Table 7.5. For comparison, the position of the detector edges are shown.

Table 7.5: Selection criteria for the vertex of the uncontained interaction based on fiducial optimization. Numbers in centimeters.

Fiducial cut (cm)	Detector edges (cm)
$12 <$ Vertex Z-pos < 5400	$(0, 5977.60)$
$-720 <$ Vertex Y-pos < 650	$(-761.50, 763.50)$
$\lvert$Vertex X-pos$\rvert < 700$	$(-761.60, 762.60)$

Values of vertex z-axis position > 12 cm prevent rock-induced muons to be classified as signal, whereas vertex z-axis position < 5400 cm comes from the fact that a 1 GeV muon will have an average track length of approximately 500 cm in the detector (assuming $dE/dx \sim 2$ MeV/cm). Therefore, this average quantity is subtracted from the detector edge. Values of vertex x-axis position $< \pm 700$ cm resemble the features discussed earlier by looking at Fig. 7.9 where we noted a high activity on the edges of the detector.

7.2.2 Track end point quality selection and exiting muon

A critical metric that was needed to monitor was the behavior of the end point of the muon-like track for selected uncontained interactions. When visually scanning simulation selected events, it was found that a small but non-zero number of events had very large reconstructed track lengths, not congruent with the expected detector sizes but with reconstruction issues (e.g. see Fig. 7.10).

In addition, the Kalman-filter inspired algorithm that reconstructs the 3D tracks, is known to match 2D tracks in each view with points that not necessarily are within the detector in one of these views (see Fig. 7.11). This features motivated the need for a track end point quality selection. Its purpose is to eliminate ill-reconstructed muon-like tracks from selected events that exit the

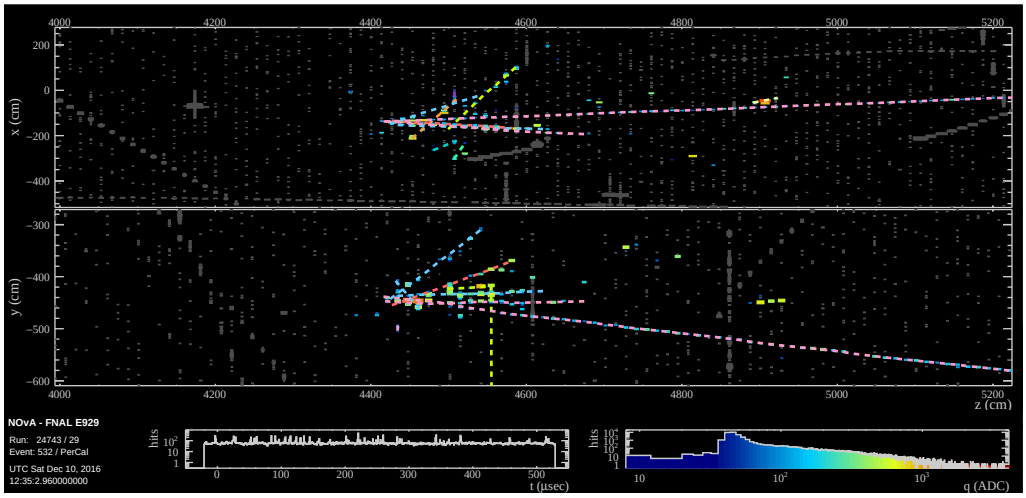

Figure 7.10: Run 24743, subrun 29, event 532, slice 31 from simulation. Yellow muon-like track greater than 60 meters, the length of the Far Detector.

detector. Following the philosophy of the previous section, the left column of Fig. 7.12 shows the area normalized distributions of the track end points for each spatial coordinate. Naturally, the majority of the selected events have their end points at the neighborhood of the detector edges.

The middle column shows the efficiency of the selection, defined as

$$\text{Efficiency(signal)} = \frac{\text{Signal AND passes BDT cut AND Fiducial}}{\text{Total events left}},$$

where the in addition to passing the cosmic rejection selection and being a signal, the events also have to pass the vertex fiducial cut, while the denominator remains the same. This metric shows slightly more events in the negative values of the End X-position (more towards the center of the NuMI beam), more events in the positive values of End Y-position (top of the detector) and almost none in the first 10 meters upstream of the detector in the z-coordinate. The purity of the selection is also slightly modified after the inclusion of the vertex fiducial

$$\text{Purity(signal)} = \frac{\text{Signal AND passes BDT cut AND Fiducial}}{\text{Signal}},$$

where we can appreciate an almost symmetric distribution for the x-coordinate, a deep region at the bottom of the detector in the y-coordinate and a drop downstream for high values in the z-coordinates.

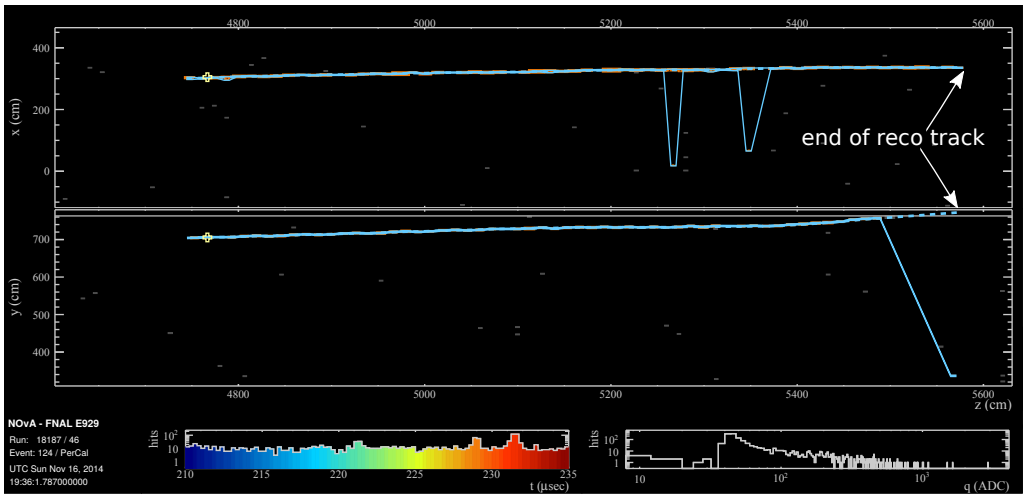

Figure 7.11: Run 18187, subrun 46, event 124, slice 29 from cosmic simulation. Reconstructed track (dashed-blue) is matched outside boundaries of detector.

The optimal track end point quality values are described in Table 7.6 where for both perpendicular coordinates to the beam (X,Y) the end points are taken outside the detector edges just enough so the overall signal does not get substantially diminished. For the z-coordinate, the minimal end point is taken such that a 2 GeV muon starting at the second plane travels its expected length and its maximal point when exits the last plane in the detector. And to enforce the absence of ill-reconstructed tracks that have lengths beyond detector-comparable sizes, a requirement in the reconstructed track length is also included.

Table 7.6: Track end point quality selection summary describing the values that define the selection. Numbers in centimeters.

Cut (cm)
Track length < 6500
End X-pos > -800
End X-pos < 775
$\lvert$End Y-pos$\rvert < 800$
End Z-pos > 1000
End Z-pos < 6500

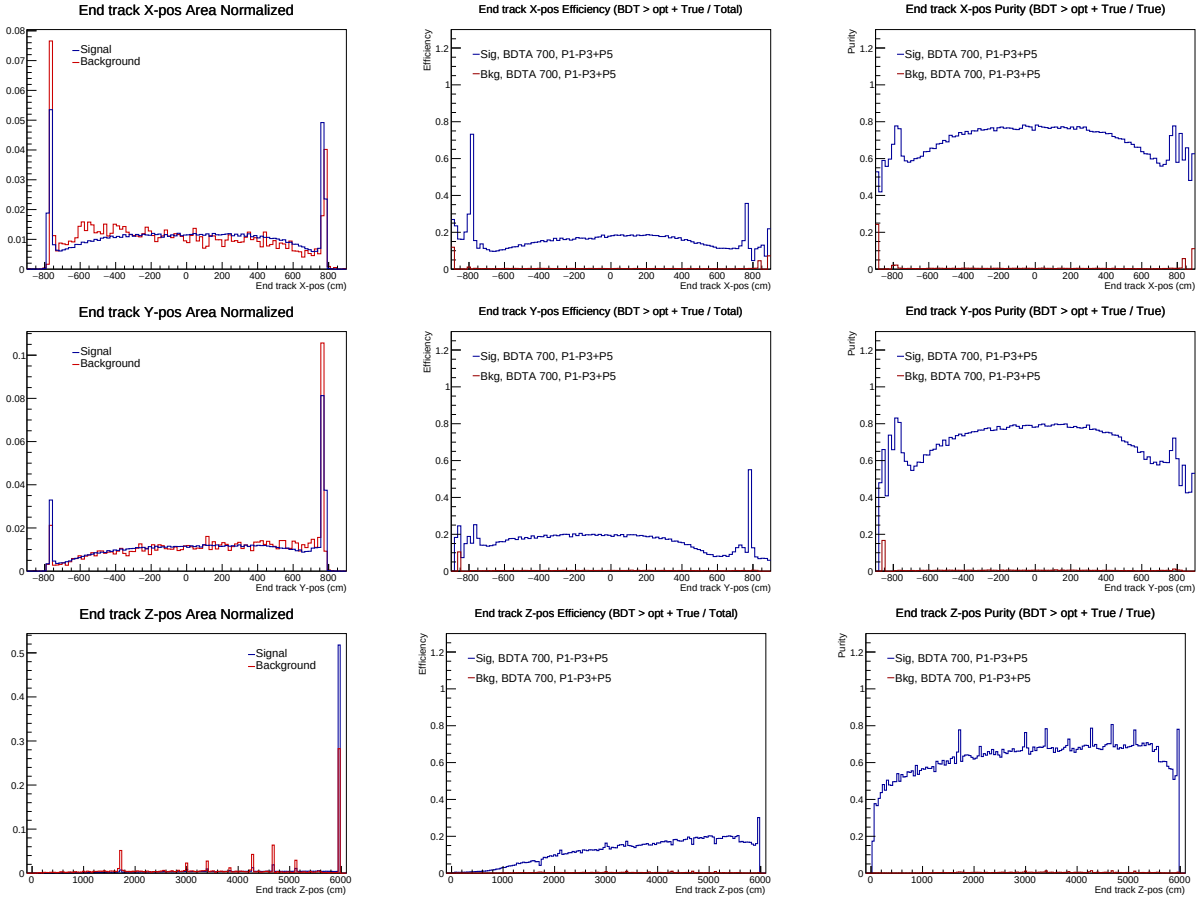

Figure 7.12: Distributions of the vertex position projected on each coordinates for signal (blue) and background (red) for selected events (left side); efficiency of vertex position spectrum for selected events (center); purity of vertex for selected events (right).

The official containment selection cut used for the main NOvA disappearance analysis is defined using reconstructed objects and metrics not necessarily associated to the end point of the final state muon. Therefore, events that have failed this cut are not guaranteed to have the main muon track exiting the detector. In order to ensure the main hypothesis of this sample of ν_μ CC events, we added a selection cut that requires the muon to "touch" the vicinity edges of detector, and those values are listed in Table 7.7.

Table 7.7: Exiting muon selection table. Numbers in centimeters.

Cut (cm)	Detector edges (cm)
End Z-pos $>$ 5961	5977.60
End X-pos $<$ -753	-761.60
End X-pos $>$ 760	762.60
End Y-pos $<$ -753	-761.50
End Y-pos $>$ 755	763.05

With the vertex and muon-like track under control for our sample of events, the next part to investigate is the hadronic system and guarantee that is within reasonable distance from the detector edges. The following section describes the requirements of the hadronic containment part for uncontained interactions.

7.2.3 Hadronic containment selection

We recall that a slice is simply a collection of hits correlated in time and space. Each slice corresponds to a single neutrino interaction in the vast majority of cases. All the hits that are in the slice and are not associated with the main muon-like reconstructed track are considered the hadronic cluster of hits. The containment of the hadronic cluster of hits within the boundaries of the detector is the main goal of the hadronic containment selection. After passing cosmic rejection and vertex fiducial with track end point quality selections applied, distributions of area normalized hadronic cluster variables are shown in Fig. 7.13. We can notice that the fraction of background events has been reduced significantly. The top row shows the distribution of most upstream plane

of a hit in the hadronic cluster system (first plane), the distribution of most downstream plane a hit has in the hadronic system (last plane) and total number of continuous planes the hadronic system took, which is a proxy for how shower-like the event was. The middle row shows the distribution of the number of calibrated hadronic hits in the interaction, the distribution of the minimum projected number of cells to a given edge for hits in the hadronic cluster, and the distribution of the total hadronic calorimetric energy of the cluster. The bottom row shows the mean position of the hadronic cluster for each of the coordinates. As expected, there is no information outside the detector edges. These distributions were the metrics that showed potential application in helping the construction of the hadronic containment selection.

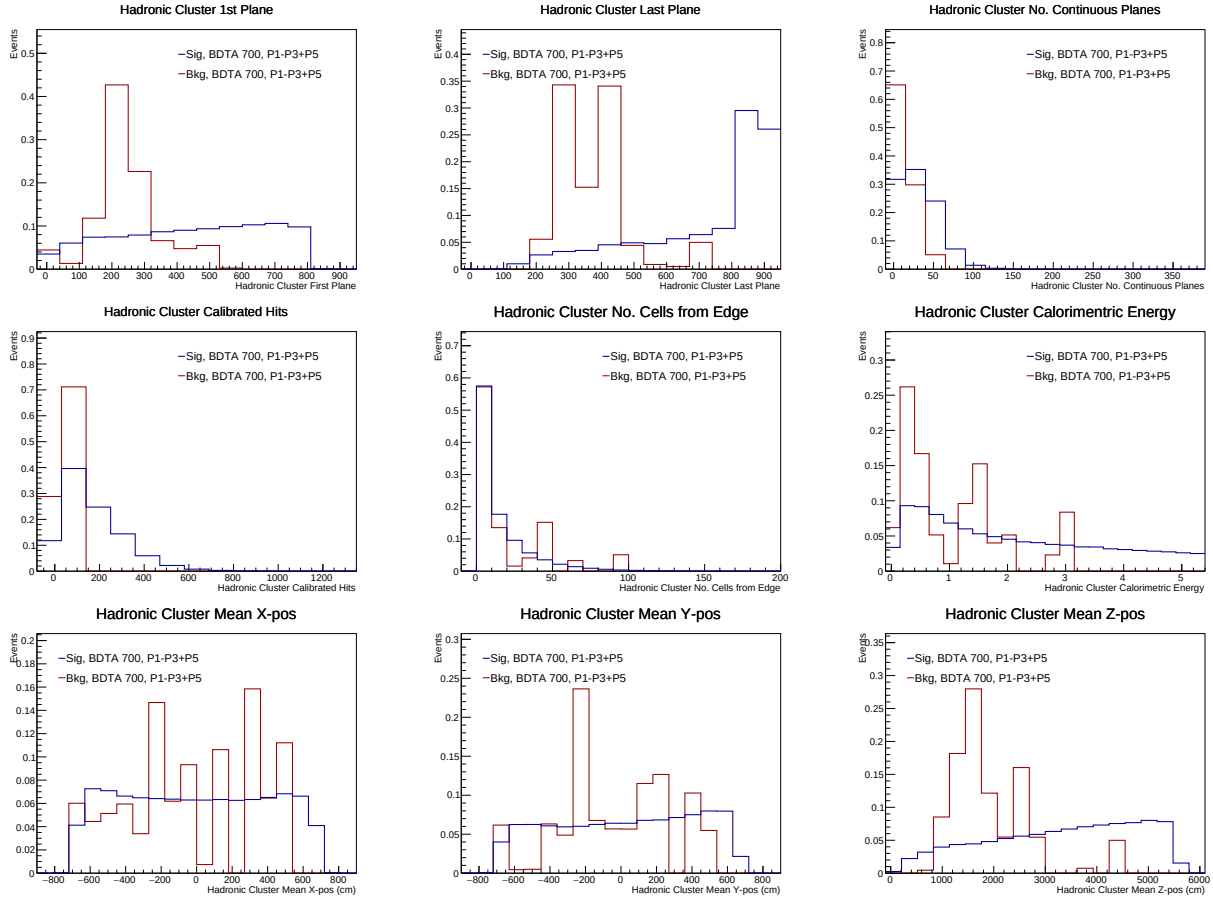

Figure 7.13: Area normalized distributions of supplementary hadronic variables for signal (blue) and background (red) for selected events.

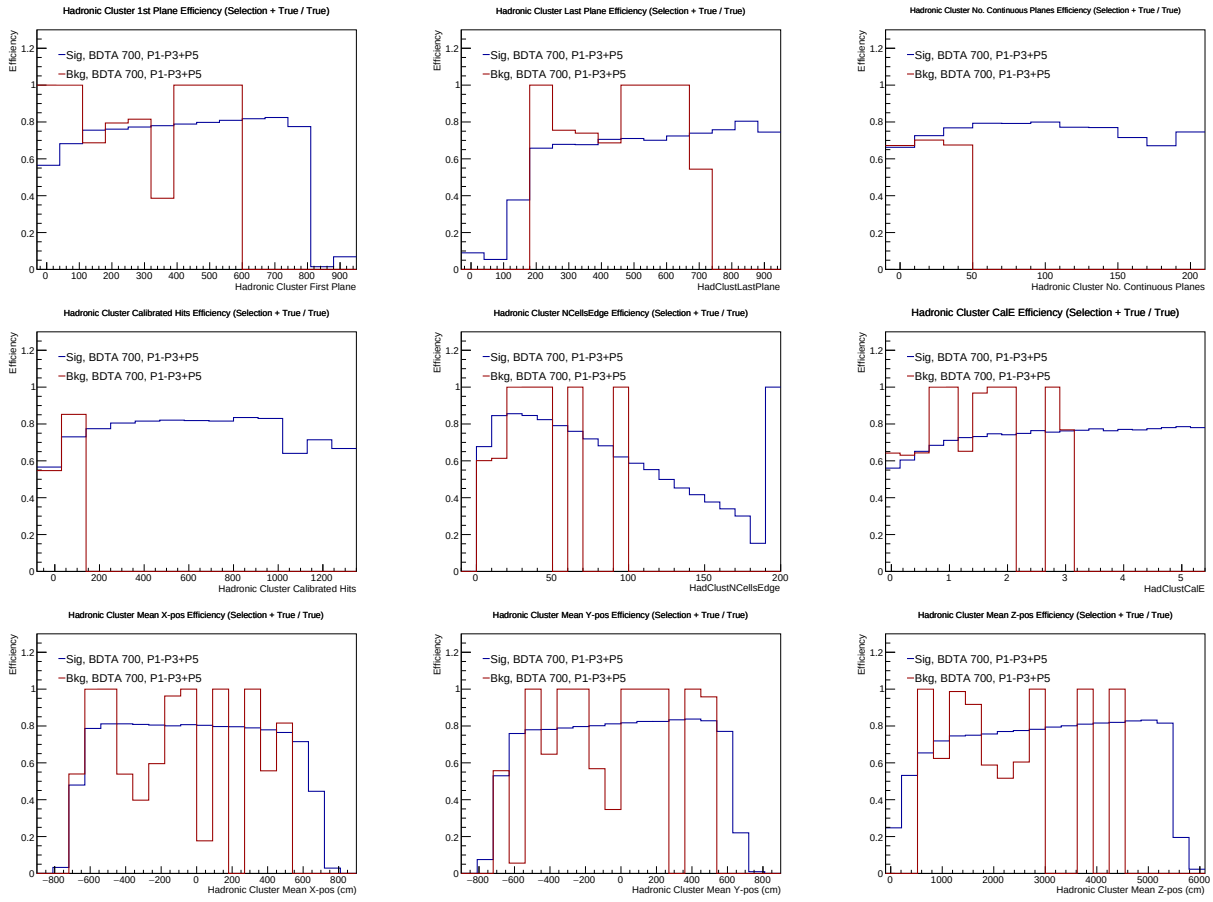

Figure 7.14: Efficiency distributions of supplementary variables for signal (blue) and background (red) for selected events.

In addition to the area normalized distributions, we looked at the efficiency of the same distributions for the selected events. This metric is defined as the ratio:

$$\text{Efficiency(signal)} = \frac{\text{Signal AND passes BDT cut AND Fiducial AND RecoQual}}{\text{Signal AND passes BDT cut AND RecoQual}},$$

where RecoQual refers to a well defined reconstructed end of track and to enforce a well reconstructed 3D hadronic cluster of hits, and Fiducial refers to vertex fiducial selection. Similarly for the background (combined neutral current and cosmic) as shown in Fig. 7.14. Although there is not clearly signal/background discrimination power in the latter set of distributions, they were used to draw quantitative values in the hadronic containment selection. We already know that no hit from the hadronic system should touch the edges of the detector, therefore we apply a restriction in the mean position for each coordinate. Also we know that a 2 GeV neutrino will not produce a hadronic cluster with more than (1000 cm / 4 cm/hit) 250 hits, and will not propagate through the entire of the planes in the detector. The proposed numbers for this selection are shown in Table 7.8.

Table 7.8: Hadronic containment selection table.

Variable name	Value
|Hadronic mean X pos.|	< 700
Hadronic mean Y pos.	$(-720$ to $650)$
Hadronic mean Z pos.	(16 to 5500)
Hadronic first plane	(2 to 800)
Hadronic last plane	(2 to 896)
Hadronic # cont. planes	(1 to 170)
# hadronic cells to edge	> 0
Hadronic # calib. hits	< 320
Hadronic calorimetric energy	> 0

As a final note, we decided to add two more constraints to the definition of the cosmic rejection, in order to guarantee the quality of the selected events. Adding a restriction on the angle between the muon-like track and the incoming neutrino beam will prevent vertical tracks to be considered part of a neutrino interaction. This is because vertical tracks are associated to cosmic ray-induced muons. Additionally, a restriction in the number of hits in the slice will prevent very high energy

events possibly associated with cosmic rays striking the top of the detector, or even interactions very close in time such that get sliced together (piled-up events). Table 7.9 shows the proposed cuts for the cosmic rejection selection for uncontained events.

Table 7.9: Cosmic rejection table.

Cut
BDTA_700 $>$ 0.5184
NHitsSlc (20 to 1200)
AngleKal $>$ 0.6

In the next section we will discuss the overall performance of our selection.

7.3 Event cut flow and preliminary performance

The question of how many uncontained neutrino interactions do we expect at the Far Detector using the set of selection cuts described in the previous sections is addressed in Table 7.10. Data comes from processing NuMI beam simulation files and each row represents a cumulative selection, progressing from top to bottom. We can see that the cosmic background, predicted using out of beam spill events, is reduced seven orders of magnitude, but the expected signal is almost 29 times this background. From the total of events, only 11% have failed the official disappearance analysis containment cut, or from the total of events passing the particle identifier, only 6% pass the tuned cosmic rejection classifier. All numbers have been normalized to 7.99×10^{20} protons-on-target (POT) corresponding to the total POT after removing all events from Period 1 (early August 2014 beam shutdown) and applying a 14 diblock spill cut, in order to ensure events with full Far Detector. The third to sixth rows (top block) represent the preselection stage for this sample. We start with events that have failed the official containment selection, in order to potentially rescue them, later we apply basic quality reconstruction and performance cuts, which also were used for the contained sample. Finally we require an interaction with a muon using the muon-identifier developed for the contained sample and tuned to its latest version, and that such interaction fails containment, either

the muon exits the detector or the vertex is outside the boundaries. The bottom block (rows seven to eleven) represent the customized and tuned uncontained selectors (note the label "UC").

Table 7.10: Cut flow for uncontained event selection. Scaling to 7.99×10^{20} POT. The simulation POT is 7.10×10^{24}, corresponding to the entire simulation dataset.

Selection	All MC	All ν_μ CC	NC	Out-of-time	All MC+Cos	(Rel %)
No cut	1.51e+03	845	547	3.79e+07	3.79e+07	100
Failed Official	1.25e+03	716	421	4.05e+06	4.05e+06	11
Failed Containment	761	559	164	4.03e+06	4.03e+06	99.5
Basic Quality	719	554	129	3.6e+06	3.6e+06	89
PID 2017	440	437	2.28	7.77e+03	8.21e+03	0.2
Tuned CosRejUC	414	412	1.45	64.5	478	6
FiducialUC	314	313	0.678	16.9	331	69
RecoQualityUC	303	302	0.58	15.2	319	96
Hadronic ContUC	212	211	0.365	7.4	219	69
Muon Exits	192	191	0.163	6.69	199	91

Complementary to the cut-flow table, the selection efficiency for the uncontained events is shown in the left side of Fig. 7.15. It is defined as the ratio

$$\text{Eff}[i] = \frac{\text{Base Cut \&\& UCSelection}[i]}{\text{Base Cut}}, \tag{7.3}$$

where "Base Cut" refers to the number of true ν_μ CC signal events that have failed the official NOvA disappearance selection and have failed containment explicitly, whereas "UCSelection" refers to each of the steps in the uncontained selection chain in the range from 0-20 GeV. The black line represents the fraction of true ν_μ CC events that have failed the official containment selection and therefore, could be rescued for further analysis, after passing basic quality selection. It is interesting to note the shape in the 0-2 GeV region, which shows the efficiency is reduced considerably. The high energy component (> 5 GeV) seems unperturbed. The dark-yellow distribution shows the events that have passed the muon identifier selector, which is constructed when combining a single cut the outputs of a k-Nearest Neighbor and a convolutional visual network (CVN) algorithms as discussed in the previous chapter. This is the last curve that uses official selection not optimized

for uncontained events. The navy blue line shows the events that have passed the cosmic rejection selector, tuned for our sample of escaping muon events. The red and gray lines show the events that have an interaction vertex within the defined fiducial volume, and the end of the muon-like track without failures in reconstruction, respectively. Finally, the light green shows the events that have the hadronic component contained within the detector and without reconstruction failures, and the magenta line shows the events that have the final state muon exiting the detector. As noted in Table 7.11, the selection efficiency is 32.36% for the whole range of energy events (0-20 GeV). For comparison purposes, the signal selection efficiency for simulated contained events at the Far Detector in the $0-5$ GeV region is 62% [11]. The right side of Figure 7.15 shows the true neutrino energy distribution for uncontained events after each selection step has been applied, in order to show the nature of the sample.

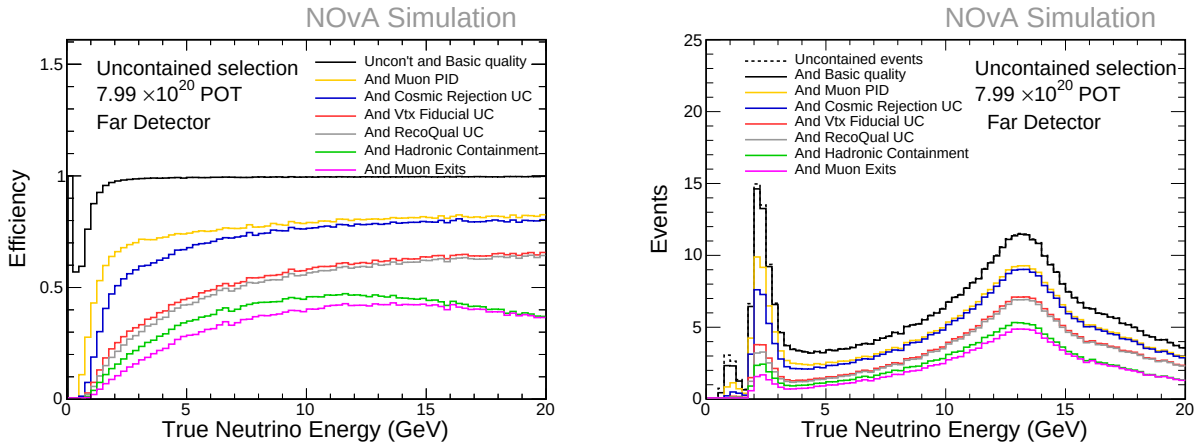

Figure 7.15: Uncontained selection performance. Left: Selection efficiency versus true neutrino energy for each selection step. Right: True neutrino energy distribution for uncontained events after each selection step is applied.

We now discuss the neutrino energy spectrum with the uncontained selection of events separated by neutrino interaction type. For example, from Fig. 7.16 we can see that there is a second peak of events around 13 GeV. If we allow a region of $10-20$ GeV, almost 74% of these events correspond to deep-inelastic events (DIS), in contrast with only 15.4% from baryonic resonance (RES), or 6.5% from quasielastic (QE) events. Table 7.12 shows the rest of the fractional components by interaction

Table 7.11: Selection efficiency table.

Selection	Efficiency (%) (0-20 GeV)
Uncont'd and basic quality	97.79
Muon PID	73.73
Cosmic Rejection	68.64
Vertex Fiducial	50.79
Reco Quality	48.85
Hadronic Containment	36.31
Muon Exits	32.36

type of the selected sample. The peak of DIS events in the $10 - 20$ GeV region will become of special interest for this work when we explore in detail its relation to neutrinos coming from kaon decay.

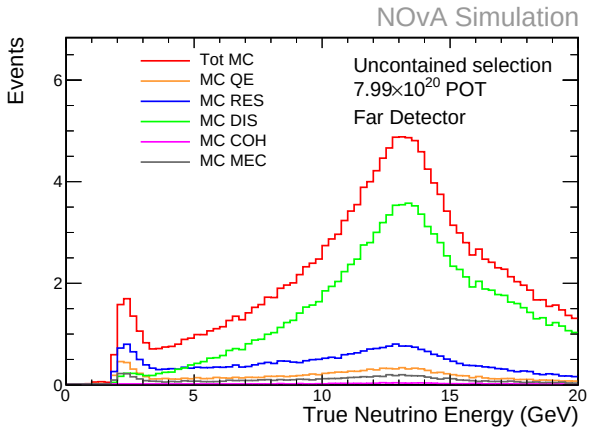

Figure 7.16: Selected uncontained events at the Far Detector shown by interaction type. The true energy events expected in the 10-20 GeV region are: DIS 73.8%, RES 15.4%, QE 6.5%, MEC 3.6%, and COH 0.8%.

We have discussed the details of the selection criteria for our analysis. In the next section, we will explain the development of a tuned energy estimator for uncontained events using multivariate analysis tools, its performance and application to our study sample.

Table 7.12: Selected uncontained events by interaction type. QE indicates quasielastic, RES indicates production of Δ-resonance particle events, DIS indicates deep-inelastic events, COH indicates coherent events, MEC indicates meson-exchange events. No cosmic ray induced muon events included.

Component	Integral (0-20 GeV)	Integral (10-20 GeV)	Percentage (%)
Total MC	166.90	121.67	100
QE	13.87	8.01	6.59
RES	32.65	18.88	15.52
DIS	111.40	89.41	73.48
COH	1.39	0.98	0.81
MEC	7.58	4.37	3.59

7.4 Uncontained muon energy estimator

A comparison between the official NOvA muon energy estimator and the true energy estimator when applied to the uncontained sample is shown in Fig. 7.17. The residual for uncontained events shows negative figures across a wide spread of energy values, indicating this estimator is always underestimating the truth energy. This is explained since the official energy estimator was not tuned for this sample of events. This motivates the development of a new estimator.

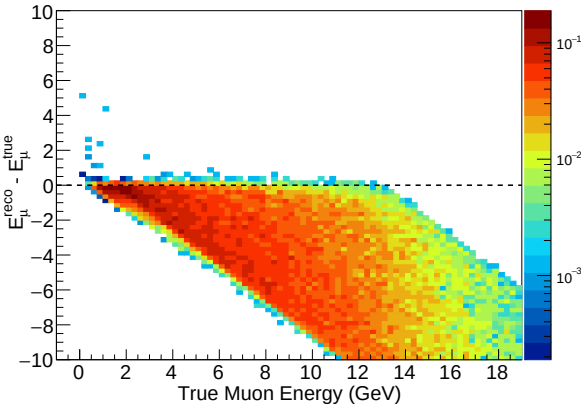

Figure 7.17: Difference between the official muon energy estimator and the muon true energy for selected events. This motivates a tuned energy estimator for uncontained muons.

The problem of energy estimation using learning methods is a *regression* problem, since the expected output values are in the continuum. In our current analysis framework, there are energy estimators for both the muon and the ν_μ-CC interactions but none of them are tuned for neutrino events that have a muon escaping our detectors. The sample of events that are going to be studied have already pass basic selection and the proposed uncontained preselection, including cosmic rejection tuned for this class of events, and fiducial/hadronic containment.

7.4.1 Input variables

A set of five input variables gave the best overall performance when tested on uncontained Far Detector events. Most of these were also used for the development of the cosmic rejection PID. Figure 7.18 shows the distributions of the five input variables, including the target muon energy from simulation. Below is a description of each of them and its purpose:

- **anglekal:** this variable was inspired by the quasielastic energy formula and is the cosine of the angle between the reconstructed muon-like kalman track and the incoming beam direction
- **tracklen:** track length (in cm) of the reconstructed muon-like kalman track; without it classifier performance is substantially damaged
- **hadclustcalE:** the calibrated hadronic calorimetric energy from the cluster of hits not in the muon-like track (hadronic system)
- **trkEPerNHit:** ratio between the calorimetric energy in the reconstructed muon-like kalman track and the number of hits of such track; similar philosophy as above
- **scatt:** the scattering angle of the reconstructed muon-like kalman track (cumulative sum of angular changes, in degrees) normalized by the track length; experimental use based in overall performance

After training and testing, the TMVA framework gives the linear correlation coefficients (shown also in percentage) among the input variables for regression. For example. Fig. 7.19 shows the

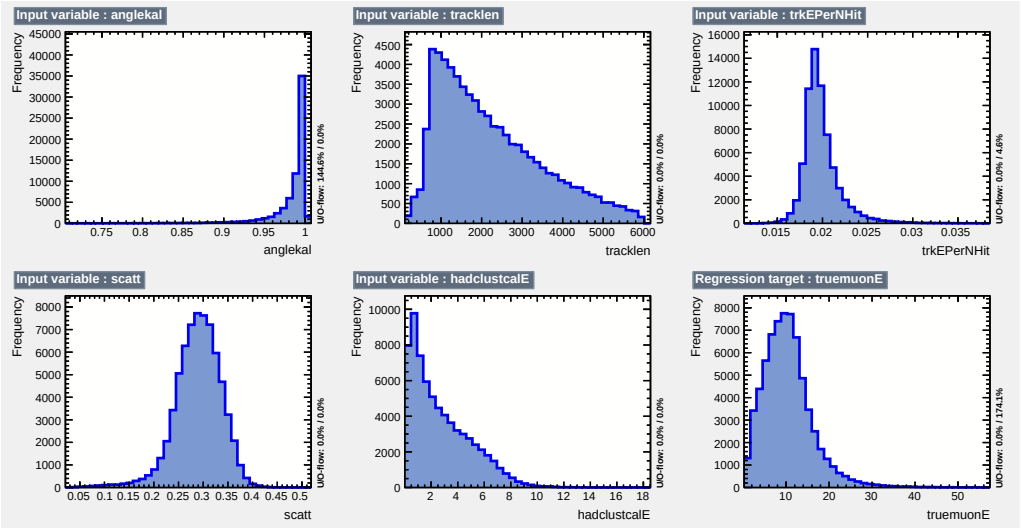

Figure 7.18: Set of input variables for the muon energy estimator for uncontained events: `anglekal, tracklen, hadclustcalE, trackEPerNHit, scatt`

5×5 matrix where the lighter color represent the value of positive correlation whereas darker colors represent a negative correlation.

If we sum the off-diagonal entries for a given column and divide by four (that is, the total number of variables minus one), we obtain the average correlation per input variable. For this case, the minimal value corresponds to the muon scattering angle `scatt` variable, and the maximum to the cosine angle `anglekal` variable. Regression performance metrics will be explained in the following section.

7.4.2 Performance

The performance for regression is based on the correlation strength between input variables and the regression target and between the multivariate (MVA) method response and the target. Several correlations metrics are implemented in the framework to characterize any dependencies.

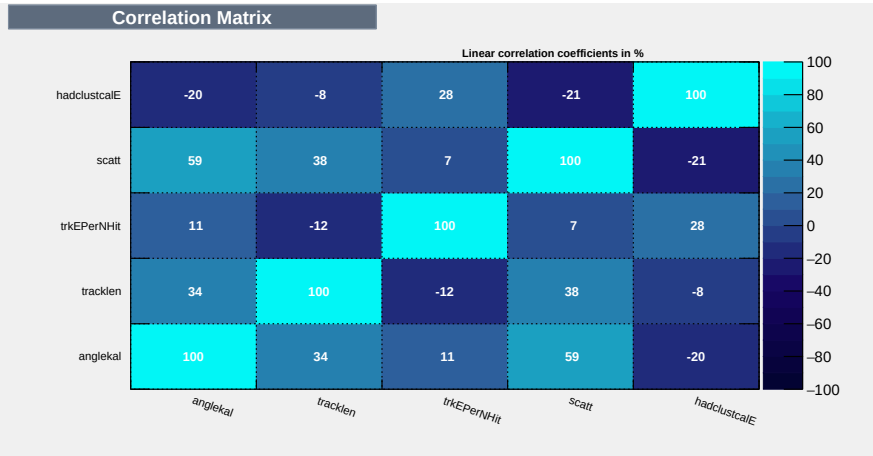

Figure 7.19: Correlation among input variables for the uncontained muon energy estimator.

For example the (Pearson's) **correlation** between two random variables X and Y is measured with the correlation coefficient ρ and defined by

$$\rho(X,Y) = \frac{\mathrm{cov}(X,Y)}{\sigma_X \sigma_Y}$$

where $\rho \in [-1,1]$, and quantifies by definition a linear relationship. The case $\rho = 0$ holds for variables with no linear correlation, but the inverse is not true. Higher non-linear relationships are usually hard to reflect in the value of ρ.

Table 7.13: Ranking of input variables according to the correlation with target distribution (top variable is best ranked).

Rank	Variable name	| Correlation with target |
1	`tracklen`	0.60
2	`scatt`	0.56
3	`anglekal`	0.51
4	`trkEPerNHit`	0.24
5	`hadclustcalE`	0.07

The absolute value of the correlation with the target for the input variables is shown on Table 7.13. Top variable is best ranked. We see that there is indication of a correlation between three out of five inputs and the true muon energy (target).

Finally, the **mutual information** metric (originated from information theory) measures mutual dependence between two variables ,

$$I(X,Y) = \sum_{X,Y} P(X,Y) \cdot \ln \frac{P(X,Y)}{P(X)P(Y)}$$

where $P(X,Y)$ is the joint probability density function and $P(X), P(Y)$ are the marginal probabilities. Mutual information is the reduction of the uncertainty in variable X due to the knowledge of Y. It takes positive values and is symmetric. Completely independent variables, $I(X,Y) = 0$. High values of ρ result in high values of I. Table 7.14 shows the values for the input variables.

Table 7.14: Ranking of input variables according to the mutual information metric for our energy estimator.

Rank	Variable name	Mutual information
1	`anglekal`	2.77
2	`scatt`	2.13
3	`hadclustcalE`	1.43
4	`trkEPerNHit`	1.35
5	`tracklen`	0.72

Several methods were tested using the input variables shown Fig. 7.18 for the uncontained muon energy estimator. Linear methods such as linear discriminant (LD), k-nearest neighbors (kNN) and non-linear methods such as multilayer perceptrons (MLP) and decision trees (gradient and adaptive boosting) were used.

In order to evaluate the performance of a regressor method on our data set, we need some way to measure how well observed data and prediction actually match. The metric that helped quantify performance across methods was the average deviation from target (e.g. the true muon energy

distribution), given by

$$\text{average deviation} = \sqrt{\sum (f_{\text{MVA}} - f_{\text{target}})^2}$$

which as shown on Fig. 7.20. The average deviation from target is smaller for the cases of gradient boosted trees and to some extent, kNN methods. The blue squares represent the score for the entire sample population (for both testing and training). The black squares corresponds to the best 90%.

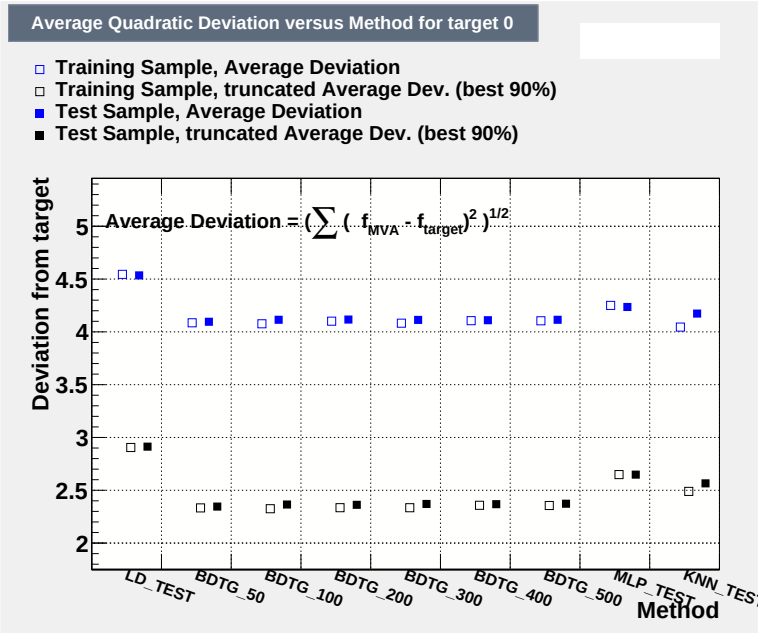

Figure 7.20: Comparison across linear and non-linear methods for the uncontained muon energy estimator. Best performance (least deviation from target) achieved by decision trees with gradient boosting, in particular, when number of trees is 100. Second best was kNN method, but needs further tuning.

The accuracy of $\hat{f}_{\text{MVA}}$ as a prediction for for f_{target} depends on two quantities, which we will name reducible and irreducible errors. We can improve the accuracy of $\hat{f}_{\text{MVA}}$ by choosing the best learning method (BDT, kNN, etc) and its best tuning, therefore decreasing the reducible error. But even if we make a perfect match, our prediction will still have some error on it. This is because f_{target} is also a function of ϵ, which by definition cannot be predicted using any of our input variables.

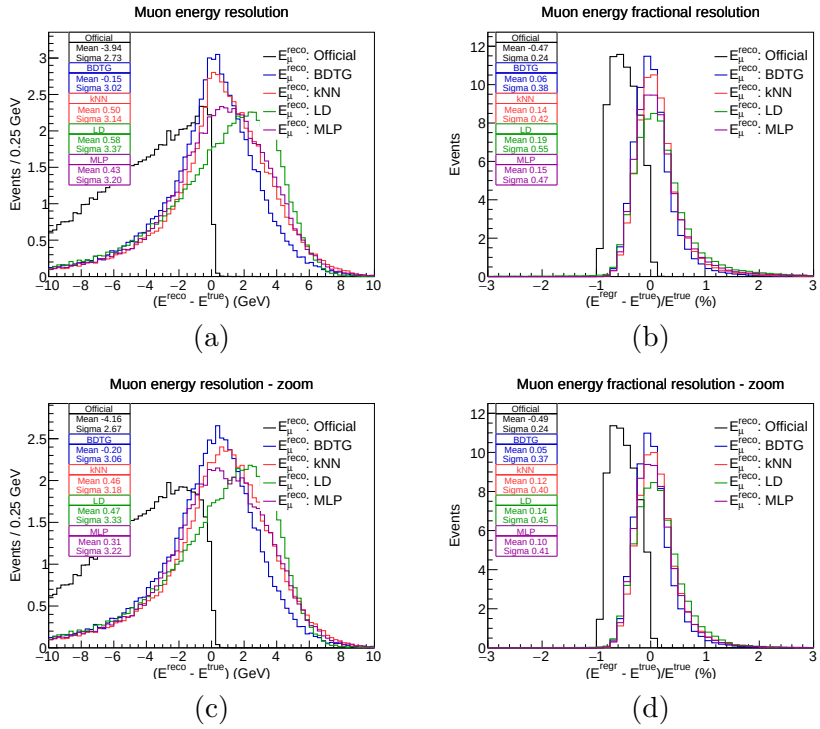

Figure 7.21: Muon energy resolution (a) and muon energy fractional resolution (b) for selected uncontained events using different algorithms. As a comparison, mean and RMS (sigma) values are shown on the top left corner. Similarly (c) and (d) but with true neutrino energy $E_\nu > 5$ GeV.

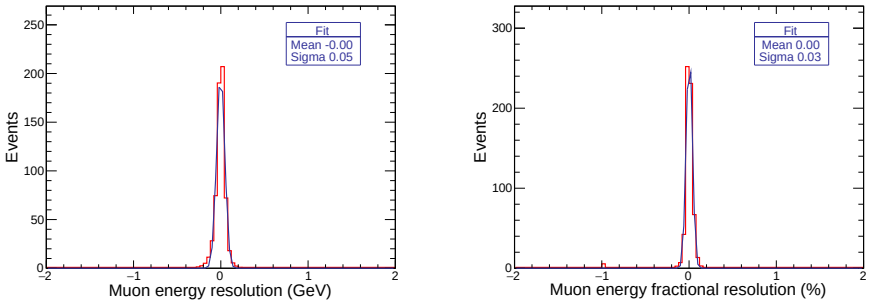

Figure 7.22: Muon energy resolution (left) and muon energy fractional resolution (right) for contained events. The fractional resolution is 3%.

It can be shown [97] that the expected test error can always be decomposed into the sum of three fundamental quantities: the variance of $\hat{f}_{\mathrm{MVA}}$, its variance and the variance of the error terms ϵ

$$E(f_{\mathrm{target}} - \hat{f}_{\mathrm{MVA}}(x_0))^2 = \mathrm{Var}(\hat{f}_{\mathrm{MVA}}(x_0)) + [\mathrm{Bias}(\hat{f}_{\mathrm{MVA}}(x_0))]^2 + \mathrm{Var}(\epsilon)$$

where the first two terms refer to the reducible error and the last one, to the irreducible error. This is know as the **bias-variance trade-off**. Variance refers to the amount by which f_{MVA} would change if we estimated it using a different training dataset. Bias refers to the error that is introduced by approximating a complex quantity, such as the energy of the uncontained muon, by a much simpler model such as its relation with the input variables in Fig. 7.18.

To address the question of how our tuned muon energy estimator compares with the official contained muon energy estimator and the outputs of other methods, distributions of the resolution and fractional resolution are shown in Fig. 7.21. The top left image shows the difference between the reconstructed muon energy estimator output and the true energy of the muon, using different algorithms (boosted decision trees, kNN, etc) represented by each color. Printed in the same image are the mean and standard deviation of the distributions. Similarly, the top right shows the muon energy fractional resolution. We can see that the boosted decision tree method with gradient boosting (BDTG) has the relative smaller standard deviation of 38%. The bottom row shows the same distributions than before but now selecting events away from oscillation region, with true neutrino energy $E_\nu > 5$ GeV. We observe that the fractional resolution of the best method (BDTG), quoted as the muon resolution for this sample is 37%. For comparison, the contained energy estimator is shown in black. The muon energy resolution and fractional resolution for the contained muon sample is quoted as 3% and is shown in Fig. 7.22. Figure 7.23 shows the effect of including the tuned muon energy estimator to the neutrino energy of the uncontained events. Once again, different methods were tested and the BDTG method showed the smaller standard deviation. The fractional resolution quoted is 28%, and for events away from the oscillation region with true neutrino energy $E_\nu > 5$ GeV is 25%. For comparison, Fig. 7.24 shows the neutrino energy resolution and fractional resolution for contained events, quoted as 8%.

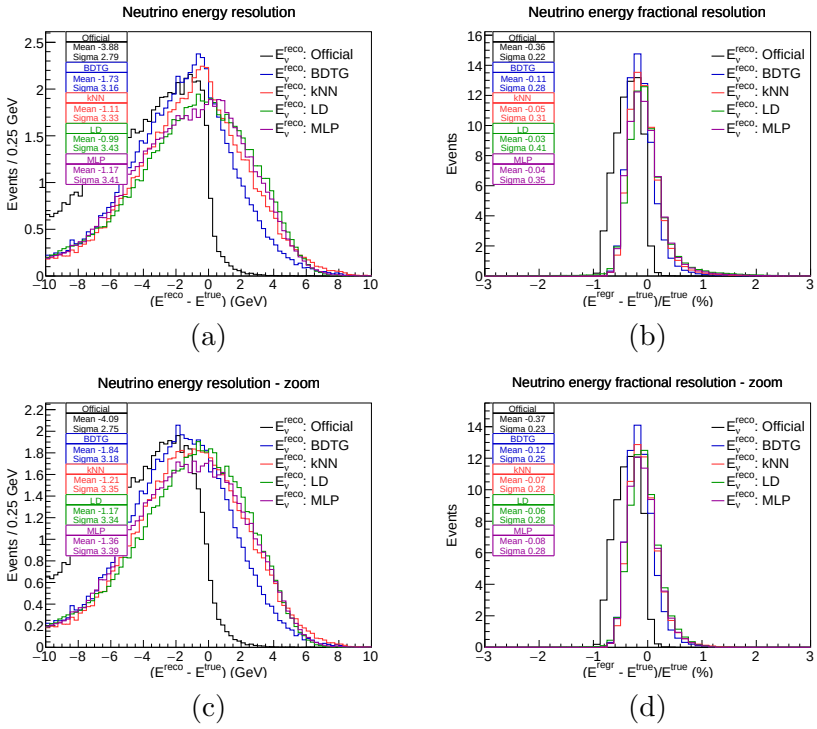

Figure 7.23: Neutrino energy resolution (a) and neutrino energy fractional resolution (b) for selected uncontained events using different algorithms. As a comparison, mean and sigma values are shown on the top left corner. Similarly (c) and (d) but with true neutrino energy $E_\nu > 5$ GeV.

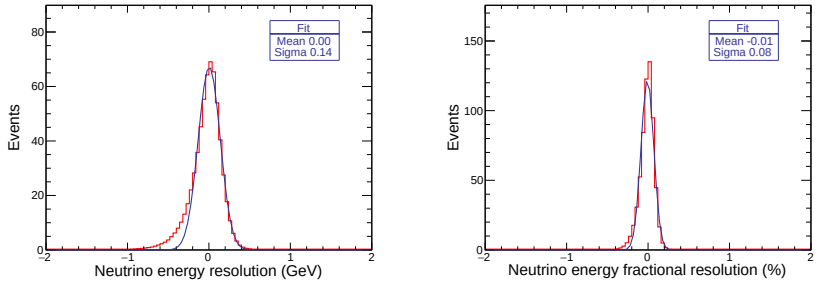

Figure 7.24: Neutrino energy resolution (left) and neutrino energy fractional resolution (right) for contained events. The fractional resolution is 8%.

In order to describe the behavior of the tuned muon energy estimator using the decision tree (BDTG) method, Fig. 7.25 shows the difference between the tuned muon estimator and the true muon energy, quantity that we have introduced earlier as the resolution (or residual) versus each of the input variables. The range of distributions (a1-a5) represent the selected uncontained events with mixing parameters set to one of the NOvA 2016 best fit points. The other range of distributions (b1-b5) represent the set of interactions with true neutrino energy $E_\nu > 5$ GeV, away from oscillation region.

As described in earlier sections, the angle between the main muon-like track and the NuMI beam direction gives information about the kinematics of the interaction. By inspection with the residual we can see that the majority of events have a large forward-like component which is parallel to the neutrino beam. Also, some indication that the regressor becomes uncertain, with tendency to overestimate, when looking at muons parallel to the beam. The calorimetric hadronic energy is a measure of the neutrino energy not deposited in the muon but in the detector by hadronization. By inspection we can note a large uncertainty across the residuals, with tendency to overestimate at low hadronic energy values. The scattering of the muon normalized by the track length was a compound metric targeted to quantify the interaction scattering of the muon-like particle through the detector. It was found that very forward-like muons have a constant value of this metric (around 0.3 degrees/cm) independently of their track length, whereas non-forward-like muons (that is, with a reasonable angle with respect to the beam) the value of this metric tends to be a small. Put it in another way, for a fixed relatively small track length (say 6 m), and a value of $\cos\theta_{NuMI} = 0.8$, the value decreases to 0.1 degrees per centimeter, which means the amount of scattering decreased. Overestimation in the residuals is again linked to forward-like muons. The ratio of track energy and number of track hits also shows similar behavior than our normalized scattering variable, in the sense that shows a high concentration at a constant value with high uncertainty in the residuals at that point. This is a consequence of the fact that the most typical energy of a track is around 10-14 GeV. Finally, the track length of the muon-like track shows a reasonable wide spread when

including all the interactions, but this is reduced when looking at only low energy events. The residuals are consistent within errors.

The combined behavior of the input variables is summarized when comparing the regression output with the true muon energy, as shown in Fig. 7.26. The top left image shows the difference between the tuned muon energy estimator and the true muon energy versus the true muon energy. At low muon energies, the residual tends to be more or less centered around zero, but at high energies, the residual tends to be negative. This can be explained as a consequence of missing information at higher energies. The top left image shows what happens when we look at the bias of the residuals versus the true energy. Taking the 2D distribution from the left, for each bin of true energy we apply a Gaussian fit. Each point then represents the mean of that fit, which is associated to the bias, and the error bar represents the sigma value of the same Gaussian fit, associated to the resolution. For a range of true muon energies between 0-2 GeV, the bias is within 0.5 GeV with very small error. But as the true energy increases, the bias increases and then it decreases, with error bars more or less constant. This is represented by the bottom right plot with the resolution versus true muon energy. The bottom left plots shows the bias versus versus the tuned reconstructed muon energy.

Since we expect to have a reconstructed muon energy resolution of approximately 2 GeV for events with true energy $E_{\text{true}} \geq 6$ GeV, we developed a custom binning based on the findings of the bottom right plot in Figure 7.26. We noticed that resolution remains more or less constant in the region above from oscillations, where the DIS and RES events take place. Table 7.15 shows the binning scheme adopted.

We showed that the BDT method with gradient boosting obtained the smallest fractional uncertainty relative to the others. A briefly description of the details of this algorithm will be presented in the next section.

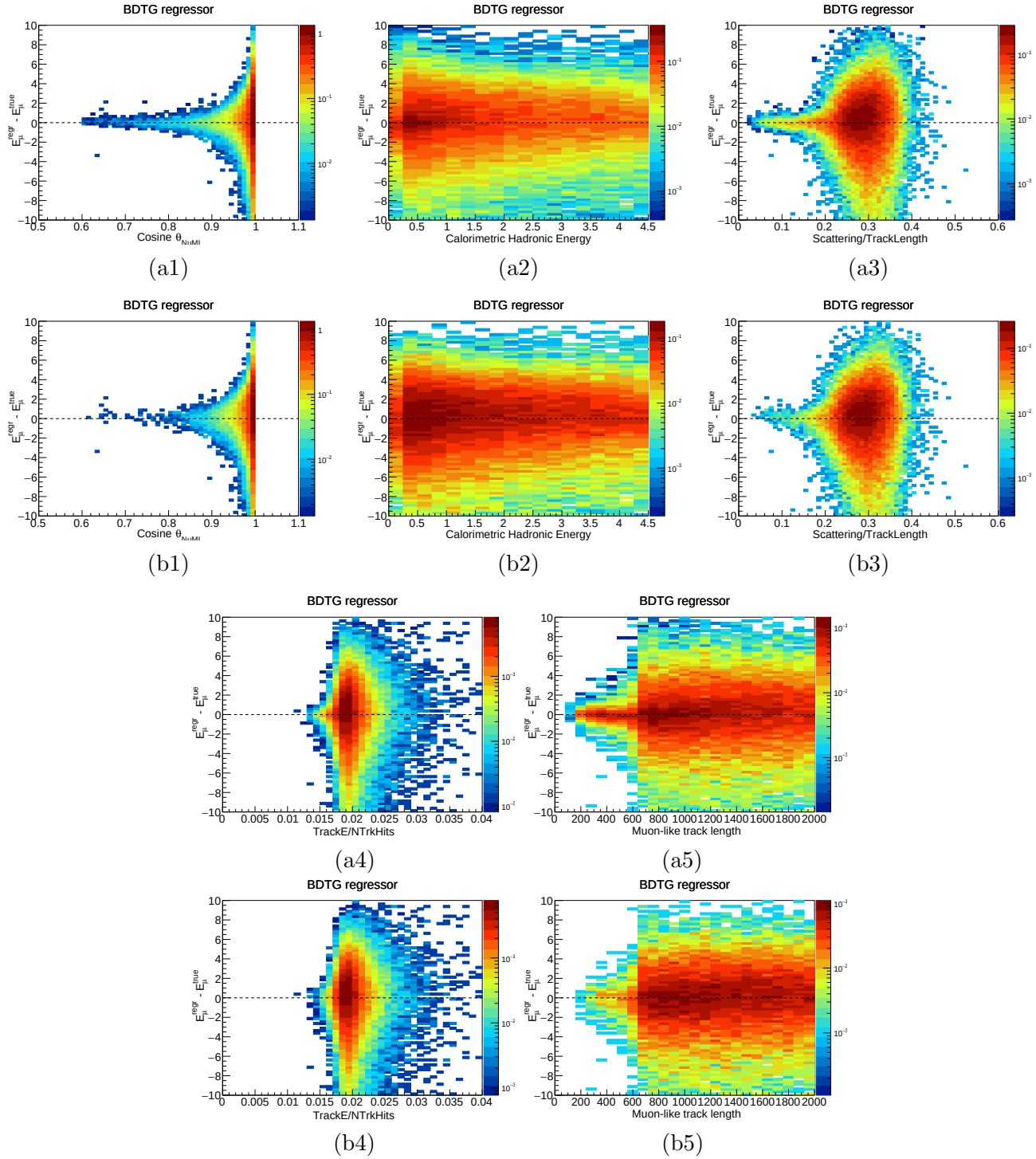

Figure 7.25: On the Y-axis, each plot represents the difference between the muon energy estimator (using gradient boosting) and the muon true energy. On the X-axis, each plot shows one of the input variables of the estimator. (a1-a5) Color represents the number of events, with oscillation parameters set to $\sin^2\theta_{23} = 0.404$ and $\Delta m^2_{32} = 2.67 \times 10^{-3}$ eV^2. (b1-b5) Shows the same input variable but with a cut in true neutrino energy of $E_\nu > 5$ GeV.

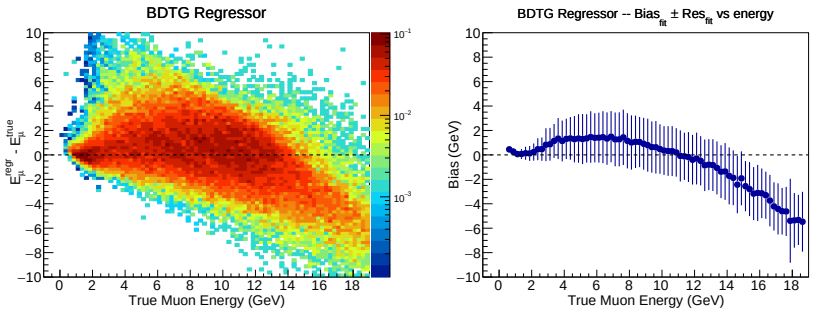

Figure 7.26: Results of regression using gradient boosted decision tree. (a) Shows the difference between the uncontained muon energy estimator and its true energy versus the muon true energy for selected events, using oscillation parameters $\sin^2\theta_{23} = 0.404$ and $\Delta m^2_{32} = 2.67 \times 10^{-3}$ eV^2. (b) Shows the bias versus true muon energy, where each point represents the mean of a Gaussian fit to all the events in that bin and the error bar is the sigma value of the same Gaussian fit. (c) Shows the bias versus tuned reconstructed muon energy, indicating a flat behavior across energies. (d) Shows the resolution versus true muon energy, where each point represents the sigma value of the Gaussian fit per bin and the error bars the uncertainty in the sigma value.

Table 7.15: Binning scheme for the uncontained sample based in the resolution of the muon selected events.

Energy range (GeV)	No of bins
0.0-2.5	5
2.5-3.5	1
3.5-5.0	1
5.0-20.0	6
Total	13

7.4.3 Gradient boosting

Gradient boosting consists in applying the method of gradient descent to the idea of boosting, which means that a set of weak learners (those which label slightly better than random guessing) when combined in a methodical manner, usually weighted, can create a stronger learner. Seminal work on this subject was done by J. H. Friedman in 2001 [78]. For the case of the uncontained muon, we have a set of input distribution variables $X_1, X_2 \ldots, X_5$ and a target distribution Y and our task is to fit a model $F(\vec{X})$ to minimize some loss function. Using the boosting idea, we can add an additional model (regression tree) h to F so the new prediction will be $F(\vec{X}) + h(\vec{X})$. Or equivalently $h(\vec{X}) = Y - F(\vec{X})$, which are nothing but the residuals. The overall role of h is to compensate for the imperfections of the existing model F. In gradient boosting, this imperfections are identified by gradients.

Minimize a function by gradient descent is to minimize a function by moving in the opposite direction of the gradient. Given a loss function $J(\vec{x})$, and a point θ_i, then $J(\vec{x})$ decreases fastest if

$$\theta_j = \theta_i - \gamma \frac{\partial J}{\partial \theta_i}$$

with γ is a step size multiplier. Given a loss function $L(Y, F(X))$, we want to minimize $J = \sum_i L(Y, F(X_i))$ by adjusting $F(X_{1i}), F(X_{2i}), \ldots$. We can interpret residuals as negative gradients

$$Y_i - F(\vec{X}_i) = -\frac{\partial J}{\partial F(\vec{X}_i)}$$

For this study, TMVA uses the Huber loss function,

$$L(Y, F(\vec{X})) = \begin{cases} \frac{1}{2}(Y - F(\vec{X}))^2 & |Y - F(\vec{X})| \leq \delta \\ \delta(|Y - F(\vec{X}) - \delta/2|) & |Y - F(\vec{X})| > \delta \end{cases}$$

which is known to be more robust to outliers. An example of the gradient boosted decision tree based on the input variables is given by Fig. 7.27.

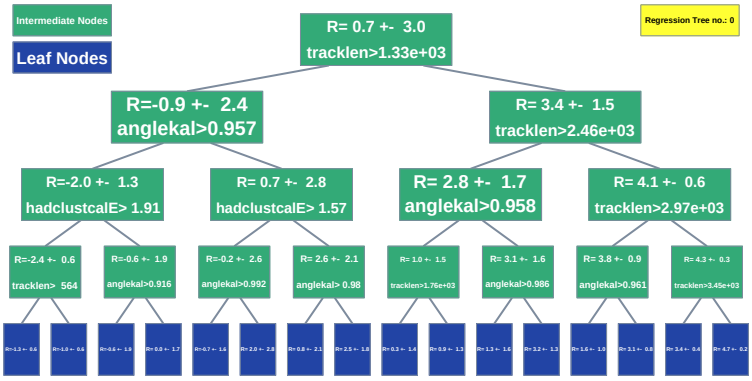

Figure 7.27: First of the 100 gradient decision trees used for the regression of the uncontained muon energy estimator. The leaves nodes show the **response** value, which is a proxy for the energy regressor.

7.4.4 Comparisons and validation

We discuss some results of the neutrino energy estimator tuned for uncontained events. From the events passing the uncontained selection, the neutrino energy is computed as simply the sum of the tuned muon energy estimator and the contained energy of the hadronic system

$$\hat{E}^{\text{unc}}_{\nu_\mu} = \hat{E}^{\text{unc}}_{\mu} + E^{\text{cont}}_{\text{Had}}. \tag{7.4}$$

The relation between the tuned neutrino energy estimator and its components is shown in Fig. 7.28. The top left distribution shows the relation between the true neutrino energy and the reconstructed energy estimator defined by Eq. 7.4, where the black points represent the average value of the Y axis. Top center shows the absolute resolution as a function of the true neutrino energy with the average values superimposed. Finally, top right shows the fractional energy resolution as a function of true energy. In a similar manner, the relations between true and reconstructed energies, absolute, and fractional resolutions for the muon and hadronic component are shown in the middle row (b1-b3) and bottom row (c1-c3).

The fact that we have small discrepancies between the tuned and the true neutrino energies raised the question of whether or not a correction to the tuned muon energy is needed. Explanation for

this discrepancy is traced back to the limitations in modeling the energy for uncontained muons given by the choice of input variables.

First, note again the comparison between tuned muon energy and true muon energy in the bottom left, for selected events. We can observe a linear behavior, as in the case of the tuned neutrino energy, but it gets broader at higher energies.

Nevertheless, we performed studies related to potential corrections to the output of the tuned muon energy and to the hadronic energy component as well [148]. The idea was to compute the residuals between the tuned energy estimator and truth, map them into a 2D distribution versus tuned muon energy estimator, and apply a spline fit to this distribution. The resulting values from the fit were later applied to the tuned muon energy and compared again, with truth. Similar mechanism was performed for the hadronic energy. In the end, findings showed no substantial improvement in the fractional resolution after applying this corrections to both the tuned muon and hadronic energy estimators.

After having established the comparison with true neutrino energy and using the customized binning given by the resolution of our events, Figure 7.29 shows the distribution of reconstructed tuned neutrino energy with the full selection applied, in the 5-20 GeV range, away from the main oscillation region. Solid red line represents the total simulation distribution with all backgrounds included, such as the cosmic ray induced in gray, and neutral current plus beam induced backgrounds added together in magenta. The total number of reconstructed events in the 10-20 GeV energy region, where the DIS events reach almost 74% of the total is expected to be 148 events.

As part of the validation performed to the neutrino energy estimator, we study the hypothesis of whether or not a flux-model dependency is present in the energy estimator, resulting in a potential bias that could affect the resulting value for our selected events. The idea was to variate the flux while keeping the true neutrino event rate in the 10-20 GeV region constant. Assuming a Gaussian distribution with parameters $A_{fit}, \mu_{fit}, \sigma_{fit}$, we want the integral between the true energy range

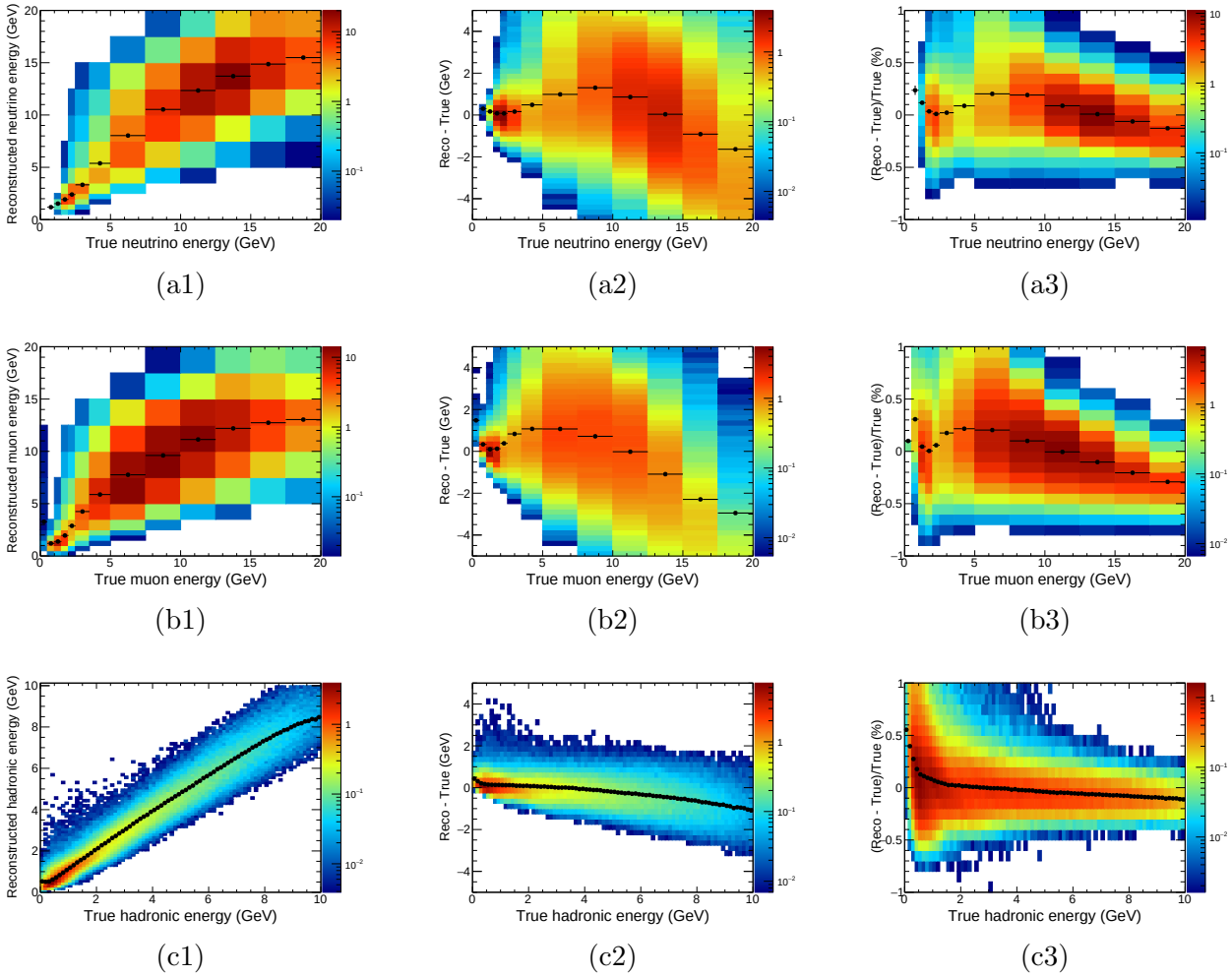

Figure 7.28: Two dimensional distributions for selected uncontained events. The true neutrino energy is shown in the top row versus reconstructed neutrino energy (a1), neutrino energy resolution (a2), and neutrino fractional resolution (a3), for oscillation parameters $\sin^2\theta_{23} = 0.558$ and $\Delta m^2_{32} = 2.444 \times 10^{-3}$ eV^2. Similarly, middle row shows true muon energy versus the reconstructed muon energy (b1), muon energy resolution (b2), and the muon fractional resolution (b3). The bottom row shows the true hadronic energy versus reconstructed hadronic energy (c1), hadronic energy resolution (c2), and hadronic fractional resolution (c3).

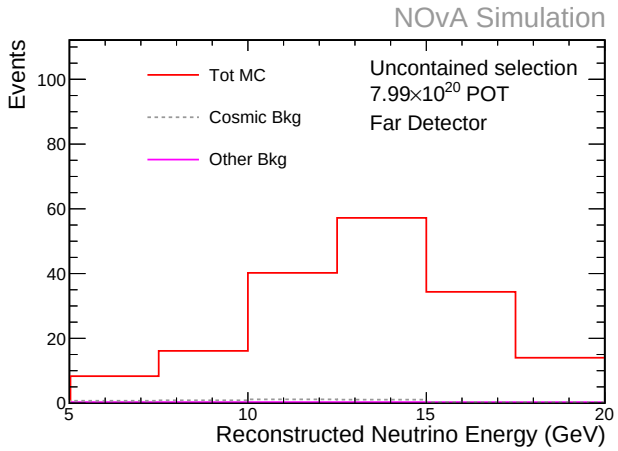

Figure 7.29: Distribution of reconstructed neutrino energy for selected events normalized to 7.99×10^{20}, using the customized binning in the 5-20 GeV region away from oscillations. A total of 148 reconstructed events are expected in the range 10-20 GeV, where the mayority of DIS events are located. Cosmic and other backgrounds included.

$10 < E_{true} < 20$ be equal to some constant C, in other words

$$\int_{10}^{20} Gauss(E_{true}|A_{fit}, \mu_{fit}, \sigma_{fit})\ dE_{true} = C. \tag{7.5}$$

The next step is to model a flux dependence acting on the neutrino energy in the form of a weight function, such that the neutrino rate remains constant,

$$\int_{10}^{20} w(E_{true}) \cdot Gauss(E_{true}|A_{fit}, \mu_{fit}, \sigma_{fit})\ dE_{true} = C. \tag{7.6}$$

For simplicity, we assume a linear model $w(E_{true}) = w_0 \pm m \cdot E_{true}$. Our task was to find the values of w_0 and m, and apply those weight functions to the neutrino energy distribution, propagating through the full sample selection. In the end we find that if the true neutrino energy E_{true} is $10 \leq E_{true} < 20$, then

$$w(E_{true}) = 0.5 + 0.0353 \cdot E_{true} \qquad \text{flux up},$$
$$w(E_{true}) = 2.0 - 0.0706 \cdot E_{true} \qquad \text{flux down},$$

otherwise, $w(E_{true}) = 1$. The results of this study is shown in Figure 7.30. The solid red distribution represents the nominal value of the reconstructed tuned neutrino energy, the solid blue represents

a flux-model dependency that increases linearly with the reconstructed energy, whereas the solid green represents a linear dependency that decreases with energy. We apply a Gaussian fit in the reconstructed energy range of 7.5-20 GeV for each distribution, with the resulting fitted mean values shown at the top corner for comparison. We concluded that applying a linear dependence in the reconstructed neutrino energy does not impact substantially the shape of its distribution. We can explain this by the fact that, since NOvA is an off-axis experiment, any changes in the flux will become relevant if the off-axis angle itself is changed.

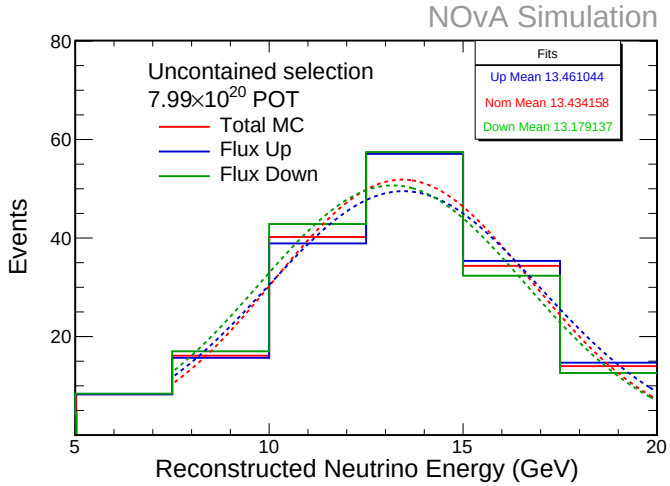

Figure 7.30: Reconstructed energy distribution for selected events. Gaussian fit applied to the region 7.5-20 GeV. Mean of each fit shown in plot.

7.5 Neutrino parent components and background constraint

Let us consider the decay of a positively charged kaon via the weak force, into a muon neutrino and an antimuon, as in the following reaction

$$K^+ \to \nu_\mu + \mu^+.$$

We say that the positively charged kaon K^+ is the **parent** of the muon neutrino ν_μ in the final state. Now, consider the subsequent decay of the antimuon from the previous reaction into a muon

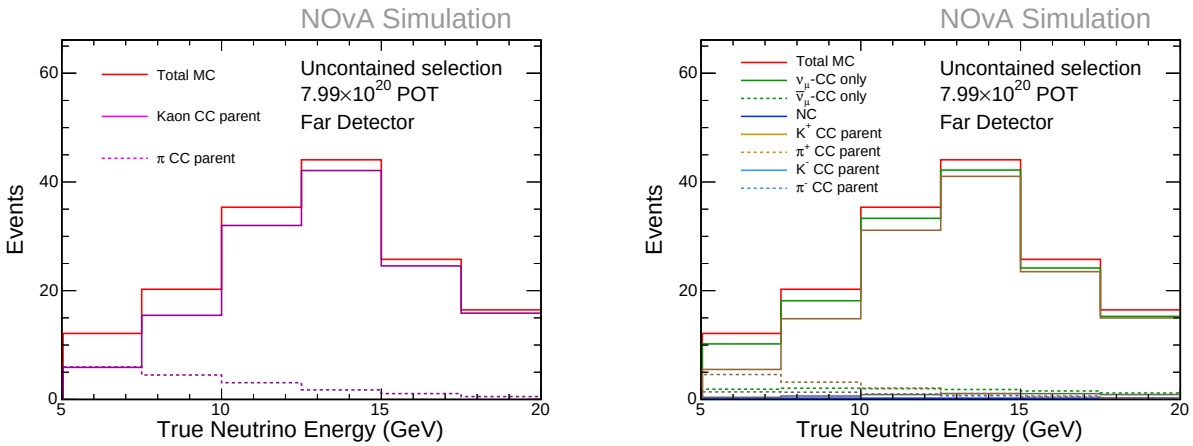

Figure 7.31: For uncontained selected events, true neutrino energy distribution for neutrinos whose parent is a kaon or pion. In the 10-20 GeV region, $\sim 94\%$ of neutrinos are coming from kaons. Our goal is to fit the high energy neutrinos, constraining the flux uncertainty from kaon production.

antineutrino, an electron neutrino and a positron,

$$\mu^+ \rightarrow \overline{\nu}_\mu + \nu_e + e^+.$$

In this case, we say that the positively charged kaon K^+ is the **ancestor** of the muon antineutrino $\overline{\nu}_\mu$. Figure 7.31 shows the distribution of true neutrino energy for selected events when looking at the neutrino parents. On the left side, the solid magenta distribution shows the contribution of neutrinos coming from the charged current decay of kaon mesons. A 94% of the neutrinos in the 10-20 GeV region comes from the decay of kaons. The dashed magenta line corresponds to the contribution of neutrinos coming from the decay of pions, which translates in a 5% from the total in the 10-20 GeV range (see Table 7.16). Therefore, we can conclude that in the 10-20 GeV range, a high component of uncontained ν_μCC events at the NOvA Far Detector are mainly produced via deep-inelastic scattering of the nucleus (74%), and come from neutrinos which are produced mostly from the decay of kaons (94%).

Given that our selection is sensitive to a majority of uncontained kaon-parent neutrinos in the Far Detector, we decided to investigate any possible link between this sample and the kaon-parent beam ν_e in the Near Detector, known to be a background for the ν_e-appearance analysis (see

Table 7.16: Neutrino parent component for the uncontained events at the Far Detector. The sample ν_μ-CC only is made of K^+ and π^+ components.

Component	Integral (0-20 GeV)	Percentage (%)	Integral (10-20 GeV)	Percentage (%)
Total MC	166.90	100	121.67	72.90
ν_μ CC	154.89	92.80	114.96	68.88
$\overline{\nu}_\mu$ CC	11.63	6.97	6.51	3.90
NC	0.15	0.09	0.08	0.05
$K^\pm$ parent	137.32	82.28	114.53	68.73
K^+ parent	132.30	79.27	110.82	66.40
K^- parent	5.02	3.00	3.90	2.34
$\pi^\pm$ parent	28.32	16.97	6.41	3.84
π^+ parent	22.31	13.37	4.03	2.41
π^- parent	6.02	3.61	2.38	1.43

Section 2.5). First, a study of the momentum space of the kaon-parent neutrinos was performed in order to characterize these two sets of events. Figure 7.32 shows the Near Detector beam ν_e-contained selection applied to simulated events resulting in blue bins, whereas the Far Detector uncontained ν_μ selection is applied to simulated events, shown in solid red boxes. The axis show the forward (p_Z) and transverse (p_T) momentum components of the neutrino as the kaon-parent exits the NuMI target. It is shown that both samples are not clustered in separate phase spaces, but rather overlaping, suggesting a kinematic equivalence.

Two more Near Detector samples were also investigated: the neutral current background from the selected ν_μ CC contained events and the uncontained ν_μ CC events. Figure 7.33 shows the momentum space distributions of the NC background (left) and uncontained ν_μ CC (right). We also see an overlap between the Near and Far Detector phase spaces, that could be used to find relationships.

Next, we performed a more quantitative study in order to answer whether or not the 10-20 GeV Far Detector uncontained kaon-parent neutrinos are influenced by the kaon-parent beam ν_e in the Near

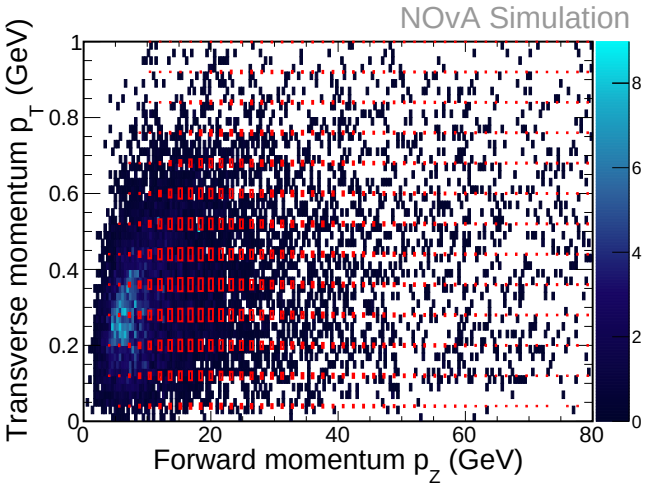

Figure 7.32: Momentum space distributions from selected neutrinos whose parent is a kaon. Near Detector beam ν_e-contained selection is applied to simulation files resulting in the blue bins. The Far Detector uncontained ν_μ selection is applied to simulation files, resulting in the solid red boxes. The horizontal axis shows the forward momentum component (p_Z) of the parent kaon as it exists the target, whereas the vertical axis shows the transverse momentum component (p_T).

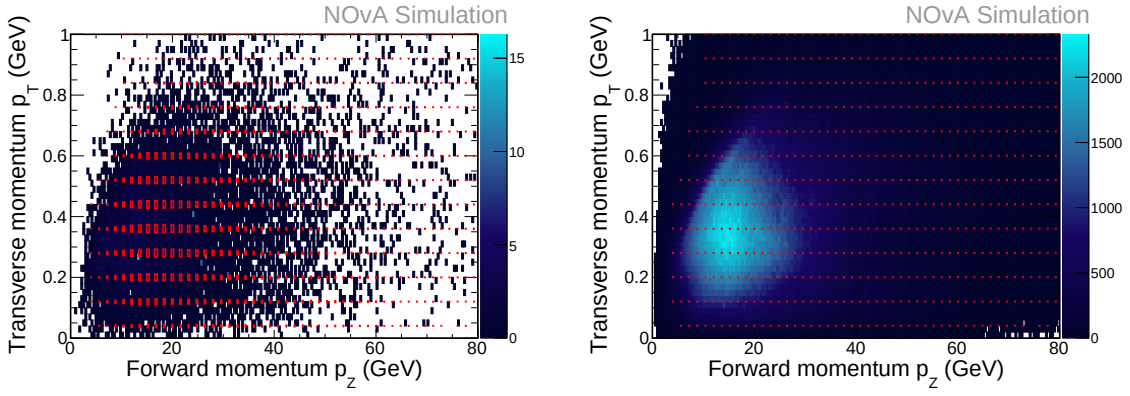

Figure 7.33: Momentum space distributions from selected neutrinos whose parent is a kaon. Near Detector in blue bins. Left: neutral current ν_μ-contained selection is applied to simulation files. Right: ν_μ-uncontained charged-current selection is applied to simulation files. The Far Detector uncontained ν_μ selection is applied to simulation files, resulting in the solid red boxes. The horizontal axis shows the forward momentum component (p_Z) of the parent kaon as it exists the target, whereas the vertical axis shows the transverse momentum component (p_T).

Detector, and if so for how much. We started by defining a covariance matrix Cov^{syst} that includes the set of flux systematics (beam transport and hadron production normalization and shape). The uncertainties are computed as [99].

$$err_i = \frac{1}{2}\left(\left|\sigma_i^{+} - \sigma_i^{nom}\right| + \left|\sigma_i^{-} - \sigma_i^{nom}\right|\right) \tag{7.7}$$

where $\sigma^{\pm 1}$ corresponds to the ± 1 shift variation from simulation, and σ^{nom} is the nominal or central value. The contribution of all the systematic uncertainties are marginalized and then combined with the nominal using a function f_i as follows

$$f_i = f_i^{nom} + \sum_{k=1}^{systs} err_{ik} \tag{7.8}$$

Finally, the entries of the covariance matrix are computed using the expected values

$$Cov_{ij}^{syst} = \langle f_i \cdot f_j \rangle - \langle f_i \rangle \langle f_j \rangle \tag{7.9}$$

and the correlation matrix becomes

$$Corr_{ij}^{syst} = \frac{Cov_{ij}^{syst}}{\sqrt{Cov_{ii}^{syst}}\sqrt{Cov_{jj}^{syst}}} \tag{7.10}$$

When applied to the sets of Near and Far Detector events, the covariance matrix becomes non-diagonal as shown in Figure 7.34. Since the beam ν_e events are selected only to values of reconstructed neutrino energy $E_{\nu_e}^{reco} < 5$ GeV, white band gaps appear, indicating no events selected. The binning size for the Far Detector sample is set to 2.5 GeV whereas for the Near Detector is set to 0.25 GeV. In a similar note, the covariance matrix for these two sample sets is shown in Figure 7.35. If we restrict ourselves to the Far Detector 10-20 GeV and Near Detector 0-5 GeV regions, we can observe that a $60 - 80\%$ correlation exist between these two samples. Therefore, any measurement of the kaon production normalization in the 10-20 GeV region of Far Detector will be correlated at the $60 - 80\%$ level when trying to constrain the beam ν_e background in the Near Detector.

When looking at the possible relationships between the NC and ν_μ CC Near Detector backgrounds with the Far Detector uncontained sample, we find interesting features too. Figure 7.36 shows the

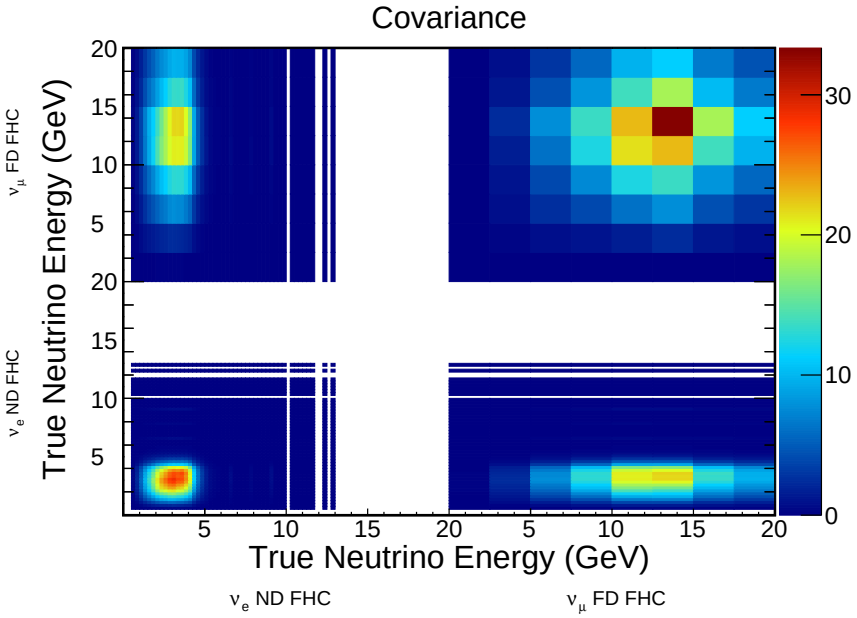

Figure 7.34: Covariance matrix between the sets of Near Detector beam ν_e-contained and Far Detector ν_μ-uncontained kaon-parent neutrinos in the 0-20 GeV true energy range. The bin size for the beam ν_e-sample is 0.25 GeV whereas for ν_μ-uncontained sample is 2.5 GeV. The Near Detector sample region is between 0-5 GeV, therefore the white bands and white region corresponds to no events selected. The Far Detector distribution is scaled by a factor of 2.6 for visualization.

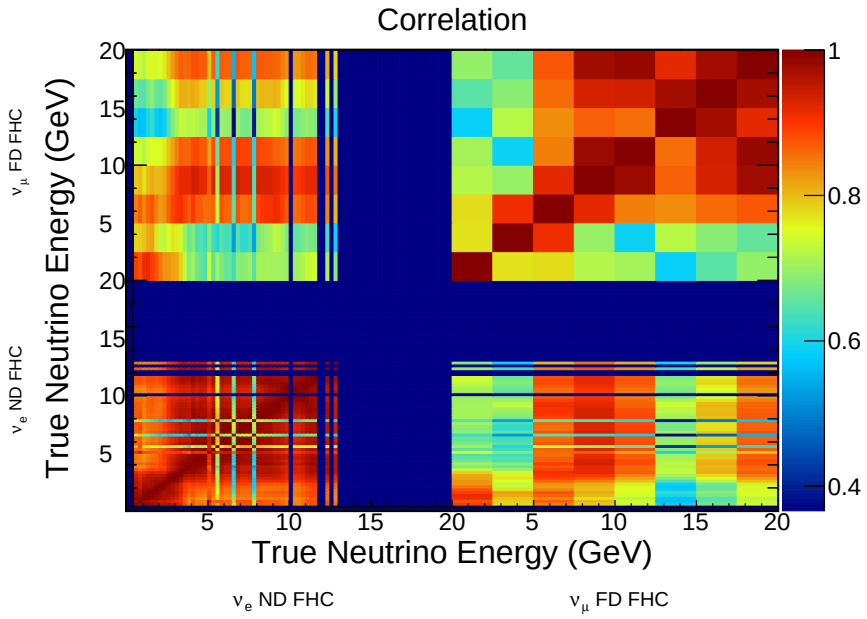

Figure 7.35: Correlation matrix between sets of Near Detector beam ν_e-contained and Far Detector ν_μ-uncontained kaon parent neutrinos in the 0-20 GeV true energy range. The bin size for the beam ν_e-sample is 0.25 GeV whereas for ν_μ-uncontained sample is 2.5 GeV. The blue bands in the Near Detector sample corresponds to no events selected. From the 10-20 GeV region in the Far Detector we can see a $60 - 80\%$ positive correlation with the 0-5 GeV region at the Near Detector.

covariance and correlation matrices these two extra samples, respectively. The Near Detector NC sample on the left (a1-b1) has less events selected, which translates in a coarser histogram. But at the same time, its peak almost matches with the Far Detector uncontained. When looking at the correlation between the two samples, we can see a 30% positive relationship between the 0-5 GeV Near Detector and 10-20 GeV Far Detector energy ranges. Finally, the Near Detector ν_μ CC uncontained sample has more events populating the covaraince matrix, with a peak around a similar energy range compared to the uncontained Far Detector sample. The correlation between these two samples shows also a 30% positive relationship between the 0-5 GeV Near Detector and 10-20 GeV Far Detector energy regions.

After looking at these three samples, we can conclude that there is a non-zero positive correlation between the 10-20 GeV signal region due to Far Detector uncontained events coming from the high energy kaon-component of the beam and the Near Detector most important backgrounds of the ν_e appearance signal.

In the next section, we will present an overview to the systematic uncertainties and discuss in detail the ones that are important for our study.

7.6 Systematic uncertainties

A description of the treatment of the systematic uncertainties for the uncontained sample is showed below. A main characteristic of this analysis is that low energy data (0-5 GeV) from the Near Detector data was not used to predict the high energy signal region (10-20 GeV) at the Far Detector.

7.6.1 Beam transport and hadron production

For the uncontained sample, both the beam transport systematic uncertainties, associated to the neutrino beam focusing, and the hadron production, which uses the PPFX method, are taken as shape only uncertainties. That is, the $\pm 1\sigma$ variation is area normalized to the nominal case and

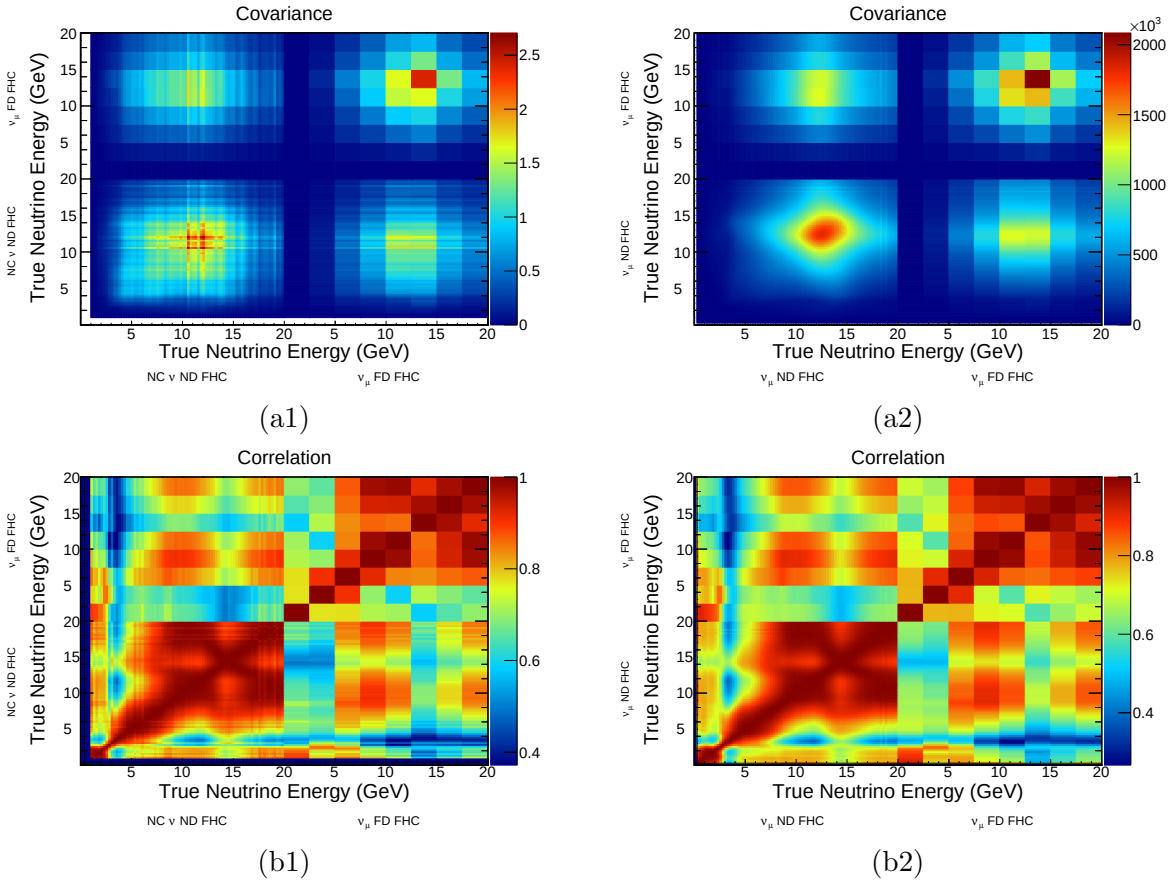

Figure 7.36: Covariance and correlation matrices between the Near Detector NC ν_μ-contained sample and the Far Detector ν_μ-CC uncontained sample (left), and the Near Detector ν_μ CC-uncontained sample and the Far Detector ν_μ-CC uncontained sample (right). Top row (a1-a2) shows the covariance between the two samples. The Far Detector has a scale of 0.7 and 6.5×10^5 was applied for visualization in order to compare to each Near Detector sample respectively. Bottom row (b1-b2) shows the correlation matrices. From the 10-20 GeV region in the Far Detector we can see a 30% positive correlation with the 0-5 GeV region at the Near Detector The bin size for the Near Detector sample is 0.25 GeV whereas for Far Detector sample is 2.5 GeV.

the resultant distribution added in quadrature to the rest. Since an indirect measurement of the neutrino flux is performed when looking at the neutrinos in the energy range 10-20 GeV, the shape only systematic uncertainty treatment helps avoid redundancy. The prescription took the top four largest principal components, optimized to cover the expected PPFX systematic uncertainty for the hadronic production. Similarly, all the eleven beam transport parameters were taken into account for the beam transport. Even the large normalization impact of the flux uncertainties, when taken the shape only, did not show as a mayor contribution to the overall uncertainty.

7.6.2 Muon and hadronic energy scales

The treatment of the muon energy scale systematic is slightly different to the one used for the main disappearance analysis, as described in Section 6.4.5. The 1% variation originally prescribed was applied to the input variable of the tuned estimator associated to the calorimetric energy of the selected track, instead of applying to the track length. Therefore, the variation gets applied at run time when requested. The prescription for the hadronic energy scale systematic did not change. It describes a 5% variation applied to both, the hadronic calorimetric energy coming from hits not associated to the muon-like track, and the hadronic energy contamination in the main muon-like track.

7.6.3 Calibration

The absolute energy calibration systematic uncertainty is expected to have a 5% variation from nominal, motivated by discrepancies between data and simulation related to non-muon particles. This variation is applied to all the events in a special dataset of files created for investigation purposes. But the tuned energy estimator developed for uncontained events is based mostly on muon-related variables, which we already know, have a 1% variation. Figure 7.37 shows the distribution of reconstructed neutrino energy for selected events with the absolute energy calibration variation. We expect the this variation to shift the distribution from right to left (or viceversa),

since increases (decreases) the energy response at the cell hit level. But given the size of the energy bins, the amount of events shifting one or more bins is expected to be small.

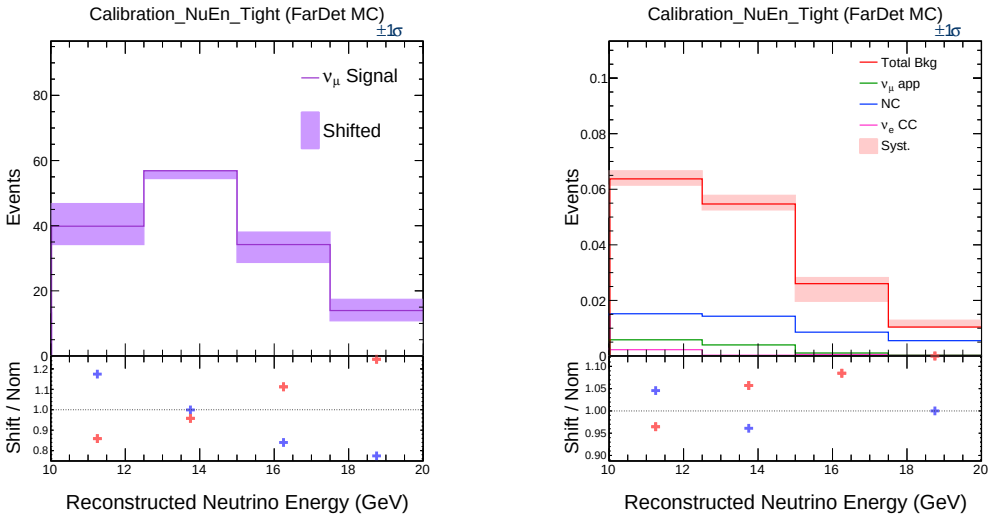

Figure 7.37: Distribution of reconstructed neutrino energy for selected simulated events in the signal region 10-20 GeV, including the absolute energy calibration variation. Left: Nominal versus shifted distributions for signal events only, with the shifted-nominal ratio. Right: Background decomposition of selected events in signal region with shifted-nominal ratio.

7.6.4 Cross section and final state interactions

The mayor impact in the overall systematic uncertainty comes from the final state interactions systematics, in particular, the ones associated with deep-inelastic interaction with pion multiplicity. GENIE prescribes that for each input physics quantity P, such as any simulated prediction, parameter of function, the uncertainty is taken into account as a systematic parameter x_P, modifying the physical quantity P as

$$P \mapsto P' = P\left(1 + x_p \cdot \frac{\delta P}{P}\right) \tag{7.11}$$

where δP is the estimated standard deviation of P. NOvA applies a 50% uncertainty to events with true hadronic invariant mass $W < 3$ GeV but only a 5% to events with $W \leq 3$ GeV (see Figure 7.38) for any DIS event with a neutrino-nucleon interacting producing 1,2 or 3 final state

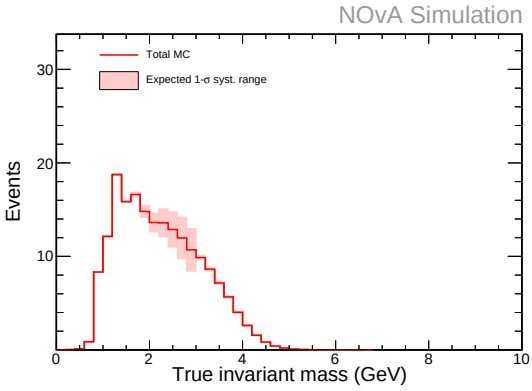

Figure 7.38: Distribution of the true invariant hadronic mass W for selected uncontained events with the deep-inelastic neutrino-neutron $CC3\pi$ interaction systematic uncertainty applied. A 50% variation is applied to events $W < 3$ whereas events with $W \leq 3$ have a 5% variation.

pions. Figure 7.39 shows the nominal and $\pm 1\sigma$ variation for both signal and background events in the case of the DIS neutrino-neutron $CC3\pi$ interaction. This systematic showed as the mayor contribution to the overall uncertainty when tabulated against all considered.

Nevertheless, evidence that the DIS pion multiplicity systematic uncertainty is overestimated in the 10-20 GeV signal region, is suggested as indicated by Figure 7.40. In the absence of any selection we notice that the systematic variations applied as weights according to Equation 7.11 tend to deviate from unity, suggesting the possibility that the well known value of the total cross section is not being conserved. Another important factor to consider is that any possible correlations between all the pion multiplicity DIS systematics are not taken into account.

7.6.5 Summary and impact

Although all the systematic uncertainties were considered in the final result, a list of the top 13 which have the largest impact in the measurement are shown in Table 7.17. The metric that helped to tabulate is given by Equation 7.12

$$val[i] = \frac{SystUp[i] - SystDown[i]}{SystUp[i] + SystDown[i]}, \qquad \text{(CC, 10-20 GeV)} \tag{7.12}$$

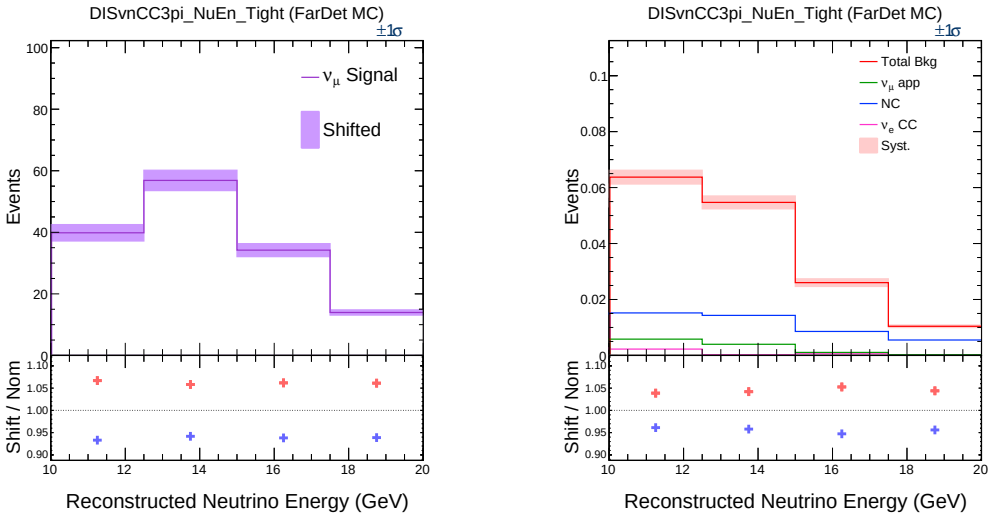

Figure 7.39: Distribution of reconstructed neutrino energy for selected simulated events in the signal region 10-20 GeV, including the deep-inelastic neutrino-neutron $CC3\pi$ reaction variation. Left: Nominal versus shifted distributions for signal events only, with the shifted-nominal ratio. Right: Background decomposition of selected events in signal region with shifted-nominal ratio.

where for the charged current component of each systematic in the region of 10-20 GeV, the integral of the difference between the $+1\sigma$ variation is subtracted from the integral of the -1σ variation and divided by their sum. As stated before, the main contributions come from the deep-inelastic neutrino-nucleon CC $N\pi$ interacting cross section. But recalling that a 15.5% of the events in the 10-20 GeV region arise from CC RES interactions, the second most important contribution comes from the axial mass M_A for CC resonance neutrino production, which is set to $\pm 20\%$.

A pictorial description of the systematic table summary is shown in Figure 7.41, where the size of each blue box reflects the uncertainty (in %) given by the Eq. 7.12 metric. The systematic uncertainty from the top 13 systematics added in quadrature corresponds to 12.39% for signal events, and 10.23% for background events. The statistical uncertainty for signal is $\approx 8\%$.

7.6.6 Systematic uncertainties not used

The following systematic uncertainties were cross-checked with thorough studies but we decided not to implement them in the final part of the analysis for reasons being explained below.

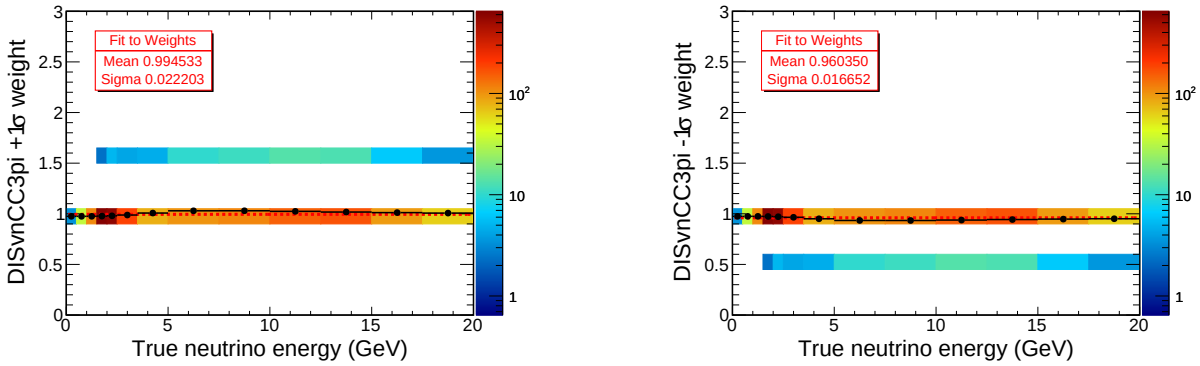

Figure 7.40: Deep-inelastic neutrino-neutron $CC3\pi$ interaction $\pm1\sigma$ weights with no selection applied.

7.6.6.1 Formation Zone

The Formation Zone systematic is a final state interaction (FSI) systematic uncertainty defined as the region in space and time needed to produce a hadron in its physical ground state. It is implemented in GENIE for all hadrons produced in deep-inleastic interactions, initialized as

$$f_z = \frac{pc\tau_0}{m},$$

where $\tau_0 = 0.342\text{fm}/c$ is the formation time, p is the hadron momentum, m is the hadron mass, and c is the speed of light. When the weights are calculated for each interaction, the formation zone is computed from the distance between the intranuclear vertex and the hadron position, as recorded at the beginning of the intranuclear cascade routine. The formation zone alters the amount of nuclear matter that the hadron must propagate before exiting the target nucleus. For example, if it gets shortened, more pions will be created out of events that began with a neutrino-neutron reaction, increasing the hadronic visible energy. As a systematic, the formation zone is modified as

$$f_z \mapsto f'_z = f_z \left(1 + x_{f_z} \cdot \frac{\delta f_z}{f_z}\right),$$

where $x_{f_z} = \{\ldots, -2, -1, +1, +2, \ldots\}$ and $\delta f_z / f_z$ is set to 50%. Figure 7.42 shows the distribution of reconstructed neutrino energy for selected uncontained events in the 10-20 GeV region. The

Table 7.17: Top 13 systematics with a variation of $\leq 1\%$ according to Eq. 7.12 in the 10-20 GeV region.

ID	Systematic name	1σ set value	Description	Impact on Signal (%)	Impact on Background (%)
1	DISvnCC3pi	50%,5%	DIS neutrino-neutron 3π uncertainty	6.17	3.95
2	MaCCRES	20%	Tweak axial mass M_a CC-RES (shape and norm)	4.39	5.20
3	DISvpCC3pi	50%,5%	DIS neutrino-proton 3π uncertainty	4.21	2.42
4	DISvnCC1pi	50%,5%	DIS neutrino-neutron 1π uncertainty	3.97	3.19
5	DISvnCC2pi	50%,5%	DIS neutrino-neutron 2π uncertainty	3.96	3.04
6	MECq0Shape	model	Empirical MEC with q_0 reshaped	3.96	3.82
7	RPAShapeenh	model	Stronger RPA enhancement at higher Q^2	3.12	2.16
8	MFP_pi	20%	Tweak to mean free path for pions	2.29	2.22
9	DISvpCC2pi	50%,5%	DIS neutrino-proton 2π uncertainty	2.16	1.42
10	MvCCRES	10%	Tweak vector mass M_v CC-RES (shape and norm)	2.09	2.55
11	DISvpCC0pi	50%,5%	DIS neutrino-proton 0π uncertainty	1.96	1.20
12	BhtBY	25%	Tweak Bodek-Yang model parameter B_{HT}	-1.43	-1.24
13	MFP_N	20%	Tweak to mean free path for neutrons	1.14	1.08

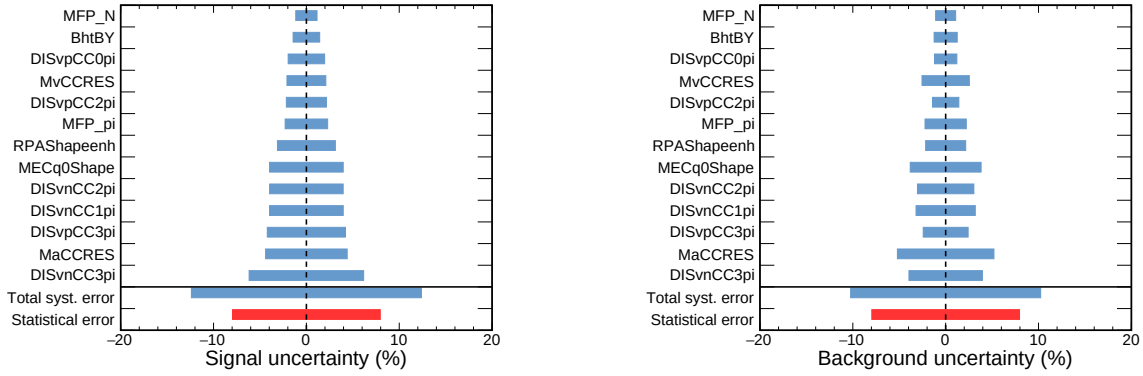

Figure 7.41: For the energy 10-20 GeV range, the total systematic uncertainty added in quadrature corresponds to 12.39% for signal events, and 10.23% for background events. The statistical uncertainty for signal is $100 \cdot \sqrt{158}/158 \approx 7.96\%$.

left side plot shows the nominal with the $\pm 1\sigma$ variation included for true signal events. The right side shows the $\pm 1\sigma$ variation but for background events. Intuitively, our expectation is that the formation zone would have no impact on the actual cross section, and only just impact the distributions of the final-state hadrons. But the large error bands in the signal region shown in the ratio as a $+5\%$, -13% effect, indicate something might be amiss at the energies relevant for this measurement.

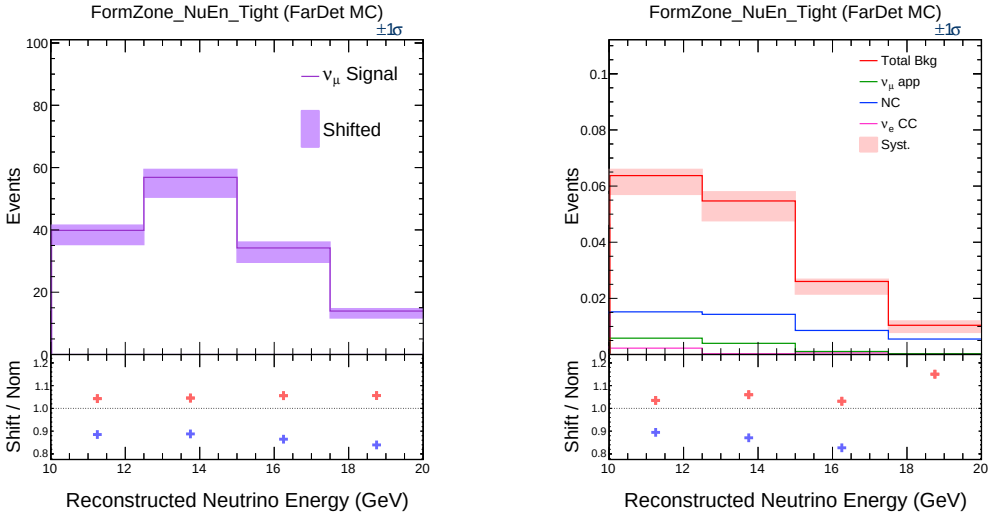

Figure 7.42: Distribution of reconstructed neutrino energy for selected simulated events in the signal region 10-20 GeV, including the formation zone variation. Left: Nominal versus shifted distributions for signal events only, with the shifted-nominal ratio. Right: Background decomposition of selected events in signal region with shifted-nominal ratio.

The result of comparing the formation zone weights applied to the neutrino events as a function of the true energy is shown in Figure 7.43. The black points represent the average value for each X-axis bin of the 2D histogram, whereas the red-dashed line shows a linear fit to a constant from 0-20 GeV. Once again, our expectation is not met since deviations from unity are clearly visible, at least for the -1σ case.

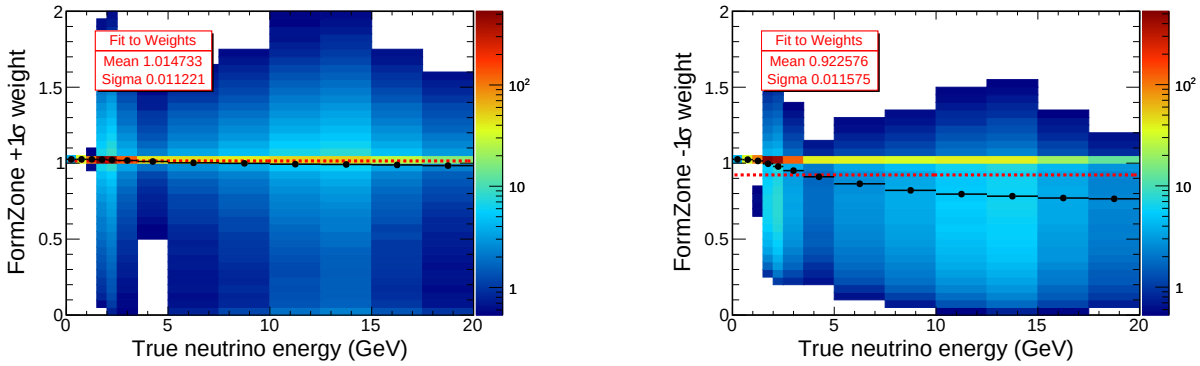

Figure 7.43: Formation zone $\pm 1\sigma$ weights with no selection applied.

7.6.6.2 Light yield modeling

The light level systematic uncertainty is related to the addition of Cherenkov light modeling into the NOvA custom simulation. As discussed in the previous chapter, three special datasets were created (a modified nominal and two shifted). Unfortunately, discrepancies in the $\pm 1\sigma$ shifted variations with respect to the nominal were found (see Fig. 7.44). When comparing with the contained sample in the oscillation region 0-5 GeV, such discrepancies are absent, indicating a possible cancellation by means of the extrapolation method, which uses the Near Detector information. But since by construction, this analysis does not use Near Detector data, the discrepancies persist. In the end, it was decided not to include this systematic in the final result.

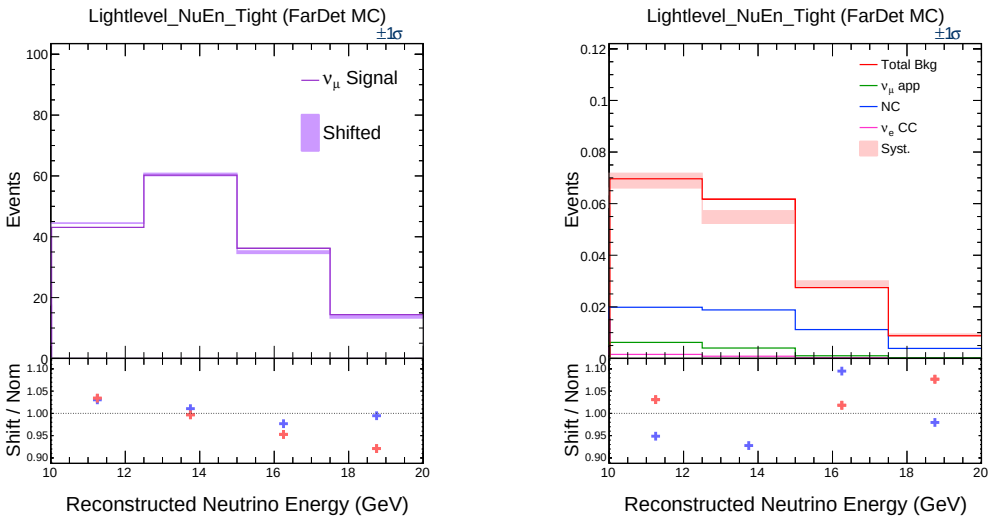

Figure 7.44: Distribution of reconstructed neutrino energy for selected simulated events in the signal region 10-20 GeV, including light level variation. Left: Nominal versus shifted distributions for signal events only, with the shifted-nominal ratio. Right: Background decomposition of selected events in signal region with shifted-nominal ratio. Note the small discrepancies between nominal and shifted distributions.

7.7 Results and discussion

We discuss the results obtained after looking at the Far Detector data in the region of 10-20 GeV. Comparison with our simulation prediction with systematics applied followed by the measurement of the kaon normalization scale will be presented.

7.7.1 Data sets and events selected

The datasets used for this analysis correspond to Periods 2, 3 and 5 in forward horn current (FHC) NuMI neutrino beam mode which dates from the 24th of October, 2014 to February 20th, 2017. The early data coming from Period 1 was decided not to be used for this analysis, given the large fraction of Far Detector runs with incomplete active detector. The total POT accumulated in the analysis without data from Period 1 corresponds to 8.25×10^{20} POT, dropping to the final

7.99×10^{20} POT after applying a full 14-diblock detector spill quality cut and a cosmic veto cut as part of data quality.

The main simulation sample corresponds to 7.11×10^{24} POT after exactly the same preselection and data quality cuts were applied as in the data.

A sample of uncontained data events are shown in Figures 7.8, 7.10, and 7.11. As expected, the interaction vertex and hadronic system are contained within the boundaries of the detector but the long track associated to the final state muon is leaving the detector. All these events are shown within the 10 μs spill window.

7.7.2 Uncontained events and $(\sin^2\theta_{23}, \Delta m^2_{32})$ sensitivity

We explored the posibility of using the uncontained muon neutrino sample in the 0-20 GeV energy region combined with the contained muon neutrino sample in order to test whether or not the sensitivity to $(\sin^2\theta_{23}, \Delta m^2_{32})$ improves. The result is shown in Figure 7.45. The solid blue line represents the 90% C.L sensitivity contour for the contained muon neutrino sample, with neither no systemtics or cosmic background applied. The dashed-red line represents the 90% C.L sensitivity contour for the uncontained muon neutrino sample, similarly with neither no systematics nor cosmic background applied. The red and blue (superimposed) dots represent the best fit values. It was found that the ν_μ-CC uncontained sample has a minimal impact ($\sim$ 3%) on the $(\sin^2\theta_{23}, \Delta m^2_{32})$ sensitivity, even when combined with the contained sample and when the uncontained events use true energy during the fit [149].

7.7.3 Measurement of the kaon normalization scale

A measurement of the normalization scale from neutrinos originated from kaons is made using the muon neutrino uncontained events in the range 10-20 GeV at the Far Detector. As we discussed earlier, a well known prediction of expected neutrino flux is required for long-baseline neutrino experiments. This flux is used to measure neutrino cross sections and sterile neutrino searches at

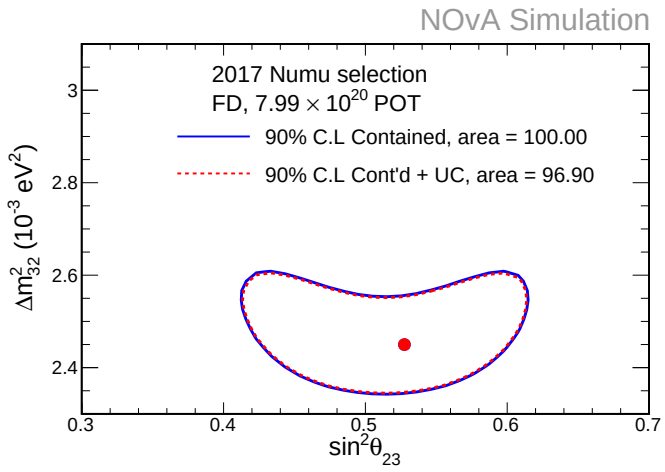

Figure 7.45: Sensitivity contours (stats only) with the contained sample (in blue) using reconstructed neutrino energy and combined uncontained sample (dashed red) using true energy assuming maximal mixing. The red and blue (superimposed) dots show the best fit result. The additional sample improves the sensitivity contour by $\sim 3\%$.

the Near Detector, while at the Far Detector it gives an estimate of the predicted number of signal events after oscillations. From Chapter 2, the NuMI beam contains neutrinos from the decay of kaons and pions, which are generated by proton collisions in the carbon target. Due to the random decay position of this pions and kaons, the neutrino beam is far from being monochromatic, and contains a significant mixture of different neutrino flavors $\nu_e, \overline{\nu}_e, \overline{\nu}_\mu$ ($\overline{\nu}_e, \nu_e, \nu_\mu$) in addition to the main component ν_μ ($\overline{\nu}_\mu$). This mixture of neutrinos from different kinds is an major source of systematic uncertainties.

Historically, there have been measurements of the charged pion production yields off the NuMI target [127] and flux predictions using all available data from hadron production [18], but the yield of kaon production has not been well measured [94].

We developed a measurement of the kaon flux normalization scale using uncontained events in the 10-20 GeV range at the Far Detector. It has been shown that the muon neutrino energy spectrum is dominated by neutrinos coming from kaons in this energy range. In addition, this sample is a relatively high statistics sample, with the main source of background -cosmic ray induced

muons- kept at a minimum thanks to the selection criteria discussed in Section 7.2. Finally, the ν_μ CC interactions have a well defined and clear signal, with a high energy muon emitted from the interaction attached to the vertex with the contained hadronic system. By measuring the data/MC ratio of the selected uncontained events at the Far Detector we expect to have a constraint in the uncertainty of the kaon normalization scale. Previous works used Near Detector data [110, 50, 170] to give an estimate of the kaon component for the ν_e-appearance analysis. But the nalysis here described uses Far Detector data for the first time.

We define the kaon scale as the ratio

$$S_K = \frac{\sum_j (N_{\nu_\mu}^{FDdata} - N_{\nu_\mu CC}^{\pi} - N_{\nu}^{beam} - N^{cosmics})}{\sum_j (N_{\nu_\mu CC}^{K})} \tag{7.13}$$

where $N_{\nu_\mu}^{FDdata}$ is the number of uncontained selected events from the Far Detector data, $N_{\nu_\mu CC}^{\pi}$ is the charged-current pion-component of neutrinos in the 10-20 GeV region, N_{ν}^{beam} is the neutral current and beam ν_e expected backgrounds, $N^{cosmics}$ the expected cosmic background and $N_{\nu_\mu CC}^{K}$ the charged current kaon component from simulation.

The results after looking at data are as follows. Figure 7.46 shows the Far Detector data in black points with poisson errors, the red solid line represents the total simulation prediction with oscillation parameter $\sin^2\theta_{23} = 0.558$ and Δm^2_{32} and all backgrounds included, the light-red error bands represent the 1σ systematic error variations in quadrature including oscillation parameters uncertainty, as well as the cosmic normalization uncertainty. The dashed cyan line represents the charged current pion component from simulation, dashed red the charged current kaon component, dashed gray the cosmic ray expected background, and in solid magenta, the neutral current with beam ν_e backgrounds combined. As we noted, the data agrees with the prediction within errors.

The result of the measurement is given by the ratio in Figure 7.47. After subtracting the charged current pion, beam and cosmic components from the selected data, the kaon data component is normalized by the kaon charged current component from simulation. The error bars are computed in quadrature using propagation of errors and including all the systematic, cosmic, and beam plus neutral current components in them. The dashed blue line represents the value of unity, for

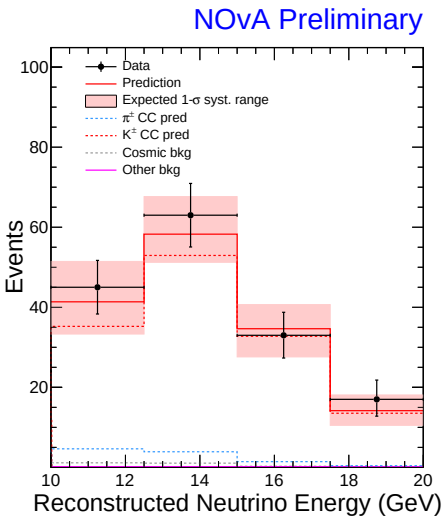

Figure 7.46: Predictions with parameter $\sin^2\theta_{23} = 0.558$ fixed and Δm^2_{32} with uncertainties.

reference, the dashed red represents the linear fit over the four data points. The final result of the fit is quoted as $S_K = 1.07 \pm 0.16$.

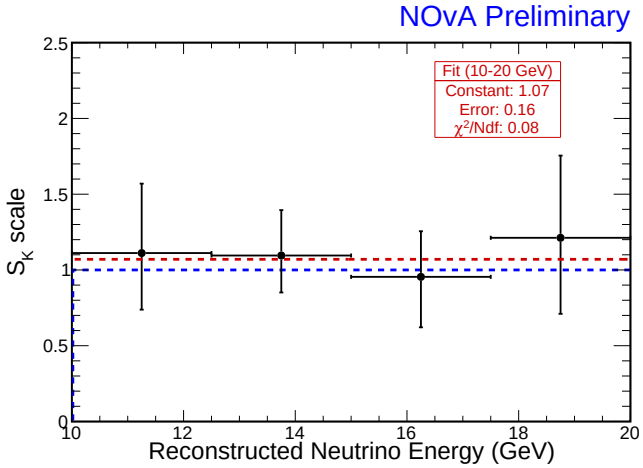

Figure 7.47: Ratio with $\sin^2\theta_{23} = 0.558$ fixed and Δm^2_{32} with uncertainties.

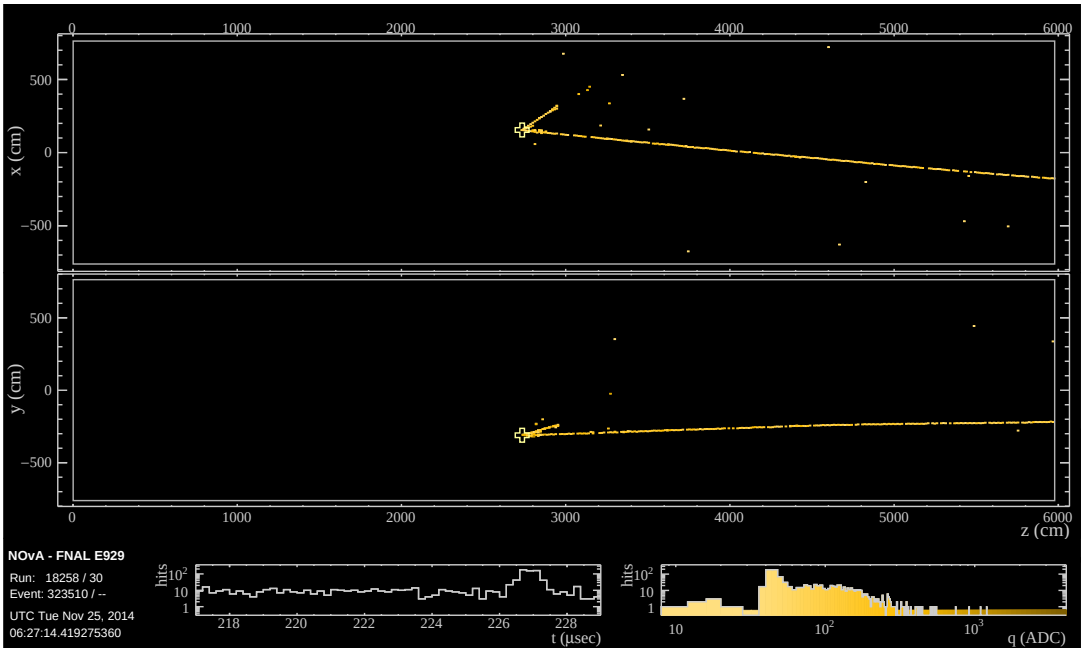

(a)

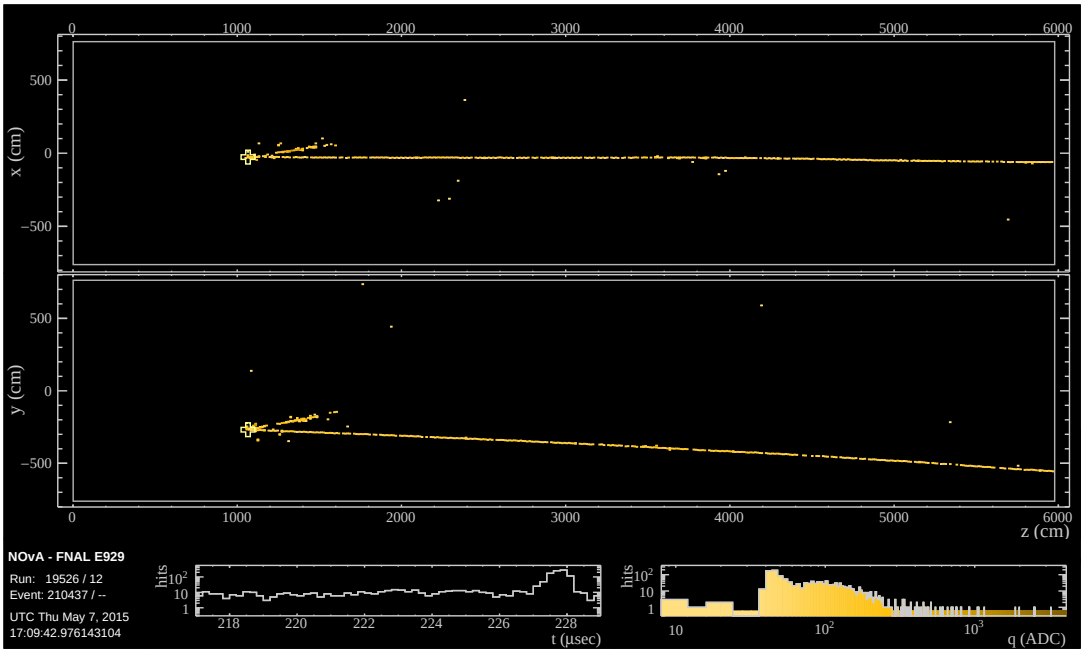

(b)

Figure 7.48: Event display of selected uncontained events in the 10-20 GeV range at the Far Detector.

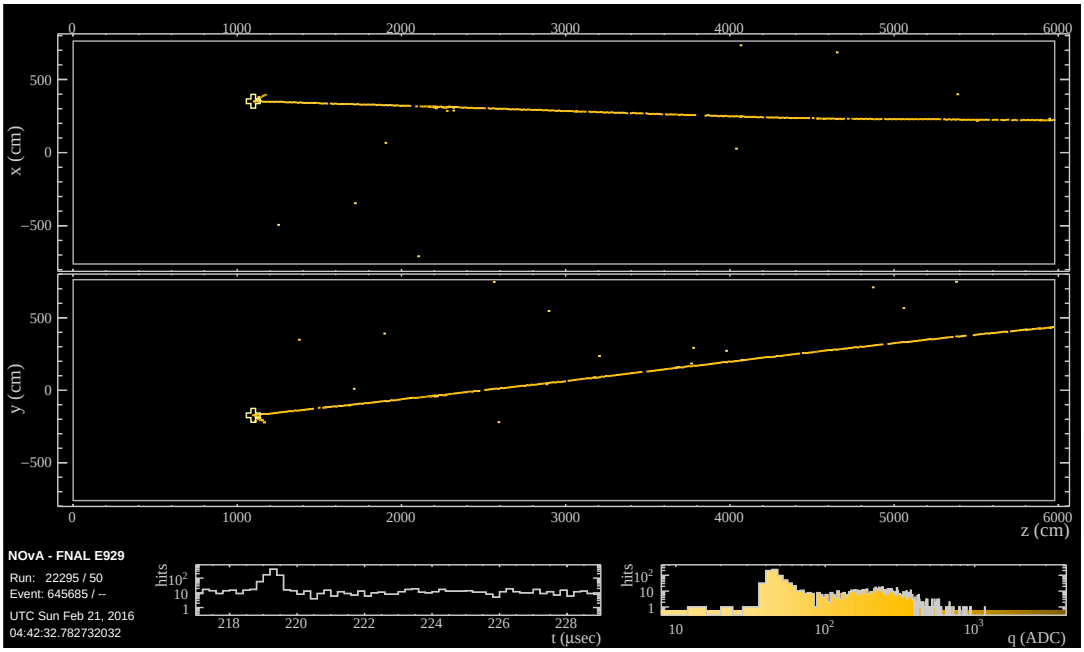

(a)

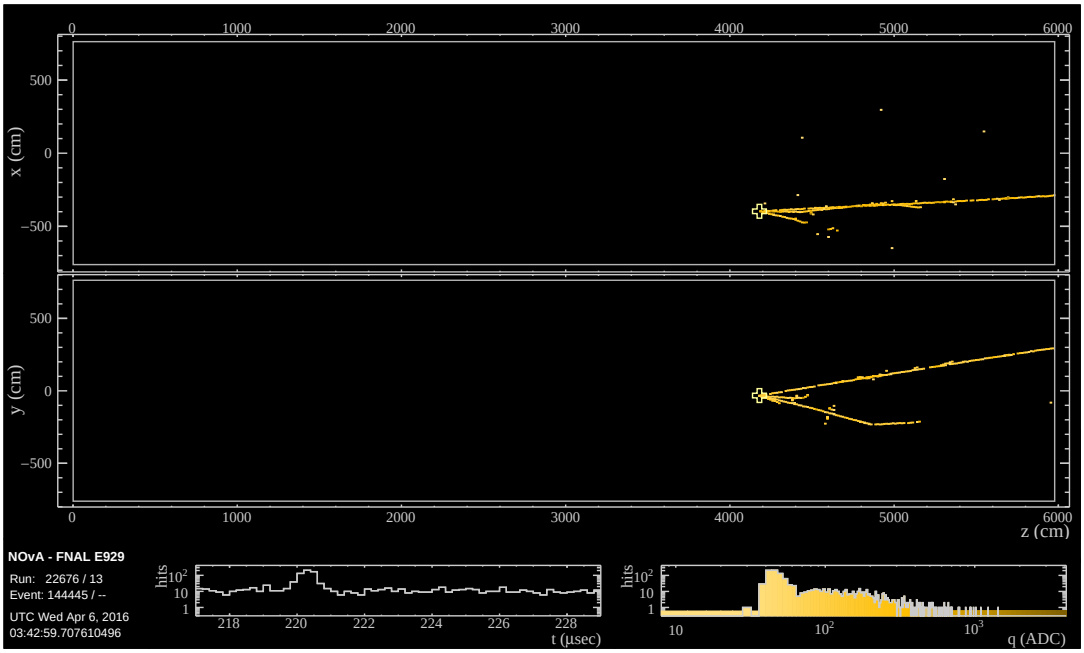

(b)

Figure 7.49: Event display of selected uncontained events in the 10-20 GeV range at the Far Detector.

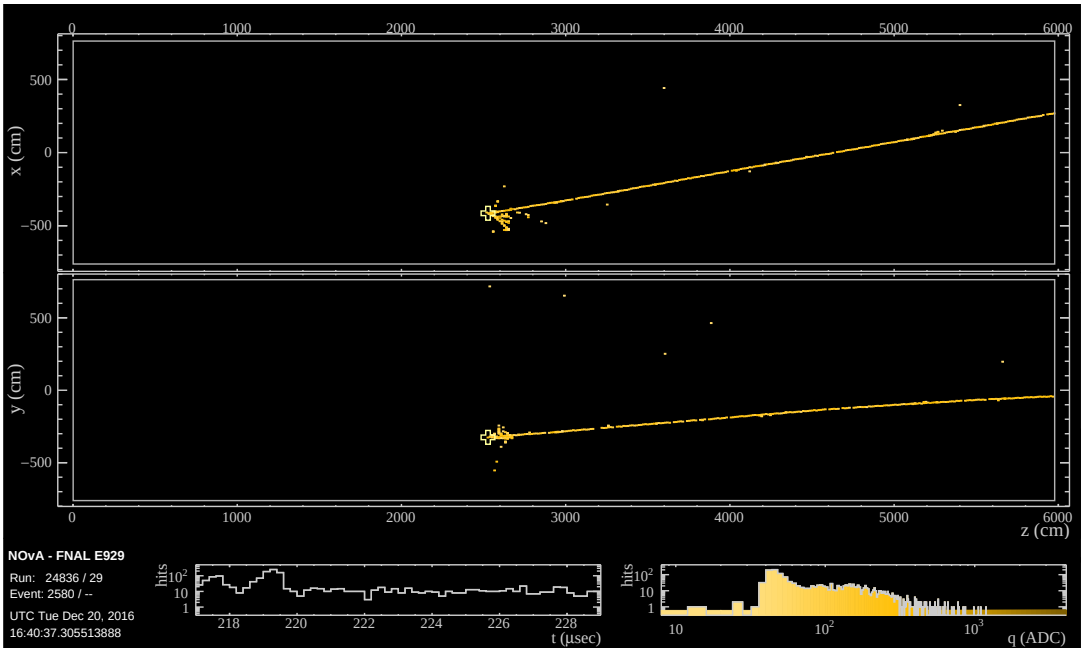

(a)

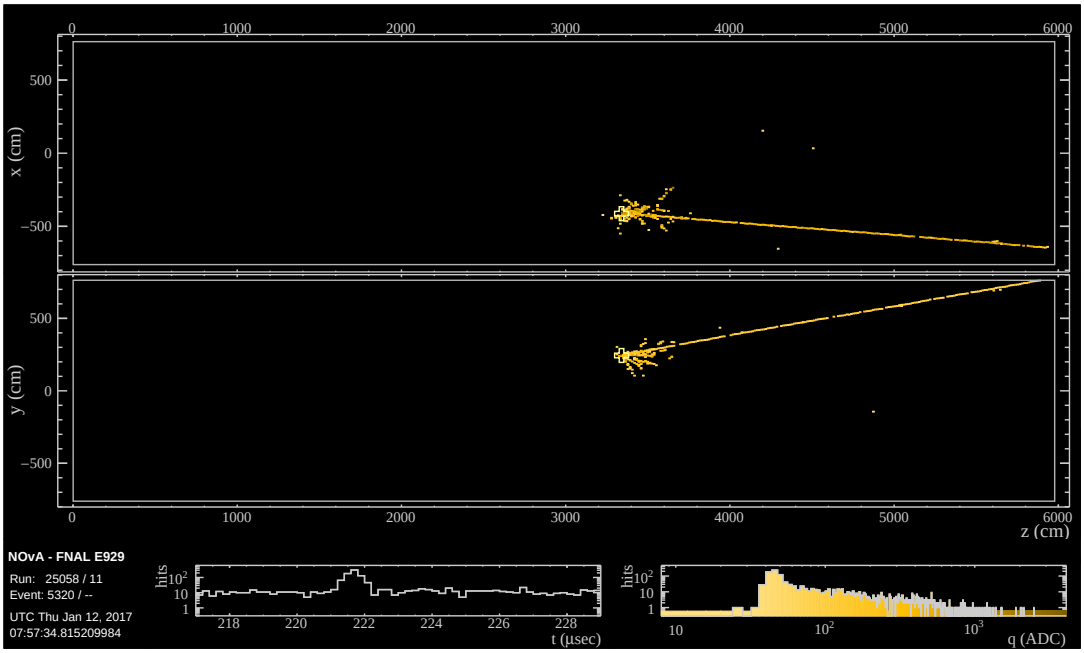

(b)

Figure 7.50: Event display of selected uncontained events in the 10-20 GeV range at the Far Detector.

CHAPTER 8. CONCLUSION

Neutrinos are among the most abundant yet most elusive known particles in the universe. Significant understanding of the neutrino properties was achieved thanks to the several experiments developed in the last six decades.

NOvA is a neutrino oscillation experiment with the longest baseline of any accelerator experiment at the time, and user of the most intense neutrino beam currently build from Fermilab. The two functionally similar, high sampling, liquid scintillator calorimeters, are 14 mrad off-axis from the beam, providing a neutrino flux narrowly peaked at around 2 GeV. It is designed to address the important open questions in the neutrino sector through precision measurements of $\nu_e/\overline{\nu}_e$ appearance and $\nu_\mu/\overline{\nu}_\mu$ disappearance.

Accelerator based experiments require a reliable prediction of both the main component of the neutrino flux and its background. This is because the neutrino flux is used as input for measuring neutrino cross sections and provides an estimate of the expected signal for neutrino oscillation analysis. The main uncertainty for the prediction of the neutrino flux in accelerator based experiments comes from uncertainties associated to the interaction of hadrons in the nuclear target. NOvA uses a comprehensive flux prediction package that uses all available and relevant hadron production data. It uses data from the pion and kaon yields measured by the MIPP and NA49 experiments. In NOvA, the uncertainty in the integrated flux prediction from the 0-20 GeV energy range is around 8%.

A measurement was made of the kaon production normalization scale using uncontained charged current muon neutrinos at the Far Detector. The kaon component of the beam contributes to the intrinsic ν_e contamination, a key background for the ν_e-appearance analysis. We also explored the link of the uncontained sample at the Far Detector to events in the Near Detector such as the

neutral current background for muon neutrinos, and the uncontained sample of muon neutrinos, another background for the ν_e-appearance analysis.

We developed a custom selection for these events, with an overall efficiency of 32% in the 0-20 GeV energy range. Using multivariate techniques, a cosmic rejection PID was developed based on boosted decision trees. The signal selection efficiency of this classifier is 95.5%, allowing to reduce the cosmic background seven orders of magnitude, while keeping the signal 29 times larger after all cuts applied. A custom energy estimator, also based on boosted decision trees, was developed in order to reconstruct the energy of the escaping muon. A neutrino energy fractional resolution of 25% was achieved after combining the muon energy estimator with the hadronic energy estimator, tuned for contained events. In terms of systematic uncertainties, the main contributions arise from deep-inelastic neutrino-nucleon CC $N\pi$ interaction cross sections. The current prescription sets the $\pm 1\sigma$ value to 50% for events with hadronic invariant mass $W < 3$ GeV, but only a 5% to events with $W \leq 3$ GeV. We believe further investigation on this topic is needed, since correlations among these systematics are not taken into account, resulting in a conservative measurement of the kaon normalization scale.

We observed that around 94% of the uncontained muon neutrinos in the 10-20 GeV region corresponds to the kaon component of the NuMI beam at the Far Detector. We also found a 60-80% correlation between the Near Detector ν_e background and the Far Detector ν_μ uncontained signal.

We measured the kaon production normalization scale to be $S_K = 1.07 \pm 0.16$ after applying a linear fit in the 10-20 GeV energy region of the data/simulation ratio.

Bibliography

[1] Abazajian, K. N. et al. (2012). Light Sterile Neutrinos: A White Paper.

[2] Abazov, A. I. et al. (1991). Search for neutrinos from the sun using the reaction ^{71}Ga(ν_e,e^-)^{71}ge. *Phys. Rev. Lett.*, 67:3332–3335.

[3] Abe, K. et al. (2017). Combined Analysis of Neutrino and Antineutrino Oscillations at T2K. *Phys. Rev. Lett.*, 118(15):151801.

[4] Abe, Y. et al. (2012). Indication of reactor $\overline{\nu}_e$ disappearance in the double chooz experiment. *Phys. Rev. Lett.*, 108:131801.

[5] Abi, B. et al. (2018). The DUNE Far Detector Interim Design Report Volume 1: Physics, Technology and Strategies.

[6] Accelerator Division, O. D. (2013 (accessed December 18, 2017)). *Concepts Rockie Book*. http://operations.fnal.gov/rookie_books/concepts.pdf.

[7] Adamson, P. et al. (2008). Study of muon neutrino disappearance using the fermilab main injector neutrino beam. *Phys. Rev. D*, 77:072002.

[8] Adamson, P. et al. (2014). Combined analysis of ν_μ disappearance and $\nu_\mu \rightarrow \nu_e$ appearance in minos using accelerator and atmospheric neutrinos. *Phys. Rev. Lett.*, 112:191801.

[9] Adamson, P. et al. (2016). The NuMI Neutrino Beam. *Nucl. Instrum. Meth.*, A806:279–306.

[10] Adamson, P. et al. (2017a). Constraints on Oscillation Parameters from ν_e Appearance and ν_μ Disappearance in NOvA. *Phys. Rev. Lett.*, 118(23):231801.

[11] Adamson, P. et al. (2017b). Measurement of the neutrino mixing angle θ_{23} in NOvA. *Phys. Rev. Lett.*, 118(15):151802.

[12] Agostinelli, S. et al. (2003). Geant4—a simulation toolkit. *Nuclear Instruments and Methods in Physics Research Section A: Accelerators, Spectrometers, Detectors and Associated Equipment*, 506(3):250 – 303.

[13] Agostini, M. et al. (2017). Background free search for neutrinoless double beta decay with GERDA Phase II. [Nature544,47(2017)].

[14] Aguilar-Arevalo, A. A. et al. (2009a). Neutrino flux prediction at miniboone. *Phys. Rev. D*, 79:072002.

[15] Aguilar-Arevalo, A. A. et al. (2009b). The MiniBooNE Detector. *Nucl. Instrum. Meth.*, A599:28–46.

[16] Ahmad, Q. R. et al. (2001). Measurement of the rate of $\nu_e + d \rightarrow p + p + e^-$ interactions produced by ^8b solar neutrinos at the sudbury neutrino observatory. *Phys. Rev. Lett.*, 87:071301.

[17] Ahn, J. K. et al. (2012). Observation of reactor electron antineutrinos disappearance in the reno experiment. *Phys. Rev. Lett.*, 108:191802.

[18] Aliaga Soplin, L. (2016). *Neutrino Flux Predictions for the NuMI Beamline*. PhD thesis, William-Mary Coll.

[19] Alion, T. (June 12, 2016). *Absolute Calibration and shape systematic*. NOvA internal document (docdb-20388).

[20] Alion, T. (September 21, 2017). *Third analysis calorimetric energy scale in the NOvA detectors*. NOvA internal document (docdb-13579).

[21] Alt, C. et al. (2007). Inclusive production of charged pions in p+C collisions at 158-GeV/c beam momentum. *Eur. Phys. J.*, C49:897–917.

[22] An, F. P. et al. (2012). Observation of electron-antineutrino disappearance at daya bay. *Phys. Rev. Lett.*, 108:171803.

[23] Andreopoulos, C. et al. (2010). The genie neutrino monte carlo generator. *Nuclear Instruments and Methods in Physics Research Section A: Accelerators, Spectrometers, Detectors and Associated Equipment*, 614(1):87 – 104.

[24] Andreopoulos, C. et al. (2015). The GENIE Neutrino Monte Carlo Generator: Physics and User Manual.

[25] Antonello, M. et al. (2015). A Proposal for a Three Detector Short-Baseline Neutrino Oscillation Program in the Fermilab Booster Neutrino Beam.

[26] Arnaboldi, C. et al. (2004). CUORE: A Cryogenic underground observatory for rare events. *Nucl. Instrum. Meth.*, A518:775–798.

[27] Arrieta-Diaz, E. (March 6, 2012). *Tracker's Performance*. NOvA internal document (docdb-7189).

[28] Ashie, Y. et al. (2005). Measurement of atmospheric neutrino oscillation parameters by Super-Kamiokande I. *Phys. Rev. D*, 71(11):112005.

[29] Auger, M. et al. (2012). Search for Neutrinoless Double-Beta Decay in ^{136}Xe with EXO-200. *Phys. Rev. Lett.*, 109:032505.

[30] Aurisano, A. (June 25, 2015). *The NOvA Detector Simulation*. NOvA internal document (docdb-13577).

[31] Aurisano, A. (September 22, 2017). *Tech note: 2017 light model*. NOvA internal document (docdb-23228).

[32] Aurisano, A. et al. (2016). A Convolutional Neural Network Neutrino Event Classifier. *JINST*, 11(09):P09001.

[33] Aurisano, A. and Samaylov, O. (November 4, 2016). *Detector Simulation sign-off*. NOvA internal document (docdb-16475).

[34] Backhouse, C. (April 5, 2012). *Threshold effects in attenuation calibration.* NOvA internal document (docdb-7247).

[35] Backhouse, C. (November 25, 2014). *The CAFAna Framework.* NOvA internal document (docdb-9222).

[36] Bahcall, J. (2002). *Solar neutrinos: the first thirty years.* Advanced book program. Westview Press.

[37] Baird, M. (November 26, 2012). *Global Vertex Reconstruction beginning with a Modified Hough Transform.* NOvA internal document (docdb-8241).

[38] Baird, M. et al. (2015). Event reconstruction techniques in nova. *Journal of Physics: Conference Series*, 664(7):072035.

[39] Baird, M. D. (2015). *An Analysis of Muon Neutrino Disappearance from the NuMI Beam Using an Optimal Track Fitter.* PhD thesis, Indiana U.

[40] Bays, K. (May 1, 2014). *NOvA Cosmic Rejection package.* NOvA internal document (docdb-11205).

[41] Bays, K. (September 13, 2017). *Cosmic rejection technical note.* NOvA internal document (docdb-11205).

[42] Behera, B. (February 9, 2017). *Drift calibration.* NOvA internal document (docdb-16484).

[43] Behera, B. et al. (2017). Event Reconstruction in the NOvA Experiment. In *Meeting of the APS Division of Particles and Fields (DPF 2017) Batavia, Illinois, USA, July 31-August 4, 2017.*

[44] Birks, J. B. (1953). Theory of the response of organic scintillation crystals to short-range particles. *Phys. Rev.*, 90:1131–1131.

[45] Bishai, M. (2012). Determining the neutrino flux from accelerator neutrino beams. *Nuclear Physics B - Proceedings Supplements*, 229-232:210 – 214. Neutrino 2010.

[46] Bodek, A. and Yang, U. K. (2003). Higher twist, xi(omega) scaling, and effective LO PDFs for lepton scattering in the few GeV region. *J. Phys.*, G29:1899–1906.

[47] Boehm, F. and Vogel, P. (1992). *Physics of massive neutrinos*. Cambridge University Press.

[48] Böhlen, T. et al. (2014). The fluka code: Developments and challenges for high energy and medical applications. *Nuclear Data Sheets*, 120:211 – 214.

[49] Campbell, M. (September 15, 2017). *3A attenuation calibration*. NOvA internal document (docdb-13579).

[50] Catano-Mur, E. (October 3, 2017). *BEN decomposition technote*. NOvA internal document (docdb-23174).

[51] Chau, L.-L. and Keung, W.-Y. (1984). Comments on the parametrization of the Kobayashi-Maskawa Matrix. *Phys. Rev. Lett.*, 53:1802–1805.

[52] Chou, C. N. (1952). The nature of the saturation effect of fluorescent scintillators. *Phys. Rev.*, 87:904–905.

[53] Cleveland, B. T. et al. (1998a). Measurement of the solar electron neutrino flux with the homestake chlorine detector. *The Astrophysical Journal*, 496(1):505.

[54] Cleveland, B. T. et al. (1998b). Measurement of the Solar Electron Neutrino Flux with the Homestake Chlorine Detector. *Astrophysical Journal*. Presented at Fourth International Solar Neutrino Conference, Heidelberg, Germany, 8-11 Apr 1997, pp. 85-108.

[55] Collaboration, T. N. and et al, D. A. (2005). Nova proposal to build a 30 kiloton off-axis detector to study neutrino oscillations in the fermilab numi beamline.

[56] Colo, M. (October 3, 2017). *Tech Note - Cross section systematics for the numu 2017 analysis*. NOvA internal document (docdb-23844).

[57] Cooper, J. (July 13, 2015b). *Summary for the mass of the NOvA Near Detector*. NOvA internal document (docdb-11906).

[58] Cooper, J. (July 8, 2015a). *Summary for the mass of the NOvA Far Detector*. NOvA internal document (docdb-11905).

[59] Cover, T. and Hart, P. (1967). Nearest neighbor pattern classification. ieee trans inf theory it-13(1):21-27. 13:21–27.

[60] Cowan, C. et al. (1956). Detection of the free neutrino: a confirmation. *Science*, 124(3212):103–104.

[61] Cremonesi, L. et al. (July 27, 2017). *Numi flux systematic uncertainties for the NOvA third analysis*. NOvA internal document (docdb-17608).

[62] Criminisi, A. et al. (2011). Decision forests for classification, regression, density estimation, manifold learning and semi-supervised learning. Technical report, Microsoft Research Ltd.

[63] Danby, G. et al. (1962). Observation of High-Energy Neutrino Reactions and the Existence of Two Kinds of Neutrinos. *Phys. Rev. Lett.*, 9:36–44.

[64] D'Angelo, D. (2012). Low Energy Neutrino Measurements. *Pramana*, 79:757–780.

[65] Davies, G. (January 5, 2012b). *CosmiTrack Review*. NOvA internal document (docdb-6890).

[66] Davies, G. (March 30, 2012a). *CosmiTrack: Performance*. NOvA internal document (docdb-7230).

[67] Davies, G. and Vasel, J. (September 15, 2017). *A tech note on cosmic overlays for NOvA analysis*. NOvA internal document (docdb-23378).

[68] Ellis, C. D. and Wooster, W. A. (1927). The average energy of disintegration of radium E. *Proceedings of the Royal Society (London)*, A117:109–123.

[69] Ester, M. et al. (1996). A density-based algorithm for discovering clusters a density-based algorithm for discovering clusters in large spatial databases with noise. In *Proceedings of the Second International Conference on Knowledge Discovery and Data Mining*, KDD'96, pages 226–231. AAAI Press.

[70] et. al., D. D. (1990). A precise determination of the number of families with light neutrinos and of the z boson partial widths. *Physics Letters B*, 235(3):399 – 411.

[71] et. al., M. P. (1976). Properties of anomalous eμ events produced in e+e- annihilation. *Physics Letters B*, 63(4):466 – 470.

[72] Fermilab. *G4NuMI*.

[73] Fermilab (2016 (accessed December 18, 2017)). *Fermilab's Accelerator Complex*. https://www.fnal.gov/pub/science/particle-accelerators/accelerator-complex.html.

[74] Fernandes, L. A. and Oliveira, M. M. (2008). Real-time line detection through an improved hough transform voting scheme. *Pattern Recognition*, 41(1):299 – 314.

[75] Ferrari, A. et al. (2005). FLUKA: A multi-particle transport code (Program version 2005).

[76] Feynman, R. P., Kislinger, M., and Ravndal, F. (1971). Current matrix elements from a relativistic quark model. *Phys. Rev.*, D3:2706–2732.

[77] Freund, Y. and Schapire, R. E. (1997). A decision-theoretic generalization of on-line learning and an application to boosting. *Journal of Computer and System Sciences*, 55(1):119 – 139.

[78] Friedman, J. H. (2000). Greedy function approximation: A gradient boosting machine. *Annals of Statistics*, 29:1189–1232.

[79] Fruhwirth, R. (1987). Application of Kalman filtering to track and vertex fitting. *Nucl. Instrum. Meth.*, A262:444–450.

[80] Fukuda, Y. et al. (1996). Solar neutrino data covering solar cycle 22. *Phys. Rev. Lett.*, 77:1683–1686.

[81] Fukuda, Y. et al. (1998). Evidence for oscillation of atmospheric neutrinos. *Phys. Rev. Lett.*, 81:1562–1567.

[82] Furry, W. H. (1939). On transition probabilities in double beta-disintegration. *Phys. Rev.*, 56:1184–1193.

[83] Gando, A. et al. (2016). Search for Majorana Neutrinos near the Inverted Mass Hierarchy Region with KamLAND-Zen. *Phys. Rev. Lett.*, 117(8):082503. [Addendum: Phys. Rev. Lett.117,no.10,109903(2016)].

[84] Germani, S. (June 13, 2017). *Recap and update on dE/dx along tracks.* NOvA internal document (docdb-20399).

[85] Giunti, C. and Kim, C. (2007). *Fundamentals of Neutrino Physics and Astrophysics.* Oxford University Press, Oxford.

[86] Gran, R. (2017). Model Uncertainties for Valencia RPA Effect for MINERvA.

[87] Groom, D. E. et al. (2001). Muon stopping power and range tables 10 mev–100 tev. *Atomic Data and Nuclear Data Tables*, 78(2):183 – 356.

[88] Grupen, C., Shwartz, B., and Spieler, H. (2008). *Particle detectors.* Number 26 in Cambridge monographs on particle physics, nuclear physics, and cosmology. Cambridge University Press.

[89] Hampel, W. et al. (1999). GALLEX solar neutrino observations: Results for GALLEX IV. *Phys. Lett.*, B447:127–133.

[90] Hartsell, B. (April 7, 2016). *Beryllium Fins in the NOvA Target.* NOvA internal document (docdb-9880).

[91] Hirata, K. et al. (1987). Observation of a neutrino burst from the supernova sn1987a. *Phys. Rev. Lett.*, 58:1490–1493.

[92] Hubel, D. H. and Wiesel, T. N. (1968). Receptive fields and functional architecture of monkey striate cortex. *Journal of Physiology (London)*, 195:215–243.

[93] Iocco, F. et al. (2009). Primordial Nucleosynthesis: from precision cosmology to fundamental physics. *Phys. Rept.*, 472:1–76.

[94] Ives, S. J. (2012). *Study of the kaon contribution to the T2K neutrino beam using neutrino interactions in the Near Detector*. PhD thesis, Imperial Coll., London.

[95] Jackson, J. (1975). *Classical electrodynamics*. Wiley.

[96] James, F. and Roos, M. (1975). MINUIT: a system for function minimization and analysis of the parameter errors and corrections. *Comput. Phys. Commun.*, 10(CERN-DD-75-20):343–367. 38 p.

[97] James, G., Witten, D., Hastie, T., and Tibshirani, R. (2014). *An Introduction to Statistical Learning: With Applications in R*. Springer Publishing Company, Incorporated.

[98] Jia, Y. et al. (2014). Caffe: Convolutional Architecture for Fast Feature Embedding. *ArXiv e-prints*.

[99] Judah, M. (May 9, 2018). *Nue CC Inclusive update*. NOvA internal document (docdb-29417).

[100] Jyoti, T. (2017). Study of a New Target Design with an Additional Horn for NuMI Beam. In *Meeting of the APS Division of Particles and Fields (DPF 2017) Batavia, Illinois, USA, July 31-August 4, 2017*.

[101] Kafka, G. (July 29, 2013). *Far over Near Extrapolation technote*. NOvA internal document (docdb-9579).

[102] Kalman, R. E. (1960). A new approach to linear filtering and prediction problems. *Journal of Basic Engineering*, 82:35–45.

[103] Kalra, D. (2017). *Private conversation*.

[104] Kanika Sachdev, X. B. (July 4, 2015). *Spill level Data Quality - technical note*. NOvA internal document (docdb-12437).

[105] Krishnapuram, R. and Keller, J. M. (1993). A possibilistic approach to clustering. *Trans. Fuz Sys.*, 1(2):98–110.

[106] Kuiper, N. H. (1960). Tests concerning random points on a circle. *Indagationes Mathematicae (Proceedings)*, 63:38 – 47.

[107] Lein, S. M. (2015). *Muon Neutrino Contained Disappearance in NOvA*. PhD thesis, Minnesota U.

[108] Lozier, J. (December 23, 2014). *Modular Extrap Technical Note*. NOvA internal document (docdb-12563).

[109] M. Del Tutto, G. K. (July 1, 2015). *Beam Simulation Plots - Blessing Package*. NOvA internal document (docdb-13524).

[110] Maan, K. K. (April 1, 2016). *K+ normalization and the electron neutrino flux using Near Detector data*. NOvA internal document (docdb-15081).

[111] Maki, Z., Nakagawa, M., and Sakata, S. (1962). Remarks on the unified model of elementary particles. *Progress of Theoretical Physics*, 28(5):870–880.

[112] Méndez, D. (April 22, 2016). *Second analysis calorimetric energy scale calibration of the NOvA detectors*. NOvA internal document (docdb-13579).

[113] Mendez, D. (July 19, 2017b). *Optimization by maximal mixing rejection*. NOvA internal document (docdb-21692).

[114] Mendez, D. (September 15, 2017a). *Event selection for the Third disappearance analysis*. NOvA internal document (docdb-23234).

[115] Messier, M. (July 10, 2013). *Neutrino detectors*. NOvA internal document (docdb-9452).

[116] Messier, M. (June 1, 2012). *Vertex reconstruction based on Elastic Arms*. NOvA internal document (docdb-7530).

[117] Mufson, S., Pla-Dalmau, A., and Elvira, P. (August 22, 2014). *Density of the NOvA liquid Scintillator at* $69^{\circ}F$. NOvA internal document (docdb-11886).

[118] Nayak, N. (October 10, 2017). *Hadron production systematics for the NOvA Oscillation analysis*. NOvA internal document (docdb-22532).

[119] Nelson, J. (Janyary 30, 2015). *Results from MINERvA low-energy test beam experiment*. NOvA internal document (docdb-12713).

[120] Niner, E. (January 5, 2015a). *Timing Calibration Technical Note*. NOvA internal document (docdb-13579).

[121] Niner, E. (July 2, 2012). *Vertex Clustering with Possibilistic Fuzzy-K Means Algorithm*. NOvA internal document (docdb-7648).

[122] Niner, E. (March 30, 2016). *CAFAna Tutorial*. NOvA internal document (docdb-15025).

[123] Niner, E. et al. (2014). Synchronization of the 14 kTon NOνA neutrino detector with the Fermilab NuMI beam. *J. Phys. Conf. Ser.*, 513:012028.

[124] Niner, E. D. (2015b). *Observation of Electron Neutrino Appearance in the NuMI Beam with the NOvA Experiment*. PhD thesis, Indiana U.

[125] Norman, A. et al. (2012). The nova timing system: A system for synchronizing a long baseline neutrino experiment. *Journal of Physics: Conference Series*, 396(1):012034.

[126] Ohlsson, M. et al. (1992). Track finding with deformable templates - the elastic arms approach. *Computer Physics Communications*, 71(1):77 – 98.

[127] Paley, J. M. et al. (2014). Measurement of Charged Pion Production Yields off the NuMI Target. *Phys. Rev.*, D90(3):032001.

[128] Para, A. and Szleper, M. (2001). Neutrino oscillations experiments using off-axis NuMI beam.

[129] Patrignani, C. et al. (2016). Review of Particle Physics. *Chin. Phys.*, C40(10):100001.

[130] Patterson, R. (August 6, 2015). *First Oscillation Results from NOvA - JETP Seminar*. NOvA internal document (docdb-13856).

[131] Perl, M. L. et al. (1977). Properties of the Proposed tau Charged Lepton. *Phys. Lett.*, 70B:487–490.

[132] Perl, M. L. e. a. (1975). Evidence for anomalous lepton production in $e^+ - e^-$ annihilation. *Phys. Rev. Lett.*, 35:1489–1492.

[133] Pershey, D. (April 11, 2015). *Birks-Chou parameter selection.* NOvA internal document (docdb-13158).

[134] Phan-Budd, S. and Goodenough, L. (July 6, 2015). *Technical note on the NOvA Beam Monitoring for 2015 Summer Analysis.* NOvA internal document (docdb-13572).

[135] Poutissou, J. M. (1995). Long baseline neutrino oscillation experiment at the AGS. In *'95 electroweak interactions, unified theories. Proceedings, Leptonic Session of the 30th Rencontres de Moriond, Moriond Particle Physics Meetings, Les Arcs, France, March 11-18, 1995*, pages 491–496.

[136] Raby, S. et al. (1997). *Celebrating the Neutrino.* Number 25. Los Alamos Science.

[137] Raddatz, N. (June 18, 2015). *KalmanTrack Technical Note.* NOvA internal document (docdb-13545).

[138] Raddatz, N. J. (2016). *Measurement of Muon Neutrino Disappearance with Non-Fiducial Interactions in the NOνA Experiment.* PhD thesis, Minnesota U.

[139] Rebel, B. (June 9, 2010). *Cosmic Ray Tracker Update.* NOvA internal document (docdb-4855).

[140] Rein, D. and Sehgal, L. M. (1981). Neutrino Excitation of Baryon Resonances and Single Pion Production. *Annals Phys.*, 133:79–153.

[141] Rodrigues, P. A. et al. (2016). Identification of nuclear effects in neutrino-carbon interactions at low three-momentum transfer. *Phys. Rev. Lett.*, 116:071802.

[142] Rosen, S. P. and Gelb, J. M. (1986). Mikheyev-smirnov-wolfenstein enhancement of oscillations as a possible solution to the solar-neutrino problem. *Phys. Rev. D*, 34:969–979.

[143] Ryan Murphy, Barnali Chowdhury, J. C. (November 7, 2017). *Good Data Selection*. NOvA internal document (docdb-13546).

[144] Sachdev, K. (September 16, 2013). *Muon-Removed Charged Current: A Technical Note*. NOvA internal document (docdb-9729).

[145] Schael, S. et al. (2006). Precision electroweak measurements on the Z resonance. *Phys. Rept.*, 427:257–454.

[146] Schroeder, R. (June 14, 2016). *Wrong sign neutrino contamination and beam nue content for FHC/RHC*. NOvA internal document (docdb-15658).

[147] Sepulveda, J. (August 23, 2017a). *Data driven threshold + shadowing: update*. NOvA internal document (docdb-22619).

[148] Sepulveda, J. (December 7, 2017b). *Muon energy corrections and binning for uncontained events*. NOvA internal document (docdb-26331).

[149] Sepulveda, J. (October 24, 2017d). *Sensitivities and predictions for uncontained FD events*. NOvA internal document (docdb-24466).

[150] Sepulveda, J. (September 14, 2017c). *Rock muons at the Far Detector*. NOvA internal document (docdb-23294).

[151] Sepulveda-Quiroz, J. A. (March 23, 2017). *Report - CosRej for uncontained events presel*. NOvA internal document (docdb-18021).

[152] Singh, P. (February 24, 2016). *Status: 2nd Analysis Calibration work*. NOvA internal document (docdb-14840).

[153] Singh, P. (September 15, 2017). *The Attenuation and Threshold calibration of the NOvA detectors*. NOvA internal document (docdb-13579).

[154] Strait, M. (April 17, 2018). *Tech note on using neutrons to find NC and RHC numu contamination.* NOvA internal document (docdb-22955).

[155] Strait, M. (October 23, 2017). *Muon energy scale systematic.* NOvA internal document (docdb-20816).

[156] Sutter, L. and Musser, J. (April 29, 2016). *SA Data Quality updates.* NOvA internal document (docdb-15307).

[157] Toner, R. (October 23, 2014). *The Drift Calibration.* NOvA internal document (docdb-11691).

[158] Torbunov, D. (September 29, 2017). *NuMu Energy Estimator Technote for Prod3 MC.* NOvA internal document (docdb-23342).

[159] Vinton, L. (2018). *Measurement of Muon Neutrino Disappearance with the NOvA Experiment.* PhD thesis, Sussex U.

[160] Vinton, L. (April 28, 2016a). *ND normalization with rock muons.* NOvA internal document (docdb-15292).

[161] Vinton, L. (July 22, 2015). *Calorimetric energy scale calibration of the NOvA detectors.* NOvA internal document (docdb-13579).

[162] Vinton, L. (May 9, 2016b). *Noise systematic for the disappearance analysis.* NOvA internal document (docdb-15216).

[163] Walcott, J. and Bays, K. (September 13, 2017). *Cross section central value tune and uncertainties for the 2017 analysis.* NOvA internal document (docdb-23264).

[164] Wolfenstein, L. (1978). Neutrino oscillations in matter. *Phys. Rev. D*, 17:2369–2374.

[165] Wu, C. S., Ambler, E., Hayward, R. W., Hoppes, D. D., and Hudson, R. P. (1957). Experimental test of parity conservation in beta decay. *Phys. Rev.*, 105:1413–1415.

[166] Xin, T. (April 19, 2016a). *Data driven Threshold and shadow correction technical note.* NOvA internal document (docdb-15223).

[167] Xin, T. (January 28, 2016c). *Discussion on Data Driven Threshold and Shadow Correction.* NOvA internal document (docdb-14566).

[168] Xin, T. (March 31, 2016b). *Data-driven threshold correction.* NOvA internal document (docdb-12483).

[169] Yang, M.-S. and Wu, K.-L. (2006). Unsupervised possibilistic clustering. *Pattern Recognition*, 39(1):5 – 21.

[170] Yu, S. (April 10, 2018). *BENDecomp Technical note for nue 2018 analysis.* NOvA internal document (docdb-27833).

[171] Zamorano, B. (July 3, 2015). *Misalignment systematic uncertainty for the first analysis.* NOvA internal document (docdb-13639).

[172] Zuber, K. (2004). *Neutrino Physics.* Series in High Energy Physics, Cosmology and Gravitation. Institute of Physics Pub, Oxford, England.

[173] Zálešák, J. et al. (2014). The nova far detector data acquisition system. *Journal of Physics: Conference Series*, 513(1):012041.